

Universidade de São Paulo  
Instituto de Astronomia, Geofísica e Ciências Atmosféricas  
Departamento de Ciências Atmosféricas

Danilo Couto de Souza

# Cyclones in Southwestern Atlantic: Life Cycle and Energetics

São Paulo

2024



Danilo Couto de Souza

# Cyclones in Southwestern Atlantic: Life Cycle and Energetics

Tese apresentada ao Programa de Meteorologia do Instituto de Astronomia, Geofísica e Ciências Atmosféricas da Universidade de São Paulo como requisito parcial para a obtenção do título de Doutor em Ciências.

Área de Concentração: Meteorologia

Orientador: Prof. Dr. Pedro Leite da Silva  
Dias

Coorientador: Prof. Dr. Ricardo de Camargo

São Paulo

2024



*To the boundless beauty of nature, which has been my greatest teacher and source of inspiration.*



# Acknowledgements

## *Acknowledgments*

First and foremost, I would like to express my deepest gratitude to my family for their unwavering support and encouragement throughout this journey. To my loving girlfriend, Juliana, your patience and understanding have been my rock, and I could not have completed this work without you.

I am immensely grateful to my advisors, Pedro Dias and Ricardo de Camargo, for their invaluable guidance, insightful feedback, continuous support, and friendship. Your expertise and dedication have greatly enriched my research experience and have inspired me every day.

I would also like to acknowledge my former advisors, Renato Ramos da Silva, Roberto Carelli Fontes, and John Beardall, for their foundational support and mentorship during the early stages of my academic career.

A heartfelt thank you to my great friend Igor Gamella, who often acted as my programming mentor and provided invaluable support. Your guidance and assistance have been indispensable to my work.

To my colleagues, Matheus Bonjour, Renan Godoy, Maria Luiza Kovalski, Luis Andres Rodrigues, Rodrigo Tecchio, Victor Ranieri, and the entire MASTER team, thank you for your camaraderie and support. Your collaboration and friendship have made this journey enjoyable and rewarding.

I am also grateful for the technical support provided by Jean Peres, Djalma, Sebastião, and Samuca. Your help in resolving technical issues was crucial for the smooth progress of my research.

A special thanks goes to the researchers and professors who provided me with invaluable assistance: Carolina Gramcianinov, Pedro Peixoto, and Felipe Bragança Alves. Your advice and guidance have been instrumental in the completion of this work.

I would also like to extend my heartfelt thanks to the entire IAG community: professors, students, and staff. Your friendliness and support have made the IAG an incredible learning environment. Thank you for fostering a welcoming and stimulating atmosphere that has greatly enriched my academic journey.

I would also like to thank Karate-dō for teaching me discipline and hard work, as well as perseverance and resilience. Additionally, I am grateful to the ocean for also imparting lessons of perseverance and resilience. These lessons have been invaluable, and I will carry them with me throughout my life.

Finally, I would like to express my appreciation to Alexandra Elbakyan, Aaron Swartz, and the entire open-source community. Your contributions to the free and open access to knowledge have been invaluable to my research and burgeoning academic career.

“一、努力の精神を養うこと”

“First, foster the spirit of effort”

“Primeiro, criar o intuito do esforço”

Kanga Sakukawa



# Resumo

Resumo



## Abstract

Abstract



## List of Figures

2.1	Air Masses . . . . .	31
2.2	Phase Diagram - Hart . . . . .	33
2.3	Bjerknes Cyclone Model . . . . .	34
2.4	Bjerknes' and Shapiro-Keyser's Cyclonic Models . . . . .	36
2.5	Tropical Cyclone - Cross Section . . . . .	38
2.6	Phase Diagram - Hart . . . . .	39
2.7	Extratropical Cyclone - Cross Section . . . . .	41
2.8	Model of development of cyclones types A and B. . . . .	44
2.9	Comparison - CISK vs. WISHE . . . . .	46
2.10	Conceptual Model: Instabilities and Types of Cyclones . . . . .	51
2.11	Global Circulation . . . . .	53
2.12	Tropical Cyclone as a Carnot Cycle . . . . .	54
2.13	Cyclogenesis Regions in the South Atlantic . . . . .	58
2.14	Extratropical Cyclone Life Cycle . . . . .	65
2.15	Effects of Heating and Cooling on Potential Energy . . . . .	68
2.16	Available Potential Energy . . . . .	69
2.17	Energy Cycle - Lorenz . . . . .	71
2.18	Energy Cycle - Muench . . . . .	72
2.19	Energy Cycle - Brennan . . . . .	74
2.20	Energy Cycle - Michaelides . . . . .	76
2.21	Eulerian LEC - Issues . . . . .	77
2.22	LEC - Discussion . . . . .	79
2.23	$C_Z$ - Representation . . . . .	84

2.24	$C_A$ - Representation . . . . .	85
2.25	Zonal and Meridional Jets . . . . .	86
2.26	Meridional Jet With Eddy . . . . .	87
2.27	LEC - Chains . . . . .	93
3.1	Flowchart depicting the methodological steps used in this thesis. (A) Retrieval of the cyclonic system track database using central relative vorticity at 850 hPa. (B) Identification of cyclone life phases with CycloPhaser, categorizing the vorticity time series into distinct phases. (C) Computation and analysis of the Lorenz Energy Cycle for the cyclones to investigate their energetic characteristics. (D) Classification of energy patterns using the K-means algorithm to determine distinct energy characteristics. (E) Examination of dynamical mechanisms related to barotropic and baroclinic instabilities influencing cyclone development. . . . .	104
3.2	Cyclophaser - Logo . . . . .	107
3.3	Cyclophaser - Methodological Steps . . . . .	108
3.4	Residual Stage - Study case . . . . .	111
3.5	Impact of Varying Threshold Values for Intensification Phase . . . . .	113
3.6	Impact of Varying Threshold Values for Decay Phase . . . . .	113
3.7	Variations in Threshold Values for Mature Phase . . . . .	114
3.8	Impact of Varying Threshold Values for Incipient Phase . . . . .	114
4.1	Cyclogenesis Climatology in the SESA Region . . . . .	125
4.2	Life Cycle Configurations . . . . .	126
4.3	Filtered Life Cycle Configurations . . . . .	127
4.4	Cyclone Life Cycles - Representative Examples . . . . .	127
4.5	Life cycle configurations by regions and season . . . . .	128
4.6	PDF - Metrics for Each Region and Season . . . . .	129
4.7	PDF - Total Time . . . . .	132
4.8	PDF - Total Distance . . . . .	133
4.9	PDF - Mean Speed . . . . .	134
4.10	PDF - Mean Vorticity . . . . .	135
4.11	PDF - Mean Growth Rate . . . . .	137

4.12	Mature Phase - Center of Mass . . . . .	137
4.13	Track Density - Incipient Phase . . . . .	139
4.14	Track Density - Intensification Phase . . . . .	141
4.15	Track Density - Mature Phase . . . . .	143
4.16	Track Density - Decay Phase . . . . .	145
4.17	Track Density - Secondary Development Stages . . . . .	147
4.18	Track Density - Intensification 2 . . . . .	149
4.19	Track Density - Mature 2 . . . . .	150
4.20	Track Density - Decay 2 . . . . .	151
4.21	Track Density - Residual Phase . . . . .	153
4.22	Illustrative Representation of Cyclone Life Cycle . . . . .	156
5.1	Box plots - Complete Lifecycle . . . . .	160
5.2	Density Plots - Energy Terms . . . . .	161
5.3	Density Plots - Conversion Terms . . . . .	164
5.4	Density Plots - Boundary Terms . . . . .	166
5.5	Density Plots - Generation Terms . . . . .	167
5.6	Density Plots - Budget Terms . . . . .	168
5.7	LEC - Mean Life Cycle . . . . .	169
5.8	EOF - Explained Variance . . . . .	171
5.9	EOF Analysis - Total Lifecycle . . . . .	172
5.10	Density Plots - Energy Terms . . . . .	176
5.11	Density Plots - Energy Terms . . . . .	178
5.12	Density Plots - Energy Terms . . . . .	181
5.13	Density Plots - Energy Terms . . . . .	183
5.14	Density Plots - Energy Terms . . . . .	185
5.15	LEC - Mean Life Cycle for Each Phase . . . . .	187
5.16	LEC - Mean Life Cycle for Each Phase . . . . .	191
5.17	EOF - Explained Variance for Each Phase . . . . .	193
5.18	Reconstructed EOF1 - Phases . . . . .	195
5.19	Reconstructed EOF2 - Phases . . . . .	196
5.20	Reconstructed EOF3 - Phases . . . . .	198

5.21 Reconstructed EOF4 - Phases . . . . .	199
6.1 LPS 1 - "Reg1" Cyclone . . . . .	204
6.2 LPS 2 - "Reg1" Cyclone . . . . .	206
6.3 Elbow Method . . . . .	207
6.4 LPS 1 - Clusters - All Life Cycle Configurations . . . . .	209
6.5 LPS 2 - Clusters - All Life Cycle Configurations . . . . .	211
6.6 LPS 1 - Clusters - Seasonality and Spatial Variability . . . . .	212
6.7 LPS 2 - Clusters - Seasonality and Spatial Variability . . . . .	213
6.8 Energy Patterns . . . . .	215
6.9 Energy Patterns - Mean Intensity . . . . .	216
6.10 Energy Patterns - Frequency by Region . . . . .	217
6.11 Energy Patterns - Seasonality . . . . .	217
6.12 Energy Patterns - Interannual Variability . . . . .	218
6.13 Ca and Ck - Vertical Distribution . . . . .	219
6.14 Rayleigh Criterion and EGR . . . . .	221
6.15 LPS for Fixed Framework Systems . . . . .	223
6.16 Rayleigh Criterion and EGR - Fixed Framework . . . . .	224
6.17 Comparative Analysis . . . . .	226
6.18 LPS 1 - Dynamical Processes . . . . .	230
6.19 LPS 2 - Dynamical Processes . . . . .	231
C.1 Reconstructed EOFs . . . . .	266
D.1 Correlation Between LEC Terms . . . . .	267
E.1 Computational Domain - Reg1 System . . . . .	269
E.2 Energy and Conversion Terms - Reg1 System . . . . .	270
F.1 LPS 1 - All Systems . . . . .	272
F.2 LPS 1 - All Systems . . . . .	273
G.1 LPS 1 - Cluster 3 - DItMD . . . . .	275
H.1 LPS 1 - Most Intense Systems . . . . .	277

I.1	Tracks - EP1	279
-----	--------------	-----



## List of Tables

5.1	Summary Statistics of Lorenz Energetics Components . . . . .	162
5.2	Statistical Analysis Results for Different Phases . . . . .	175



# Contents

1. <i>Introduction</i> . . . . .	25
1.1 Motivation . . . . .	25
1.2 Scientific goals . . . . .	26
2. <i>Theoretical Background</i> . . . . .	29
2.1 Cyclones: Categories and Definitions . . . . .	29
2.1.1 Material Causes . . . . .	30
2.1.2 Formal Causes . . . . .	34
2.1.3 Efficient Causes . . . . .	39
2.1.4 Final Causes . . . . .	51
2.1.5 Summary . . . . .	55
2.2 Cyclones in South America . . . . .	56
2.2.1 Climatological aspects . . . . .	56
2.2.2 Genesis mechanisms . . . . .	58
2.2.3 Subtropical cyclones . . . . .	60
2.2.4 Tropical cyclones . . . . .	61
2.3 Life cycle of extratropical cyclones: objective classification procedures . . . . .	62
2.4 Atmosphere Energetics . . . . .	67
2.4.1 Lorenz Energy Cycle: Historical Background . . . . .	67
2.4.2 Lorenz Energy Cycle: Mathematical expressions and physical interpretation . . . . .	80
2.4.3 Lorenz Energy Cycle applied to cyclonic systems . . . . .	93

3.	<i>Data &amp; Methods</i>	103
3.1	Methodological Steps	103
3.2	Databases	104
3.2.1	ERA5 Reanalysis	104
3.2.2	Cyclone Tracks in the South Atlantic	105
3.3	Cyclone's Life Cycle Detection	106
3.3.1	Cyclophaser Program Description	106
3.3.2	Cyclophaser Settings	112
3.4	Lorenz Energetics Computation	115
3.5	Analysis methods	116
3.5.1	Probability Density Functions	116
3.5.2	Cyclone Track Densities	117
3.5.3	Statistical Analysis	117
3.5.4	Empirical Orthogonal Functions	118
3.5.5	K-means Algorithm	119
3.6	Investigation of Dynamical Mechanisms	120
3.6.1	Criteria Used	120
3.6.2	Composites	121
4.	<i>Life Cycle of Cyclones in the Southwestern Atlantic</i>	123
4.1	Climatology and Statistics	123
4.1.1	Climatological Aspects and Life Cycle Configurations	124
4.1.2	Mean Cyclone Statistics	126
4.1.3	Life Cycle Phase Statistics	131
4.2	Spatial Distribution of Cyclone Life Cycle Phases	138
4.2.1	Incipient Phase	138
4.2.2	Intensification Phase	140
4.2.3	Mature Phase	142
4.2.4	Decay Phase	144
4.2.5	Secondary Development Phases	146
4.2.6	Residual Phase	152
4.3	Summary and Concluding Remarks	154

5.	<i>Southwestern Atlantic Cyclones Energetics Climatology</i>	159
5.1	Complete Life Cycle Climatology	159
5.1.1	Descriptive Statistics	159
5.1.2	Mean Energy Cycle	168
5.1.3	EOFs	170
5.2	Climatology Across Life Phases	173
5.2.1	Descriptive Statistics	173
5.2.2	Mean Energy Cycle	186
5.2.3	EOFs	192
5.3	Summary and Concluding Remarks	200
6.	<i>Energetic Patterns of Cyclones in the Southwestern Atlantic</i>	203
6.1	Lorenz Phase Space and Energy Patterns	203
6.1.1	Introducing the Lorenz Phase Space	203
6.1.2	Energetic Patterns for All Life Cycle Configurations	207
6.1.3	Energetic Patterns - Seasonality and Spatial Variability	210
6.1.4	Energy Patterns - Characteristics	214
6.2	Physical Mechanisms	218
6.2.1	Barotropic and Baroclinic Instability	218
6.2.2	Comparing with the Fixed Framework	222
6.3	Summary and Concluding Remarks	227
7.	<i>Conclusions</i>	233
7.1	Summary of Main Findings	233
7.2	Final Remarks and Recommendations for Future Work	234
	<i>Bibliography</i>	237
	<i>Appendix</i>	259
A.	<i>Lanczos Filter</i>	261
A.1	Formulation	261
A.2	Related Issues	261

<i>B. Lorenz Energy Cycle Program Description</i>	263
<i>C. Complete Life Cycle LEC EOFs Reconstructed</i>	265
<i>D. LEC - Terms Correlation</i>	267
<i>E. LEC Results for Reg1 System</i>	269
<i>F. Lorenz Phase Space - All Systems</i>	271
<i>G. Lorenz Phase Space 1 - Early Decay</i>	275
<i>H. Lorenz Phase Space - Most Intense Systems</i>	277
<i>I. Tracks - Energy Pattern 1</i>	279

# Chapter 1

---

## Introduction

Cyclones are an important part of the Earth's climate system. These systems are characterized by low atmospheric pressure at their center and rotating winds. Cyclones can be classified into different types, including tropical cyclones, extratropical cyclones, and subtropical cyclones, each distinguished by their physical characteristics. Cyclones play a significant role in the redistribution of heat and moisture across the Earth's surface, impacting weather patterns and climatic conditions. Additionally, cyclones can lead to severe weather events such as heavy rainfall, strong winds, and storm surges, posing substantial risks to life, property, and ecosystems. Understanding cyclones is vital for improving weather forecasting, disaster preparedness, and mitigating the adverse effects of these systems.

### 1.1 Motivation

Surface cyclones are crucial features for weather and climate in South America and the Southwestern Atlantic sector. They significantly influence the precipitation regimes on the continent, impacting both seasonal and annual rainfall patterns (Reboita et al., 2010, 2018). These cyclones can potentially cause extreme precipitation events, leading to flooding and landslides that can disrupt communities and infrastructure (de Souza and da Silva, 2021; de Souza et al., 2024). Furthermore, the occurrence of cyclones is related to natural hazards along the South American coast due to their extreme winds (de Souza and da Silva, 2021; Cardoso et al., 2022), which can cause substantial damage to buildings, power lines, and other structures. High sea waves generated by cyclones (Guimarães et al., 2014; Gramcianinov et al., 2023, e.g.) pose risks to maritime activities and can affect

shipping routes and port operations. The potential for cyclones to cause storm surges (?Albuquerque et al., 2018; Leal et al., 2023, e.g.) can lead to significant coastal flooding, endangering coastal communities and ecosystems, while also contributing to coastal erosion (Parise et al., 2009, e.g.) that can undermine coastal defenses and infrastructure. Overall, the economic costs of cyclones in South America can be substantial, affecting livelihoods, infrastructure, and economic stability across various sectors. This reinforces the necessity of a detailed understanding of the mechanisms related to their genesis and intensification so that this knowledge can be incorporated into numerical models, ultimately improving forecasts.

## 1.2 Scientific goals

Given the importance of cyclonic systems for weather and climate in the South Atlantic sector, it is crucial to ensure accurate and precise forecasts of these systems. Recent studies have investigated cyclonic systems' projections for this region, primarily focusing on climatological trends (Reboita et al., 2018; de Jesus et al., 2022, e.g.). How cyclone dynamics will change under climate change scenarios, especially in the South Atlantic region, remains an open question. However, a deep understanding of their current dynamics is necessary first. Although recent investigations have advanced the understanding of cyclone genesis and development in the South Atlantic (Dias Pinto and Rocha, 2011; Dias Pinto et al., 2013; Gozzo et al., 2014; Reboita et al., 2018; Gramcianinov et al., 2019, e.g.), most studies focus on case studies, and a climatological view of the dynamic mechanisms is still lacking. Furthermore, current cyclone climatologies offer only a unified view of the cyclone life cycle, not allowing for the geographical positioning and dynamical mechanisms of each phase to be investigated. Given this context, the main goal of the current thesis is to **determine the main dynamical mechanisms related to cyclone development in each of their development phases**. For this, the Lorenz Energy Cycle will be employed. Secondary scientific goals include:

- Devise a climatology for each cyclone life phase
- Investigate the mean spatial distribution for each development phase
- Create a climatology of the energetics of cyclonic systems in the Southern Atlantic

and Southeast South America regions

- Define patterns in the energy climatology
- Reveal the main energy fluxes related to cyclonic development in each life cycle phase



## Chapter 2

---

# Theoretical Background

### 2.1 Cyclones: Categories and Definitions

For an effective analysis and study, a phenomenon must first be accurately defined. The Glossary of Meteorology by American Meteorological Society (2012) characterizes a "cyclone" as "An atmospheric cyclonic circulation, a closed circulation. A cyclone's direction of rotation (counterclockwise in the Northern Hemisphere) is opposite to that of an anticyclone. (...) Because cyclonic circulation and relative low atmospheric pressure usually coexist, in common practice the terms cyclone and low are used interchangeably. Also, because cyclones are nearly always accompanied by inclement (often destructive) weather, they are frequently referred to simply as storms". This definition categorizes cyclones into sub-types based on their occurrence location: tropical, extratropical, and subtropical cyclones (Reboita et al., 2017, e.g.). This classification is supported by the assumption that cyclones within the same latitude bands share genesis environments and dynamic maintenance processes. There are also cyclones whose genesis is found in high latitudes, called polar lows (Emanuel and Rotunno, 1989; Harrold and Browning, 1969, e.g.). These will not be discussed in depth as the focus of the present study is on the systems generated in the adjacent regions to the South American coast.

The aforementioned definition, while broad, lacks precise criteria. Thus, subsequent sections will employ the Aristotelian approach to elucidate physical phenomena (Aristotle and Aristotle, 1933). Aristotelian causes, foundational to Aristotle's philosophy, offer a comprehensive explanation for an object or phenomenon's existence through four types: material, formal, efficient, and final causes. The ensuing subsections will detail each cause, enhancing the understanding of related phenomena. For each cyclone type — extratropical

and tropical — a discussion of the causes will facilitate a direct comparison between the systems.

It is important to note that the structure and mechanisms underlying the genesis and development of cyclones have been well-documented since the mid-twentieth century, leading to the inclusion of many historical references. The aim is to highlight distinctions between cyclone types, a comparison not commonly made in literature. Meteorologists often specialize as "tropical meteorologists" or "mid-latitude meteorologists", a division reflected in educational materials. Some texts focus exclusively on mid-latitude or tropical dynamics (Chan and Kepert, 2010; Bluestein, 1992, e.g.), while others that address both, treat them separately (Holton, 1973; Donald Ahrens and Henson, 2015, e.g.). Although this separation is customary and beneficial, juxtaposing the two offers novel insights, as explored in the following sections.

### 2.1.1 Material Causes

Material cause, within the Aristotelian framework, denotes the substance or constituents that form an object. It encompasses the matter or physical elements constituting an entity, serving as the foundation for its existence. For instance, wood acts as the material cause for a table, just as water serves as the material cause for a river. Applied to cyclonic systems, the material cause encompasses the air masses forming these systems, particularly emphasizing their thermal structure. This section elaborates on this concept, showcasing its relevance in defining and categorizing cyclonic systems.

The concept of an air mass, as introduced by Swedish meteorologist Tor Bergeron in 1928, describes a large body of air characterized by uniform temperature, moisture, and other properties, extending over 500 to 5000 km and encompassing the troposphere's full height (Stull, 2015). Air masses are classified based on their temperature, moisture content, stratification, and turbidity levels. Additionally, air masses originate from specific source regions, areas conducive to their formation. The characteristics of an air mass are significantly influenced by its source region's surface conditions, necessitating a flat terrain and mild winds for its development (Donald Ahrens and Henson, 2015). Heat transfer between the surface and the air is gradual, requiring the air mass to remain over its source region for an extended period to assimilate its properties (Spiridonov and Ćurić, 2021). Therefore, mid-latitudes, characterized by variable meteorological conditions and strong

winds, are generally unsuitable for air mass formation.

Bergeron's classification system is the most widely accepted methodology for categorizing air masses. It utilizes letters to denote the moisture content and the origin of air masses (Spiridonov and Ćurić, 2021). The initial letter signifies the air mass's moisture source—continental (dry) or maritime (moist)—while the subsequent letter indicates the geographical origin of the air mass, whether it be tropical (T), polar (P), arctic/antarctic (A), equatorial (E), or monsoonal (M). Figure 2.1 illustrates the spatial distribution of air masses according to Bergeron's scheme. Upon the encounter of two distinct air masses, immediate mixing does not occur, resulting in a temporary discontinuity at their intersection, known as fronts (Spiridonov and Ćurić, 2021; Donald Ahrens and Henson, 2015).

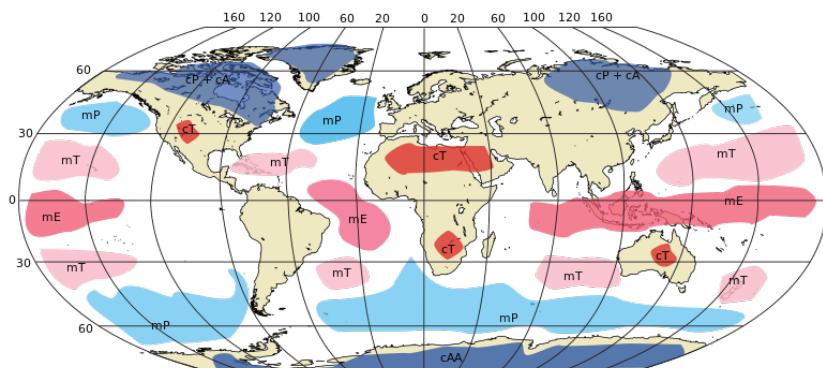


*Figure 2.1:* Spatial distribution of air masses according to Bergeron's classification. Credit: public domain (<https://commons.wikimedia.org/w/index.php?curid=12526643>).

Therefore, the validity of the traditional cyclone classification—tropical, extratropical, and subtropical—relies on the premise that different types of cyclones are initiated by distinct air masses. Specifically, tropical cyclones originate from warm, moist air masses that span the entire troposphere and form over warm tropical waters (Gray, 1968; Frank, 1977a; Ramage, 1959; Riehl, 1948). In contrast, extratropical cyclones are associated with frontal zones at mid-latitudes, where two different air masses meet, and are typically linked to cold cores (Bjerknes and Holmboe, 1944; Shapiro and Keyser, 1990; Hart, 2003). However, intense marine extratropical cyclones can experience warm seclusion, resulting in a warm core at the system's center (Hart, 2003; Shapiro and Keyser, 1990). Subtropical cyclones feature a hybrid structure between tropical and extratropical systems, with warm, moist cores that are less pronounced and shallower than those in tropical cyclones (Hart, 2003).

Hart (2003) offers an objective methodology for identifying the thermal structure of cyclonic systems. This analysis focuses solely on tropospheric levels (up to 300 hPa) because cyclones display an opposing thermal signal in the stratosphere. The study examines layers between 900 and 600 hPa and between 600 and 300 hPa, which have comparable masses. Levels below 900 hPa are excluded to prevent extrapolation below the ground or into the boundary layer, which may not accurately represent the cyclone's structure in the free atmosphere. Consequently, the variable corresponding to the cyclonic perturbation in height is defined as follows:

$$\Delta Z = Z_{MAX} - Z_{MIN} \quad (2.1)$$

Where  $Z_{MAX}$  and  $Z_{MIN}$  represent the maximum and minimum geopotential heights at a specific isobaric level, measured within a 500 km radius from the cyclone's center. Following this definition:

$$\Delta Z = \frac{dg|V_g|}{f} \quad (2.2)$$

Here,  $d$  denotes the distance between the geopotential height extremes,  $g$  is the acceleration due to gravity,  $f$  represents the Coriolis parameter, and  $V_g$  is the geostrophic wind speed. Consequently, the cyclone's vertical structure (indicative of a cold or warm core) is determined by the vertical gradient of  $\Delta Z$ , which is proportional to the magnitude of the scaled thermal wind ( $V_T$ ) for a constant  $d$ , applied across two tropospheric layers of equal mass:

$$\left. \frac{\partial(\Delta Z)}{\partial \ln p} \right|_{600hPa}^{300hPa} = -|V_T^U| \quad (2.3)$$

$$\left. \frac{\partial(\Delta Z)}{\partial \ln p} \right|_{900hPa}^{600hPa} = -|V_T^L| \quad (2.4)$$

where  $V_T^U$  and  $V_T^L$  symbolize the thermal winds at upper and lower levels, respectively. As such, positive values of  $-V_T$  signify a warm core within the respective layer, whereas negative values indicate a cold core.

The relationship between the temperature and depth of the core within cyclonic systems is detailed through a phase diagram by Hart (2003), depicted in Figure 2.2. This diagram utilizes the abscissas to represent the parameter  $-V_T^L$ , illustrating the low-level core's

thermal structure. The ordinates display  $-V_T^U$ , portraying the high-level core's thermal structure. Integrating these metrics allows for discerning whether a system possesses a warm or cold core, and if it is shallow or deep. Figure 2.2 includes typical positions representative of different cyclonic types within the phase space. As noted by Hart (2003), a system may shift within this diagram throughout its lifecycle, making the depiction general for each cyclone category. Additionally, Hart proposes a diagram for the horizontal structure of these systems, related to their formal causes, which is addressed in Section 2.1.2.

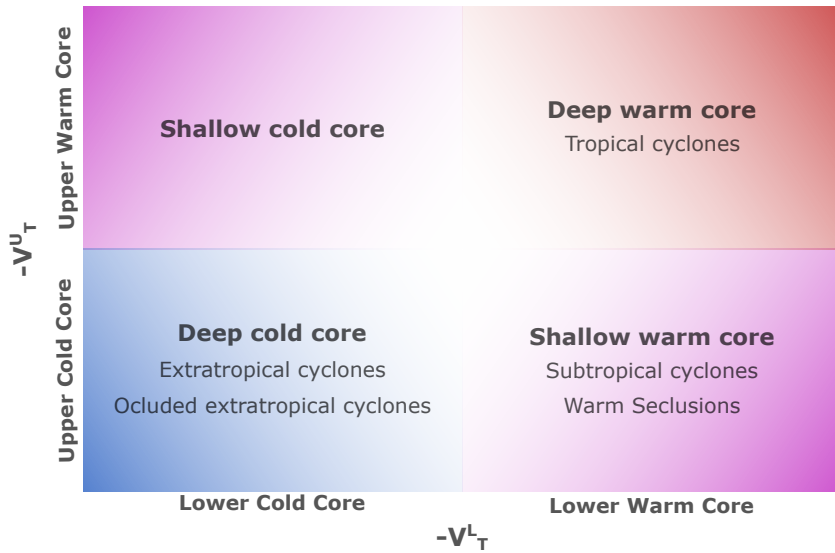


Figure 2.2: Phase diagram showing the relationship between the core temperature of cyclonic systems and their classification. Adapted from Hart (2003).

Thus, material causes, tied to the thermal structure of cyclonic systems, offer a foundational method for classifying and differentiating cyclone types. This classification leverages the phase diagram by Hart (2003) for an objective categorization. Accordingly, extratropical cyclones are characterized by cold, deep cores, whereas tropical cyclones feature warm, deep cores. This spectrum isn't binary; there exists a gradient of thermal structures with systems exhibiting intermediate features classified as subtropical cyclones. Nevertheless, relying solely on thermal attributes for classification is insufficient. For instance, extratropical cyclones, through the warm seclusion process (Shapiro and Keyser, 1990, e.g.), can develop warm, shallow cores (Hart, 2003), indicating the necessity for a broader analysis incorporating additional Aristotelian causes for a comprehensive classification.

### 2.1.2 Formal Causes

The formal cause concerns the essence or identity that defines a thing, essentially its design, structure, or conceptual blueprint that marks it as a particular type. To revisit the earlier example of a table from Section 2.1.1, its formal cause is the design that qualifies it as a table rather than a chair. In the context of cyclones, the formal cause refers to the system's organizational structure, such as the configuration of convection bands and/or fronts, along with the low-pressure pattern.

Extratropical cyclones, typically associated with mid-latitudes and frontal structures, exhibit an average diameter between 1200 and 1800 km. This size fluctuates over their lifecycle, with the cyclone's diameter expanding by up to 150% during its intensification phase (Simmonds, 2000; Rudeva and Gulev, 2007). However, the spatial complexity and variability of these systems throughout their lifecycle pose methodological challenges for accurately estimating their dimensions and comparing findings across different studies.

The seminal model describing the formation and horizontal structure of extratropical cyclones was introduced by Bjerknes (1919), illustrated in Figure 2.3. This model showcases the cyclone's movement along a central horizontal line, with the "steer line" demarcating the boundary that influences the cyclone's trajectory, characterized by warm air masses to its left. The "squall line" indicates a zone of intense meteorological activity, marked by strong winds and often heavy precipitation, with cold air masses located to its left. The "fore runner" represents a region of diverging airflow.

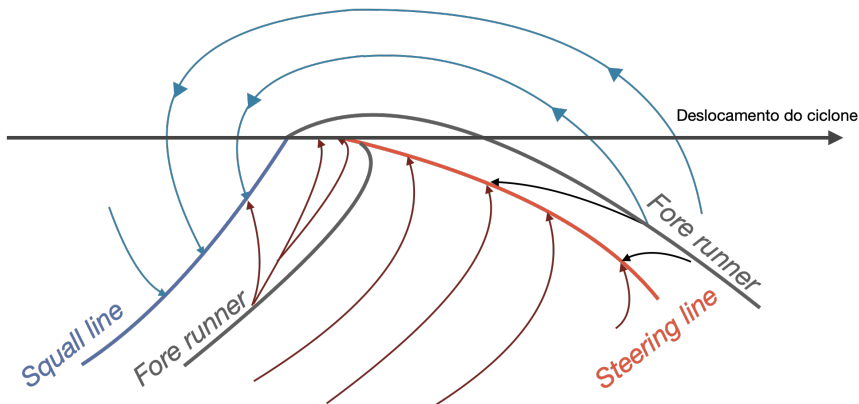


Figure 2.3: Representation of the Bjerknes model for the extratropical cyclone formation process and its horizontal structure. Cold air regions are illustrated with blue lines, while warm air regions with red lines. Adapted from Bjerknes (1919).

Bjerknes and Solberg (1922) realized that the model proposed in Bjerknes (1919) repre-

sented just one phase in the life cycle of cyclones, indicating that there are several stages of development. Bjerknes and Solberg (1922) established the Polar Front Theory, which is the foundation of the so-called Norwegian cyclone model. Schultz et al. (1998) synthesizes and describes the development of extratropical cyclones according to this theory, so that a visual representation of the horizontal structure at the surface during different stages of cyclone evolution is found in Figure 2.4a. In the first stage, the incipient cyclone presents a narrow and long cold front, and a wide and short warm front (Figure 2.4aI). After this, the cyclone deepens, with a narrowing of the warm section of the cyclone through the rotation of the cold front towards the warm front (Figure 2.4aII). As cold air is denser and, therefore, facilitates more intense horizontal pressure gradients, it moves faster than the warm air. As the cold air at the front of the cyclone approaches the cold air at the rear of the system (Figure 2.4aIII), the warm air is trapped in the center of the system, a phenomenon called warm seclusion. As the cold front continues to move, the warm air at the surface is overtaken by the cold air and is forced to ascend to upper levels. This process is called occlusion, being responsible for trapping the cold air in the core of the system (Figure 2.4aIV). With the continuation of occlusion, the baroclinicity along the warm front can become so diffuse that the cyclone appears not to have a well-defined warm front.

Bjerknes and Solberg (1922) acknowledged that the model presented in Bjerknes (1919) captured only a singular phase in the life cycle of cyclones, leading to the development of the Polar Front Theory. This theory defines what is known as the Norwegian cyclone model. Schultz et al. (1998) provides a synthesis of extratropical cyclone development according to this theory, including a depiction of the surface horizontal structure at various stages of cyclone evolution in Figure 2.4a. Initially, the nascent cyclone features a narrow, elongated cold front and a broader, shorter warm front (Figure 2.4aI). Subsequently, the cyclone deepens as the cold front rotates toward the warm front, narrowing the cyclone's warm sector (Figure 2.4aII). Given the greater density of cold air, which generates stronger horizontal pressure gradients and moves more swiftly than warm air, the cold front eventually encroaches on the system's rear cold air (Figure 2.4aIII), trapping warm air at the system's center—a process known as warm seclusion. As the cold front progresses, the surface-level warm air is displaced by cold air and forced upward, a phenomenon termed occlusion, which entraps cold air at the system's core (Figure 2.4aIV). The occlusion process may eventually diffuse the baroclinicity along the warm front to such an extent that

the cyclone seems to lack a distinct warm front.

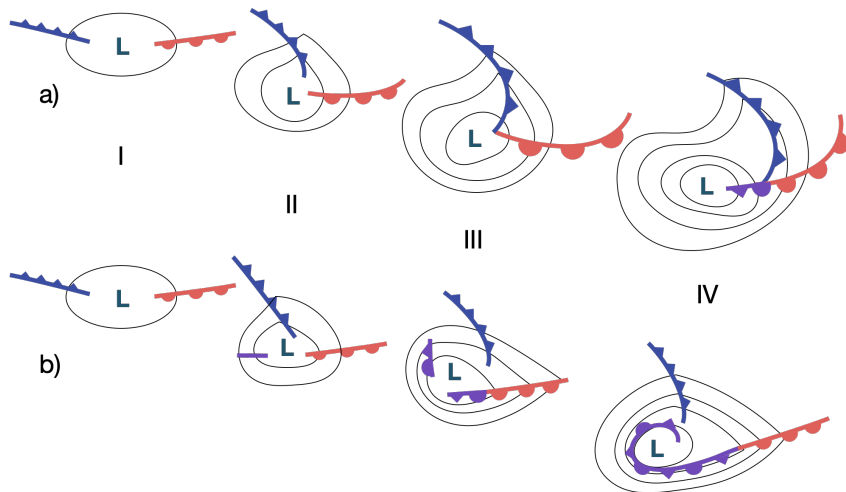


*Figure 2.4: Cyclonic models by Bjerknes (1919) (a) and Shapiro and Keyser (1990) (b), illustrating the systems' horizontal structure across different developmental stages (I to IV). Adapted from Schultz et al. (1998).*

From the advancements enabled by the satellite era, Shapiro and Keyser (1990) introduced a revised cyclonic model, acknowledging that not all observed cyclones conformed to the Norwegian model. Termed the Shapiro-Keyser model, it is also summarized by Schultz et al. (1998), with its visualization in (Figure 2.4b). Initially mirroring the development outlined by Bjerknes and Solberg (1922) (Figure 2.4bI), this model diverges as the cold front extends perpendicularly to the warm front instead of encircling the system (Figure 2.4bII). As the system strengthens, the polar side of the cold front weakens, allowing the warm front to encircle the system's western sector (Figure 2.4bIII). At peak intensity, cold air encases the warm air near the cyclone's center, creating a warm seclusion (Figure 2.4bIV).

Schultz et al. (1998) emphasizes that these models are complementary rather than mutually exclusive, suggesting that the Norwegian model is more applicable to systems forming under diffluent flow with significant amplitude, often at the terminal end of storm tracks and on western continental edges, characterized by a meridional elongation of the cyclone and its fronts. Conversely, the Shapiro-Keyser model is more suited to systems emerging under confluent, low amplitude base flow, typically exhibiting east-west elongation. However, these models alone do not fully account for the formal causes of extratropical cyclones, indicating a continuum where different systems may align more closely with one

model or the other (Schultz et al., 1998).

Tropical cyclones, unlike their extratropical counterparts, lack frontal structures and exhibit organized, symmetric circulation near the surface, forming over warm tropical or subtropical waters with intense winds below the surface (Frank, 1977a; Gray, 1968). Their diameters vary, ranging from 100 to 1000 km at maturity, expanding up to 2000 km during intensification. However, the area of intense convection and stronger winds typically spans a radius of about 100 km (Holton, 1973).

Characterized by a central cyclonic circulation at lower tropospheric levels and anticyclonic circulation in the upper troposphere, tropical cyclones are associated with intense precipitation and horizontal pressure gradients, leading to spiraled winds near the surface that become increasingly circular towards the system's center, or eye (Frank, 1977a,b; Terry, 2007; Weatherford and Gray, 1988). These systems exhibit more intense pressure gradients—and consequently stronger winds—than extratropical cyclones (Spiridonov and Ćurić, 2021). Based on wind speed, they are classified into tropical depressions (maximum winds less than 60 km/h), tropical storms (winds between 60 and 110 km/h), and tropical cyclones (winds exceeding 110 km/h) (Spiridonov and Ćurić, 2021). Their nomenclature varies by region: "hurricanes" in the North Atlantic and North Pacific, "typhoons" in the Northwest Pacific, and "cyclones" in the Indian Ocean (Donald Ahrens and Henson, 2015).

The structure of tropical cyclones comprises three main components: the eye, the eye wall, and surrounding convection bands (Figure 2.5). The eye is the calm, warm central region, with a radius of 5 to 50 km, encircled by the eye wall—a cloud ring about 10 to 20 km wide where intense upward vertical movements occur, facilitating mass transport to higher levels (Shea and Gray, 1973; Jorgensen et al., 1985). Although these vertical movements are typically less vigorous than those in extratropical cyclones (Jorgensen et al., 1985), the inner core, consisting of the eye and eye wall, hosts the most intense winds and lowest atmospheric pressures (Weatherford and Gray, 1988). The primary convection band, a nearly stationary feature, spirals inward from the system's outer edges towards the eye wall, where it becomes roughly tangent (Willoughby et al., 1984).

Given the delineated formal causes (organizational structure) for both extratropical and tropical cyclones, it's evident that their structures diverge significantly. Simplified, extratropical cyclones, forming at the interface between distinct air masses, are associated with frontal systems, providing them an asymmetric feature. Conversely, tropical cyclones

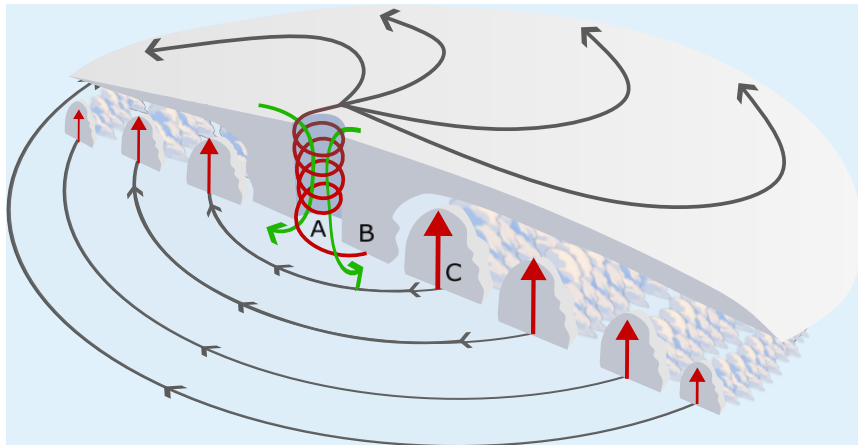


*Figure 2.5:* Cross-sectional view of a mature tropical cyclone in the Southern Hemisphere, illustrating the eye (A), eye walls (B), and convection bands (C), along with upward (red arrows) and downward (green arrows) vertical movements, horizontal wind movement (grey arrows), and sea-level pressure contours. Inspired from: Bluestein (1992).

exhibit symmetry, characterized by a circular eye and spiraled convection bands extending from the eye wall. Addressing this distinction, Hart (2003) introduces a metric assessing the relative thickness asymmetry between the 900 and 600 hPa levels, termed the *B* parameter:

$$B = h \left( \overline{Z}_{600\text{hPa}} - \overline{Z}_{900\text{hPa}} \right)_R - \left( \overline{Z}_{600\text{hPa}} - \overline{Z}_{900\text{hPa}} \right)_L \quad (2.5)$$

where  $Z$  represents the isobaric height,  $R$  and  $L$  denote the right and left sides relative to the system's motion, the overbar signifies an average over a 500 km semicircle, as defined in Equation 2.1, and  $h$  is a constant set to +1 or -1 for the northern and southern hemispheres, respectively. Mature tropical cyclones exhibit a  $B$  value near zero, indicating thermal symmetry (non-frontal), while extratropical cyclones show significant  $B$  values, signaling thermal asymmetry (frontal). Positive  $B$  values suggest the presence of warm air to the right of the cyclone in the southern hemisphere (and vice versa in the northern hemisphere), aligning with the thermal wind relationship from quasi-geostrophic theory (Sutcliffe, 1947; Trenberth, 1978).

Hart (2003) proposed a diagram correlating symmetry with  $V_T^L$  (Equation 2.4), depicted in Figure 2.6, offering a supplementary classification to that shown in Figure 2.2. Here, extratropical cyclones are categorized as cold and asymmetric (frontal), whereas tropical cyclones are warm and symmetric (non-frontal). Like the earlier diagram, this classification suggests a continuum, with systems displaying intermediate features labeled as subtropical.

Unlike solely thermal-based classifications, this model allows for differentiation of extra-tropical cyclones undergoing occlusion, as these systems begin to exhibit symmetry during this phase. Hence, the diagram involving the  $B$  parameter and  $V_T^L$  presents an objective methodology to classify cyclones' formal causes.

While the phase diagrams by Hart (2003) facilitate objective classification criteria for cyclonic systems, gaps remain. For instance, warm seclusions share formal and material causes with hybrid systems, leading to potential misclassification by forecasters and climate data analysis algorithms using these diagrams exclusively. Additionally, polar lows, characterized by both a warm core and symmetric structure, were initially likened to hurricanes (Rasmussen, 1989; Emanuel and Rotunno, 1989; Nordeng and Rasmussen, 1992; Rasmussen, 1985, 1979). However, recent studies, such as Stoll et al. (2021), suggest their spiral bands and thermal core may result from the warm seclusion process, as per the Shapiro-Keyser cyclone development model. These discussions underscore that material and formal causes alone do not suffice for a comprehensive cyclone classification, necessitating further analysis.

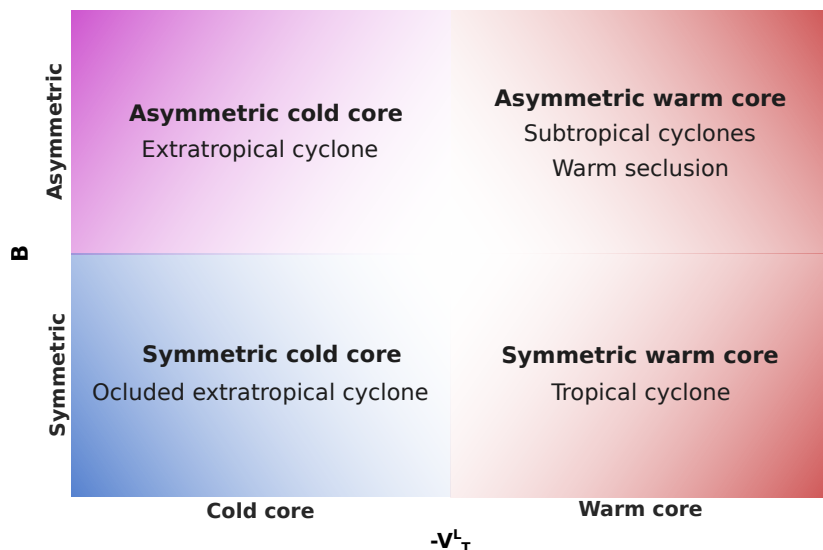


Figure 2.6: Phase diagram illustrating the relationship between cyclonic systems' core temperature and symmetry, offering a distinct classification procedure. Adapted from Hart (2003).

### 2.1.3 Efficient Causes

The efficient cause represents the agent or process that leads to the creation or transformation of something, answering the "how" or "why" behind an occurrence. It encompasses

the actions or processes that result in the existence of an entity. For example, in the creation of a table, the carpenter serves as the efficient cause. In the context of cyclones, the efficient cause includes the physical and dynamic processes responsible for their formation and intensification. These processes essentially act as destabilization mechanisms, triggering atmospheric disturbances that evolve into a cyclonic configuration.

While the polar front theory offers a descriptive perspective, it falls short of providing a comprehensive theoretical model for the physical processes involved in system formation. Still, it related these processes with thermal contrasts in the atmosphere, or baroclinic zones (Bjerknes, 1919; Bjerknes and Solberg, 1922), describing cyclones as emergent phenomena arising at the boundary of two distinct air currents—polar and tropical—flowing in opposite directions (east-west and west-east, respectively), differentiated by thermal contrasts (cold and warm, respectively). A destabilization of the flow occurs when the velocity difference between these currents surpasses a critical threshold, generating a frontal wave that intertwines the currents and reduces their velocity contrast. Some of these frontal waves are unstable and can spontaneously amplify, representing the genesis mechanism of cyclones according to this theory.

The Polar Front Theory provides a detailed account of the structure and formation processes of extratropical cyclones, as shown in Figure 2.7, depicting a transverse model of a developing cyclone (Bjerknes and Solberg, 1922). This model features horizontal isotherms indicative of temperature variations parallel to the ground, with warm air central to the model, characteristic of the warm front, and cold air on the edges. Initially (Figure 2.7a), the isotherms of cold air extend horizontally until convergence forces the ascent of warm air to higher atmospheric levels. This conversion of potential to kinetic energy continues as the cold air from both sides of the cyclone advances to mid-atmospheric levels, further driving the ascent of warm air. The adiabatic cooling of ascending warm air leads to temperature equalization and depletion of the system's potential energy reserve, while the air mass movement is then sustained by inertia. After occlusion (Figure 2.7b and c), inertia maintains the ascent of cold air, which cools adiabatically, utilizing the system's kinetic energy to counteract gravity. Initially, there is still kinetic energy production at high levels and its consumption at low levels. However, as the elevated warm sector cools and temperatures equalize (Figure 2.7d), kinetic energy production halts. Eventually, friction outweighs kinetic energy production, leading to its dissipation.

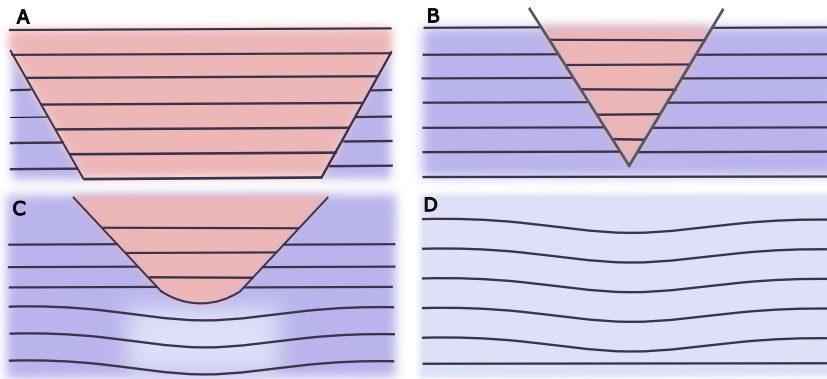


*Figure 2.7:* Cross-sectional depiction of an extratropical cyclone’s development through its various stages, adapted from Bjerknes and Solberg (1922). Stage A shows horizontal isotherms where cold air converges, leading to the ascent of warm air. In Stage B, the system begins occlusion as cold air advances to mid-atmospheric levels, further promoting the ascent of warm air. Stage C continues the occlusion, with sustained ascent of cold air by inertia and kinetic energy consumption. Stage D represents the cessation of kinetic energy production as temperatures equalize and friction begins to dominate, leading to energy dissipation. Warm (red) and cold (blue) sectors are indicated alongside the isotherm lines.

Since the advent of the polar front theory, our comprehension of atmospheric dynamics has evolved significantly, incorporating new concepts into the understanding of extratropical cyclones. This evolution has led to a diverse array of approaches aimed at describing the dynamic and thermodynamic processes underlying the genesis and development of these systems. Consequently, there is no singular, unified theory regarding extratropical cyclogenesis. For instance, Bjerknes and Holmboe (1944) identified the formation regions of extratropical cyclones as zones of dynamic instability associated with the westward-flowing jet stream, employing the tendency equation to analyze atmospheric instability. Other studies have approached cyclogenesis through various lenses, including slantwise convection, the omega equation, potential vorticity, primitive equations, and diabatic processes (Hoskins, 1990, e.g.). Additionally, Schultz et al. (1998)’s work categorizes cyclones into those aligning with the Norwegian model versus the Shapiro-Keyser model, differentiating them based on environmental conditions related to the base state flow (diffluent for the former and confluent for the latter). This section will primarily focus on the development of these systems from the perspective of dynamic destabilization mechanisms in the atmosphere, linking these mechanisms to the energetics of transient atmospheric systems, further explored in Section 2.4.

Baroclinic instability ( $I_{BC}$ ) is identified as the principal mechanism behind the deve-

lopment of typical extratropical cyclones (Charney, 1947; Bjerknes and Solberg, 1922). As Holton (1973) explains,  $I_{BC}$  involves the amplification of small disturbances in areas with strong velocity shears, such as jet streams, where the disturbances extract energy from the jet and grow in size and intensity. In the Earth's atmosphere,  $I_{BC}$  is primarily driven by the meridional temperature gradient, especially at lower levels, and is linked to vertical shear via the thermal wind ( $V_T$ ) relationship, frequently occurring in the polar frontal zone. Baroclinic disturbances can also intensify existing temperature gradients, leading to the formation of frontal zones.

Charney (1947)'s seminal study on  $I_{BC}$  sheds light on the intricate mechanisms behind the formation and evolution of weather patterns, including cyclones and long waves in middle and high latitudes. Employing a simplified model that allows for analytical solutions, Charney not only corroborated previously theorized concepts about atmospheric behavior but also deepened the understanding of how wind shear and temperature variations vertically contribute to atmospheric instability. His analysis indicates that mid-latitude westward-flowing currents are inherently dynamically unstable. This insight elucidates how specific disturbances can exponentially grow within a large-scale atmospheric flow field, explicating the process through which such disturbances can amplify and culminate in the characteristic weather systems observed in middle and high latitudes.

Eady (1949) made significant advancements in the understanding of  $I_{BC}$  in the atmosphere, building on the work of Charney (1947). Eady's research, which employed a solvable simplified model, delved into the atmospheric instability arising from disturbances that exponentially grow within a large-scale atmospheric motion context. His analysis elucidated how specific conditions of stability, wind shear, and vertical temperature variations contribute to  $I_{BC}$ , proposing a mechanism for the formation and evolution of weather patterns such as cyclones and long waves in middle and high latitudes. Eady highlighted how these disturbances grow exponentially faster than others, akin to a process of natural selection in the atmosphere, leading to the emergence of predominant weather patterns observed in middle latitudes, including cyclonic systems.

Following the seminal works of Charney (1947) and Eady (1949), Palmén and Newton (1969) synthesized the main findings from the subsequent extensive literature on  $I_{BC}$ . Firstly, it is noted that the amplification of atmospheric disturbances is wavelength-dependent, with disturbances below a critical length never amplifying. The optimal growth occurs

in intermediate wavelengths (between 2500 and 5000 km), with an inverse relationship between this optimum and latitude—the closer to the Equator, the larger the critical size below which all waves are unstable. Additionally, there exists a proportional relationship between the intensification rate and vertical wind shear for wavelengths of maximum instability, and for longer waves, an increase in wavelength necessitates stronger shear to maintain equivalent growth rates.

In their analysis, Petterssen and Smebye (1971) categorizes extratropical cyclones into types based on the dynamic processes driving their development. Type A cyclones follow the Polar Front Theory model, with the initial disturbance arising at low levels within a maximal baroclinic zone (frontal), beneath a nearly zonal upper-level jet (Figure 2.8iA). As these cyclones develop, a cold trough forms at high levels (Figure 2.8iB), remaining inclined to the cyclone's axis until occlusion occurs and surface baroclinicity diminishes (Figure 2.8iC). Conversely, type B cyclones initiate from high-level forcing, as an upper-level trough moves over an area not necessarily featuring a frontal zone (Figure 2.8iiA). As these systems mature, the gap between the high-level trough and the surface system narrows, with an increase in surface baroclinicity relative to the initial stage (Figure 2.8iiB), culminating in the alignment of the high-level cyclonic vortex with the surface low, leading to system occlusion (Figure 2.8iiC).

Just as Hart (2003)'s classification presents a continuum, so too does Petterssen and Smebye (1971)'s delineation of cyclone types, with A and B not being distinct categories due to the existence of systems displaying hybrid characteristics. Petterssen and Smebye (1971) observed that purely type A cyclones are more common, whereas purely type B cyclones are rare, attributing this to the fact that some type of baroclinicity is often present in the mid-latitudes. However, Petterssen noted a tendency for type A cyclones to develop over oceans and type B cyclones over continents, though subsequent research, such as by McLennan (1988) and Deveson et al. (2002), has identified type B systems forming over oceanic regions as well. Furthermore, Deveson et al. (2002) introduced a new classification, type C cyclones, found in high latitudes with similarities to polar lows, characterized by an even stronger high-level forcing related to the movement of a broad trough over oceanic regions. This study also highlighted the potential for cyclones to transition between types throughout their lifecycle.

The central role of baroclinic instability ( $I_{BC}$ ) in the development of extratropical cy-

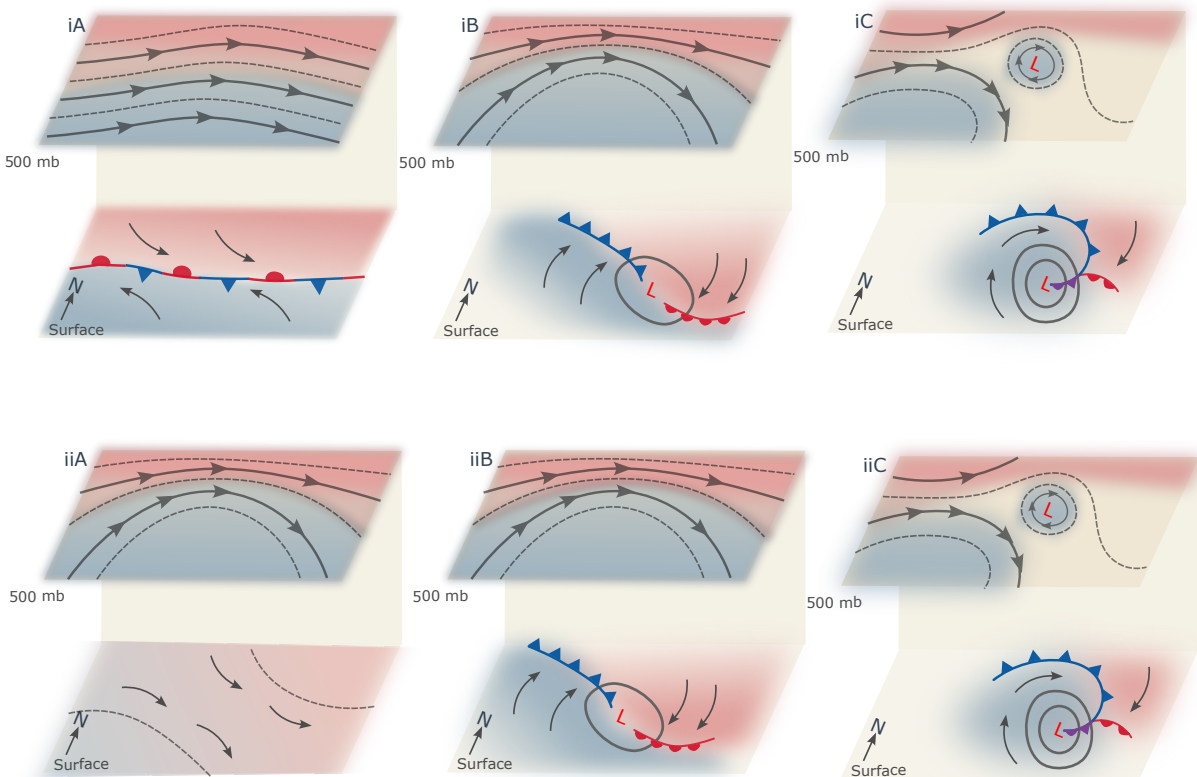


*Figure 2.8:* Illustration of the development model for cyclones types A (i) and B (ii), depicting the stages of formation (A), intensification (B), and maturity (C), as proposed by Petterssen and Smebye (1971). Inspired by Donald Ahrens and Henson (2015).

clones is well-established, yet the significance of heat flows and diabatic heating cannot be overstated. Diabatic heating involves heat exchanges between a system and its surroundings through processes such as condensation, evaporation, or radiation. Convective activities leading to upward atmospheric movements cause diabatic expansion and thus cooling in air parcels, leading to saturation and the release of latent heat. Such mechanisms provide an additional energy source for the development of extratropical cyclones, as documented in the literature (Chang et al., 2002, e.g.). Numerical models incorporating  $I_{BC}$  alongside heat flows have shown that instabilities generated under these conditions yield more intense cyclones with faster development rates (Gall, 1976; Whitaker and Davis, 1994; Gutowski et al., 1992), a phenomenon referred to as moist baroclinic instability.

A pivotal study by Hoskins and Valdes (1990) underscores the importance of diabatic fluxes in the development of extratropical cyclones, demonstrating that cyclonic development is preferentially located in regions of maximal baroclinicity over the oceans. However,

the heat transport facilitated by these systems tends to mitigate the baroclinicity. The study suggests that diabatic heating, through the latent heat release from individual systems, contributes to sustaining regional baroclinicity. It also highlights the role of sensible heat exchanges between the cold air associated with these systems and the warm ocean currents along the eastern coastlines of continents.

Tropical cyclone formation, a topic of ongoing discussion among meteorologists, typically occurs over tropical or subtropical oceans, a region where the scarcity of in situ observations challenges the validation of theoretical models for formation and intensification. During World War II, data collected from the military base in Guam facilitated Riehl (1948) in proposing that the instability necessary for typhoon formation originates within the trade winds, contradicting the then-prevailing belief of inter-hemispheric air mass interactions being the primary cause. Subsequently, Yanai (1961)'s study on Typhoon Doris furthered the understanding of typhoon genesis, highlighting the significant role of latent heat released by convection. Yanai suggested a model for typhoon development, beginning with a disturbance in the trade winds and culminating in the formation of a typhoon characterized by a stabilized warm core.

Charney and Eliassen (1964) detailed the process of tropical cyclone intensification known as conditional instability of the second kind (CISK), which was the most accepted theory at the time (Figure 2.9i). According to CISK, the condensation of water vapor within convective areas releases latent heat, which can amplify pre-existing atmospheric vortices given an adequate moisture supply. This release of heat not only promotes further convection but also lowers sea-level pressure, thereby strengthening surface winds, enhancing moisture influx, and establishing a positive feedback loop. Charney underscored the ocean's surface role in providing the moisture necessary for sustaining convection, as well as the importance of surface friction in dissipating kinetic energy and fostering wind convergence within the moist surface boundary layer, thereby fueling the system with thermal energy from latent heat. This mechanism emphasizes the pivotal role of latent heat release at the cyclone's center as a disturbance amplification factor, leading to the intensification of the tropical depression.

While Charney and Eliassen (1964)'s work introduces a mathematical model for understanding tropical cyclone intensification through the CISK process, it doesn't offer a straightforward, didactic explanation of the involved mechanisms. This has left room for

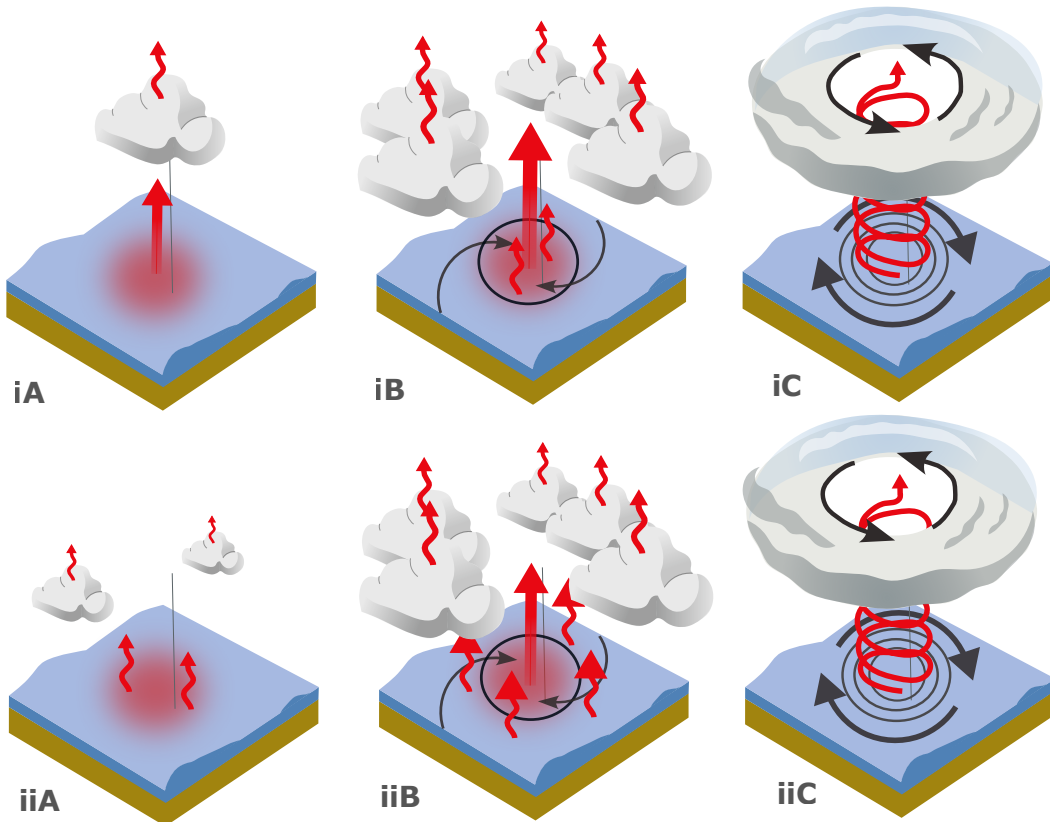


*Figure 2.9:* Comparative illustration of the CISK (i) and WISHE (ii) theories. A depicts the initial disturbance over warm ocean temperatures. Under CISK, the disturbance is initially fueled by latent heat from convection, whereas WISHE attributes the initial energy source to latent heat transfer from the ocean to the atmosphere. In the early development stage (B), both theories observe an increase in convection. CISK suggests this leads to reduced central pressure, drawing in more moisture and enhancing convection, which releases additional heat. WISHE proposes that surface wind interaction with the sea surface at low central pressure enhances heat release from surface water evaporation, further driving convection and subsequent latent heat release. By the tropical storm phase (C), the theories align on the feedback mechanisms fueling system intensification.

various interpretations over the years, not all of which have been accurate, as noted by Ooyama (1982). The explanation provided here aims to simplify the main processes proposed by Charney's for clarity.

Challenging the CISK theory, Emanuel (1986), later refined by Yano and Emanuel (1991), introduced the Wind-Induced Surface Heat Exchange (WISHE) theory, emphasizing ocean-atmosphere interaction as the primary intensification mechanism for tropical cyclones (Figure 2.9ii). WISHE posits that the development of these systems depends on the thermal contrast between the atmosphere and the sea surface, mediated by latent heat transfer from the ocean to the atmosphere. This transfer is significantly amplified

by surface wind speeds, with intense winds elevating evaporation rates and thus, moisture transfer. An initial atmospheric disturbance that promotes wind convergence toward its center can enhance this moisture transfer and convection intensity, fostering a positive feedback cycle. WISHE theory emphasizes the necessity of ocean temperatures exceeding 26°C for sufficient boundary layer convergence, vital for maintaining the system. Similar to CISK, interpretations of WISHE vary, with not all encapsulating the theory's full scope or accuracy (Montgomery and Smith, 2014); thus, the provided explanation concentrates on fundamental aspects for comparative purposes with CISK.

Despite advancements in identifying the prerequisites for tropical cyclone development—such as requisite sea surface temperatures, minimal vertical wind shear, and specific atmospheric conditions—consensus on the precise dynamic processes driving both formation and intensification remains elusive. This ongoing debate in meteorology is exemplified by the contrasting theories of CISK and WISHE, each proposing different intensification mechanisms for tropical cyclones (Craig and Gray, 1996; Gray, 1998; Montgomery et al., 2015; Ooyama, 1982; Montgomery and Smith, 2014, e.g.). Nonetheless, a common point between them is the acknowledgment that diabatic processes, fueled by ocean-atmosphere interactions and given an initial disturbance, are critical for providing energy and further intensifying the system. This section's goal is to delineate the development mechanisms of tropical versus extratropical cyclones, for which the simplified descriptions provided herein offer an adequate overview.

The role of diabatic heating in the intensification of tropical cyclones is underscored by the need for an initial atmospheric disturbance. Frank (1970) conducted an analysis of systems in the North Atlantic that give rise to disturbances capable of developing into tropical cyclones. He identified several sources of these disturbances, including those originating from the Intertropical Convergence Zone (ITCZ) and convection zones within the Caribbean Sea. However, the majority are associated with tropical waves primarily emanating from the African continent. Frank also highlighted the process whereby baroclinic systems transition into warm-core structures through the convection-driven release of latent heat, effectively diminishing the system's original baroclinicity. This phenomenon is now recognized as the tropical transition of extratropical cyclones, a process further explored and detailed in works such as those by Hart (2003).

The genesis of tropical cyclones in the North Atlantic is intricately linked to the for-

mation and development of African easterly waves, with the thermal contrast between the Sahara Desert and cooler southern regions playing a pivotal role in creating the African Easterly Jet (AEJ)—a key factor in generating these waves (Holton, 1973). The foundation for understanding such phenomena was laid by Kuo (1949), who pinpointed barotropic instability in zonal atmospheric flows as a vital mechanism. This instability, marked by a change in the sign of absolute vorticity, involves horizontal wind shear and allows vortexes to extract kinetic energy from the zonal wind flow (Holton, 1973).

Burpee (1972) initially connected African easterly wave development with the instability of the AEJ, due to both horizontal and vertical shears, pointing to the complex interaction between barotropic and baroclinic instabilities in the region. Following this, Rennick (1976) applied a linear pseudo-spectral model based on primitive equations, deducing that barotropic instability acts as a primary catalyst for wave development, while downplaying the roles of vertical shear and latent heat release in the early stages. This assertion was supported by Reed et al. (1977) through observational data, demonstrating that medium and low-level easterly waves meet the criteria for barotropic instability.

An energetic analysis by Norquist et al. (1977) differentiated the destabilization processes over land and ocean, with baroclinic conversion dominating over the continent and barotropic instability gaining importance over oceanic regions—where tropical cyclones predominantly form. More recently, Wu et al. (2012) employed reanalysis data to establish a geographical link between the AEJ’s barotropic instability and the origination points of North Atlantic tropical cyclones, affirming the significance of the AEJ’s barotropic instability in relation to tropical cyclogenesis.

The exploration of barotropic instability’s role in tropical cyclone genesis extends beyond the North Atlantic, encompassing various global regions where similar dynamics foster local tropical cyclogenesis. While initial studies illuminated the significance of barotropic instability in the genesis of African easterly waves and their impact on North Atlantic tropical cyclone formation, subsequent research has broadened our understanding to include other tropical areas. For instance, Zehr (1992) discovered that most tropical cyclogenesis events in the North Pacific are associated with a monsoon trough that encourages local convection.

In addition to easterly waves, different types of tropical disturbances can also disrupt the base state and instigate tropical cyclogenesis. Ferreira and Schubert (1997) used a

shallow water model to show how barotropic instability related to the ITCZ's collapse can initiate a series of tropical disturbances, with some progressing to become tropical cyclones. Further, Bembene et al. (2021) employed a global aquaplanet circulation model to illustrate the significant roles played by the ITCZ's latitudinal position and moisture effects in modulating barotropic instability and, consequently, tropical cyclone genesis, indicating the global influence of barotropic instability on tropical cyclogenesis through theoretical studies.

Observational evidence supports these theoretical insights. Maloney and Hartmann (2001) observed that the Madden-Julian Oscillation (MJO) phases conducive to westerly winds along the Pacific enhance barotropic conversions at low levels, thereby aiding tropical cyclone formation in both the Western and Eastern Pacific. Molinari et al. (1997) noted that temporal variations in the MJO can create conditions favorable for easterly wave growth, thereby affecting tropical cyclogenesis in the Eastern Pacific. Molinari et al. (2000) identified a link between the barotropic instability of the base state, associated with easterly wave occurrence, topographical effects, and the monsoon trough in fostering tropical cyclogenesis in the Eastern Pacific. Lastly, Cao et al. (2012) found that enhanced ITCZ convection during active phases of the Intraseasonal Oscillation generates a mean flow state conducive to barotropic instability, promoting tropical cyclogenesis in the Northwest Pacific.

While subtropical cyclones were identified in earlier works (Simpson, 1952), it wasn't until the study by Hart (2003) that they began receiving significant attention. The body of literature on these systems is still developing, with the processes behind subtropical cyclogenesis and development remaining an active area of research. Yanase et al. (2014) advanced the understanding of cyclone genesis by developing an Environmental Parameter Space, analyzing how cyclone genesis latitude correlates with factors like baroclinicity, relative humidity, vertical velocity, and potential intensity. This last metric predicts a tropical cyclone's maximum possible strength based on environmental conditions such as sea surface temperature and atmospheric temperature profiles. The study found a clear correlation: extratropical cyclones are closely linked to baroclinicity, while tropical cyclones are associated with potential intensity. Conversely, an inverse relationship was noted—extratropical cyclones inversely relate to potential intensity and tropical cyclones to baroclinicity. Subtropical cyclones emerged in a transitional space, influenced by both

baroclinicity and potential intensity, which supports the notion of these systems as hybrids between tropical and extratropical cyclones (Hart, 2003, e.g.). Additionally, da Rocha et al. (2019) suggested that subtropical cyclogenesis could be linked to various synoptic patterns, such as a shallow trough at mid-upper levels, a mid-upper level cutoff low, or a Rex blocking pattern. However, a comprehensive discussion delineating the principal environmental dynamics associated with subtropical cyclone development remains elusive, indicating a need for further investigation in this area.

The discussion provided thus far can be synthesized by comparing the efficient causes related to the development of both extratropical and tropical cyclones. Extratropical systems primarily develop through baroclinic instability, which may be initiated by disruptions in the surface meridional temperature gradient or by the influence of an upper-level trough, linking to baroclinic regions via the thermal wind relationship (Holton, 1973; Spiridonov and Ćurić, 2021). In contrast, tropical cyclone genesis is largely influenced by barotropic instability within the base state atmosphere, with subsequent disturbances intensifying through processes related to latent heat release, as explained by either CISK or WISHE theories.

This comparison illustrates that extratropical cyclone formation is closely tied to thermal variance driving baroclinic instability, whereas tropical cyclone genesis hinges on barotropic instability, succeeded by a reinforcing latent heat release feedback mechanism. Despite the absence of a unified diagram akin to Hart (2003)'s material and formal causes of cyclones, Silva Dias et al. (2004) proposed a conceptual model potentially bridging this gap (Figure 2.10). This model situates extratropical cyclones within the domain of baroclinic instability; tropical cyclones under barotropic instability; and subtropical cyclones where both instabilities might coexist or compete. The model also distinguishes systems by their reliance on diabatic processes, particularly latent heat release.

The viewpoint of Silva Dias et al. (2004) gains partial validation through Yanase et al. (2014)'s analysis, which linked different cyclone types to specific environmental parameters. Furthermore, Yanase et al. (2014) emphasized the critical role of relative humidity across all cyclone categories, supporting Silva Dias et al. (2004)'s emphasis on the essential role of latent heat release in cyclone dynamics. The current study will introduce a conceptual model, detailed in Chapter 6, aiming to synthesize the primary mechanisms driving cyclonic development and explore their broader implications.

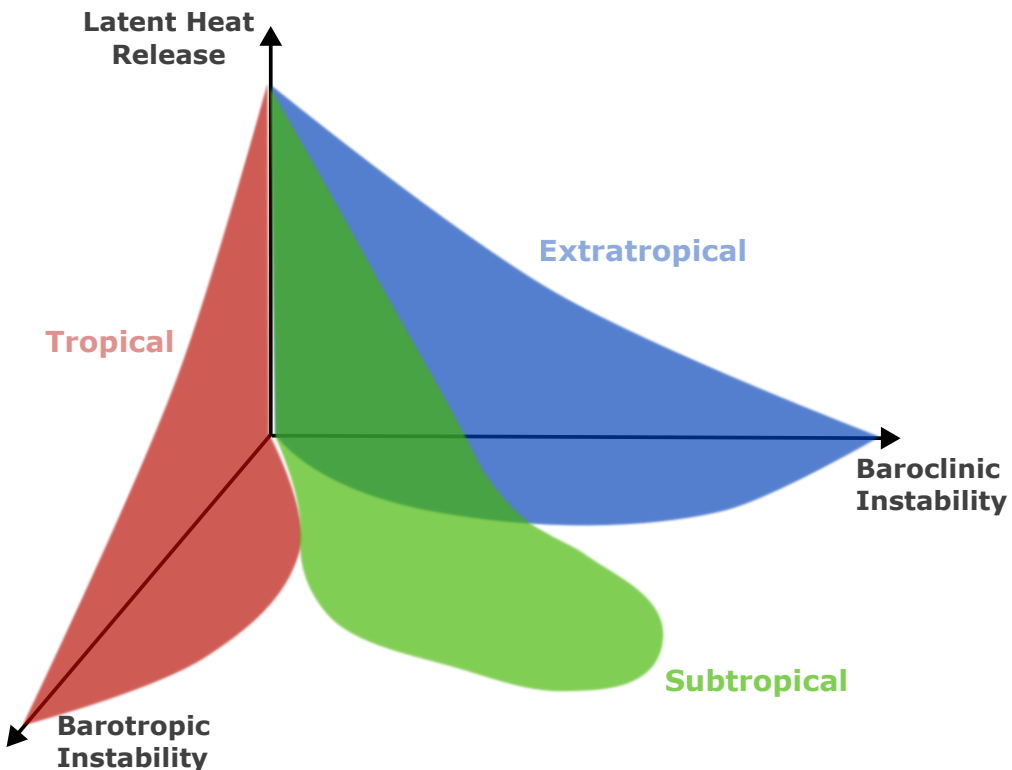


*Figure 2.10:* Proposed conceptual model correlating atmospheric destabilization mechanisms with cyclone types. Each axis within the three-dimensional schema represents a different process of atmospheric destabilization, allowing the categorization of cyclone types across the spectrum. Adapted from Silva Dias et al. (2004).

#### 2.1.4 Final Causes

Final causes delve into the purpose or ultimate reason for the existence of something, offering insights into the "why" behind its occurrence. For instance, the final cause of a table is to serve as a platform for activities such as writing, eating, or working. When considering cyclones, their final cause could be viewed as the facilitation of heat and moisture redistribution within the atmosphere, thus playing a crucial role in maintaining global climatic equilibrium and acting as a mechanism for dissipating excess heat.

The Earth's climate system is fundamentally driven by solar radiation, while simultaneously losing heat through infrared radiation emitted into space. The unequal distribution of solar radiation, exacerbated by the tilt of the Earth's axis, results in energy surpluses in equatorial regions and deficits in polar areas. This differential heating prompts the formation of warm air masses near the equator and cold air masses in polar regions, instigating atmospheric circulation as an effort to achieve thermal equilibrium, a state that remains

elusive due to ongoing differential heating between tropical and polar zones.

Historical and recent advancements in atmospheric science have underscored the significance of general atmospheric circulation in climate dynamics (Lorenz, 1967; Hadley, 1735; Stull, 2015; Schneider, 2006). The Hadley Cell emerges as a critical response to the disparity in solar radiation received at the equator compared to the poles (Figure 2.11). Warmed air rises near the equator, creating low-pressure zones at the surface and high pressure aloft. This ascending air, replaced by cooler air from higher latitudes, moves poleward at elevated altitudes due to mass conservation. The conservation of angular momentum is crucial as this air, moving away from the equator (where surface rotational speed is maximum), must increase its eastward velocity as it approaches the poles. This dynamic leads to the formation of subtropical jet streams around 30° latitude. The Polar Cell, integral to high-latitude atmospheric circulation, is driven by the thermal contrast between the poles and regions at 60° latitude. This temperature difference induces opposing north-south pressure gradients, generating equatorward winds that, due to the Coriolis force, become polar easterlies. At higher levels, winds flow poleward but are deflected eastward, forming an upper-level westerly flow around the polar low, thus completing the Polar Cell circulation.

Together, the Hadley and Polar Cells underscore a comprehensive circulation pattern that transports warm air and angular momentum from the equator towards the poles and vice versa, facilitating Earth's energy balance. Although initially conceptualized as symmetrical circulations extending from the equator to the poles, subsequent research has emphasized the pivotal role of large-scale eddies in heat and angular momentum transfer (Schneider, 2006). These eddies, critical to atmospheric dynamics, emerge due to baroclinic zones in mid-latitudes and are intrinsic to the structure and function of the Ferrel Cell in mid-latitudes (Held, 1999; Schneider, 2006). Arising from mid-latitude baroclinic zones, they are indispensable to the Ferrel Cell's operation, influencing wind patterns across latitudes and enhancing heat transfer between the tropics and poles (Stull, 2015; Held, 1999).

Due to their relatively small scale compared to extratropical cyclones, tropical cyclones are not directly associated with the three-cell model of global circulation. They arise in regions of low baroclinicity, where thermal contrasts are minimal, relying instead on the atmosphere's ability to generate energy from internal heat sources. These sources are largely

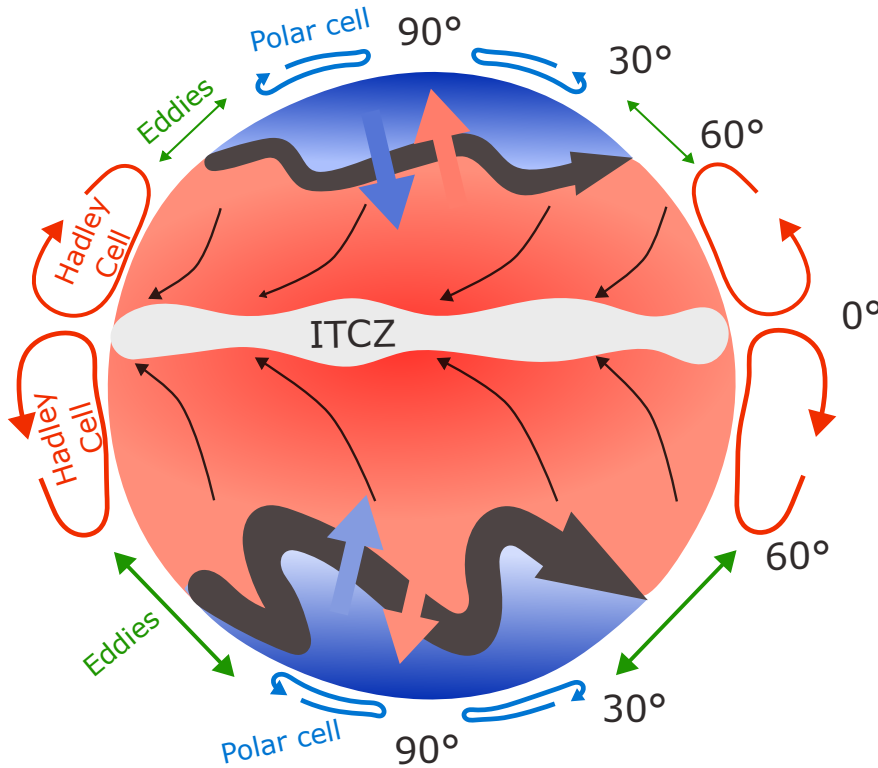


*Figure 2.11:* Representation of the global circulation pattern, showing the Hadley Cell circulation prominent at low latitudes, the transport of momentum and heat by eddies at mid-latitudes, and the polar cell circulation at high latitudes. Inspired by Stull (2015).

the warm temperatures of tropical oceans and the air above them (Palmén and Newton, 1969). Often conceptualized as a Carnot heat engine (Figure 2.12), tropical cyclones draw heat from the ocean surface—primarily through the latent heat of vaporization—and release it into space via longwave radiation (Emanuel, 1987; Ozawa and Shimokawa, 2015; Wang et al., 2022, e.g.,). The cyclone’s intensity depends on the efficiency of this heat engine, which is determined by the temperature difference between the heat source (ocean) and sink (upper atmosphere). Friction, especially near the ocean surface within the boundary layer, plays a crucial role by causing energy loss that can lessen wind speeds and alter angular momentum, impacting the cyclone’s energy conversion efficiency.

We can see then that tropical cyclones serve to dissipate excess heat in the tropics, utilizing oceanic heat to fuel the system while dissipating energy through radiation at the upper levels or friction at the surface. Given this model’s applicability, Emanuel (1987) predicted that rising atmospheric  $CO_2$  levels would lead to more intense tropical cyclones in the future. Recent climate models suggest an increase in tropical cyclone intensity, though

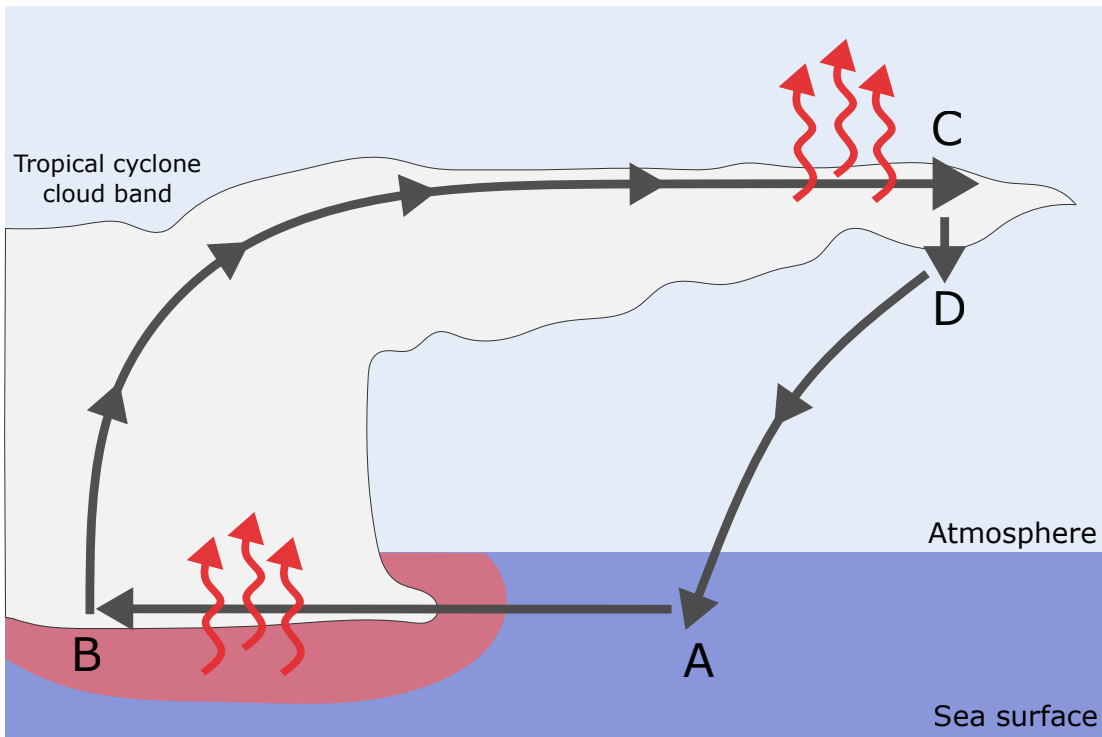


*Figure 2.12: Diagrammatic Representation of a Tropical Cyclone as a Carnot Heat Engine.* The process begins with isothermal inflow (A-B) at the surface, drawing energy from warm ocean waters into the cyclone's core. This stage is succeeded by the upward movement of air (convection) and outward flow just below the tropopause, characterized by radiative cooling and energy loss (B-C). Subsequently, cooled air descends away from the cyclone's center (C-D) and cycles back towards the cyclone, completing the circuit (D-A). Adaptation based on the COMET Program.

there's no global consensus on frequency changes (Knutson et al., 2010; Walsh, 2004; Walsh et al., 2016, 2019). As discussed in Section 2.1.3, understanding tropical cyclone development remains a significant scientific endeavor, complicating precise predictions of their response to climate change and their regulatory effect on climate.

In exploring subtropical cyclones, much remains to be discovered. The global distribution of cyclonic activity exhibits a bimodal pattern, with tropical cyclones forming in tropical regions and extratropical cyclones in mid-latitudes, leaving subtropical areas relatively calm in terms of cyclonic development (Yanase et al., 2014). It's speculative—emphasis on "speculate"—to suggest that subtropical systems share the final causes of their tropical and extratropical counterparts, acting to erase thermal gradients by redistributing heat globally or dissipating excess heat. However, subtropical cyclones might perform these functions under hybrid environmental conditions, possibly moderating gradients in regions with an abundance of heat. Ongoing research into subtropical cyclones promises to pro-

vide further clarity on their impact on global circulation patterns and their role within the broader climatic system.

### 2.1.5 Summary

This section has explored the Aristotelian causes as they pertain to cyclones, comparing the various types—extratropical, tropical, and subtropical—while also acknowledging the existence of other cyclonic phenomena like warm seclusions and polar lows. For succinctness, the discussion primarily centered on the main types, suggesting that cyclonic systems form a continuum: extratropical systems at one end, tropical cyclones at the other, and subtropical systems exhibiting hybrid characteristics.

Initially, we discussed that cyclones' material causes are linked to the air masses constituting them. Extratropical cyclones are associated with cold cores throughout the troposphere, whereas tropical cyclones are characterized by warm cores. Subtropical cyclones, however, display warm cores at the surface and cold cores at higher tropospheric levels.

Regarding formal causes, the cyclones differ in structure. Extratropical cyclones, identified by their frontal features, show asymmetry. Tropical cyclones, described as symmetric, feature convection bands spiraling the central eye. Subtropical cyclones, meanwhile, may present a range of spatial configurations, neither fully asymmetric nor symmetric.

Efficient causes, the dynamic mechanisms behind cyclone development, vary. Extratropical cyclones are primarily driven by baroclinic instability, a comprehensive mechanism underlying their formation. Tropical cyclone genesis and intensification lack a unified theoretical model, with current theories suggesting that barotropic instability in tropical waves—coupled with diabatic processes like latent heat release—might describe their development. Subtropical systems, given the incipient state of research, are speculatively linked by the author to both baroclinic and barotropic instabilities, with diabatic heat playing a role.

The final causes reflect cyclones' contributions to global circulation. Extratropical cyclones are recognized for redistributing heat, mitigating temperature gradients in mid-latitudes. Tropical cyclones, functioning as thermal engines, dissipate excess heat in tropical regions. The role of subtropical cyclones in the climate system remains speculative; they are hypothesized to simultaneously embody the functions of the other two types.

One important feature noted is that most classifications adopted for cyclone classi-

fication are based on Hart (2003) diagrams that objectively distinguishes these systems based on their material and formal causes. Although much knowledge exists regarding the efficient and final causes of tropical and especially extratropical systems, such objective criterion for these causes is still lacking. The current research proposes such objective classification procedure in the hopes of aiding the investigation of such causes related to cyclonic systems.

A notable point is the reliance on Hart (2003)'s diagrams for cyclone classification, objectively differentiating systems by their material and formal causes. While extensive knowledge exists on the efficient and final causes of tropical and particularly extratropical systems, a clear criterion for these causes is absent. This work proposes an objective classification procedure to aid in investigating cyclonic systems' related causes.

## 2.2 *Cyclones in South America*

This section transitions to examining cyclonic phenomena within South America, with a particular emphasis on systems originating in or adjacent to this region. While previous sections have provided a comprehensive overview of various cyclone categories, their structures, formation mechanisms, and roles in atmospheric circulation, here we delve into cyclonic systems that have genesis in South America or its neighboring oceanic regions. Although systems originating along the western coast of South America are noted (Crespo et al., 2023, e.g.), our primary focus is on cyclones forming in the southern and eastern sectors of South America and the Southeastern Atlantic region. These systems significantly influence the regional climate, particularly in South and Southeastern Brazil (de Souza et al., 2022; Reboita et al., 2010, e.g.), and can cause extreme weather events (Cardoso et al., 2022; de Souza and da Silva, 2021; Gramcianinov et al., 2020, e.g.). From this point on, we refer to this region encompassing the Southeastern Atlantic and the adjacent South American region as SESA.

### 2.2.1 *Climatological aspects*

The first cyclone climatology for SESA region was performed by Gan and Rao (1991), utilizing sea level pressure data from surface charts spanning a decade. Despite methodological constraints, the authors identified two primary cyclogenesis regions: one over

Uruguay and another in Southeast Argentina, with the latter being more active in austral summer and the former in winter. They hypothesized that the cyclogenesis in these regions was driven by baroclinic instability of the westerlies and lee cyclogenesis—cyclogenesis influenced by the interaction between baroclinic disturbances and topography (Gan and Rao, 1994; Tibaldi et al., 1980).

Later studies, employing automated techniques to detect cyclones' minimum central pressure, validated the cyclogenesis regions identified by Gan and Rao (1991) (Simmonds and Murray, 1999; Simmonds and Keay, 2000; Mendes et al., 2010). Meanwhile, analyses based on relative vorticity fields, as opposed to minimum central pressure, found a third significant cyclogenesis area near Southeast Brazil (Hoskins and Hodges, 2005; Sinclair, 1995; Reboita et al., 2010; Gramcianinov et al., 2019). The shift towards relative vorticity for cyclone tracking, as discussed by Hoskins and Hodges (2002); Sinclair (1994), offers several technical advantages. In mid-latitudes, the background pressure gradient's intensity can foreshadow closed isobars in developing cyclones, making it challenging to detect cyclones until they intensify or reach higher latitudes. Thus, employing relative vorticity enables the identification of weaker and faster-moving systems, as well as cyclones in their nascent stages, when closed isobars might not yet be evident.

In the SESA region, previous research has successfully identified three key areas of cyclogenesis, and this current study will adopt the nomenclature established by Gramcianinov et al. (2019) for consistency and clarity. The ARG region, situated in Southeast Argentina, emerges as the most active, with a relatively steady cyclogenesis rate throughout the year, though it peaks during the austral summer (Crespo et al., 2021; Gramcianinov et al., 2019; Reboita et al., 2010). The LA-PLATA region, over the La Plata River basin, ranks second in genesis density, displaying heightened activity in the austral winter (Crespo et al., 2021; Gramcianinov et al., 2019; Reboita et al., 2010). It's noteworthy that Reboita et al. (2010) identified the LA-PLATA region along the Uruguayan coast rather than over the continent, influenced by the application of a continental mask in cyclone tracking, which biases detection towards maritime regions. The final region, SE-BR, located near the Southeastern Brazilian coast, records the fewest genesis events, with a significant increase in activity during the austral summer compared to winter (Reboita et al., 2010; Gramcianinov et al., 2019; Crespo et al., 2021). Figure 2.13 summarises these findings.

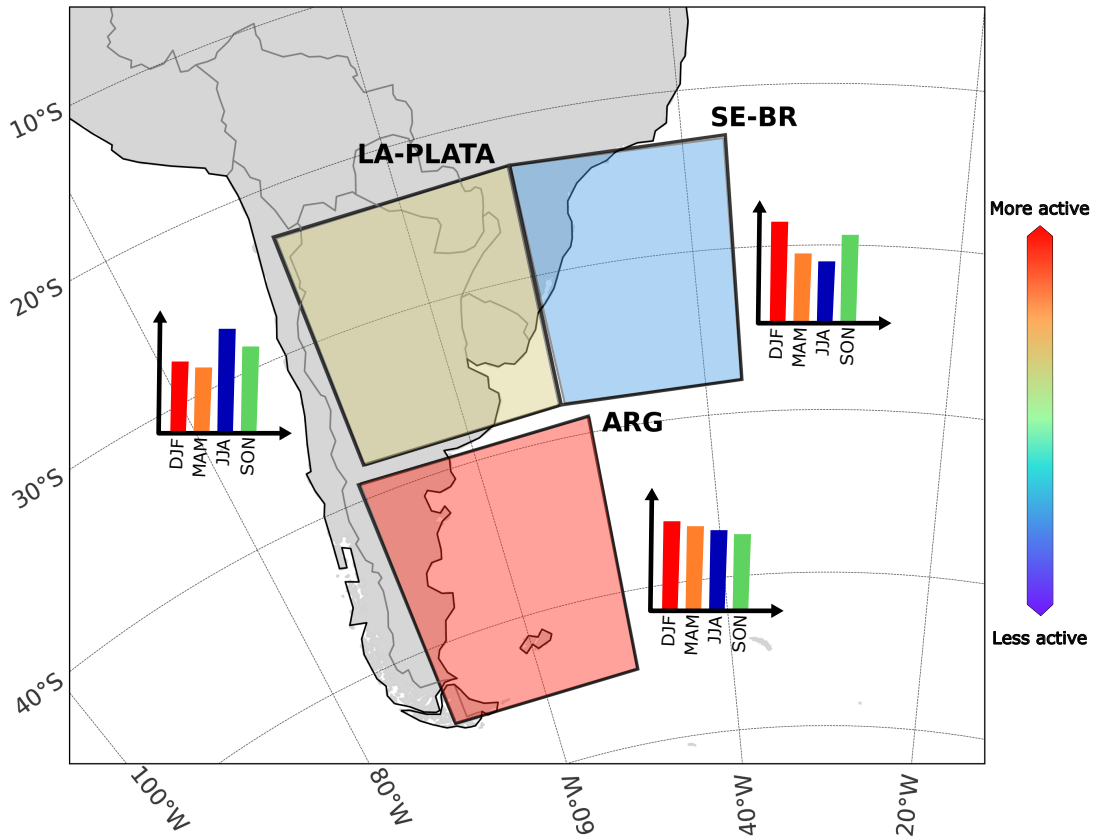


*Figure 2.13:* Illustrative mapping of cyclogenesis activity within the South American/Southeastern Atlantic (SESA) region, categorized into three primary genesis areas: ARG (Southeast Argentina), LA-PLATA (La Plata River basin), and SE-BR (Southeastern Brazilian coast). The diagram highlights the cyclogenesis frequency and seasonal patterns in each region, with a visual scale indicating activity levels from more active to less active.

### 2.2.2 Genesis mechanisms

The majority of systems in SESA region are extratropical (Marrafon et al., 2022), thus baroclinic instability serves as the primary genesis mechanism across all regions, as discussed in Section 2.1.3. However, each region is also influenced by secondary mechanisms. Notably, all regions lie on the lee side of the Andes, where baroclinic development of troughs crossing the mountain range can prompt surface cyclogenesis (Gan and Rao, 1994; Vera et al., 2002; Hoskins and Hodges, 2005; Gramcianinov et al., 2019). Additionally, downstream development, marked by system decay on the Andes' upslope and regeneration on the downslope facilitated by vortex stretching over the mountain barrier, is observed (Hoskins and Hodges, 2005).

Subsequent analyses by Gramcianinov et al. (2019) and Crespo et al. (2021) delve into

the specific genesis mechanisms for each cyclogenesis region. Their findings, synthesized in this section, compare summer and winter mechanisms, as transitional seasons typically exhibit intermediate characteristics (Gan and Rao, 1991; Hoskins and Hodges, 2005; Gramcianinov et al., 2019; Crespo et al., 2021).

In both seasons, cyclones in ARG region tend to follow a traditional baroclinic development pathway, heavily influenced by low level cold advection (Gramcianinov et al., 2019). This advection is crucial in reducing static stability, due to the contrast between the warmer surface and cold air aloft, thereby facilitating cyclogenesis. The cyclogenesis position relative to the jet stream provides upper-level support, either at the poleward exit during summer or the equatorward entrance during winter (Crespo et al., 2021). During summer, a slightly more baroclinic environment and more pronounced potential vorticity anomalies promote conditions favorable for ascending vertical movements (Crespo et al., 2021).

Cyclone development in the LA-PLATA region is initially driven by moisture transport from the South American low-level jet on the eastern slope of the Andes and from the South Atlantic Subtropical High towards the southeastern coast (Gramcianinov et al., 2019). This transport feeds cyclone development with warm, moist air, promoting low-level instability. Furthermore, cyclogenesis in this region is influenced by potential vorticity anomalies in both summer and winter (Crespo et al., 2021). The area is positioned beneath the equatorial entrance of a jet streak in both seasons, with a slightly more pronounced baroclinic environment in winter (Crespo et al., 2021).

During summer, cyclogenesis in the SE-BR region is significantly influenced by the transport of warm and moist air from the tropics, associated with the South Atlantic Convergence Zone (SACZ) (Gramcianinov et al., 2019). This process contributes to cyclogenesis through diabatic heating and convective processes. In winter, upper-level forcing becomes more prominent, with baroclinic conditions intensified by the presence of strong temperature gradients and jet stream dynamics (Gramcianinov et al., 2019). Moreover, during summer, cyclogenesis occurs in a more barotropic environment, with the jet stream significantly displaced from the genesis region, and is highly influenced by high-level potential vorticity anomalies (Crespo et al., 2021). Conversely, in winter, cyclogenesis occurs beneath the equatorial entrance of a jet streak in a more baroclinic environment compared to summer, influenced by low-level potential vorticity anomalies (Crespo et al., 2021).

### 2.2.3 Subtropical cyclones

It was only after Hart (2003) work that the scientific community started to take a closer look to subtropical cyclones. It wasn't until about 20 years ago that the first detailed climatology for subtropical cyclones in the South Atlantic was conducted by Evans and Hart (2003). This study uncovered an average occurrence of roughly one subtropical cyclone per year in the region, with a relatively uniform distribution across seasons. Notably, subtropical cyclogenesis was found to occur in diverse environments: genesis in the open ocean primarily involves Rossby wave breaking, similar to systems in the North Atlantic, whereas coastal genesis is often related to lee cyclogenesis, influenced by the warmer sea surface temperatures of the Brazilian Current, which create conducive conditions for subtropical cyclone formation.

More recently, Gozzo et al. (2014) introduced modifications to the criteria used by Evans and Hart (2003), aiming to capture weaker and shallower systems in their analysis. This adjustment led to the identification of an average of 7 cyclones per year, a significant increase from the findings of the previous study. Gozzo et al. (2014) emphasized the subtropical cyclones' lower traveled distance and displacement speed compared to their extratropical counterparts, allowing them more time to interact with the unstable conditions that facilitated their genesis and to exert greater impact on the South American coastal zone.

Moreover, Gozzo et al. (2014) noted distinctions in seasonal activity, with a peak during summer but stronger systems occurring in autumn. The Southeastern Brazil region (SE-BR) emerged as the predominant genesis area, with over a third of the cyclones developing there exhibiting hybrid characteristics. These systems typically originate from upper-level potential vorticity anomalies and divergence within a low-shear environment. At lower levels, warm and moist air advection, primarily from the subtropical high, is crucial for their formation. During summer, an additional moisture source from the tropics is also significant. Also, the authors used numerical simulation for demonstrating the importance of local latent heat fluxes for the systems development.

Gozzo et al. (2017) reinforced the findings of Gozzo et al. (2014), confirming the role of moisture fluxes in the formation of subtropical cyclones in the SE-BR region. They highlighted that moisture transport from the subtropical high is particularly crucial during

the summer months when it shifts closer to the Brazilian southeastern coast. The reduced number of genesis events observed in the winter can be attributed to the diminished strength of this moisture transport. In contrast, during autumn, transient high-pressure systems serve as the primary source of moisture. Moreover, through numerical simulations, the authors demonstrated the significance of local latent heat fluxes in the development of these systems.

Subtropical cyclones in the South Atlantic remain an area ripe for exploration due to their relatively sparse coverage in scientific literature. From the limited climatologies available, and the few study cases (Reboita et al., 2018, 2022; Dias Pinto and Rocha, 2011, e.g.) it is evident that the formation of these systems is closely linked to Rossby wave breaking and are fueled by both local and non-local latent heat fluxes. However, the door remains open for more comprehensive studies to explore the their dynamics, climatological impacts, and the potential influence of broader atmospheric and oceanic processes on their formation.

#### 2.2.4 Tropical cyclones

Historically, it was believed that the SESA was not conducive to Tropical Cyclone formation due to insufficiently high sea-surface temperatures and relatively strong vertical wind shear, a perspective dating back to Gray (1968), which identified the South Atlantic as the sole oceanic basin without such systems. This view was upended by Hurricane Catarina in 2004, the first recorded hurricane in the South Atlantic, challenging previous assumptions despite some evidence of weak tropical cyclones in the region before the satellite era (da Silva Dias et al., 2004).

Catarina, which originated from an extratropical system near the southeastern Brazilian coast, underwent a tropical transition and made landfall in Southern Brazil (Pezza and Simmonds, 2005). The system's trajectory and development were significantly influenced by unique environmental conditions, including a dipole-blocking pattern in the upper atmosphere, guiding the system back toward Brazil over relatively cool sea surface temperatures (SSTs) of around 25°C (McTaggart-Cowan et al., 2006). This development over cooler SSTs was facilitated by a unique combination of extreme blocking conditions, low wind shear favored by an extreme positive phase of the Southern Annular Mode (Pezza and Simmonds, 2005; Pezza et al., 2009), and latent heat release from air-sea interacti-

ons. Strong interactions with sub-superficial warm waters by Ekman pumping led to the upwelling of isotherms and mixed layer waters, allowing for a significant air-sea temperature gradient and vigorous heat exchange between the ocean and atmosphere, fueling the system through latent heat release (Vianna et al., 2010; Pereira Filho et al., 2010).

Hurricane Catarina, while a landmark event, did not originate from a purely tropical process; it was a baroclinic cyclone that underwent tropical transition. This distinction was pivotal until the emergence of a system near Brazil's Northeast oceanic region in 2019, reported as the first instance of pure tropical cyclogenesis in the South Atlantic. This system, named Iba, marked a significant departure from previous understandings of cyclonic activity in the region (Reboita et al., 2021). Additionally, research on subtropical cyclone Anita in March 2010 suggested its potential for tropical transition under warmer sea surface conditions and without interference from a neighboring extratropical cyclone (Dias Pinto and Rocha, 2011; Reboita et al., 2019). In March 2024, another system named Akará, originating near Southeastern Brazil and featuring eye-like characteristics and a symmetric form, ignited discussions regarding its potential classification as a tropical cyclone, although a detailed examination of its characteristics is pending.

The sporadic nature of these systems in the SESA region precludes the formation of a comprehensive tropical cyclone climatology. While there is some conjecture about the influence of climate change on the emergence of these systems (Pezza and Simmonds, 2005; McTaggart-Cowan et al., 2006; Pezza et al., 2009; Pereira Filho et al., 2010, e.g.), establishing a direct connection between recent tropical cyclone occurrences in SESA and global climatic shifts remains elusive. The rarity of such events continues to challenge researchers, suggesting a complex interaction between regional climatic conditions and broader atmospheric patterns influenced by climate change.

## *2.3 Life cycle of extratropical cyclones: objective classification procedures*

This section explores lifecycle and classification procedures for extratropical cyclones, building upon conceptual models and evolution patterns discussed in Sections 2.1.2 and 2.1.3. These models, derived from case studies and numerical simulations, seek to generalize cyclone development phases due to the absence of standardized methods for analyzing

distinct lifecycle stages across extensive datasets. Herein, we introduce an automated approach for detecting the lifecycle of cyclones, thereby advancing the discussion on objective classification methodologies for these atmospheric phenomena.

The Polar Front Theory, as detailed by Bjerknes and Solberg (1922), was among the first to describe the lifecycle of extratropical cyclones, delineating distinct phases based on structural transformations and large-scale dynamics. Nonetheless, Shapiro and Keyser (1990) later argued that not all cyclones adhere strictly to the progression outlined by Bjerknes, proposing an alternative model that complements the original theory. These developmental models, including their respective stages, are elaborated in Section 2.1.2 and illustrated in Figure 2.4. While these descriptions offer detailed insights into the structural changes cyclones undergo, they fall short of directly associating each phase with specific atmospheric variables in a way that allows for algorithmic detection and statistical and/or spatial analysis.

Whittaker and Horn (1984) conducted one of the earliest cyclone climatology studies, identifying cyclogenesis regions based on the formation of the first closed isobar. This definition has been widely used since (Gramcianinov et al., 2019; Trigo, 2006; Hoskins and Hodges, 2005; Simmonds and Keay, 2000, e.g.). Whittaker and Horn (1984) also defined cyclone intensification as the rate of sea level pressure deepening, a definition echoed and expanded upon by later studies through metrics like relative vorticity growth rate (Grise et al., 2013; Gramcianinov et al., 2019; Hoskins and Hodges, 2005) and the baroclinic Eady growth rate (Pinto et al., 2005). However, Whittaker's study lacked a comprehensive method for classifying cyclone evolution.

A classification of the developmental phases throughout the life cycle of cyclones was conducted by Evans and Hart (2003), with a particular focus on tropical cyclones undergoing extratropical transition. This study explored the structural evolution of such systems, employing a classification framework grounded in the environmental parameters outlined by Hart (2003). The authors partitioned the life cycle of the cyclones into two main phases: one preceding and the other following the peak intensity of the tropical cyclone. This demarcation enabled a detailed analysis of the transformation these cyclones undergo from their genesis as tropical entities to their eventual extratropical characteristics.

Gray and Dacre (2006) implemented the classification scheme originally proposed by Deveson et al. (2002), as detailed in Section 2.1.3, to study the climatology of Northern

Atlantic extratropical cyclones. Their analysis focused on the separation between the upper-level trough and the lower-level cyclone throughout the cyclones' intensification periods, which were identified when the cyclones' central relative vorticity surpassed a specified threshold. While this approach proved beneficial for classification purposes, it overlooked the exploration of dynamical forcing during the development of cyclones. Furthermore, the rationale behind the selected threshold value, including its potential applicability across various scenarios, remained unexplored.

Building upon the foundation laid by Gray and Dacre (2006), Dacre and Gray (2009) delved into the environmental forces influencing the evolution of different types of cyclones. To achieve a granular understanding of variations throughout the cyclones' life cycle, they segmented the cycle at the juncture of maximum relative vorticity. This segmentation delineated the period leading up to this juncture as the intensification stage and the subsequent period as the decaying stage. Additionally, by categorizing cyclones based on their overall lifespan, the study facilitated the identification of specific areas prone to cyclone intensification and the environmental characteristics predominant in those regions.

Rudeva and Gulev (2007) delved into the study of changes in the radius of cyclones throughout their life cycle, introducing the concept of "nondimensional cyclone lifetime." This methodology facilitates the comparison of different stages of cyclone development by normalizing their lifespan to a uniform scale, achieved by dividing the current time step within the system's life cycle by its total duration. Similar approaches were employed by Booth et al. (2018) and Schemm et al. (2018). Specifically, Booth et al. (2018) focused on analyzing precipitation rates through the cyclone life cycle, identifying the cyclones' peak dynamical strength with the point of maximum relative vorticity. Concurrently, Schemm et al. (2018) applied normalization to the cyclone life cycles using the duration from genesis to lysis, thereby examining the periods when the systems were associated with frontal structures.

Trigo (2006) explored the spatial distribution of cyclogenesis (i.e., the initial detection point of each low-pressure system), cyclolysis (the final detected position), and the locations where these systems attained their minimum central pressure. Similarly, Bengtsson et al. (2009), albeit not explicitly defining developmental stages, observed distinguishable phases centered around the maximum intensity of the system, characterized as the period when maximum central relative vorticity is reached. Meanwhile, Azad and Sorteberg (2014a,b)

dissected the cyclone life cycle into distinct stages, identifying the mature phase as the period during which geostrophic vorticity experiences its most rapid increase, with the incipient stage occurring beforehand. Moreover, they categorized the life cycle of a cyclone based on the maximum geostrophic vorticity attained; the time leading up to this peak is labeled as the intensification stage, while the subsequent period is known as the decaying stage.

The diverse methodologies highlighted in the literature offer a range of objective criteria for delineating the lifecycle of extratropical cyclones, each linked to the temporal dynamics of specific atmospheric variables. Commonly, cyclone genesis is identified at the algorithm's first detection, with intensification and decay phases typically defined by changes in central pressure or, when using relative vorticity for tracking, by the increase (intensification) or decrease (decay) of vorticity in the Northern Hemisphere. The peak of the system's intensity is often marked as the point of maturity, while lysis is recognized at the algorithm's final detection of the system. A schematic illustration of this lifecycle, emphasizing the use of relative vorticity at the 850 hPa isobaric level ( $\zeta_{850}$ ) for cyclone detection, is depicted in Figure 2.14.

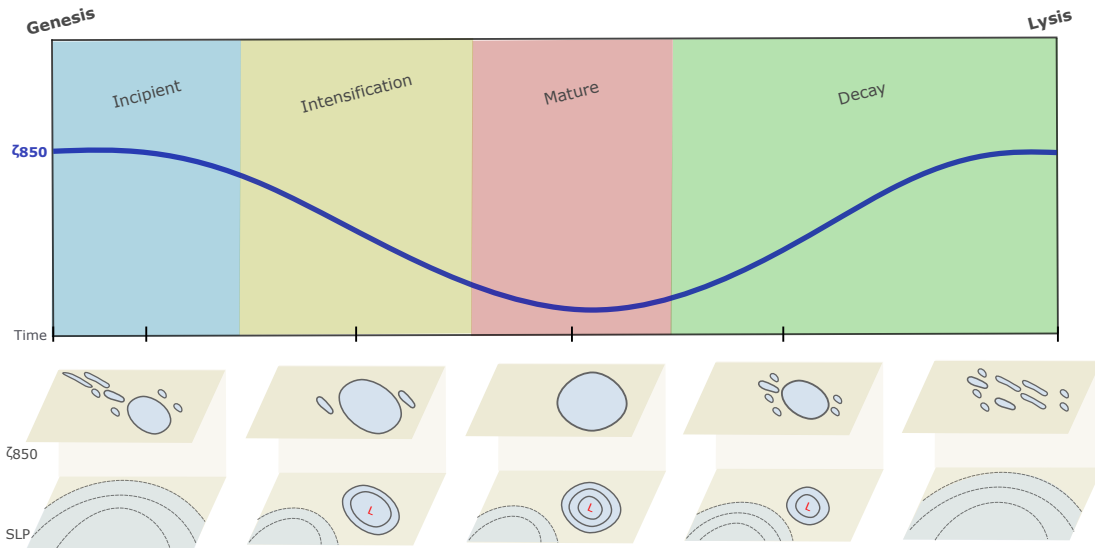


*Figure 2.14:* Schematic representation of an extratropical cyclone's life cycle, depicted through the relative vorticity field at the 850 hPa isobaric level ( $\zeta_{850}$ ). The central figure displays the temporal progression of central  $\zeta_{850}$  at the cyclone's core across various phases. The bottom figures illustrate the evolution of the  $\zeta_{850}$  field and sea level pressure (SLP) spatial distributions during each phase.

Despite these advancements, several limitations persist in current approaches. First,

the initial phase of cyclone development, where the system is present but not yet fully formed, is often overlooked. In such instances, a cyclone may exhibit closed central relative vorticity without corresponding closed isobars at sea level pressure (Sinclair, 1995, e.g.). Second, defining cyclone maturity as merely the point of maximum intensity overlooks the broader period during which atmospheric dynamics illustrates the cyclone's evolution. Finally, characterizing all stages between genesis and maturity as intensification, and those between maturity and lysis as decay, presupposes a singular, linear progression of these stages. This assumption fails to account for the potential complexity of cyclone lifecycle stages, including the possibility of multiple intensification and decay phases.

The ability to discern the distinct life cycle phases of cyclones is crucial for several reasons. As highlighted in Section 2.2, most climatologies currently focus on either the entirety of a cyclone's life cycle or specific points, such as its genesis or lysis. Enhanced techniques for dissecting a cyclone's life cycle could unlock the potential for more granular analyses of the processes and environmental dynamics associated with different stages of cyclone development. For example, while the initial baroclinicity associated with extratropical cyclones is well-documented, the environmental shifts that trigger their cessation of intensification remain less understood. Case studies have shed light on these aspects, but comprehensive testing under climatological conditions is yet to be conducted.

By identifying the environmental conditions pertinent to various stages of cyclone development, researchers can leverage climate change projections to assess potential future shifts in these conditions. Moreover, given the absence of a universally recognized conceptual model for tropical cyclone development, detailed climatological analyses of environmental parameters across distinct life cycle phases could offer critical insights toward establishing such a model. Thus, the potential applications of a refined procedure for analyzing cyclone life cycle phases are vast, limited only by the creativity and curiosity of the research community. Such advancements would not only enhance our understanding of cyclone dynamics but also improve our ability to predict and respond to these powerful weather systems in the context of a changing climate.

## 2.4 Atmosphere Energetics

Solar radiation serves as the primary energy source within the Earth's system. Concurrently, the atmosphere globally dissipates heat by emitting infrared radiation into space. The tilt of the Earth's axis causes a significant variation in radiative incidence between the tropical and polar regions: tropical areas receive more solar energy than they emit, creating an energy surplus, whereas polar regions experience an energy deficit, losing more energy to space than they absorb. This differential heating leads to the formation of warm air masses in tropical regions and cold air masses in polar regions. The resulting heat imbalance drives atmospheric circulation, an ongoing process attempting to balance these temperature disparities. However, this equilibrium is never fully achieved due to the constant differential heating between the tropical and polar regions (Stull, 2015).

### 2.4.1 Lorenz Energy Cycle: Historical Background

The Lorenz Energy Cycle, introduced by Lorenz (1955), is a framework for understanding how energy is distributed and transformed within the atmosphere. This framework offers insights into the general circulation that shapes the dynamic and thermodynamic structures of the atmosphere, influencing atmospheric flows and the transport of heat, moisture, and angular momentum. In his groundbreaking work, Lorenz delineated a method to analyze atmospheric energetics by focusing on two primary forms of energy: kinetic energy ( $K$ ) and available potential energy (APE), each further divided into zonal and eddy (turbulent) components. This section explores these energy forms and their interactions.

Lorenz argued that the total potential energy ( $P$ ) of the atmosphere does not effectively represent the energy available for conversion into  $K$  to drive global circulation. To illustrate this concept, Lorenz proposed a thought experiment: Imagine the atmosphere is uniformly horizontally stratified; in such a scenario, despite the presence of  $P$ , the lack of horizontal gradients precludes air mass movement, resulting in no generation of  $K$  (Figure 2.15a). However, if part of the atmosphere is heated, it triggers vertical upward movements, establishing pressure gradients and disrupting the horizontal stratification (Figure 2.15b). Conversely, cooling in a region induces similar effects but with vertical downward movements (Figure 2.15c). Both scenarios alter the  $P$  of the system, converting it into  $K$ . Yet, in the first case,  $P$  increases, while in the second, it decreases; that is, both increases

and decreases of P are responsible for making energy available for atmospheric circulation.

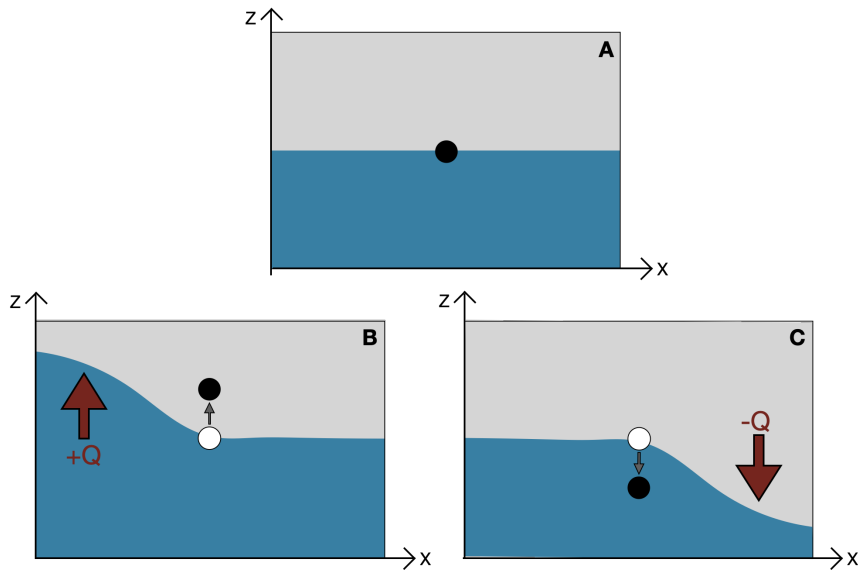


*Figure 2.15:* Mental experiment proposed by Lorenz (1955) to illustrate the relationship between total P and K, depicted through a two-layer atmospheric model: (A) Initially horizontally stratified atmosphere. (B) Perturbation caused by localized heating ( $+Q$ ) leading to vertical upward movements. (C) Similar perturbation caused by cooling ( $-Q$ ) resulting in vertical downward movements. Black circles represent the atmosphere's center of mass post-perturbation, and white circles indicate the center of mass prior to perturbation.

The concept of Available Potential Energy (APE) was initially proposed by Margules (1903), who was interested in the processes that generate kinetic energy (K) in storms (Marquet, 2017). To understand this concept, we can start from the same situation proposed by Lorenz (1955), where differential heating results in ascending movements and a heterogeneous distribution of mass in the atmosphere (Figure 2.16a). In this case, the resulting pressure gradients cause acceleration of the wind field (Figure 2.16b), redistributing the mass in the atmosphere. Assuming this flow is adiabatic, the final result is a horizontally stratified atmosphere (Figure 2.16c). In the first step, both forms of potential energy (total and available) are at their maximum. With the redistribution of mass, there is an increase in K, while the total and available potential energy decreases. In the final stage, P is minimal, yet not zero, while the APE is zero. Thus, APE can be defined as the amount of potential energy available for conversion into K under an adiabatic distribution of mass.

According to Lorenz (1955), APE serves as the primary source of K in the atmosphere, fundamentally driving the general circulation. While APE and K dominantly shape at-

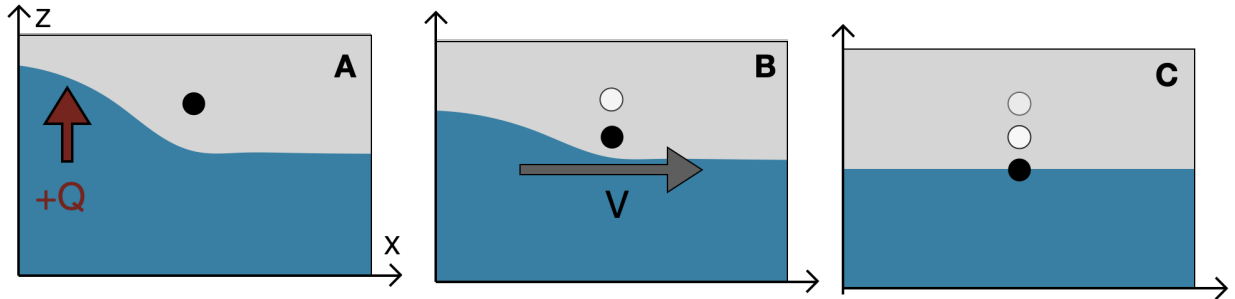


*Figure 2.16: Depiction of Available Potential Energy (APE) transformations in response to atmospheric heating and cooling. (A) Initial state with differential heating causing heterogeneous mass distribution. (B) Redistribution of mass via wind fields leading to homogenization. (C) Final state of horizontal atmospheric stratification. Black circles indicate the center of mass at each stage, with white circles showing previous positions.*

mospheric dynamics, Lorenz acknowledged that diabatic processes and friction also play critical roles, though these elements were less detailed in his work due to their complex nature and the challenges associated with their quantification. In his theoretical framework, Lorenz treated the atmosphere as a closed system, distinguishing between the zonal and eddy (turbulent) components of APE and K to clarify the energetics involved in atmospheric processes.

This distinction is crucial as it aligns with earlier observations by Starr (1953), who emphasized the significance of eddies in maintaining atmospheric circulation, particularly their role in transferring K from turbulent to zonal flows. This perspective challenged earlier assumptions and highlighted the necessity of including eddy dynamics in any comprehensive atmospheric circulation theory. Subsequent research by Wiin-Nielsen et al. (1963) demonstrated the importance of eddies in global heat and momentum transport, illustrating how different wave numbers contribute to these processes. Through these insights, Lorenz's separation of energy components facilitates a deeper understanding of how meteorological systems, such as cyclones, develop and influence broader atmospheric circulation patterns.

The energy cycle can be represented by the following equations, which represent the energy balance for each component of the cycle:

$$\frac{\partial A_Z}{\partial t} = -C_Z - C_A + G_Z \quad (2.6)$$

$$\frac{\partial A_E}{\partial t} = -C_E + C_A + G_E \quad (2.7)$$

$$\frac{\partial K_Z}{\partial t} = C_Z - C_K - D_Z \quad (2.8)$$

$$\frac{\partial K_E}{\partial t} = C_E + C_K - D_E \quad (2.9)$$

In these equations, available potential energy (APE) is divided into zonal ( $A_Z$ ) and eddy ( $A_E$ ) components, as is kinetic energy ( $K_Z$  and  $K_E$ , respectively). The transformations between these forms of energy are denoted by  $C$ , with subscripts  $Z$  and  $E$  for conversions between zonal and eddy forms, and  $A$  and  $K$  indicating conversions between APE and kinetic energy, respectively. Thus,  $C_A$  represents the conversion between  $A_Z$  and  $A_E$ ,  $C_E$  denotes the conversion from  $A_E$  to  $K_E$ ,  $C_K$  signifies the transformation from  $K_E$  to  $K_Z$ , and  $C_Z$  describes the conversion from  $A_Z$  to  $K_Z$ . Generation of APE and dissipation of kinetic energy are indicated by  $G$  and  $D$ , with  $G_Z$  and  $G_E$  marking the generation of  $A_Z$  and  $A_E$ , and  $D_Z$  and  $D_E$  representing the dissipation of  $K_Z$  and  $K_E$ , respectively. Full mathematical formulations for these processes are discussed in Section 2.4.2.

After the seminal work by Lorenz (1955) on the global energy cycle, numerous subsequent studies aimed to quantify this cycle, primarily focusing on the Northern Hemisphere due to observational constraints at the time (Starr, 1959; Saltzman and Fleisher, 1961; Holopainen, 1964; Jensen, 1961; Brown Jr, 1964; Wiin-Nielsen, 1959, e.g.). Oort (1964) synthesized these results to depict the annual energy cycle of the Northern Hemisphere. He innovatively categorized the energy analysis into distinct domains: the spatial domain, where variables are analyzed based on spatial averages, aiding in the understanding of large-scale zonal patterns such as jet streams and westerlies; the temporal domain, focusing on averages and deviations over time, which facilitates insights into long-term trends and transient disturbances; and the mixed space-time domain, which offers an integrated perspective on how average states and disturbances, both transient and stationary, interact and are sustained. Oort noted that while there was considerable focus on spatial domain analyses, studies addressing the mixed domain were scarce, and those considering the temporal domain were virtually absent.

From these estimates, Oort (1964) presented a diagram that visually encapsulates the

energy cycle (Figure 2.17). This diagram illustrates the generation, conversion, and dissipation of different energy forms, providing a dynamic overview in a graphical format. Notably, the diagram allows for straightforward comparisons of diverse study results. It is important to mention, as Oort (1964) did, that friction terms are typically calculated as residuals due to the challenges in direct computation, balancing the zonal and turbulent terms of kinetic energy.

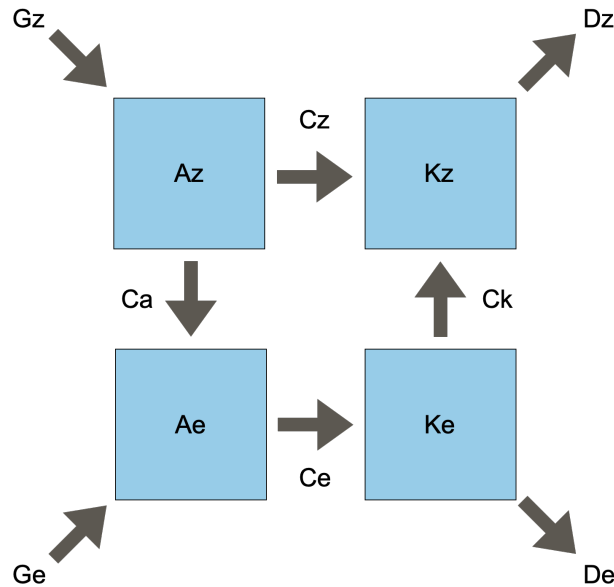


*Figure 2.17:* Representation of the energy cycle as formulated by Lorenz (1955) and schematized by Oort (1964). This diagram displays the interplay among the four forms of energy (zonal and turbulent terms of K and APE), illustrating their conversions, generation, and dissipation.

As previously mentioned, the formulation proposed by Lorenz (1955) estimates the energetics of the atmosphere assuming a closed system, that is, without energy exchanges at the boundaries. The first study to consider energetics for an open system was by Reed et al. (1963), which analyzed a sudden stratospheric warming event in the Northern Hemisphere. This study treated the stratosphere as an open system, permitting energy exchanges with other atmospheric layers, such as the troposphere. Building on this, Muench (1965), who was interested in stratospheric dynamics, refined Lorenz (1955)'s theory and proposed a new representation of the energy cycle.

Muench's model adds boundary flow terms ( $BA_Z$ ,  $BA_E$ ,  $BK_Z$ , and  $BK_E$ ) to the original Lorenz equations, representing respectively the zonal and eddy flows of APE and K across the system boundaries (Figure 2.18). The updated energy balance equations are:

$$\frac{\partial A_Z}{\partial t} = BA_Z - C_Z - C_A + G_Z \quad (2.10)$$

$$\frac{\partial A_E}{\partial t} = BA_E - C_E + C_A + G_E \quad (2.11)$$

$$\frac{\partial K_Z}{\partial t} = BK_Z + C_Z - C_K + B\Phi_Z - D_Z \quad (2.12)$$

$$\frac{\partial K_E}{\partial t} = BK_E + C_E + C_K + B\Phi_E - D_E \quad (2.13)$$

Where  $BA_Z$ ,  $BA_E$ ,  $BK_Z$ , and  $BK_E$  represent, respectively, the flows of zonal and eddy APE and K across the boundaries. The terms  $B\Phi_Z$  and  $B\Phi_E$  are represented together with the terms  $C_Z$  and  $C_E$ , respectively, because both arise from the same process of deriving the balances of  $K_Z$  and  $K_E$ . Muench (1965) recognizes the difficulty in interpreting the terms  $B\Phi_Z$  and  $B\Phi_E$ , indicating that they are related to the flow of kinetic energy towards lower altitudes, representing the emergence of kinetic energy at the boundaries of the computational domain.

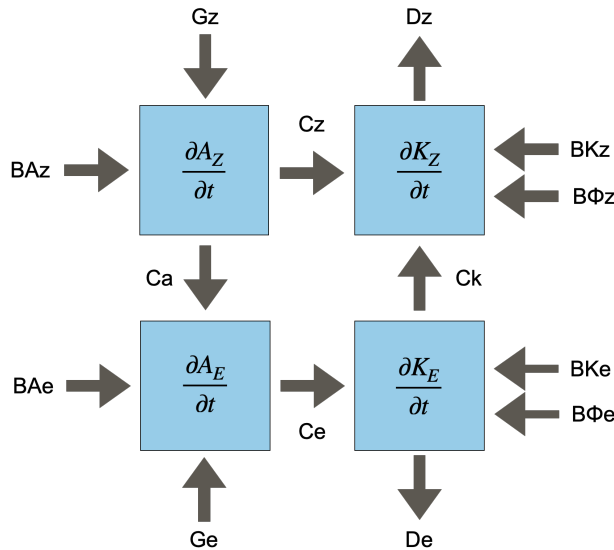


Figure 2.18: Energy cycle as formulated by Lorenz (1955) and updated by Muench (1965). This diagram includes additional terms representing energy flows across boundaries, illustrating both the local derivatives of the zonal and eddy partitions of APE and K and the interactions at the system edges.

Although Muench's model considers boundary flows, his domain was partially open, extending up to the polar regions and encompassing the entire Northern Hemisphere longitudinally, with the only boundary at the southern part of the domain at 30°N. The notion of a fully regional energy cycle was later approached by Smith (1969), who aimed to assess

the contribution of a limited region to global energetics. Smith clarified that while his work presented a framework for regional analysis, an exact computation of local energetics was outside its scope, and his model did not differentiate between zonal and eddy components of APE and K.

Parallel to the work by Smith (1969), Johnson (1970), following the theoretical framework proposed by Dutton and Johnson (1967), introduced a semi-Lagrangian framework for analyzing the energy cycle of limited areas. In this formulation, the delineated area for performing energetic calculations moves with the meteorological system of interest, spanning  $N$  fixed regions that shift in space. This analysis highlights that global Available Potential Energy (APE) is the aggregate of all possible open atmospheric regions, plus a term representing the thermodynamic contrast among these regions. It's crucial to note that Smith (1969) and Dutton and Johnson (1967) argued that the APE of a limited region should be viewed as its contribution to the global energetics rather than a standalone quantity. This perspective stems from the interconnected nature of the atmosphere, where local and global energetics are mutually influential.

Dutton and Johnson (1967) also critiqued Lorenz (1955)'s formulation, pointing out its underestimation of APE, particularly during the winter months. The alternative set of equations introduced by Johnson (1970), which utilizes isentropic coordinates, however, included simplifications that were seen as limitations by Vincent and Chang (1973), such as neglecting the impact of diabatic heating, rendering it impractical for diagnostic applications. Following this rationale, Vincent and Chang (1973) developed a system of equations in isobaric coordinates that account for the balances of APE and Kinetic Energy (K) in an open atmospheric system from a semi-Lagrangian perspective.

This formulation partitions APE into the reference state APE of the region and two components representing barotropic and baroclinic contributions to the APE of the delineated area. The balance equations for APE now included terms for boundary movement in the semi-Lagrangian frame and the advection of air masses with varying properties across these boundaries. This formulation was first applied by Edmon and Vincent (1979) in an energy cycle analysis of Hurricane Carmen (1974). Building on this, Brennan and Vincent (1980) adapted Vincent's approach to incorporate zonal and eddy components of APE and K, marking the first instance of such a detailed and realistic equation set being applied to a limited area within the troposphere. However, Brennan and Vincent (1980) utilized a

traditional Eulerian approach for their energy analysis.

Furthermore, Brennan and Vincent (1980) reinterpreted the boundary terms  $B\Phi_Z$  and  $B\Phi_E$  as the work done by zonal and meridional wind components against atmospheric pressure at the computational domain boundaries. However, they noted that these terms, as calculated, were unrealistically large due to minor errors in the geopotential height field, which could escalate in major errors and significantly skew the results. Consequently, these terms were combined with the dissipation terms ( $D_Z$  and  $D_E$ ) and treated as residuals in the balance equations for  $K_Z$  and  $K_E$ , resulting in new terms  $RK_Z$  and  $RK_E$ . This approach and the updated energy cycle are depicted in Figure 2.19.

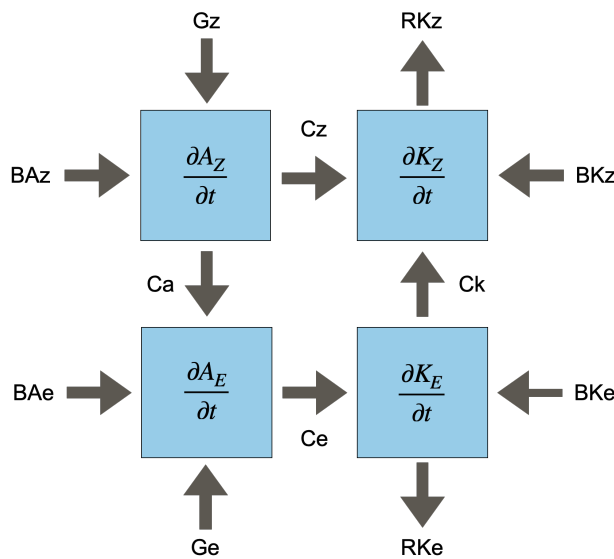


Figure 2.19: Updated energy cycle as reformulated by Brennan and Vincent (1980). This diagram includes the integrated terms for boundary energy flows ( $B\Phi_Z$  and  $B\Phi_E$ ) merged with dissipation processes ( $D_Z$  and  $D_E$ ), represented as residual terms  $RK_Z$  and  $RK_E$ .

The modified energy balance equations are as follows:

$$\frac{\partial A_Z}{\partial t} = -C_A - C_Z + G_Z + BA_Z \quad (2.14)$$

$$\frac{\partial A_E}{\partial t} = C_A - C_E + G_E + BA_E \quad (2.15)$$

$$\frac{\partial K_Z}{\partial t} = C_K + C_Z + BK_Z + RK_Z \quad (2.16)$$

$$\frac{\partial K_E}{\partial t} = -C_K + C_E + BK_E + RK_E \quad (2.17)$$

And the residual terms are defined as:

$$RK_Z = B\Phi_Z + D_Z \quad (2.18)$$

$$RK_E = B\Phi_E + D_E \quad (2.19)$$

Robertson and Smith (1983) adapted the formulation presented by Brennan and Vincent (1980) for limited area domains, particularly revising the term  $A_E$ . Building upon the framework of APE for limited domains outlined by Smith et al. (1977), Robertson integrates the first law of thermodynamics into the Eulerian derivatives of the APE and  $A_Z$  formulations. This results in a significantly different balance equation for  $A_E$ , introducing a novel term associated with variations in the reference pressure field, which alters the computation of the conversion term  $C_A$ . This approach was driven by the goal of evaluating, through numerical modeling, the influence of moist processes on the energetics of extratropical cyclones. However, the adaptation necessitated computations over isentropic coordinates, introducing complexities in the numerical implementation.

In an effort to analyze the energetics of cyclogenesis in the Gulf of Genoa within the Mediterranean Sea, Michaelides (1987) advanced the energy cycle formulation further. Echoing concerns from Brennan and Vincent (1980) regarding unrealistic results for the terms  $B\Phi_Z$  and  $B\Phi_E$ , Michaelides introduced additional residual terms  $RK_Z$  and  $RK_E$ , and a correction factor ( $\epsilon$ ) to account for numerical errors in the estimation of these terms, as shown in the equations and Figure 2.20. The modified set of equations is as follows:

$$\frac{\partial A_Z}{\partial t} = C_K - C_A + BA_Z + \Delta G_Z \quad (2.20)$$

$$\frac{\partial A_E}{\partial t} = C_A - C_E + BA_E + \Delta G_E \quad (2.21)$$

$$\frac{\partial K_Z}{\partial t} = C_K - C_Z + BK_Z - \Delta R_Z \quad (2.22)$$

$$\frac{\partial K_E}{\partial t} = C_E - C_K + BK_E - \Delta R_E \quad (2.23)$$

Where the residual terms are defined as:

$$\Delta R_Z = B\Phi_Z - D_Z + \epsilon_{KZ} \quad (2.24)$$

$$\Delta R_E = B\Phi_E - D_E + \epsilon_{KE} \quad (2.25)$$

$$\Delta G_Z = G_Z + \epsilon_{GZ} \quad (2.26)$$

$$\Delta G_E = G_E + \epsilon_{GE} \quad (2.27)$$

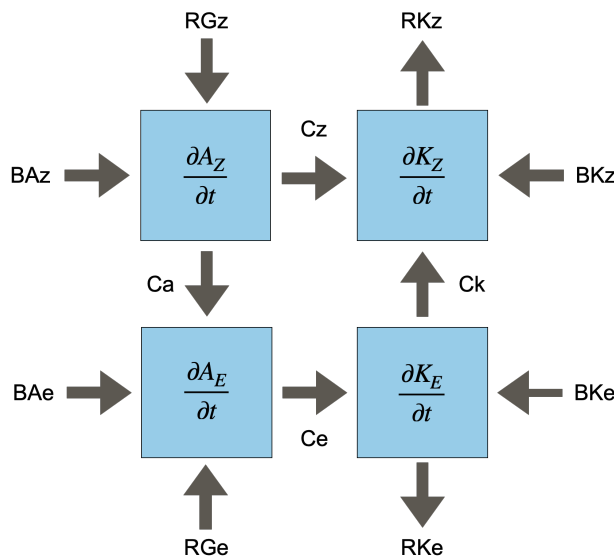
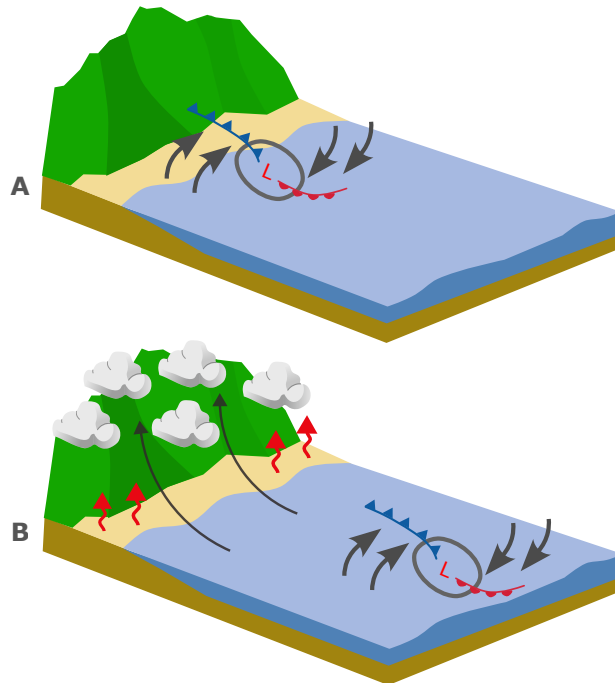


Figure 2.20: Refined depiction of the energy cycle incorporating modifications by Michaelides (1987). This representation includes error correction terms within the residual balances, addressing previous challenges with the quantification of boundary terms and dissipation factors.

In Michaelides et al. (1999), the author extends the energetic formulations presented in Michaelides (1987), exploring calculations for limited areas using both Eulerian and semi-Lagrangian reference frames. This study evaluates the energy cycle during a cyclogenesis event in the Mediterranean from these two perspectives, providing a nuanced discussion on the methodological implications of each. It highlights that the Eulerian approach is commonly preferred for energy analysis in limited atmospheric areas. This method necessitates defining a sufficiently large spatial domain to encapsulate all developmental stages of the system, including its movement and size changes. However, this approach has interpretative limitations; a broad spatial domain may inadvertently include adjacent synoptic circulations, thus diluting the specific energetics of the primary system under study.

Figure 2.21 illustrates this issue with a scenario akin to cyclogenesis in the coastal region of Southeast Brazil (Reboita et al., 2010; Gramcianinov et al., 2019, e.g.). Here,

the computational domain must encompass both the initial coastal genesis area and the subsequent oceanic trajectory of the cyclone. As the cyclone progresses to the ocean in its later stages, mesoscale circulations near the coast, such as updrafts due to surface heating and convection from sea breeze interactions with local topography, emerge. These processes can significantly alter the computed values of APE and K within the domain, affecting the energy conversion, boundary, dissipation, and generation terms, thereby complicating the interpretation of the cyclone's energy dynamics.



*Figure 2.21:* Illustration of challenges in using an Eulerian reference frame for energy cycle analysis. A) A cyclone forming near the continent, where the newly developed cyclonic system is the main meteorological feature inside the domain. B) The system is in its later oceanic phase, while meso-scale circulations develop in the coastal region, such sea-breeze and, consequently, orographic ascent over the mountain range near the coast.

Despite the inherent limitations associated with the Eulerian approach, Michaelides et al. (1999) discusses the methodological challenges of employing a purely Lagrangian framework to study extratropical cyclones. Such a study would require tracking the system in a three-dimensional space, isolated from external influences, using specific conservative variables for the encapsulated air masses. This is complicated by the diverse origins of the air masses involved in extratropical cyclones, which include both polar and tropical sources, affecting their conservative properties. Additionally, the system must be isolated from any spurious external circulations.

Consequently, Michaelides et al. (1999) advocates for a quasi-Lagrangian approach as a practical solution that minimizes the impact of neighboring circulations on the system's energy dynamics. This approach, similar to that proposed by Vincent and Chang (1973), utilizes multiple fixed domains at different temporal intervals to effectively track the cyclonic system. However, unlike Vincent and Chang (1973), Michaelides et al. (1999)'s formulation does not include terms for the displacement of computational domain boundaries. The author conducts a comparative analysis between the Eulerian and quasi-Lagrangian methods, revealing that they can yield significantly different results depending on the specific energetic terms analyzed. This highlights the complications in using the Eulerian method for comparative studies, as it can incorporate the energetic contributions of adjacent systems. Michaelides et al. (1999) concludes that the semi-Lagrangian method offers a more robust framework for analyzing the energetics of cyclonic systems.

Nevertheless, critiques of the quasi-Lagrangian approach exist (Dias Pinto and Rocha, 2011, e.g.). One major criticism is that this method does not allow for the local time derivatives of energy terms due to the absence of a fixed computational volume, which impedes a complete closure of the energy balance — a limitation acknowledged by Michaelides et al. (1999). Additionally, there is debate over whether changes in the energetics through the cyclone lifecycle can be attributed to the system's dynamics or to the fact that the tracking box may capture varying environmental conditions. However, these perceived limitations can be addressed by understanding that the distinct boxes used at each time-step through the cyclone's lifecycle are effectively "snapshots" of its dynamics. Consider the following thought experiment: we compute the LEC using both quasi-Lagrangian and Eulerian frameworks. The quasi-Lagrangian experiment tracks the trajectory of an extra-tropical cyclone, using a distinct  $15^\circ \times 15^\circ$  domain for each hourly time step. Meanwhile, the Eulerian experiment employs a fixed  $15^\circ \times 15^\circ$  domain in a specific location, which will coincide with the cyclone's trajectory at a given time step, thereby exactly matching the domain used in the quasi-Lagrangian framework. As demonstrated in Section 2.4.2, the equations used in LEC computation do not have temporal dependencies; therefore, for this specific time where the domains of both frameworks overlap, the results will be identical. At this time step, the quasi-Lagrangian domain likely contains only the cyclonic system, thus the computed energetics are indisputably linked to its development at that moment — or, using Smith (1969)'s interpretation: the system's contribution to global energetics.

Following this reasoning, it is logical to assume that each domain in the quasi-Lagrangian approach represents the cyclone energetics for each specific time step, effectively providing snapshots of the energetics.

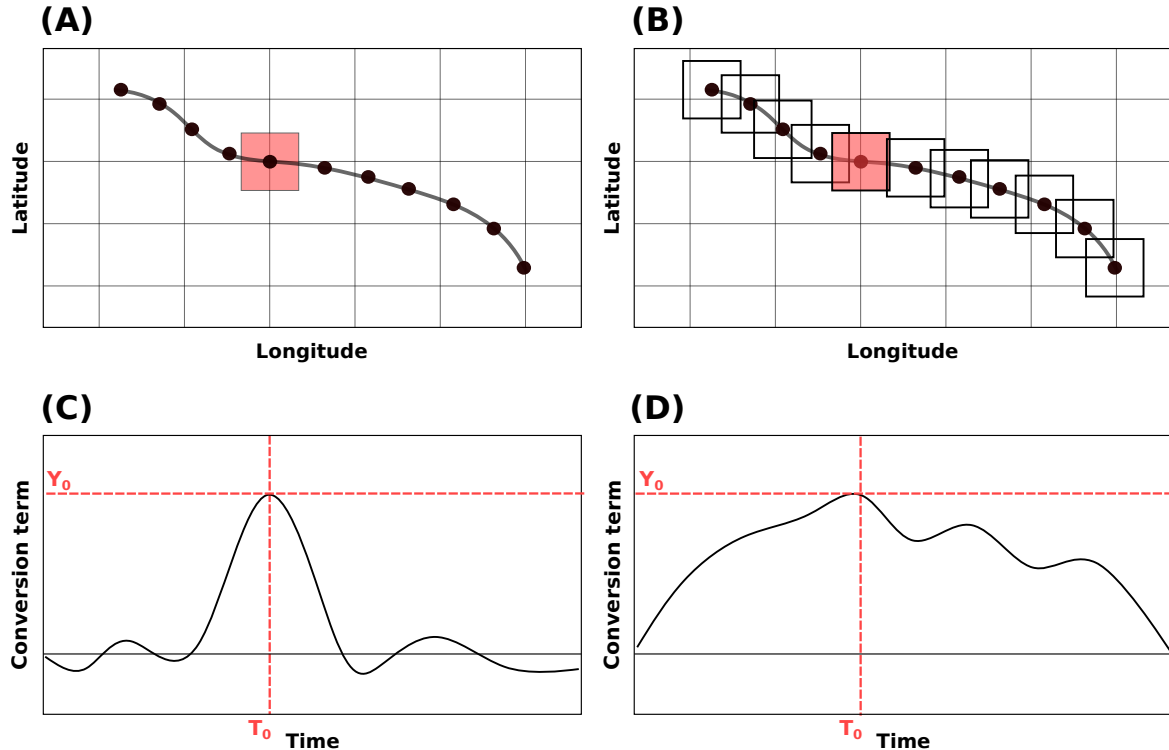


*Figure 2.22:* Illustration of the quasi-Lagrangian and Eulerian frameworks employed in the LEC computation for analyzing cyclonic energetics. Panel (A) shows the Eulerian approach with a fixed  $15^\circ \times 15^\circ$  domain, overlapping with the cyclone's trajectory at a specific time step ( $T_0$ ). Panel (B) depicts the quasi-Lagrangian approach, tracking a  $15^\circ \times 15^\circ$  domain that moves with the cyclone, providing hourly snapshots. The highlighted domain in Panel (B) indicates the domain at  $T_0$  that overlaps with the Eulerian domain from Panel (A). Panels (C) and (D) display a hypothetical conversion term used solely for demonstrating that both frameworks yield identical results ( $Y_0$ ) when the domains coincide. This alignment supports the argument that each quasi-Lagrangian domain snapshot accurately reflects the system's energetics at each respective time step.

Several methodologies have been developed to refine diagnostic equations for atmospheric energetics, each offering unique advancements. The approach introduced by Plumb (1983) critiques traditional energy formulations for wave propagation and employs transformed Eulerian-mean equations to enhance the physical accuracy of eddy-mean flow interactions. Similarly, Marquet (1991)'s redefinition of exergy and available enthalpy provides a more complete analysis of atmospheric dynamics, accommodating factors such as static

instabilities and topographical variations often oversimplified in previous models. The local APE density framework proposed by Novak and Tailleux (2018), on the other hand, introduces a positive-definite local form of potential energy, akin to kinetic energy, which can be transported, converted, and dissipated locally. Unlike the global and volume-integrated nature of Lorenz's APE, this local APE density theory adapts potential energy calculations to specific atmospheric conditions, enhancing diagnostic precision in regional climate studies. However, these methods significantly complicate the mathematical formulations, requiring increased computational resources and extending computation times, which pose substantial limitations, especially for operational purposes. Additionally, each of these frameworks introduces new challenges in the physical interpretation of the terms.

The present work adopts the formulation presented by Michaelides et al. (1999), which offers a balance between computational feasibility and physical accuracy. This framework provides results that serve as a useful diagnostic tool, facilitating an understanding of the dynamical mechanisms involved in cyclone development without requiring extensive computational resources. While the primary goal of this thesis is scientific, there is significant interest in developing an operational tool for diagnosing the energy cycle of cyclones that can be made available to the scientific community. This tool is envisioned to function similarly to the Hart phase diagrams, which are accessible online (<https://moe.met.fsu.edu/cyclonephase/ecmwf/fcst/index.html>) and widely used for real-time cyclone analysis. The complete mathematical formulation and physical interpretation of each term in the Lorenz Energy Cycle (LEC) are detailed in Section 2.4.2. Additionally, Section 3.4 describes the computational methods used to calculate the LEC.

#### 2.4.2 Lorenz Energy Cycle: Mathematical expressions and physical interpretation

This section provides a detailed description of the symbols and expressions used for the calculation of the Lorenz Energy Cycle (LEC), adopting the notation from Michaelides (1987).

Firstly, we define the zonal mean of a variable  $X$ , between longitudes  $\lambda_1$  and  $\lambda_2$ :

$$[X]_\lambda = \frac{1}{\lambda_2 - \lambda_1} \int_{\lambda_2}^{\lambda_1} X d\lambda \quad (2.28)$$

The eddy component of this variable is its deviation from the zonal mean:

$$(X)_\lambda = X - [X]_\lambda \quad (2.29)$$

The domain mean of the variable  $X$ , defined over the computational domain bounded by longitudes  $\lambda_1$  and  $\lambda_2$ , and latitudes  $\phi_1$  and  $\phi_2$ , is given by:

$$[X]_{\lambda\phi} = \left( \frac{1}{\lambda_2 - \lambda_1} \right) \left( \frac{1}{\sin \phi_2 - \sin \phi_1} \right) \int_{\lambda_2}^{\lambda_1} X \cos \phi d\lambda d\phi \quad (2.30)$$

Similarly, we define the deviation of the zonal mean from the domain mean:

$$([X]_\lambda)_\phi = [X]_\lambda - [X]_{\lambda\phi} \quad (2.31)$$

From the definitions above, the four energy components used in the LEC computation are defined as follows:

$$A_Z = \int_{p_t}^{p_b} \frac{[(T)_\lambda]_\phi^2}_{2[\sigma]_{\lambda\phi}} dp \quad (2.32)$$

$$A_E = \int_{p_t}^{p_b} \frac{[(T)_\lambda^2]_{\lambda\phi}}{2[\sigma]_{\lambda\phi}} dp \quad (2.33)$$

$$K_Z = \int_{p_t}^{p_b} \frac{[(u)_\lambda^2 + (v)_\lambda^2]_{\lambda\phi}}{2g} dp \quad (2.34)$$

$$K_E = \int_{p_t}^{p_b} \frac{[(u)_\lambda^2 + (v)_\lambda^2]_{\lambda\phi}}{2g} dp \quad (2.35)$$

where  $p$  is the atmospheric pressure, with subscripts  $b$  and  $t$  denoting the lower (base) and upper (top) pressure boundaries of the atmosphere, respectively.  $T$  represents temperature,  $g$  is the acceleration due to gravity, and  $u$  and  $v$  are the zonal and meridional wind components, respectively. The static stability parameter  $\sigma$  is defined as:

$$\sigma = \left[ \frac{gT}{c_p} - \frac{pg}{R} \frac{\partial T}{\partial p} \right]_{\lambda\phi} \quad (2.36)$$

where  $c_p$  is the specific heat at constant pressure, and  $R$  is the ideal gas constant for dry air.

The APE terms  $A_Z$  and  $A_E$  are discussed in Section 2.4 and illustrated in Figure 2.16. The term  $A_Z$  quantifies the latitudinal temperature gradient, where higher values in the numerator indicate larger differences in mean temperature between latitudes — characteristically, the equator being warmer than the poles. Moreover, lower values of

the denominator suggest a more unstable atmosphere, which can more readily redistribute vertical motions and thus intensify the latitudinal temperature gradients. The term  $A_E$  is analogous to  $A_Z$  but referring to longitudinal temperature gradients caused by eddy motions, suggesting a higher presence of eddy available potential energy, which can be converted into kinetic energy, driving atmospheric motions.

The kinetic energy terms  $K_Z$  and  $K_E$  quantify the intensity of atmospheric motions.  $K_Z$  correlates with the zonal mean of the wind components; opposing winds cancel out, thus higher  $K_Z$  values occur when winds at the same latitude align directionally. The term  $[u]\lambda$  denotes the large-scale east-west circulations, including the trade winds, westerlies, and jet streams, while  $[v]\lambda$  relates to the north-south circulations, such as those in the Hadley and polar cells. Higher  $K_Z$  values therefore indicate stronger mean circulations, contributing to the overall momentum and energy in the atmospheric system. In contrast,  $(u)\lambda$  and  $(v)\lambda$  represent deviations from these mean values, capturing smaller-scale, turbulent motions and deviations from the average flow, including phenomena like cyclones, anticyclones, and other mesoscale and synoptic-scale disturbances. Thus, elevated  $K_E$  values signal increased eddy activity, enhancing turbulence and mixing within the atmosphere.

The four conversion terms are defined as follows, integrating over the atmospheric column from the base ( $p_b$ ) to the top ( $p_t$ ) pressures:

$$C_Z = \int_{p_t}^{p_b} -[(T)_\lambda]_\phi ([\omega]_\lambda)_\phi]_{\lambda\phi} \frac{R}{gp} dp \quad (2.37)$$

$$C_E = \int_{p_t}^{p_b} -[(T)_\lambda(\omega)_\lambda]_{\lambda\phi} \frac{R}{gp} dp \quad (2.38)$$

$$C_A = \int_{p_t}^{p_b} - \left( \frac{1}{2a\sigma} \left[ (v)_\lambda(T)_\lambda \frac{\partial([T]_\lambda)_\phi}{\partial\phi} \right]_{\lambda\phi} + \frac{1}{\sigma} \left[ (\omega)_\lambda(T)_\lambda \frac{\partial([T]_\lambda)_\phi}{\partial p} \right]_{\lambda\phi} \right) dp \quad (2.39)$$

$$C_K = \int_{p_t}^{p_b} \frac{1}{g} \left( \left[ \frac{\cos\phi}{a} (u)_\lambda (v)_\lambda \frac{\partial}{\partial\phi} \left( \frac{[u]_\lambda}{\cos\phi} \right) \right]_{\lambda\phi} + \left[ \frac{(v)_\lambda^2}{a} \frac{\partial[v]_\lambda}{\partial\phi} \right]_{\lambda\phi} \right. \\ \left. + \left[ \frac{\tan\phi}{a} (u)_\lambda^2 [v]_\lambda \right]_{\lambda\phi} + \left[ (\omega)_\lambda (u)_\lambda \frac{\partial[u]_\lambda}{\partial p} \right]_{\lambda\phi} + \left[ (\omega)_\lambda (v)_\lambda \frac{\partial[v]_\lambda}{\partial p} \right]_{\lambda\phi} \right) dp \quad (2.40)$$

where  $a$  is the Earth's radius and  $\omega$  is the vertical velocity in isobaric coordinates.

The term  $C_Z$  (Equation 2.38) shares some similarities with  $A_Z$ , as it represents the covariance product of temperature and vertical motion, averaged over the same latitudinal circle. Positive values of  $C_Z$  indicate a conversion from zonal available potential energy

$(A_Z)$  to kinetic energy ( $K_Z$ ), and vice versa. This conversion is detailed in the integrand, which contains the covariance product of the zonal deviation from the domain mean of  $-T\omega$ . Thus, positive values of  $C_Z$  correspond to either the vertical ascent of warm air or the descent of cold air. Conversely, negative values of  $C_Z$  are associated with the ascent of cold air or the descent of warm air. This phenomenon is depicted in Figure 2.23, which illustrates a region characterized by meridional gradients of temperature and vertical velocity. In warmer areas where the temperature deviation is positive and the  $\omega$  deviation is negative, the product  $T\omega$  is negative. With the additional negative sign in the equation for  $C_Z$ , this results in positive values of  $C_Z$ , signifying a conversion from  $A_Z$  to  $K_Z$ . On the other hand, in situations where air descends in warmer regions and ascends in colder regions, the covariance product  $-T\omega$  would be positive, leading to negative  $C_Z$  values, indicating a conversion from kinetic energy ( $K_Z$ ) to available potential energy ( $A_Z$ ).

Figure 2.23 provides a visual interpretation of  $C_Z$ , showing a region with meridional gradients of temperature and vertical velocity. In this scenario, the combination of positive temperature deviations and negative  $\omega$  deviations in warmer regions results in a negative product of  $T\omega$ , which when combined with the equation's negative sign, yields a positive  $C_Z$ , indicative of energy conversion from  $A_Z$  to  $K_Z$ . Conversely, in colder regions where temperature deviations are negative and  $\omega$  deviations are positive, the product is also negative, leading to a positive  $C_Z$ . In the reverse situation, where air descends in warmer areas and rises in colder ones, the product  $-T\omega$  turns positive, resulting in a negative  $C_Z$ , which signifies a reverse energy conversion from  $K_Z$  to  $A_Z$ .

The term  $C_E$  analogously represents the conversion between eddy forms of energy, from available potential energy ( $A_E$ ) to kinetic energy ( $K_E$ ). The interpretation of  $C_E$  mirrors that of  $C_Z$ , but it pertains to gradients and deviations along the longitudinal axis (x-axis) rather than the latitudinal (y-axis). Swapping the axes in Figure 2.23 would illustrate a scenario indicative of a positive  $C_E$ .

The term  $C_A$  (Equation 2.39) describes the energy conversion between zonal mean available potential energy ( $A_Z$ ) and eddy available potential energy ( $A_E$ ). Positive values of  $C_A$  signify energy transfer from  $A_Z$  to  $A_E$ , whereas negative values indicate the opposite. The equation for  $C_A$  can be divided into two components, each capturing how deviations from the zonal mean of the meridional (north-south) and vertical winds (addressed in the first and second components, respectively) interact with latitudinal temperature gradients.

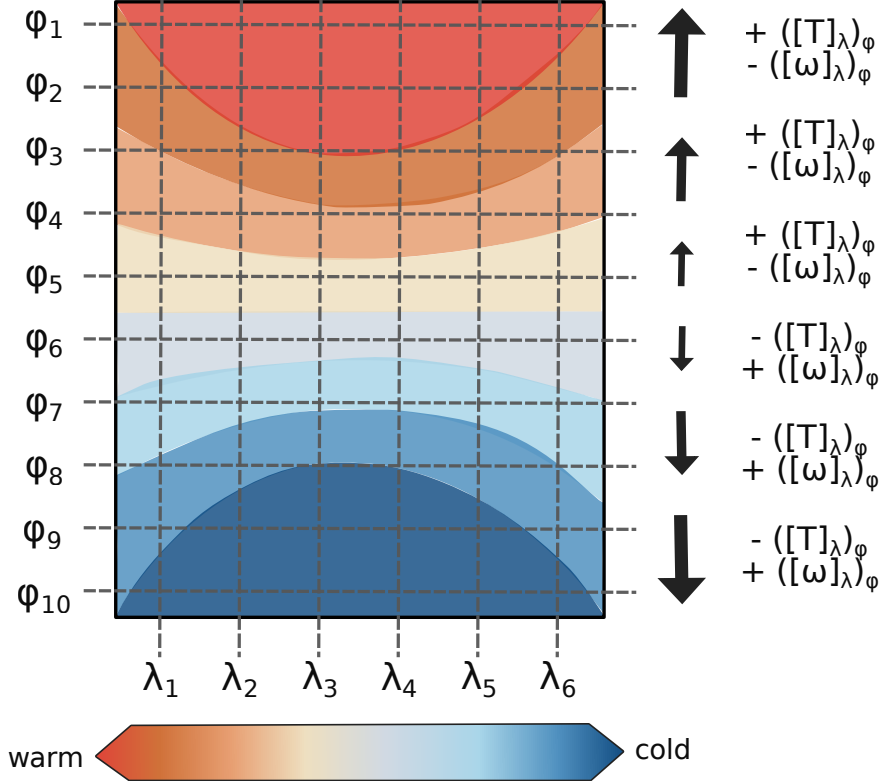


Figure 2.23: Hypothetical situation illustrating the conversion term between available potential energy ( $A_Z$ ) and kinetic energy ( $K_Z$ ), represented by  $C_Z$ . The y-axis represents latitude circles ( $\phi$ ), showing a decrease in temperature and vertical velocity  $\omega$  (indicated by vertical arrows) toward the pole in the Southern Hemisphere. The x-axis represents longitude ( $\lambda$ ).

In the first component, we have  $(v)_\lambda(T)_\lambda \frac{\partial([T]_\lambda)\varphi}{\partial\varphi}$ . The negative sign within the equation implies that for  $C_A$  to be positive, this term must be negative. To understand each term's contribution to the sign of  $C_A$ , consider an illustrative case: a midlatitude low-pressure system in the Southern Hemisphere with a cold front propagating west to the system and a warm front east (Figure 2.24). In the cold front region,  $(v)_\lambda$  is positive (northward),  $(T)_\lambda$  is negative (cooler), and  $\frac{\partial([T]_\lambda)\varphi}{\partial\varphi}$  is positive (temperature increases equator-ward). Conversely, in the warm front region,  $(v)_\lambda$  is negative (southward),  $(T)_\lambda$  is positive (warmer), and  $\frac{\partial([T]_\lambda)\varphi}{\partial\varphi}$  remains positive. This configuration is consistent across both hemispheres when accounting for the appropriate directional changes in wind and temperature gradient.

The second component,  $(\omega)_\lambda(T)_\lambda \frac{\partial([T]_\lambda)\varphi}{\partial p}$ , must also be negative to contribute positively to  $C_A$ . The term  $\frac{\partial([T]_\lambda)\varphi}{\partial p}$  reflects the zonal average atmospheric lapse rate, which typically presents as negative over the cold air mass between  $\phi_3$  and  $\phi_6$  and between  $\lambda_1$  and  $\lambda_3$ , indicating an increase in temperature with height. Above this level, the lapse rate reverses. In contrast, across the rest of the domain, particularly behind the warm front, this lapse

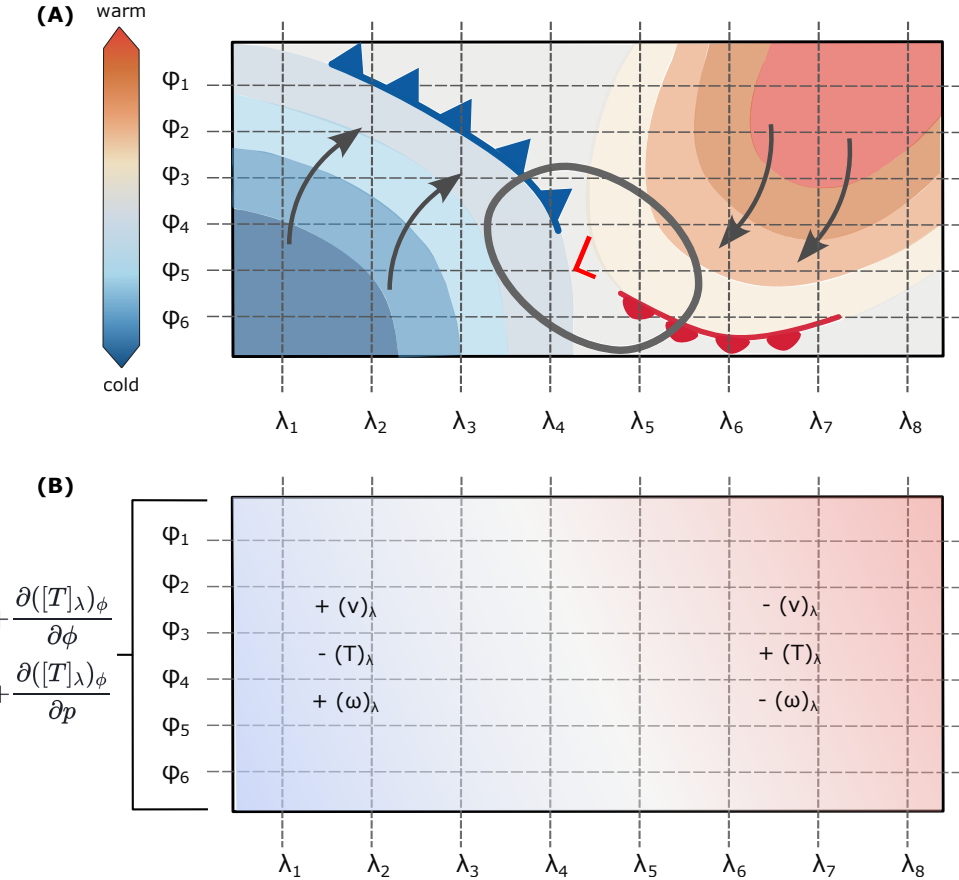


Figure 2.24: Representation of the conversion process between  $A_Z$  and  $A_E$ . (A) Illustration of an idealized situation of a midlatitude low-pressure system in the Southern Hemisphere, with a cold front propagating west and a warm front east. (B) Analysis of the variables involved in the formula for  $C_A$  (Equation 2.39). The y-axis represents latitude circles ( $\phi$ ), and the x-axis represents longitude ( $\lambda$ ). In the Southern Hemisphere, latitude decreases from  $\phi_1$  to  $\phi_6$ .

rate term is positive. Consequently, when averaged across the domain and integrated over vertical levels, the overall contribution of this term tends to be positive. Furthermore, in the area behind the warm front, where  $(\omega)_\lambda$  is negative (indicating ascending air) and  $(T)_\lambda$  is positive (indicating warmer air), the product  $(\omega)_\lambda(T)_\lambda$  is negative. This, in turn, results in a positive contribution to  $C_A$ , aligning with the term's requirement for a negative input to yield a positive output.

This analysis shows how an extratropical cyclone can influence global energetics. By transforming meridional into zonal temperature gradients,  $C_A$  converts zonal APE into eddy APE. The described scenarios are generalizations and do not capture all atmospheric variations during frontal passages; however, they do reflect significant energetic contributions, especially at lower atmospheric levels. Additionally, it is important to note that the

signs of the first and second components of  $C_A$  do not need to match;  $C_A$  will be positive if the magnitude of the negative component exceeds that of the positive component.

The last conversion term,  $C_K$  (Equation 2.40), represents the conversion of kinetic energy from eddies to the zonal mean state. Positive values indicate an energy transfer from  $K_E$  (eddy kinetic energy) to  $K_Z$  (zonal kinetic energy), and vice versa. This term's formulation is more complex than others, comprising five distinct components: 1) meridional advection of zonal momentum, 2) meridional shear of meridional wind, 3) interaction of eddy zonal wind with zonal meridional wind, 4) vertical advection of zonal momentum, and 5) vertical advection of meridional momentum.

For simplicity, in analyzing the first term—meridional advection of zonal momentum—we consider  $(u)_\lambda$ ,  $(v)_\lambda$ , and  $\frac{\partial[u]_\lambda}{\partial\phi}$ , omitting variables related to the transformation from Cartesian to spherical coordinates. Consider a purely zonal westerly jet (Figure 2.25a), where as latitude decreases from  $\phi_1$  to  $\phi_{10}$ ,  $\frac{\partial[u]_\lambda}{\partial\phi}$  transitions from negative in the northern part of the domain to positive in the southern part. However, both  $v$  and  $(u)_\lambda$  are null in this scenario. Similarly, for a purely meridional northerly jet (Figure 2.25b),  $(v)_\lambda$  varies from negative to positive across the domain, but  $(u)_\lambda$  and  $\frac{\partial[u]_\lambda}{\partial\phi}$  remain null. Therefore, averaged over the entire domain, this term is null for both scenarios.

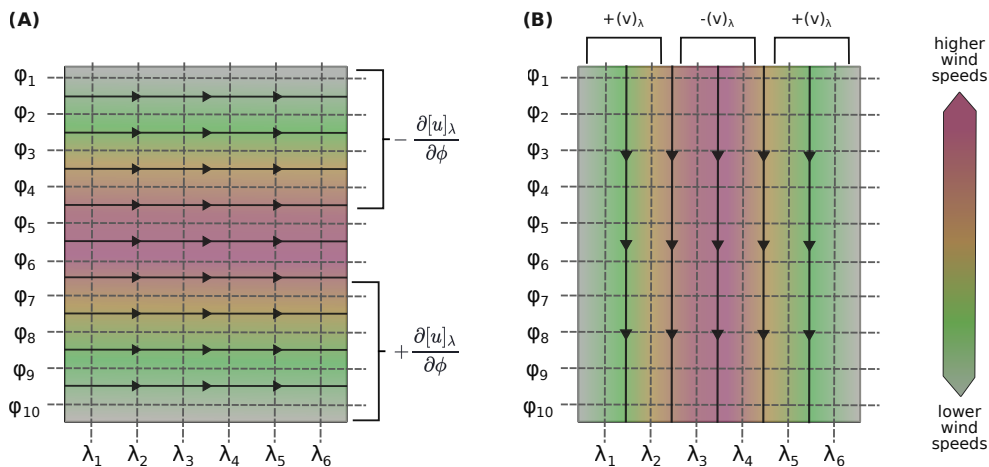


Figure 2.25: Illustration of (A) a zonal westerly jet and (B) a meridional northerly jet in the Southern Hemisphere. The y-axis represents the latitude circles ( $\phi$ ) and the x-axis represents longitude ( $\lambda$ ).

In situations where small instabilities arise in the zonal or meridional flow, they may initiate the development of larger instabilities. For example, consider a zonal jet becoming unstable with a cyclonic (clockwise) deviation in its flow at the southern part of the domain (Figure 2.26a). Similarly as in a purely zonal jet,  $\frac{\partial[u]_\lambda}{\partial\phi}$  exhibits negative values in

the northern part of the domain and positive values in the southern part (Figure 2.26b). With the onset of instability,  $(v)_\lambda$  and  $(u)_\lambda$  are no longer null across the domain: they are negative on the eastern flank and positive on the western flank of the perturbation. This leads to a positive contribution to  $C_K$  from the first term, indicating that the eddy is transferring energy to the zonal flow and thus depleting its own energy over time.

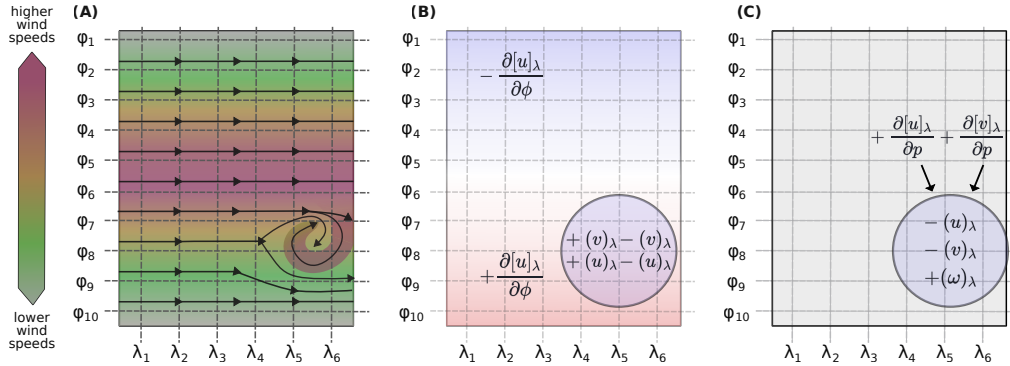


Figure 2.26: (A) Illustration of an eddy developing in the southern part of a purely meridional jet, (B) signal analysis for the first, (C) fourth and fifth terms of  $C_K$  (Equation 2.40), for this scenario. The y-axis represents the latitude circles ( $\phi$ ) and the x-axis represents longitude ( $\lambda$ ).

The second term in  $C_K$  - meridional shear of meridional wind - contains  $(v)_\lambda^2 \frac{\partial[v]_\lambda}{\partial\phi}$ . It is evident that  $(v)_\lambda^2$  is null for purely zonal jets, but otherwise is always positive, hence  $\frac{\partial[v]_\lambda}{\partial\phi}$  dictates this term's contribution to the signal of  $C_K$ . While  $\frac{\partial[v]_\lambda}{\partial\phi}$  is typically null for purely zonal and meridional jets, its contribution becomes significant for small instabilities in the zonal flow. For the eddy development illustrated in Figure 2.26a, as  $|v|$  decreases from the western to the eastern flank of the perturbation,  $[u] < 0$ , so  $\frac{\partial[v]_\lambda}{\partial\phi} > 0$ , making this term's contribution to  $C_K$  positive.

The third term - interaction of eddy zonal wind with zonal meridional wind - contains  $(u)_\lambda^2 [v]_\lambda$ . Both  $(u)_\lambda^2$  and  $[v]_\lambda$  are null for purely zonal jets. However, similar to the previous terms, their combined signal can be investigated for perturbations in the zonal flow. As  $(u)_\lambda^2$  is invariably positive, the signal of this term is influenced by  $[v]_\lambda$ . In the situation depicted in Figure 2.26a,  $[v]_\lambda < 0$  leads to a negative contribution of this term to  $C_K$ .

For the fourth and fifth terms - vertical advection of zonal and meridional momentum, respectively - the analysis is more complex due to the three-dimensional variations in wind throughout the troposphere. The fourth term involves  $(\omega)_\lambda (u)_\lambda \frac{\partial[u]_\lambda}{\partial p}$ , while the fifth includes  $(\omega)_\lambda (v)_\lambda \frac{\partial[v]_\lambda}{\partial p}$ . In scenarios of purely zonal jets, both terms are null, but they

become significant with perturbations in the zonal flow.

Specifically, at mid-latitudes, we can assume that  $\frac{\partial[u]_\lambda}{\partial p}$  is generally negative ( $[u]$  increases with height) in the troposphere. However, in the scenario illustrated in Figure 2.26a, where the flow intensifies on the eastern flank of a perturbation,  $[u]_\lambda$  becomes negative (westward), making  $\frac{\partial[u]_\lambda}{\partial p} > 0$  (Figure 2.26c). Additionally, if the jet is at a higher altitude (e.g., 250 hPa), the convergence caused by the perturbation results in descending air, thus  $(\omega)_\lambda$  is positive. These conditions render the contribution of this term to  $C_K$  negative. The analysis for the fifth term follows similarly, where  $\frac{\partial[v]_\lambda}{\partial p} > 0$ ,  $(u)_\lambda > 0$ , and  $(\omega)_\lambda > 0$  (Figure 2.26c), resulting in a negative contribution for this term to  $C_K$ .

Collectively, the first two terms contribute positively to  $C_K$  while the last three terms provide negative contributions. Thus, the terms that, when summed, present the highest magnitude, will dictate the overall signal for  $C_K$ . It is essential to recognize that the illustrative examples provided - zonal and meridional flows and a perturbation developing in the zonal flow - are simplifications of atmospheric motion. They are not intended to present a comprehensive picture of all conditions under which conversion between  $K_Z$  and  $K_E$  might occur but serve as guiding thought experiments to aid understanding of this conversion in real atmospheric motions. To the author's knowledge, due to the complexity of such analysis, no comprehensive attempt has been made previously in the literature.

The APE generation and K dissipation terms are defined as:

$$G_Z = \int_{p_t}^{p_b} \frac{([q]_\lambda)_\phi ([T]_\lambda)_\phi]_{\lambda\phi}}{c_p[\sigma]_{\lambda\phi}} dp \quad (2.41)$$

$$G_E = \int_{p_t}^{p_b} \frac{[(q)_\lambda (T)_\lambda]_{\lambda\phi}}{c_p[\sigma]_{\lambda\phi}} dp \quad (2.42)$$

$$D_Z = - \int_{p_t}^{p_b} \frac{1}{g} [[u]_\lambda [F_\lambda]_\lambda + [v]_\lambda [F_\phi]_\lambda]_{\lambda\phi} dp \quad (2.43)$$

$$D_E = - \int_{p_t}^{p_b} \frac{1}{g} [(u)_\lambda (F_\lambda)_\lambda + (v)_\lambda (F_\phi)_\lambda]_{\lambda\phi} dp \quad (2.44)$$

Here,  $F_\lambda$  and  $F_\phi$  represent the zonal and meridional frictional components, respectively, and  $q$  is the diabatic heating term, computed as a residual from the thermodynamic equation:

$$\frac{q}{c_p} = \frac{\partial T}{\partial t} + \vec{V}_H \cdot \vec{\nabla}_p T - S_p \omega \quad (2.45)$$

where  $\vec{V}_H \cdot \vec{\nabla}_p T$  represents the horizontal advection of temperature and  $S_p$  approximates the static stability, given by:

$$S_p \equiv -\frac{T}{\theta} \frac{\partial \theta}{\partial p} \quad (2.46)$$

where  $\theta$  is the potential temperature.

The terms  $G_Z$  and  $G_E$  functionally resemble  $A_Z$  and  $A_E$ , respectively. The variable  $q$  quantifies the heat added to or removed from an air parcel through external sources such as radiation, latent heat release (e.g., condensation), and sensible heat exchange (e.g., conduction from the surface). The variable  $\sigma$  represents the overall stratification of the atmosphere. Generation of  $G_Z$  or  $G_E$  occurs when anomalous heating aligns with regions of anomalously high temperature, and anomalous cooling coincides with regions of anomalously low temperature. If the temperature/heating gradients are meridional (e.g., differential heating from the equator to the poles),  $G_Z$  is generated. Conversely, if the gradients are within the same latitude belt (e.g., differential heating between ocean and land),  $G_E$  is generated. Additionally, higher static stability, indicating a more stratified atmosphere, reduces the efficiency of APE generation, while lower static stability enhances it. Maximum generation of APE is analogous to the situation illustrated in Figure 2.24.

The terms  $D_Z$  and  $D_E$  represent the dissipation of kinetic energy from the zonal mean state and the eddies, respectively. The variable  $F$  denotes the frictional forces acting on the wind, which includes elements such as surface drag and turbulent friction. These frictional forces, notably surface drag and turbulent friction within the boundary layer, oppose the wind direction, causing a reduction in wind speed and consequently dissipating kinetic energy. Additionally,  $D_Z$  and  $D_E$  can also represent energy exchanges between different scales, specifically the transfer of energy from the grid scale to the subgrid scale. These forces not only convert kinetic energy into thermal energy but also facilitate the transfer of energy to smaller scale motions, thereby contributing to the overall energy dissipation within the atmospheric system.

The boundary terms are given by:

$$\begin{aligned} \text{BAZ} &= c_1 \int_{p_1}^{p_2} \int_{\varphi_1}^{\varphi_2} \frac{1}{2[\sigma]_{\lambda\varphi}} \left( 2([T]_\lambda)_\varphi (T)_\lambda u + ([T]_{\lambda\varphi})_\varphi^2 u \right)_{\lambda_1}^{\lambda_2} \\ &\times d\varphi dp + c_2 \int_{p_1}^{p_2} \frac{1}{2[\sigma]_{\lambda\varphi}} \left( 2[(v)_\lambda (T)_\lambda]_\lambda ([T]_\lambda)_\varphi \cos \varphi + ([T]_\lambda)_\varphi^2 [v]_\lambda \cos \varphi \right)_{\varphi_1}^{\varphi_2} dp \\ &- \frac{1}{2[\sigma]_{\lambda\varphi}} \left( [2(\omega)_\lambda (T)_\lambda]_\lambda ([T]_\lambda)_\varphi + \left[ [\omega]_\lambda ([T]_\lambda)_\varphi^2 \right]_{\lambda\varphi} \right)_{p_1}^{p_2} \end{aligned} \quad (2.47)$$

$$\begin{aligned} \text{BAE} &= c_1 \int_{p_1}^{p_2} \int_{\varphi_1}^{\varphi_2} \frac{1}{2[\sigma]_{\lambda\varphi}} [u(T)_\lambda^2]_{\lambda_1}^{\lambda_2} d\varphi dp \\ &+ c_2 \int_{p_1}^{p_2} \frac{1}{2[\sigma]_{\lambda\varphi}} \left( [(T)_\lambda^2 v]_\lambda \cos \varphi \right)_{\varphi_1}^{\varphi_2} dp \\ &- \left( \frac{[\omega(T)_\lambda^2]_{\lambda\varphi}}{2[\sigma]_{\lambda\varphi}} \right)_{p_1}^{p_2} \end{aligned} \quad (2.48)$$

$$\begin{aligned} \text{BKZ} &= c_1 \int_{p_1}^{p_2} \int_{\varphi_1}^{\varphi_2} \frac{1}{2g} \left( u [u^2 + v^2 - (u)_\lambda^2 - (v)_\lambda^2] \right)_{\lambda_1}^{\lambda_2} \\ &\times d\varphi dp + c_2 \int_{p_1}^{p_2} \frac{1}{2g} \left( [v \cos \varphi [u^2 + v^2 - (u)_\lambda^2 - (v)_\lambda^2]]_{\varphi_1}^{\varphi_2} \right) dp \\ &- \left( \frac{1}{2g} [\omega [u^2 + v^2 - (u)_\lambda^2 - (v)_\lambda^2]]_{\lambda\varphi} \right)_{p_1}^{p_2} \end{aligned} \quad (2.49)$$

$$\begin{aligned} \text{BKE} &= c_1 \int_{p_1}^{p_2} \int_{\varphi_1}^{\varphi_2} \frac{1}{2g} \left( u [(u)_\lambda^2 + (v)_\lambda^2] \right)_{\lambda_1}^{\lambda_2} d\varphi dp \\ &+ c_2 \int_{p_1}^{p_2} \frac{1}{2g} \left( [v \cos \varphi [(u)_\lambda^2 + (v)_\lambda^2]]_\lambda \right)_{\varphi_1}^{\varphi_2} dp \\ &- \left( \frac{1}{2g} [\omega [(u)_\lambda^2 + (v)_\lambda^2]]_{\lambda\varphi} \right)_{p_1}^{p_2} \end{aligned} \quad (2.50)$$

where  $c_1 = -[a(\lambda_2 - \lambda_1)(\sin \varphi_2 - \sin \varphi_1)]^{-1}$ ,  $c_2 = -[a x (\sin \varphi_2 - \sin \varphi_1)]^{-1}$ .

The boundary terms  $BA_Z$ ,  $BA_E$ ,  $BK_Z$ , and  $BK_E$  represent the fluxes of  $A_Z$ ,  $A_E$ ,  $K_Z$ , and  $K_E$ , respectively, from the lateral and vertical boundaries. Each boundary term has three components and shares a similar structure. For exemplification purposes, let's look into the  $BA_Z$  term. The first component represents the contribution of the zonal temperature flux anomalies to the  $A_Z$  term at the western and eastern boundaries. This term is computed for the westernmost and easternmost longitudes, integrated over all latitudes and pressure levels, and averaged over the entire domain. The second component is similar to the first one, representing the contribution of the meridional temperature flux anomalies to the  $A_Z$  term at the southern and northern boundaries. This term is computed for the southernmost and northernmost latitudes, integrated over all longitudes and pressure levels, and averaged over the entire domain. The third component represents

the contribution of the vertical temperature flux anomalies to the  $A_Z$  term at the top and bottom boundaries. This term is computed for the topmost and bottommost pressure levels, integrated over all longitudes and latitudes, and averaged over the entire domain. The same logic can be applied to all other terms, substituting  $A_Z$  with  $A_E$ ,  $K_Z$ , and  $K_E$ , respectively.

The boundary terms  $BA_Z$ ,  $BA_E$ ,  $BK_Z$ , and  $BK_E$  represent the fluxes of  $A_Z$ ,  $A_E$ ,  $K_Z$ , and  $K_E$ , respectively, from the lateral and vertical boundaries. Each boundary term includes three components, all sharing a similar structure. To exemplify, consider the  $BA_Z$  term. The first component quantifies the contribution of zonal temperature flux anomalies to the  $A_Z$  term at the western and eastern boundaries. This term is calculated for the westernmost and easternmost longitudes, integrated over all latitudes and pressure levels, and averaged over the entire domain. The second component mirrors the first, representing the contribution of meridional temperature flux anomalies to the  $A_Z$  term at the southern and northern boundaries. This term is evaluated for the southernmost and northernmost latitudes, integrated across all pressure levels, and averaged domain-wide. The third component accounts for the contribution of vertical temperature flux anomalies to the  $A_Z$  term at the top and bottom boundaries. This term is calculated at the topmost and bottommost pressure levels and similarly averaged over the entire domain. Applying the same logic, the  $BA_E$ ,  $BK_Z$ , and  $BK_E$  terms are structured analogously, with adjustments to the specific energetic terms they represent—substituting  $A_Z$  with  $A_E$ ,  $K_Z$ , and  $K_E$  respectively.

Lastly, the terms  $B\Phi Z$  and  $B\Phi E$  are given by:

$$\begin{aligned} B\Phi Z = & c_1 \int_{p_1}^{p_2} \int_{\varphi_1}^{\varphi_2} \frac{1}{g} \left( [v]_\lambda ([\Phi]_\lambda)_\varphi \right)_{\lambda_1}^{\lambda_2} d\varphi dp \\ & + c_2 \int_{p_1}^{p_2} \frac{1}{g} \left( \cos \varphi [v]_\lambda ([\Phi]_\lambda)_\varphi \right)_{\varphi_1}^{\varphi_2} dp \\ & - \frac{1}{g} \left( \left[ ([\omega]_\lambda)_\varphi ([\Phi]_\lambda)_\varphi \right]_{\lambda_\varphi} \right)_{p_1}^{p_2} \end{aligned} \quad (2.51)$$

$$\begin{aligned} B\Phi E = & c_1 \int_{p_1}^{p_2} \int_{\varphi_1}^{\varphi_2} \frac{1}{g} ((u)_\lambda (\Phi)_{\lambda_\lambda})_{\lambda_1}^{\lambda_2} d\varphi dp \\ & + c_2 \int_{p_1}^{p_2} \frac{1}{g} \left( [(v)_\lambda (\Phi)_{\lambda_\lambda}]_\lambda \cos \varphi \right)_{\varphi_1}^{\varphi_2} dp \\ & - \frac{1}{g} \left( [(\omega)_\lambda (\Phi)_\lambda]_{\lambda_\varphi} \right)_{p_1}^{p_2} \end{aligned} \quad (2.52)$$

The terms  $B\Phi Z$  and  $B\Phi E$  describe the dynamical mechanisms that produce or destroy kinetic energy. As elucidated by Muench (1965), these terms, along with  $C_Z$  and  $C_E$ , involve a arise from the derivation of the term  $\vec{V} \cdot \nabla \Phi$ . This expression represents the generation of kinetic energy through cross-isobaric flow towards areas of low pressure. Conversely, the destruction of kinetic energy occurs when there is cross-isobaric flow towards areas of high pressure.

Apart from examining the individual contributions of each term to the energy cycle, the Lorenz Energy Cycle (LEC) highlights specific interactions between terms that elucidate distinct dynamical mechanisms (Figure 2.27). The  $A_Z$  term, involving meridional gradients of temperature and atmospheric stability, interacts in such a way that  $C_A > 0$  acts to diminish these gradients through the meridional transport of sensible heat. This process sets the stage for  $C_E > 0$ , driven by the zonal temperature gradient and vertical motions. In contrast, the conversion from  $K_Z$  to  $K_E$  ( $C_K$ ) redistributes kinetic energy without altering the thermal structure and is primarily influenced by the horizontal shear of the mean flow. Therefore, the processes  $A_Z \rightarrow A_E \rightarrow K_E$  are often referred to as the "baroclinic chain," while  $C_K$  is known as the barotropic conversion term (Michaelides, 1992; Veiga et al., 2013; Pezza et al., 2014; Okajima et al., 2021, e.g.). Additionally, the term "moist baroclinic chain" is used here to refer to the process where  $G_E$  supplies energy to  $A_E$ , acting in consonance with the baroclinic chain.

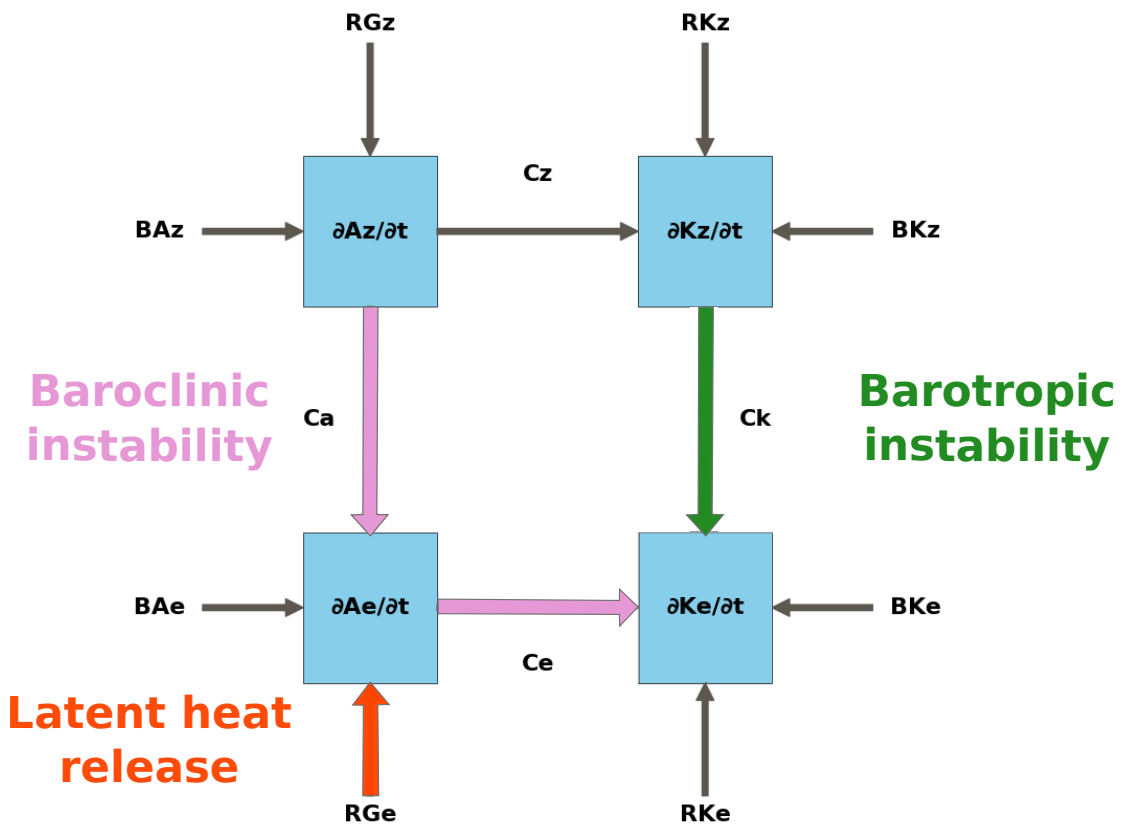


Figure 2.27: Schematic representation of the different energy conversion chains in the Lorenz Energy Cycle. The diagram illustrates the "baroclinic chain" ( $A_Z \rightarrow A_E \rightarrow K_E$ ), indicating the role of baroclinic instability, the contribution of latent heat release by the  $G_E$  term and the "barotropic chain" ( $K_Z \rightarrow K_E$ ).

#### 2.4.3 Lorenz Energy Cycle applied to cyclonic systems

During the 1960s and 1970s, extensive research was conducted on the energetics of extratropical cyclonic systems. Smith (1980) reviewed these studies, offering a detailed summary of their outcomes. According to the mean kinetic energy (K) budgets, cyclones are areas of relatively higher concentrated kinetic energy compared to the rest of the hemisphere, though the difference is not markedly substantial. Cyclones are characterized by significant energetic activity, with substantial  $K_E$  generation through cross-contour flow. This generation is nearly balanced by the horizontal export of energy and its dissipation. Mature cyclones typically exhibit negative values for  $D_E$ ; however, in certain scenarios,  $D_E$  can act as an energy source ( $D_E > 0$ ), especially in regions characterized by intense convection or the presence of short upper air waves, predominantly above the planetary boundary layer. This dynamic might be associated with energy transfer from sub-grid scales to the grid scale. Additionally, latent heat release from convective processes plays

a critical role in the generation of APE in extratropical cyclones. Generally, cyclones are inefficient thermodynamic systems; a significant portion of  $A_E$  is not converted into  $K_E$ , leading to an energy conversion efficiency of only 3% to 4%. Cyclones account for approximately 6% of the hemispheric energy contribution. However, intense cyclones, which are about 50% more energetically active than average, can contribute up to 20% of the hemispheric energy.

More recently, the study by Black and Pezza (2013) provides a detailed climatology of the energetics of cyclonic systems, specifically focusing on explosive cyclones. This research spans four major regions—the Northwest Pacific, the North Atlantic, the Southwest Pacific, and the South Atlantic—utilizing a 32-year climatology to analyze these phenomena. The analysis reveals that anomalous energy conversions begin approximately 48 hours before the explosive cyclone development and remain strong for up to 120 hours. The results demonstrate that the baroclinic chain is the primary mechanism driving the energy dynamics during explosive cyclogenesis, and this holds true across different regions and times of the year. Furthermore, the study finds that within the analyzed domains, the energetic signatures of regular cyclones often merge with background noise, making them indistinguishable.

The review by Smith (1980) provides a broad overview of the energy budget of extratropical cyclones, focusing primarily on their contributions to general circulation rather than on the dynamical mechanisms essential for their development, intensification, and decay. Meanwhile, Black and Pezza (2013) offers a more detailed picture, especially of explosive cyclones. However, the difficulty in distinguishing the energetic signatures of regular cyclones from background noise may be attributed to the large computational domains used, which are extensive enough to include multiple cyclonic systems simultaneously, potentially complicating the analysis. To overcome these challenges and gain a deeper understanding of cyclonic energetics, specific case studies are essential. These studies provide insights into how various energy transformations within a cyclone contribute to its lifecycle. The literature reviewed in the next paragraphs highlights the pathways that supply energy to the eddy energy reservoirs, with particular emphasis on the  $K_E$  term, which serves as a proxy for the system's intensity. Special attention is given to the contributions of the baroclinic ( $A_Z \rightarrow A_E \rightarrow K_E$ ) and barotropic ( $K_Z \rightarrow K_E$ ) chains, as well as to the contributions from latent heat release ( $G_E$ ) due to the eddy's convective activity. These elements are crucial

for understanding the energetic dynamics that drive cyclone behavior and evolution.

There are only a few studies accessing the Lorenz Energy Cycle in the context of tropical cyclones. For instance, Brennan and Vincent (1980) analyzes the synoptic-scale energy budget of Hurricane Carmen (1979) as it intensified from a tropical depression to a major hurricane. During the tropical depression stage,  $K_E$  serves as a source of energy for both  $A_E$  and  $K_Z$ , while also exporting energy ( $BK_E < 0$ ), primarily sustained by  $RK_E$ . Concurrently,  $A_E$  exports energy ( $BA_E < 0$ ) and experiences energy destruction due to diabatic cooling and/or descending movements ( $G_E < 0$ ). This suggests that during this phase, the system predominantly relies on up-scaling of energy from subgrid scales and/or cross-isobaric flow ( $B\Phi E > 0$ ). However, during the hurricane stage, diabatic heating (from  $G_E$ ) begins to supply energy to  $A_E$ , further supported by the import of energy ( $BA_E > 0$ ) and conversion from  $A_Z$ . Most of this energy is transformed into  $K_E$ . Additionally, the zonal circulation contributes to the eddy energy ( $C_K < 0$ ). Consequently, during the hurricane phase, moist baroclinic processes drive the system's development, supplemented by barotropic conversions. Despite an overall reduction in  $K_E$  and  $K_Z$ , the storm's circulation intensifies. The author attributes this paradox to mesoscale processes not being adequately resolved due to the poor resolution of the dataset, with negative values for both  $D_Z$  and  $D_E$  indicating an energy transfer from the resolved synoptic scale to the mesoscale. These observations imply that higher resolution datasets might reveal different dynamics for  $K_E$  and  $K_Z$  budgets.

Although the study by Brennan and Vincent (1980) provided important insights into the environmental energetics changes during hurricane formation, several caveats merit discussion. First, the dataset used features a coarse resolution with  $2.5^\circ$  grid spacing, which is insufficient to accurately represent mesoscale phenomena associated with the hurricane. Additionally, the data consisted primarily of point-source rawinsonde observations, surface observations, and daily infrared satellite imagery, with gaps filled by linear interpolation. Lastly, the computational domain was excessively large ( $50^\circ \times 50^\circ$ ), raising concerns that the system's energetics could be confounded with background environmental influences. These limitations suggest that the study's findings should be interpreted with caution, considering the potential blending of cyclone energetics with broader atmospheric processes.

Using data from the NCEP/NCAR reanalysis, Veiga et al. (2008) analyzed the energy

budget for Hurricane Catarina, distinguishing its development into distinct phases. During the extra-tropical phase, the moist baroclinic chain was active, with both  $A_Z$  and  $G_E$  supplying energy to  $A_E$ , which was predominantly converted into  $K_E$ . As the system transitioned into the tropical phase, this chain loss intensity, notably as  $G_E$  decreased significantly, making the conversion from  $K_Z$  to  $K_E$  the primary contributor to  $K_E$ . However, much of this energy was exported from the domain, leading to a decrease in  $K_E$ . Upon reaching Category 1 Hurricane status, there was a reversal in the sign of the baroclinic chain, characterized by conversions from  $K_E$  to  $A_E$  to  $A_Z$ , with both  $C_K$  and  $RK_E$  playing roles in augmenting  $K_E$ .

More attention was given to the energetics of subtropical cyclones than to the tropical systems. Michaelides (1987) analyzes the synoptic-scale energy budget of a frontal depression that initially formed in the Mediterranean region, categorizing its evolution into four distinct phases. Although the nomenclature was not established at the time, the system might potentially have been classified as a medicane, a type of subtropical cyclone that originates in the Mediterranean (da Rocha et al., 2019). During the precyclogenetic period ("incipient stage"),  $A_E$  is sustained by contributions from  $A_Z$ ,  $K_E$ , and  $BA_E$ . However, it experiences a net decrease due to negative generation from cooling and descending motions. Meanwhile,  $K_E$  sees an increase, fueled by conversions from  $K_Z$  and energy import. As cyclogenesis begins ("intensification stage"), the signals for both  $C_A$  and  $C_E$  reverse, enabling  $A_E$  to feed both  $A_Z$  and  $K_Z$ , supported by energy import and positive  $G_E$ . Although  $K_Z$  continues to enhance  $K_E$ , increased dissipation begins to diminish  $K_E$ . In the development phase ("mature phase"),  $A_E$  reaches its peak, primarily due to latent heat generation and significant energy import.  $A_E$  is actively converted to  $K_E$ , yet  $K_E$  continues to decline overall, affected by heightened dissipation and energy conversions to  $K_Z$ . In the post-cyclogenesis phase ("decay phase"), both  $A_E$  and  $K_E$  diminish as the system weakens, with marked reductions in import, conversion rates, and  $D_E$  reaching its maximum.

In their study, Dias Pinto et al. (2013) investigate the potential for tropical transition of Subtropical Cyclone Anita near the southeast Brazilian coast. During the early stages of the system, the barotropic chain primarily fueled  $K_E$ . As the system evolved into a hybrid stage and approached its potential for tropical transition, both moist baroclinic and barotropic chains actively supplied energy to  $K_E$ , complemented by positive values of  $G_E$

due to convective processes. Concurrently, the system exported both  $A_E$  and  $K_E$  through its boundaries. Eventually, Anita entered a baroclinic environment and transitioned to an extratropical system. This phase was marked by a reversal in the sign of  $C_K$  and a dominance of the baroclinic chain in its energetics.

The study by Pezza et al. (2014) explores the energetics of the hybrid subtropical cyclone known as "Duck," which occurred over the Tasman Sea. Influenced by a persistent mid-latitude blocking high, the genesis of Duck created a conducive environment for cyclogenesis, with the system undergoing a partial tropical transition. During the genesis phase, a significant peak in  $C_K$  was observed, reaching a maximum near 350 hPa, facilitated by the presence of the blocking system — a similar environmental condition to that observed during Catarina's tropical transition. As Duck evolved, a secondary peak in baroclinic conversion coincided with the development of an upper-level warm core for the first time. However, the energy supply for  $K_E$  during this stage was insufficient for a full tropical transition. The authors speculate that the baroclinic conversion prevented Duck from achieving a complete tropical transition, hence not reaching hurricane status.

The energetics of the Duck storm were also investigated by Cavicchia et al. (2018), with comparisons made to an extratropical cyclone, the Pasha Bulker storm. Similar to findings by Pezza et al. (2014), the Duck storm's lifecycle was predominantly influenced by the barotropic chain, which was the main source of energy for  $K_E$ . In contrast, the Pasha Bulker storm was primarily driven by the baroclinic chain, with the most significant baroclinic energy conversions occurring during its intensification phase. However, Cavicchia et al. (2018) does not present results for generation and boundary terms, which limits the depth of the analysis.

For extratropical cyclones, a larger body of literature exploring their energy cycle can be found, especially for the Mediterranean and South Atlantic regions. For instance, in Michaelides (1992), an extratropical system originating in the Mediterranean region is analyzed, providing a basis for comparison with the earlier study by Michaelides (1987). During the initial development phase,  $A_E$  increases due to significant latent heat release and the advection of colder air over warmer waters, which enhances  $G_E$  and  $C_A$ . Concurrently,  $K_E$  is sustained by conversions from both  $A_E$  and  $K_Z$ . As cyclogenesis progresses, the energetic profile remains similar to the previous stage; however, convective activity and imports of  $A_E$  decline, leading to a decrease in this term. Simultaneously, an increase in

$D_E$  causes a reduction in the absolute value of  $K_E$ . During this stage,  $K_E$  is primarily maintained by  $C_K$ . In the mature phase, there is a further decline in  $G_E$  and imports of  $A_E$ , causing  $A_E$  to decrease further. Additionally, as  $D_E$  increases and conversion from other terms decreases,  $K_E$  also diminishes over time. During the decay phase,  $G_E$  reaches its lowest level; however,  $A_E$  increases due to enhanced  $C_A$  and weakened  $C_E$ . Conversely,  $K_E$ , despite the weakened  $C_A$  and  $C_K$ , increases as dissipation becomes minimal.

Wahab et al. (2002) also analyzed the energy budget throughout the development of a Mediterranean cyclone. The cyclogenesis phase is characterized by a significant increase in  $K_E$ , primarily supported by the residual term ( $RK_E$ ), while  $A_E$  is initially sustained by  $K_E$ . However, as the  $RG_E$  term increases,  $A_E$  begins to feed  $K_E$ . The growth period of the cyclone is marked by  $K_E$  being bolstered by  $C_K$  and imports of energy, which are subsequently either dissipated or converted to  $A_E$ , with  $RG_E$  acting as a sink of energy. During the dissipation period,  $A_E$  serves as a source of energy for both  $K_E$  and  $A_Z$ . Concurrently, while  $K_E$  is supported by  $K_Z$  and imports of energy, dissipation acts as a significant sink of energy, resulting in a decrease in  $K_E$ .

The study by Bulic (2006) investigates the energy budget associated with a deep and rapid cyclogenesis over the Mediterranean region, utilizing the ALADIN model. Before cyclogenesis,  $K_E$  is converted into  $A_E$ , a process that reverses after the cyclone forms. Throughout the cyclone's lifecycle,  $C_K$  consistently supplies energy to  $K_E$ . This conversion, most intense at upper levels around 350 hPa, is identified as crucial for the system's development. Additionally,  $B_{K_E}$  is responsible for exporting eddy energy throughout the entire lifecycle, except during the time of cyclone formation. The study highlights the cyclone's dependency on both baroclinic and barotropic processes; however, it also notes that the results may be limited to the dynamics captured by the model and might not fully reflect observational data.

Dias Pinto and Rocha (2011) analyzed the energy cycle for three extratropical cyclones, one for each genesis region in South America, detailing each system's development across formation, mature, and decay phases. For the first system, with genesis in the SE-BR region, the energetics were most active during the formation phase, where both baroclinic and barotropic chains provided energy to  $K_E$ , with significant contributions from the  $C_K$  term. In the mature phase, the baroclinic chain reversed, making  $C_K$  the sole contributor to  $K_E$ . During the decay phase,  $K_E$  transferred energy to  $K_Z$  and  $A_E$  to  $A_Z$ . The

second system, originating in the LA-PLATA region, maintained a consistent energy supply throughout its lifecycle via the moist baroclinic chain, most prominently during the mature phase. Throughout all phases,  $K_E$  consistently supplied energy to  $K_Z$ . The third system, with its genesis in the ARG region, was primarily sustained by the baroclinic chain, with contributions from latent heat release ( $G_E$ ) only during the mature phase. Although less significant, there was also an energy supply from  $C_K$  during the formation and mature phases.

The study by Pezza et al. (2010) examines the Lorenz energetics of a high-latitude baroclinic storm that caused severe flooding in Nome, Alaska. The trajectory and intensity of the storm were significantly influenced by a blocking high-pressure system that steered its path a week prior to its formation. From the onset of cyclogenesis to the rapid intensification phase, the environment transitioned from lower to higher energy states, marked by peaks in  $A_E$  and  $K_E$ . During these phases, both the baroclinic and barotropic energy chains supplied energy to  $K_E$ , with a smaller contribution from  $G_E$  to  $A_E$ . The computational domain included the blocking region, highlighting the role of this high-pressure system in facilitating the energy conversion  $C_K$ , which supplied  $K_E$  to the cyclonic system. As the storm reached its peak activity, the barotropic chain reversed, with  $K_E$  feeding energy back to zonal kinetic energy ( $K_Z$ ). Thus, during this stage, the maintenance of the system was predominantly sustained by the baroclinic chain. Additionally, the peak in baroclinic energy transfer occurred approximately 18 hours before the storm reached maximum intensity, indicating significant preconditioning of the environment by the baroclinic processes.

Michaelides et al. (1999) analyze the energetics of an intense Mediterranean cyclone, employing both Eulerian and quasi-Lagrangian frameworks for comparison. The quasi-Lagrangian framework reveals a significant increase in  $A_E$  during the cyclone's development, driven by diabatic heating processes such as latent heat release in the warm sector. Concurrently,  $K_E$  increases from the early stages to the maturity phase and then decreases as the cyclone decays. This initial rise in  $K_E$  is propelled by  $C_K$ , especially prominent at the jet level in the upper troposphere. The transformations between  $A_E$  and  $K_E$  are characterized by initial conversions of  $A_E$  to  $K_E$ , fueling the cyclone's intensification, followed by a reversal where  $K_E$  converts back to  $A_E$  as the system weakens. Notably, there are substantial imports of  $K_E$  during the cyclone's intensification phase and exports during its dissipation. The quasi-Lagrangian analysis indicates higher  $A_E$  and lower  $K_E$  compared

to the Eulerian method, suggesting that the fixed volume method captures more ambient kinetic energy from surrounding regions. Both methods confirm an overall conversion from  $K_Z$  to  $K_E$ , although the values are greater in the Eulerian method, and the conversions from  $A_E$  to  $K_E$  change signs. Additionally, there are reversals in signs for the boundary terms. The semi-Lagrangian method is considered to more genuinely represent the energetics characteristics of the synoptic system under study, as it isolates the cyclone as much as possible at all times. In contrast, the Eulerian method allows for circulations other than the cyclonic system under study to infringe into the computational region, potentially spuriously contaminating the cyclone's energetics.

The reviewed literature provides valuable insights into the energetics of different cyclonic systems. For tropical cyclones, although the limited body of literature prevents definitive conclusions, it appears that the barotropic chain, aided by the  $G_E$  term and subsequent conversions from  $A_E$  to  $K_E$ , is a primary driver for cyclone development. This emphasis on barotropic instability aligns well with research highlighting the role of barotropic instability in tropical waves for the initial development of tropical cyclones, with further intensification facilitated by latent heat release *via* CISK/WISHE mechanisms, as discussed in Section 2.1.3. Meanwhile, studies on subtropical cyclones indicate a shared contribution from barotropic and baroclinic processes, with the moist contributions to the baroclinic chain being variably active. The barotropic chain seems particularly important in the initial stages, with the baroclinic chain gaining significance in later stages. For extratropical cyclones, contrary to expectations, the baroclinic chain is not the sole driver of their energy cycle; most case studies indicate a role for the barotropic chain in their development. From Black and Pezza (2013)'s results, we can infer that the primary difference in the Lorenz Energy Cycle (LEC) between regular and explosive cyclones is the heightened importance of the baroclinic chain in the latter. Additionally, it is noteworthy that for both subtropical and extratropical systems, barotropic conversions occur predominantly at upper tropospheric levels. Nevertheless, while these energy pathways are crucial for system development, other terms also play important roles. For instance,  $D_E$  is often indicated as a significant sink for  $K_E$ , with larger values as  $K_E$  increases. Additionally, imports of  $K_E$  ( $BK_E$ ), particularly in the early stages of development, also contribute to system development.

From the reviewed literature, it is evident that the LEC methodology is a valuable

diagnostic tool for studying cyclonic system dynamics. However, despite the methodology dating back to the 1960s and still being in use today, the body of literature on this topic is still expanding, primarily comprising case studies, with the only comprehensive climatology provided by Black and Pezza (2013). Furthermore, most case studies utilize the Eulerian framework, which may underestimate contributions from certain terms, as the large-scale environment might overshadow the systems' energetics. There is a need for more climatologies assessing the LEC for cyclonic systems—or at least analyses of a large number of systems—to better understand the energy pathways related to their development.



# Chapter 3

---

## Data & Methods

### 3.1 Methodological Steps

The primary objective of this thesis was to identify the key dynamical mechanisms influencing cyclone development in the Southwestern Atlantic and Southeast American regions across their various development phases. This was achieved through a series of methodological steps as detailed below and illustrated in Figure 3.1.

A comprehensive database of cyclonic system tracks was used, encompassing all systems with genesis in the South Atlantic region from 1979 to 2020. The cyclones were detected based on their central relative vorticity at 850 hPa using the TRACK algorithm. This extensive dataset served as the foundational input for subsequent analyses.

The CycloPhaser program was developed to delineate the distinct life phases of each cyclone. CycloPhaser decomposes the relative vorticity time series into distinct phases using its maximum, minimum, and derivative values. This tool facilitated the construction of a climatology of cyclone life cycle phases, enabling a detailed investigation of the mean characteristics and spatial distribution of cyclones during each phase of their development.

An application was programmed to compute the Lorenz Energy Cycle (LEC) for all cyclones in the database. This analysis provided insights into the energetics of the systems, allowing for a detailed examination of the mean energy characteristics across different life cycle phases.

To further refine the analysis, the K-means clustering algorithm was employed to identify distinct energy patterns (EPs) within the cyclones. This classification enabled the grouping of cyclones based on their energy characteristics, facilitating a more detailed understanding of the dynamical processes at play.

The final step involved a detailed investigation of the dynamical mechanisms associated with cyclonic system development. By examining absolute vorticity ( $\eta$ ) fields, the Rayleigh-Kuo criterion was employed for detecting the occurrence of barotropic instability during cyclone development, while the occurrence of baroclinic instability was assessed using maximum Eady Growth Rate fields.

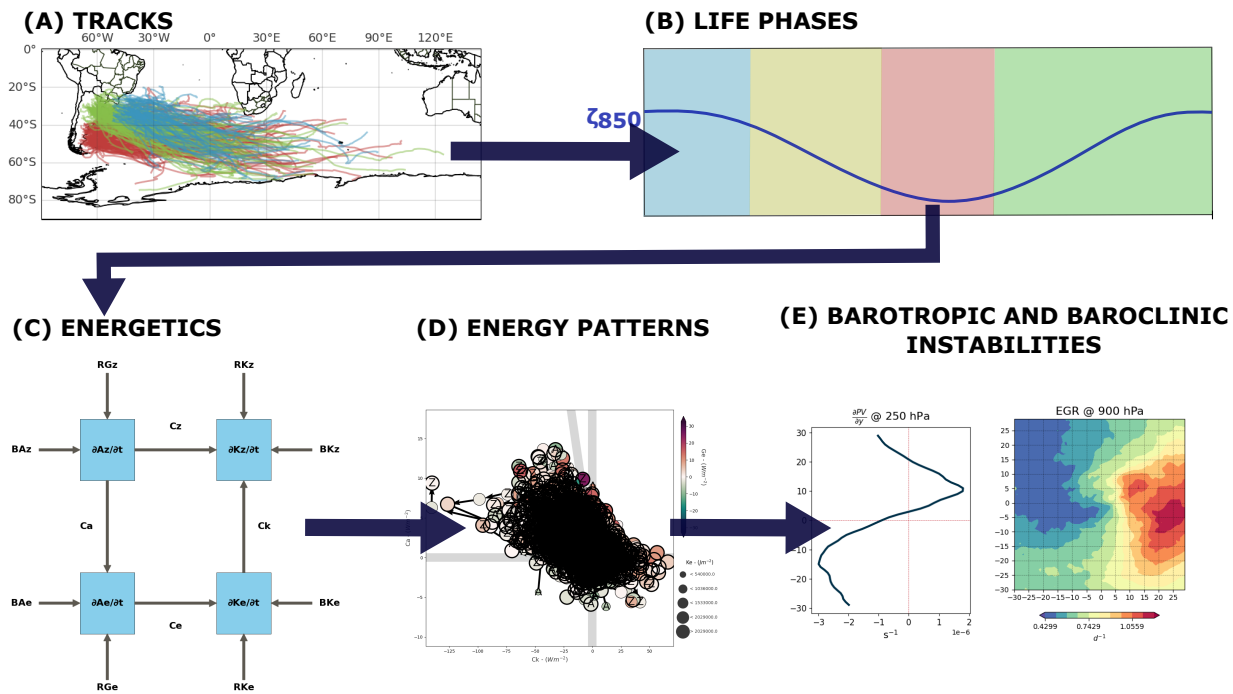


Figure 3.1: Flowchart depicting the methodological steps used in this thesis. (A) Retrieval of the cyclonic system track database using central relative vorticity at 850 hPa. (B) Identification of cyclone life phases with CycloPhaser, categorizing the vorticity time series into distinct phases. (C) Computation and analysis of the Lorenz Energy Cycle for the cyclones to investigate their energetic characteristics. (D) Classification of energy patterns using the K-means algorithm to determine distinct energy characteristics. (E) Examination of dynamical mechanisms related to barotropic and baroclinic instabilities influencing cyclone development.

## 3.2 Databases

### 3.2.1 ERA5 Reanalysis

For both the cyclone tracking procedure and for the energetics computation, the database used was the ERA5 (Hersbach et al., 2020). The ERA5 is a comprehensive reanalysis dataset developed by the European Centre for Medium-Range Weather Forecasts (ECMWF). It represents the fifth generation of ECMWF reanalysis, providing global climate and weather data with an unprecedented level of detail and accuracy. This dataset

spans from January 1940 to the present, with ongoing updates ensuring its relevance for current and historical climate studies.

ERA5 reanalysis data are produced using the Integrated Forecasting System (IFS) Cy41r2, which assimilates a vast array of observations, including satellite and in-situ measurements (Hersbach et al., 2020). The dataset offers hourly estimates of a multitude of atmospheric, ocean-wave, and land-surface parameters, making it highly valuable for various meteorological and climate research applications. The spatial resolution of ERA5 is approximately 31 km, with 137 vertical levels from the surface to 1 hPa, providing detailed information into the vertical structure of the atmosphere.

The ERA5 reanalysis dataset has been evaluated for the Southern Hemisphere. It can provide precipitation patterns comparable to observations, although the reanalysis presents more accurate results for the extratropics, especially in winter, than for tropical regions (Balmaceda Huarte et al., 2021; Lavers et al., 2022). The dataset also provides accurate results for surface winds, particularly outside the tropical region, although the associated errors increase with wind intensity (Campos et al., 2022). However, for near-surface winds, Ramon et al. (2019) demonstrated that the ERA5 is currently the reanalysis that presents the best results. For temperature, although the ERA5 captures accurately the spatial distribution of temperature indices it can present warm biases near the Andes and on southern South America (Balmaceda Huarte et al., 2021). For temperature, while ERA5 accurately captures the spatial distribution of temperature indices, it can present warm biases near the Andes and in southern South America (Balmaceda Huarte et al., 2021).

### 3.2.2 *Cyclone Tracks in the South Atlantic*

For this study, precise information about the positioning (track) and central vorticity at the 850 hPa level ( $\zeta_{850}$ ) of cyclones was essential. These data were sourced from the "Atlantic Extratropical Cyclone Tracks Database" as detailed by Gramcianinov et al. (2020). Spanning from 1979 to 2020, this database covers the entire Atlantic Ocean within the spatial domain of 15°S–55°S and 75°W–20°E. Cyclone tracking within this database utilizes the ERA5 reanalysis fields, employing the TRACK algorithm (Hodges, 1994, 1995) and the method outlined by Hoskins and Hodges (2002), which computes relative vorticity from wind components at the 850 hPa level. The TRACK algorithm has previously been used for obtaining cyclone climatologies in the South Atlantic region (Gramcianinov et al.,

2019, 2020). The ERA5 dataset was chosen for its superior resolution, offering significant advantages in analyzing regions with complex orography and temperature gradients, such as the SESA region, ensuring a comprehensive and consistent representation of cyclone climatology (Gramcianinov et al., 2020).

The tracking criteria included a minimum cyclone duration of 24 hours and a displacement threshold of 1000 km. These requirements align with previous climatologies of South Atlantic cyclones (Sinclair, 1995; Gramcianinov et al., 2019). Additionally, systems that spent over 80% of their lifecycle over continental regions were excluded to avoid counting thermal lows and lee troughs, which are not the focus of this study (Crespo et al., 2021). While the primary focus was on extratropical cyclones, due to the specific calibration and sensitivity of the TRACK algorithm to features typical of these systems, the methodology does not explicitly exclude subtropical or tropical cyclones. Despite their rarity in the South Atlantic, subtropical systems, which occasionally exhibit characteristics similar to extratropical cyclones (Hart, 2003), may still be detected but remain a minority in the dataset. Further details on the methodology and database evaluation are discussed in Gramcianinov et al. (2020).

### 3.3 Cyclone’s Life Cycle Detection

This section outlines the procedure for detecting the life cycle phases of cyclones. In the current study, an automated method, the Cyclophaser program, was developed and employed to facilitate this process. Section 3.3.1 provides an in-depth examination of the Cyclophaser program, highlighting its functionalities and the methodologies it employs. Subsequently, Section 3.3.2 explores the specific settings and configurations of the Cyclophaser used in this study.

#### 3.3.1 Cyclophaser Program Description

To facilitate the detection of individual life cycle phases of cyclones, an automated Python package named Cyclophaser (Figure 3.2) was developed (de Souza et al., 2024). This package is open-source and freely available on the PyPI repository. It can be installed using the pip package manager with the command `pip install cyclophaser`. Comprehensive documentation, including usage examples, is available on ReadTheDocs

at <https://cyclophaser.readthedocs.io/en/latest/>, and the complete source code, which is open to contributions, can be found on GitHub at <https://github.com/daniloceano/CycloPhaser>.



Figure 3.2: The logo of the Cyclophaser program.

The program is designed to detect cyclone lifecycle phases using series of relative vorticity at the system's central position and its first derivative (Figure 3.3). While Cyclophaser was specifically developed and tested for this purpose, other variables such as sea level pressure or geopotential data might also be effective, although tests using these variables have not yet been conducted. Exploring how the lifecycle of cyclones might vary with different variables and how the geographical positioning of each stage might differ is an open research question.

The program begins with a preprocessing stage where users have the option to apply the Lanczos filter (Duchon, 1979) to the vorticity time series (Figure 3.3b). Based on the *sinc* function, the ideal mathematical representation of a low-pass filter, the Lanczos filter is adapted by windowing the *sinc* function to a finite range. Cyclophaser utilizes a band-pass filtering technique where weights are calculated using two cutoff frequencies, creating a differential of two *sinc* functions. This allows the filter to pass a specific frequency range while attenuating frequencies outside this range, permitting customization based on the spatio-temporal resolutions of different reanalysis datasets.

The Lanczos filter's primary use in Cyclophaser is to remove noise unrelated to the development of extratropical cyclones on synoptic scales, including fluctuations due to topography-induced circulations, sea breezes, and spatial and temporal variations in sea surface structures (Steele et al., 2015; Da et al., 2017; Acevedo et al., 2010). High-resolution datasets like ERA5 benefit from this filtering, which effectively reduces noise from structures like frontal systems (Hoskins and Hodges, 2002). However, this filtering step may be omitted for datasets that have been preprocessed by tracking algorithms incorporating

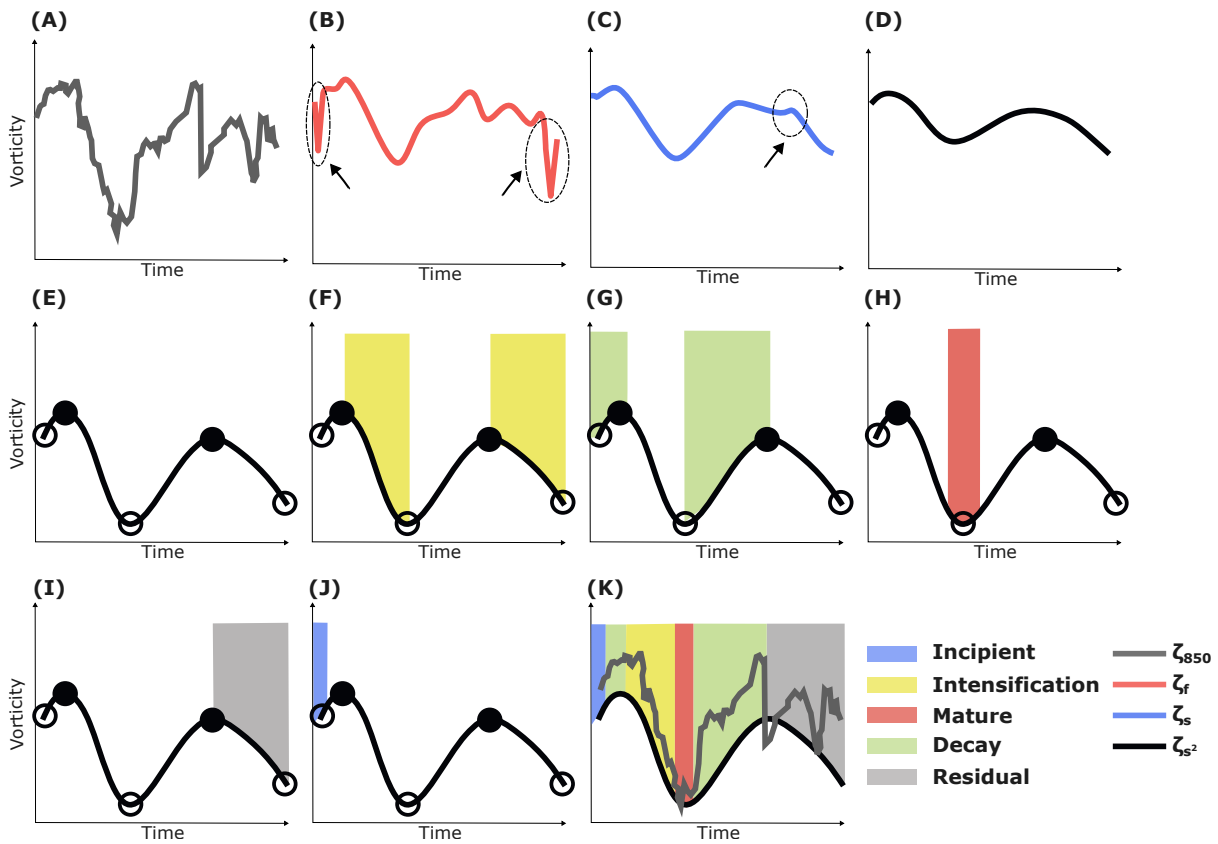


Figure 3.3: Illustrative representation of the methodological steps employed by Cyclophaser in analyzing cyclone lifecycle phases using vorticity series. The detailed steps demonstrate the application of data processing techniques including the Lanczos filter.

spatial filters (Murray and Simmonds, 1991; Pinto et al., 2005; Flaounas et al., 2014; Hoskins and Hodges, 2002, e.g.). As the track database used in the present study employed a filtering technique, the Lanczos filtering was not needed. Thus, a detailed formulation, explanation, and exploration of the issues related to such a filtering technique are provided in Appendix A.

After the initial filtering, the CycloPhaser program employs the Savitzky-Golay filter (Savitzky and Golay, 1964), as implemented in SciPy's package (Virtanen et al., 2020), to further reduce residual noise. This step is crucial for ensuring that the derivative curves form a sinusoidal pattern, which is essential for precise phase detection (Figure 3.3c). The Savitzky-Golay filter operates by fitting a polynomial of degree  $k$  to a window of  $2m + 1$  data points centered at each point  $y_i$  in the input signal. The coefficients of this polynomial are determined by minimizing the least squares error between the polynomial and the data points within the window. The smoothed value  $\hat{y}_i$  at the point  $y_i$  is then calculated by

evaluating the fitted polynomial at  $x_i$ :

$$\hat{y}_i = \sum_{j=-m}^m c_j y_{i+j}$$

where  $c_j$  are the coefficients derived from the polynomial fit, and  $m$  represents half the window size.

Users have the option to apply this smoothing twice (Figure 3.3d), adjusting the window size  $2m + 1$  and the polynomial order  $k$  to optimize the balance between noise reduction and data fidelity. This flexibility allows users to fine-tune the filter settings to meet specific requirements based on the spatio-temporal resolutions of various reanalysis datasets.

Subsequently, the first derivative of the relative vorticity is calculated predominantly using second-order finite differences, with central differences applied to interior points and first-order forward or backward differences used for endpoints. This derivative is then subjected to double smoothing with the Savitzky-Golay filter to maintain a sinusoidal pattern in the derivative series. This step is critical for accurately identifying cyclone lifecycle phases, making the dual smoothing process mandatory; omitting this could result in a noisy derivative series, potentially leading to erroneous phase detections, which emphasizes its necessity for reliable analysis.

The first phases to be detected are the intensification and decay stages. The program achieves this by analyzing peaks and valleys in the relative vorticity time series data, as shown in Figure 3.3e. The intensification phase is defined as the period between a peak and the subsequent valley (Figure 3.3f). Conversely, the decay phase is defined as the interval between a valley and the following peak (Figure 3.3g). To ensure that only significant phases are considered, each intensification and decay interval must span at least 7.5% of the total length of the time series. This threshold helps filter out minor fluctuations that are not indicative of true phase changes. To further refine the accuracy of phase detection, the program checks for multiple blocks of consecutive intensification or decay periods. If the gap between these blocks is smaller than 7.5% of the total series length, the program merges them into a single period. This merging process is crucial as it prevents the fragmentation of significant phases due to short gaps, thereby providing a more accurate and continuous representation of the intensification and decay stages.

After detecting the intensification and decay stages, the program proceeds to identify the mature stage of the cyclone's life cycle (Figure 3.3h). This stage is determined by

analyzing not only the peaks and valleys in the relative vorticity but also the smoothed derivative of vorticity. Between a peak and the subsequent valley (or a valley and the subsequent peak) of the vorticity series, there is always a corresponding valley (or peak) in its derivative. These points indicate periods of maximum intensification or decay of vorticity. The mature stage is defined as the interval between a vorticity valley and an adjusted point calculated based on the derivative of vorticity. Specifically, the mature stage spans from 12.5% of the time between the preceding derivative valley to 12.5% of the time to the following derivative peak. To be recognized as a significant mature stage, each interval must span at least 3% of the total length of the time series. This threshold ensures that only substantial periods are classified as mature stages. Additionally, the program verifies that all mature stages are preceded by an intensification stage and followed by a decay stage. This verification step ensures that the mature phase is accurately identified within the context of the entire cyclone life cycle.

Our methodology introduces the 'residual' stage, which is not directly related to the intrinsic development of extratropical cyclones but rather to peculiarities arising from the tracking algorithms (Figure 3.3i). This stage is exemplified in Figure 3.4. Panel (a) illustrates the intensification of a cyclonic system near the southernmost part of Argentina. The system reaches maturity, characterized by closed isobars at 850 hPa (Panel b). As the system begins to decay, it displays open isobars and diminished relative vorticity cohesion (Panel c). During its decay, it is influenced by a nearby system that leads to a temporary increase in the magnitude of its central relative vorticity, indicating a temporary re-intensification (Panel d). The tracking algorithm eventually discontinues its tracking, categorizing this late period of intensification as 'residual'—a phase of late intensification that is not associated with the primary development of the cyclone, as depicted in the relative vorticity series (Panel e).

The CycloPhaser classifies stages as residual by analyzing the previously detected cyclone phases. For phases classified as mature that do not transition to a decay stage, these instances are classified as residual. Similarly, if a full cycle of intensification, maturity, and decay is followed by another intensification that does not lead to a mature phase, it is also classified as residual (Figure 3.3i). This criterion accounts for scenarios where the tracking algorithm may continue to follow a cyclone post-decay, potentially capturing a re-intensification that does not culminate in a mature stage due to tracking limitations.

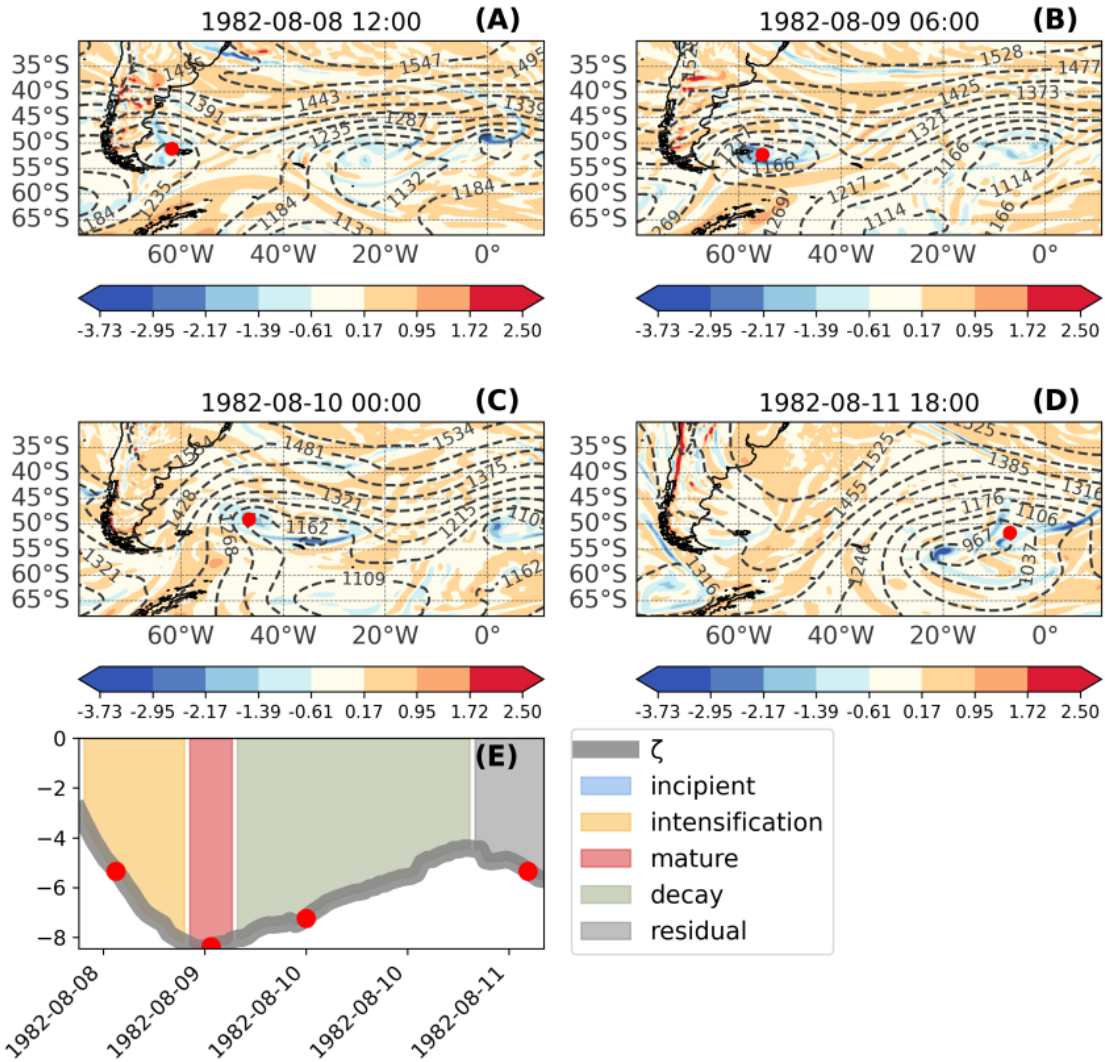


Figure 3.4: Relative vorticity (shaded) and geopotential heights (contours) at 850 hPa, illustrating distinct stages of a cyclone's lifecycle where a residual stage is present. Panel (A) shows the intensification stage with isobars still open, indicating a strengthening system. Panel (B) depicts the mature stage, characterized by maximum organization and extent. Panel (C) illustrates the decay stage, with open isobars and reduced relative vorticity cohesion. Panel (D) captures the residual phase, where, despite a general trend of weakening, there is a temporary increase in vorticity influenced by external factors, not directly associated with the primary development of the cyclone. The complete lifecycle of the system is depicted in Panel (E), where each red dot on the vorticity series corresponds to the specific moments shown in Panels (A) to (D).

Following the residual phase classification, a post-processing step is applied to refine cyclone phase identification. This step bridges any gaps that may appear between consecutive periods identified as intensification or decay phases. Specifically, the program scans for discontinuities within consecutive phase blocks and fills any identified gaps with the adjacent phase to ensure smooth and continuous phase transitions. Additionally, this

step involves correcting isolated phases—those misclassified phases that last only one time step—by aligning them with the subsequent phase if they occur at the start of the series, or with the preceding phase elsewhere. This adjustment enhances the consistency of phase identification throughout the cyclone lifecycle.

Ironically, the final step of the CycloPhaser program involves identifying the incipient stage, which marks the beginning of cyclone development (Figure 3.3j). Initially, all undefined periods in the time series are labeled as incipient. Subsequently, the program analyzes the sequence of already labeled phases. If the life cycle commences with an intensification phase, the program searches for a vorticity valley preceding the next mature stage. Should such a valley be present, it designates the period from the start of the intensification phase to 40% of the duration to this valley as incipient. Conversely, if the life cycle starts with a decay phase, the program looks for a subsequent vorticity peak before the next mature stage. Upon identifying such a peak, it marks the time from the start of the decay phase to 40% of the duration to this peak as incipient.

The specific thresholds for phase detection, including the 7.5% duration for intensification and decay intervals, the 3% minimum for the mature stage, and the 12.5% intervals defining the boundaries of the mature stage, along with 40% of the series length for the incipient stage, were established through rigorous testing. This testing involved an iterative trial-and-error calibration process where various percentage thresholds were applied to a representative sample of cyclone tracks. The objective was to determine the most accurate parameters for delineating the phases. The chosen percentages proved effective in capturing the true progression of cyclogenesis while filtering out inconsequential fluctuations in vorticity. This meticulous calibration ensures that the CycloPhaser program reliably identifies each phase, providing a consistent and objective methodology for analyzing the life cycle of extratropical cyclones. This process is illustrated in Figures 3.5 and 3.6, 3.7, 3.8. For most of these thresholds, and in most cases analyzed, even altering the parameters to 25% or 150% of their original values did not result in significant modifications to the identified life cycle, reinforcing the method's reliability.

### 3.3.2 Cyclophaser Settings

In this study, the default settings of the CycloPhaser were primarily utilized to identify the life cycle phases of cyclones. Since the TRACK algorithm already incorporates spatial

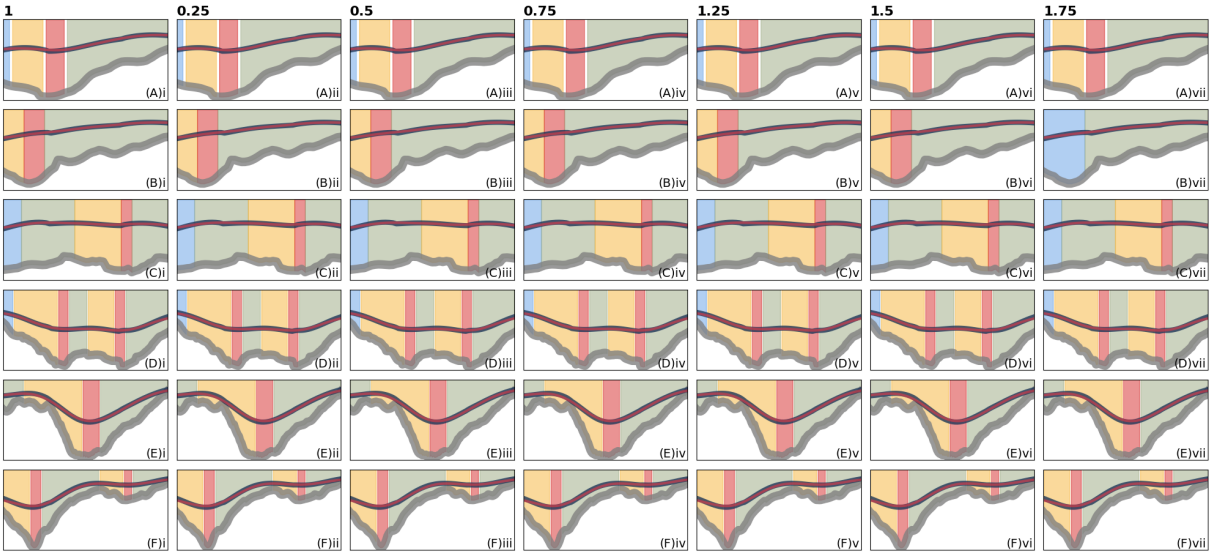


*Figure 3.5:* Impact of varying threshold values for the minimum length of the intensification phase across the six study cases. The original threshold value is maintained at 7.5% of the cyclone's total life cycle duration in panel (i). Panels (ii) to (vii) depict variations where the threshold is adjusted from 25% to 175% of the original value, illustrating the method's sensitivity to threshold changes. Adapted from de Souza et al. (2024).

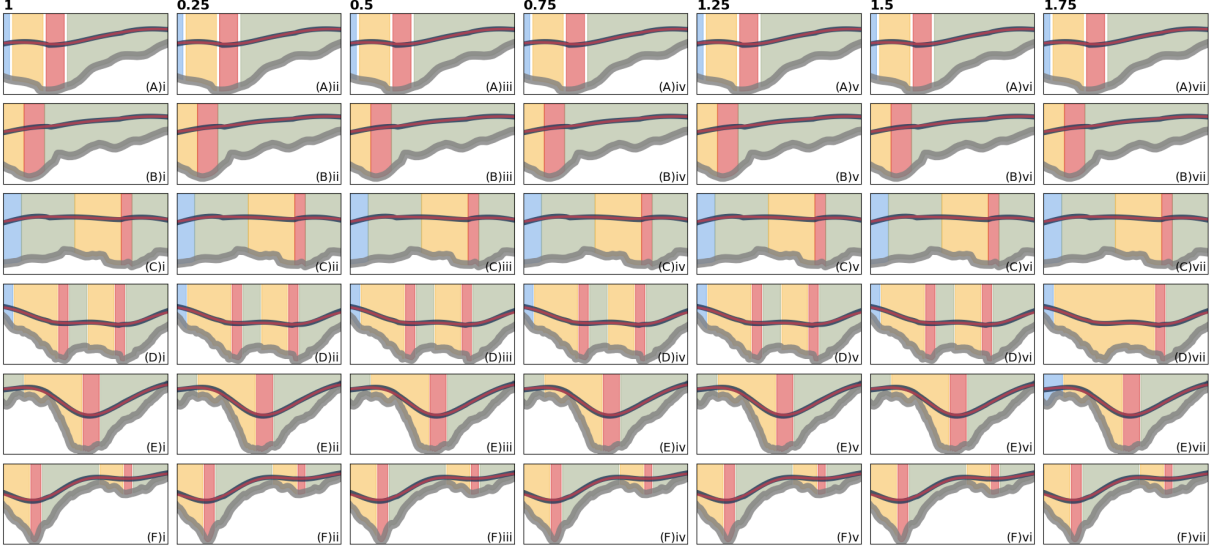


*Figure 3.6:* Same as Figure 3.5, but for the minimum length of the decay phase. Adapted from de Souza et al. (2024).

filtering on the  $\zeta_{850}$  vorticity fields, application of the Lanczos filter was deemed unnecessary (Hodges, 1994, 1995). Nevertheless, the Savitzky-Golay filter was applied twice to ensure that the  $\zeta_{850}$  series exhibited a smooth sinusoidal profile. The window length of this filter was adjusted specifically for each system's life cycle duration: for systems with a total life

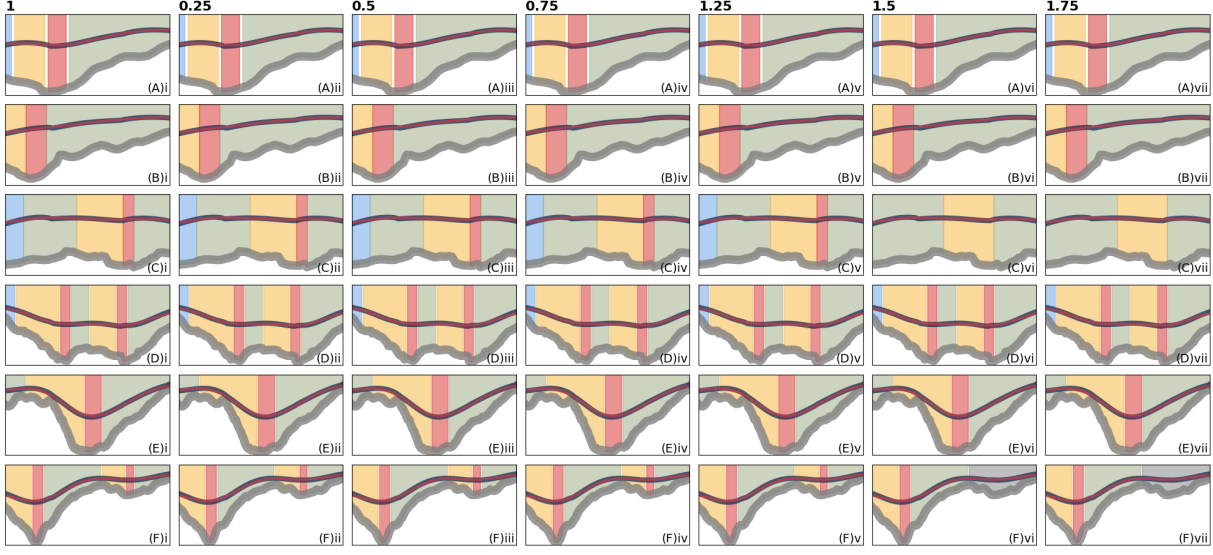


*Figure 3.7:* Variations in threshold values for the time intervals between the valley of vorticity and the preceding derivative valley, as well as from the vorticity valley to the subsequent derivative peak, used for determining the mature stage. The original threshold is set at 12.5%. Subsequent panels adjust this threshold from 25% to 175% of the baseline value, evaluating the robustness of phase detection across six study cases. Adapted from de Souza et al. (2024).

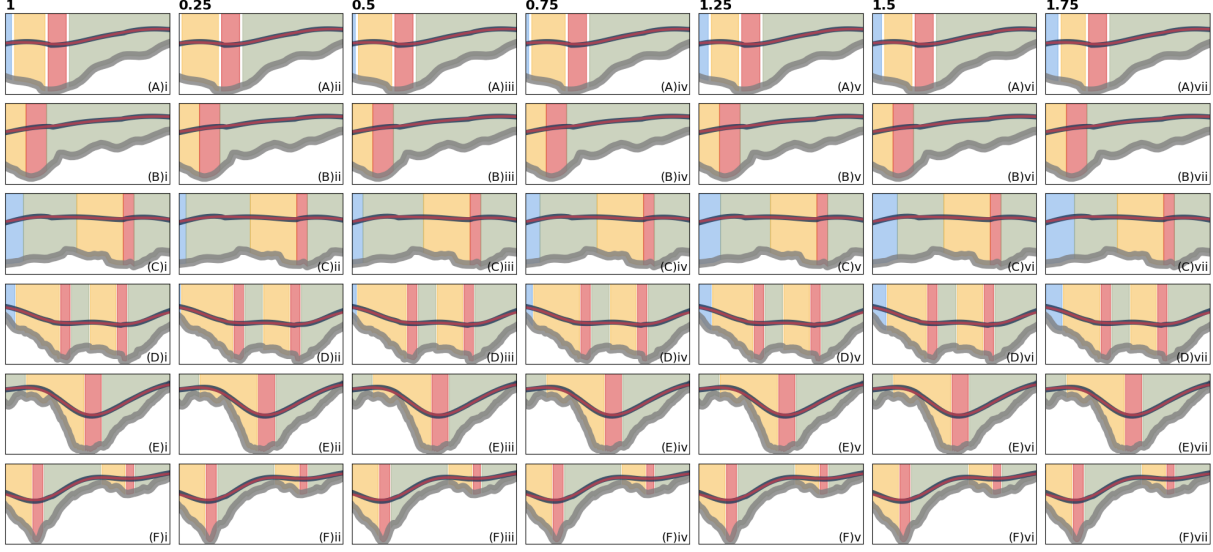


*Figure 3.8:* Impact of varying the minimum length threshold for the incipient phase of cyclone development. The incipient phase is identified from the beginning of the vorticity series to the next peak or valley in vorticity. The original threshold (shown in panel i) is set based on a percentage of the total vorticity series length. Panels ii to vii display the results when this threshold is modified from 25% to 175% of its original value across six study cases. Adapted from de Souza et al. (2024).

cycle spanning 8 days, the window length was set to an odd integer approximately 25% of the series length. For systems with shorter life cycles, the window length was adjusted to

an odd integer approximately 50% of the series length. In the second smoothing process, for life cycles exceeding 8 days, the window length was set to an odd integer close to 50% of the series length; however, for shorter cycles, it was kept consistent with the initial smoothing step.

### 3.4 Lorenz Energetics Computation

To compute the Lorenz Energy Cycle (LEC), an open-source Python application named "lorenz-cycle" was developed and is available on GitHub. The application is designed for collaboration and transparency, allowing peers to freely use, modify, and review the computation procedures. Full documentation and a user guide with illustrative examples can be found at <https://github.com/daniloceano/lorenz-cycle>. The program uses the formulation described at Section 2.4.2 and its complete description can be found at Appendix B.

In this study, the lorenz-cycle program was configured to compute the dissipation terms as residuals, following the methodologies of Brennan and Vincent (1980); Michaelides (1987); Veiga et al. (2008); Pezza et al. (2010); Dias Pinto and Rocha (2011), and to use the Semi-Lagrangian framework (Michaelides et al., 1999). A  $15^\circ \times 15^\circ$  computational domain centered at the cyclone's central position, obtained from the TRACK database (Section 3.2.2), was created for each time step. Given the impracticality of manually selecting an appropriate domain size for each cyclone in the dataset, a fixed size was employed.

The focus here is on the environmental energetics directly related to cyclone development, aiming to minimize interactions with other non-related circulations while capturing the main structure of the cyclone. Defining cyclone size is challenging due to both methodological and physical factors (Rudeva and Gulev, 2007, e.g.). The choice of a  $15^\circ \times 15^\circ$  computational domain is justified as it is large enough to capture the effective radius of most cyclonic systems (Rudeva and Gulev, 2007). The effective cyclone radius is defined as a measure of cyclone size, determined by establishing a coordinate system centered on the cyclone and measuring the distance at which the radial pressure gradient first falls to zero. This domain size also accounts for the cyclone's structure (Gramcianinov et al., 2019, e.g.).

Given the primary interest in the Southwestern Atlantic Ocean, only cyclones with

genesis near the South American coast (ARG, LA-PLATA, and SE-BR genesis regions) were included in the LEC computation. A significant challenge in determining energetic patterns across this dataset is the variable life durations of cyclones. Averaging values across the entire life cycle of systems would aggregate distinct dynamical processes (e.g., intensification and decay), while technical limitations exist in dissecting the life cycle into distinct periods. For example, Black and Pezza (2013) averaged cyclone energetics over periods of 48 hours before explosive cyclogenesis, during explosive deepening, and for 24 and 72 hours after it. However, cyclone life cycles can range from less than 24 hours to over 10 days (Trigo, 2006; Reboita et al., 2010; Gramcianinov et al., 2019), presenting significant physical limitations to such approaches. To address these limitations, the Cyclophaser program was used. After computing the LEC for each system, Cyclophaser was employed to define the life cycle phases for all analyzed systems, and then the mean LEC values for each phase were computed. The files containing the mean LEC results for each development phase are available on GitHub at [https://github.com/daniloceano/energetic\\_patterns\\_cyclones\\_south\\_atlantic](https://github.com/daniloceano/energetic_patterns_cyclones_south_atlantic).

## 3.5 Analysis methods

### 3.5.1 Probability Density Functions

In the present study, the probability density functions (PDFs) of distinct variables analyzed were represented using the Kernel Density Estimation (KDE) from the Python open-source library Seaborn (Waskom, 2021). KDE is a non-parametric method employed to estimate the PDF of a continuous random variable (Parzen, 1962; Rosenblatt, 1956). Unlike parametric approaches that assume a specific distribution form, KDE makes minimal assumptions about the underlying data distribution, providing flexibility and robustness in density estimation. The technique involves placing a kernel — a symmetric, smooth function, typically Gaussian — on each data point and summing the contributions from all kernels to produce a smooth, continuous estimate of the PDF. The bandwidth of the kernel, a crucial parameter, controls the level of smoothing: a smaller bandwidth captures more details of the data's structure, while a larger bandwidth yields a smoother, more generalized density function. KDE is particularly useful in visualizing the distribution of data and identifying features such as multimodality, skewness, and the presence of outliers,

making it a valuable tool in exploratory data analysis and various scientific applications.

### 3.5.2 Cyclone Track Densities

The spatial statistics from the TRACK program were produced using the spherical kernel method developed by Hodges (1996). This method provides a robust framework for estimating statistical properties from feature track data on a global scale. Unlike previous exponential kernels, these spherical kernels — such as power, quadratic, and biweight kernels — are computationally efficient and locally defined, meaning their influence is confined to a local region around each data point. The spherical kernel estimation is achieved by calculating probability density functions directly on the sphere, thus avoiding distortions caused by projection methods. This method includes an adaptive smoothing technique that adjusts the smoothing parameter based on local data density, ensuring optimal balance between detail retention and noise suppression. Cross-validation is employed to determine the optimal smoothing parameters, enhancing the reliability of the statistical estimates. This approach is particularly valuable for analyzing climatological data.

### 3.5.3 Statistical Analysis

To determine if there were significant differences in LEC terms across different phases of cyclone life cycles, we conducted a series of statistical tests. Initially, we assessed the assumptions required for Analysis of Variance (ANOVA), which included normality and homogeneity of variances. Normality was evaluated using the Shapiro-Wilk test, and homogeneity of variances was assessed using Levene's test. All statistical tests performed here were employed using the open source Python package SciPy (Virtanen et al., 2020).

We used the Shapiro-Wilk test to assess the normality of each term's distribution. The p-value from this test indicates whether the data significantly deviate from a normal distribution. A p-value greater than 0.05 implies that the data do not significantly deviate from normality, indicating that the assumption of normality is met.

Levene's test was used to evaluate the homogeneity of variances across different phases for each term. The test statistic indicates the extent to which variances are equal across groups. A high Levene's test statistic suggests greater differences in variances. The p-value associated with Levene's test statistic indicates the probability that the observed differences in variances could have occurred by chance. A p-value greater than 0.05 suggests that the

variances are not significantly different across the phases, implying that the assumption of homogeneity is met.

Given that many of our data sets did not meet these assumptions, we primarily employed the non-parametric Kruskal-Wallis (KW) test, which does not assume normality or equal variances, to compare the distributions of each term across different phases. The KW test is particularly useful when the data do not follow a normal distribution or exhibit heterogeneous variances.

The KW test statistic measures the extent to which the medians of the groups differ. A higher KW statistic value indicates a greater difference between group medians. The corresponding p-value for the KW test statistic indicates the probability that the observed differences in medians could have occurred by chance. A p-value less than 0.05 suggests significant differences among the phases for that term.

To compare the vorticity data among different clusters, we conducted a non-parametric statistical analysis due to the non-normal distribution of the data. Initially, we used the KW test to assess if there were statistically significant differences in the vorticity distributions across the clusters. Following the identification of significant differences with the KW test, we performed pairwise comparisons using the Mann-Whitney U test to determine which specific clusters differed significantly. The Mann-Whitney U test is also non-parametric and assesses whether the distributions of two independent groups are different. For each pairwise comparison, the test yields a U statistic and a p-value, where a p-value less than 0.05 indicates a significant difference between the clusters. All statistical analyses were executed using the SciPy package (Virtanen et al., 2020), and significant differences were visually annotated on box plots to enhance interpretability.

### 3.5.4 Empirical Orthogonal Functions

To understand the dominant LEC variability patterns within the TRACK dataset, an Empirical Orthogonal Function (EOF) analysis was employed using the Python open-source library pyEOF (Zheng, 2021). EOF analysis is a statistical technique used to identify the dominant modes of variability in spatial-temporal datasets (Fukuoka, 1951; Lorenz, 1956). It is one of the most used methods in atmospheric sciences, widely adopted for exploratory analysis (Hannachi et al., 2007). The method involves decomposing the dataset into orthogonal patterns by performing an eigenvalue decomposition on the covariance

matrix of the data. Each EOF represents a spatial pattern, while the associated time series, or Principal Component (PC), describes the temporal evolution of that pattern. This analysis reduces the dimensionality of the dataset, retaining the most significant variability, and is particularly useful for uncovering underlying structures and patterns in complex environmental data. In this context, instead of representing a spatial pattern, each EOF presents a mode of variability of the LEC, while the PCs represent the evolution across distinct cyclones.

### 3.5.5 K-means Algorithm

In the present study, the K-mean algorithm was used for determining the energetic patterns associated with the cyclones in the SESA region. The K-Means algorithm (MacQueen et al., 1967) is an iterative clustering method that partitions a dataset into  $K$  distinct clusters, where each data point belongs to the cluster with the nearest mean (centroid). The choice of  $K$ , the number of clusters, is crucial and is based on calculations to obtain ideal values that explain the maximum variability. The initial theory of K-Means was improved by Arthur and Vassilvitskii (2007) with the creation of K-Means++, which is used for initializations in the K-Means implementation of the Python package "Scikit-Learn" (Pedregosa et al., 2011), utilized in this study. Instead of choosing all centroids randomly, K-Means++ selects the first centroid randomly and then chooses subsequent centroids based on a probability distribution proportional to the squared distance of data points to the nearest already chosen centroid. This increases the likelihood that the initial centroids are spread out across the data, reducing the probability of convergence to a local optimum. In each iteration, the points are assigned to the cluster whose centroid is closest. After the assignment, the centroids are recalculated as the mean of the points assigned to each cluster. This calculation is performed until convergence, which the user can define as the maximum number of iterations. At the end of these updates, the algorithm returns the final clusters. The algorithm iterates between the steps of cluster assignment and centroid updating until a stopping criterion is met. Typically, the algorithm terminates when the centroids do not move significantly between consecutive iterations or when a maximum number of iterations is reached.

Before applying the K-Means algorithm, we used the Elbow Method, a technique designed to determine the optimal number of clusters. This method seeks a balance between

the explained variance and the number of clusters by identifying the inflection point in the decrease of explained variance. Specifically, by plotting the explained variance against the number of clusters, the inflection point on the graph indicates the optimal cluster count (Thorndike, 1953).

### 3.6 Investigation of Dynamical Mechanisms

#### 3.6.1 Criteria Used

In this study, we utilized the Rayleigh–Kuo criterion for barotropic instability to determine the presence of instability within cyclonic systems (Rayleigh, 1895; Kuo, 1949). According to this criterion, the necessary condition for barotropic instability is the existence of a point where the gradient of absolute vorticity ( $\eta$ ) with respect to the meridional direction is zero and changes sign within the flow. This can be mathematically expressed as:

$$\frac{\partial \eta}{\partial y} = 0 \quad (3.1)$$

Meanwhile, baroclinic instability was accessed using the Eady growth rate, a quantitative measure of the maximum rate of growth for baroclinic instabilities. This is a measure of the maximum rate at which baroclinic instability can amplify disturbances in a stratified fluid, formulated by Hoskins and Valdes (1990) as:

$$\sigma_E = 0.31 \frac{f}{N} \left| \frac{\partial u}{\partial z} \right| \quad (3.2)$$

where  $f$  is the Coriolis parameter,  $\frac{\partial u}{\partial z}$  represents the vertical wind shear and  $N$  is the Brunt-Väisälä frequency, a measure of the stability of the stratification in a fluid such as the atmosphere or ocean. It is given by the formula:

$$N = \sqrt{\frac{g}{\theta} \frac{d\theta}{dz}} \quad (3.3)$$

where  $g$  is the acceleration due to gravity,  $\theta$  is the potential temperature and  $\frac{d\theta}{dz}$  is the vertical gradient of potential temperature.

A larger value of  $N$  indicates greater stability, meaning the atmosphere is more resistant to vertical displacements. The Eady's growth rate highlights the exponential growth of

certain atmospheric disturbances under favorable conditions of wind shear and stability.

### 3.6.2 Composites

For applying the criteria described in Section 3.6.1, a composite procedure was implemented. Firstly, it was necessary to determine the vertical levels at which baroclinic and barotropic instabilities are indicated to be occurring, using the vertical profiles of  $C_A$  and  $C_E$ , respectively. Then, mean values for atmospheric fields for the ERA5 reanalysis were computed for the intensification phase at these vertical levels. The atmospheric fields used were zonal, meridional, and vertical wind components, temperature, and geopotential.

For the composites using the Semi-Lagrangian framework, firstly, the mean atmospheric fields for the intensification phase for each system were averaged. These mean atmospheric fields were then re-gridded to a non-dimensional spatial domain. Given that the ERA5 reanalysis has a  $0.25^\circ$  horizontal spatial resolution, each mean field contained 60 grid points ( $15^\circ \times 15^\circ$ ). As the Semi-Lagrangian domains are centered on the cyclone's center, the composite domain ranged from -30 to 30 in both the x and y axes.

Furthermore, the differences between the Semi-Lagrangian and Fixed frameworks were also assessed. While the methodology for the Semi-Lagrangian framework is explained in Section 3.4, a distinct approach had to be taken for the Fixed framework. For each system analyzed, a computational domain was automatically detected by using the minimum and maximum latitude and longitude values, adding a  $15^\circ \times 15^\circ$  buffer. By doing so, it is ensured that the system's complete development cycle is represented in the LEC computation.

For the composite procedure, firstly, the meteorological fields were averaged for each computational domain during the intensification phase. Then, the minimum and maximum latitude and longitude values across all fixed computational domains were detected. After this, a synthetic domain was built using these coordinates, and the mean meteorological fields were interpolated to this domain. Finally, the results interpolated to the common grid for each case were averaged into a single composite.



## Chapter 4

---

# Life Cycle of Cyclones in the Southwestern Atlantic

This chapter delves into the varied life cycle configurations, statistical characteristics, and geographical distribution of cyclones within the Southwestern Atlantic, with a particular focus on the South American Southeastern region (SESA). Employing the Cyclophaser program, this analysis facilitates a detailed examination of cyclone behaviors and patterns. While some of the results discussed herein are also presented in (de Souza et al., 2024), this chapter narrows its focus to the SESA region, unlike the cited study which includes all cyclogenesis regions across the South Atlantic, extending to the Antarctic Peninsula and the Weddell Sea. Section 4.1 examines statistical metrics for the selected cyclonic systems' whole life cycle, as well as for individual development phases, while Section 4.2 explores the spatial distribution of the distinct phases across the SESA and adjacent regions. These two approaches combined not only provide a novel perspective on the South Atlantic storm tracks and on the development of cyclonic systems but also open avenues for future research, as will be discussed.

### 4.1 *Climatology and Statistics*

This section delves into the climatology and statistical characteristics of cyclones in the Southwestern Atlantic, focusing on their frequency, seasonality, and developmental metrics such as average duration and intensity. Previous analyses have explored these aspects for systems originating in the SESA region; here, they serve both for comparative purposes and for validating the database generated during this study. A novel aspect of this analysis is the dissection of these metrics not just over the cyclones' complete lifecycles but also across distinct developmental phases. Section 4.1.1 presents the overall characteristics and

life cycle configurations of the detected cyclonic systems, Section 4.1.2 explores lifecycle statistics for different genesis regions and seasons, and Section 4.1.3 provides detailed statistical breakdowns by individual development phases.

#### 4.1.1 Climatological Aspects and Life Cycle Configurations

Using the tracking methodology described in Section 3.2.2, the TRACK algorithm identified 33,376 cyclone systems in the South Atlantic region from 1979 to 2020. The focus here was on systems originating from the SESA region, specifically from SE-BR, LA-PLATA, and ARG genesis regions. After filtering to include only these tracks, the number of systems was narrowed down to 7,931 (Figure 4.1). Among these, 56% originated in the ARG region, 23.6% in LA-PLATA, and 20.4% in SE-BR. This distribution and general seasonality aligns with previous studies by Gramcianinov et al. (2019) and Crespo et al. (2021). However, the SE-BR region exhibited a higher relative frequency in this analysis, potentially attributable to the finer resolution of the ERA5 dataset used here compared to previous studies (Gramcianinov et al., 2020). However, comparing the seasonal distribution with earlier studies introduces complexities due to variations in the definitions and boundaries of genesis regions (Reboita et al., 2010; Crespo et al., 2021, e.g.,).

During the period from 1979 to 2020, cyclonic systems originating from the ARG, LA-PLATA, and SE-BR regions demonstrated 41 distinct life cycle configurations (Figure 4.2). Most configurations did not account for more than 1% of the total system count, typically lacking a mature stage. This phenomenon is likely due to these systems having maturation stages shorter than the CycloPhaser's threshold for detecting this phase. Adjusting the threshold to recognize shorter mature stages would risk identifying spurious cycles.

To focus on significant life cycle patterns, it was filtered the configurations to include only those comprising at least 1% of all types (Figure 4.3). This criterion reduced the sample size to 7,531 systems, accounting for approximately 95% of the original database. It was also merged life cycle counts that differed solely by the inclusion of a residual stage, as these are not indicative of the system's actual development (as discussed in Section 3.3.1). Further, to avoid bias in phase statistics, it was excluded life cycles lacking a mature phase. For instance, systems exhibiting only intensification and/or decay phases might have longer durations for these phases compared to others, potentially skewing statistics. Such configurations might represent undeveloped systems exiting the tracking

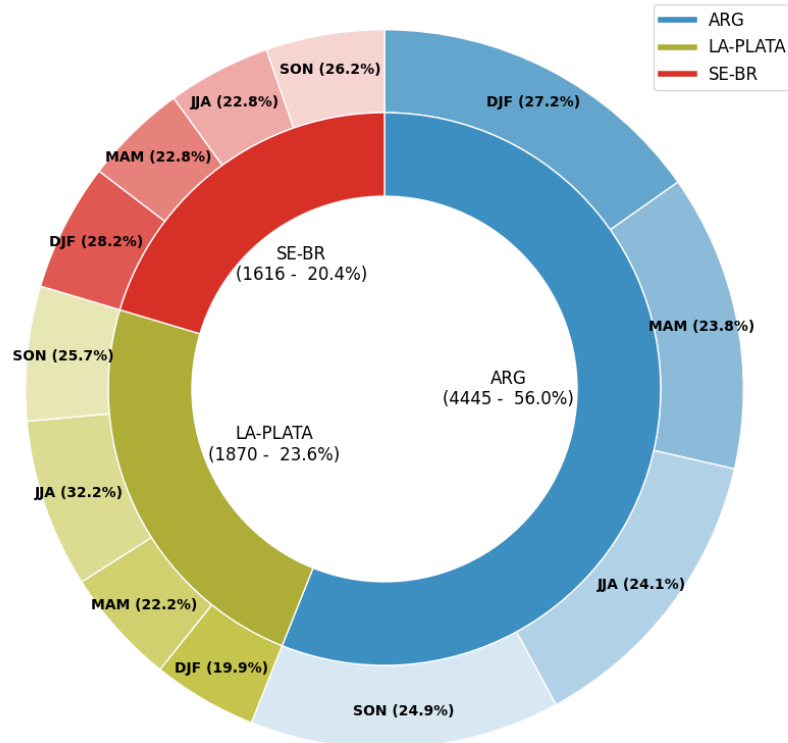


*Figure 4.1:* Number of systems and their relative frequencies by genesis region in the SESA region for the period 1979-2020. The inner pie chart displays the total frequency of systems by region, while the outer ring shows the seasonal distribution of cyclogenesis within each region.

domain before maturation. With these filters applied, the number of systems analyzed was reduced to 7,151, representing about 90% of the initial count of systems with genesis in the SESA region (Figure 4.3b).

Figure 4.4 depicts representative cases for each life cycle configuration retained for analysis (as shown in Figure 4.3b). The most common configuration in the SESA region typically follows the expected development pattern of extratropical cyclones: incipient, intensification, mature, and decay stages (Figure 4.4a), accounting for 68% of all evaluated systems. The second most common type mirrors this sequence but omits the incipient stage, indicating a rapid intensification process (Figure 4.4b). The third and fourth most frequent types depict a repeated complete cycle, including a secondary intensification, mature, and decay phases, with the third type including an incipient stage (Figure 4.4c) and the fourth lacking one (Figure 4.4d). The fifth and sixth configurations exhibit an early decay stage, differentiated by the presence (Figure 4.4e) or absence (Figure 4.4f) of an incipient phase.

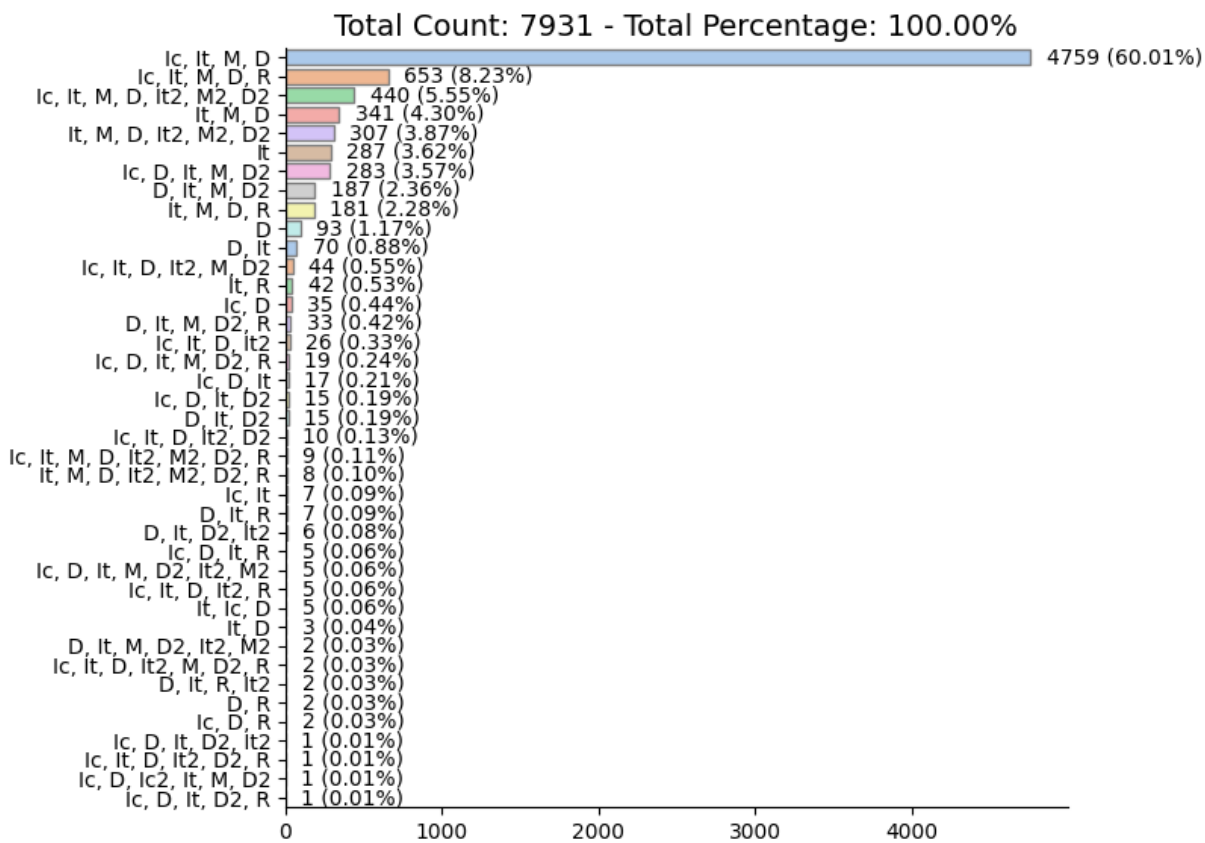


Figure 4.2: Distribution of all identified cyclone lifecycle configurations in the SESA region, spanning from 1979 to 2020. The configurations are sorted by their total count (frequency), with each bar representing the total number of cyclones exhibiting a specific lifecycle pattern, containing distinct stages: incipient (Ic), intensification (It), mature (M), decay (D), and residual (R), showing their sequence within the lifecycle.

The analysis reveals minimal to negligible seasonal variability in the frequency of each life cycle configuration across different genesis regions (Figure 4.5). The configurations "Ic, It, M, D" and "Ic, It, M, D, It2, M2, D2" are consistently more frequent, jointly accounting for 60% to 68% of all cases across all regions. However, exceptions include the "It, M, D" configuration emerging as the second most frequent in ARG during JJA, and in SE-BR during MAM and JJA. Additionally, the "Ic, D, M, D2" configuration appears significantly more often in LA-PLATA during JJA and in SE-BR during SON.

#### 4.1.2 Mean Cyclone Statistics

This section explores the statistical analysis of cyclones in the SESA region, comparing the constrained data utilized in this study with extant literature. Results are presented both for an aggregate view across all genesis regions and individually by region. To capture

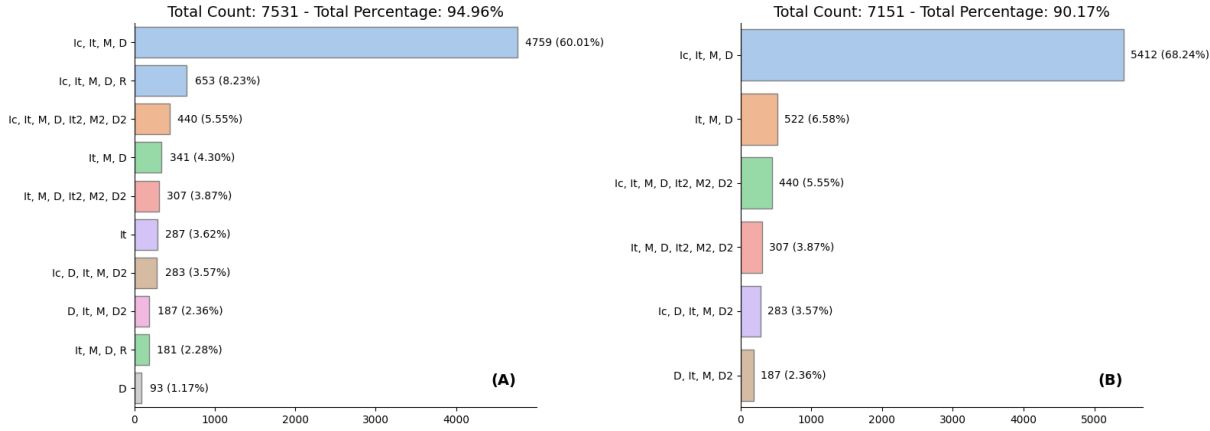


Figure 4.3: (a) Lifecycle configurations of cyclones that represent at least 1% of the total identified patterns. (b) Adjusted lifecycle configurations after merging periods classified as residual and removing stages not contributing to a standard development pattern, focusing analysis on the core developmental stages of cyclones.

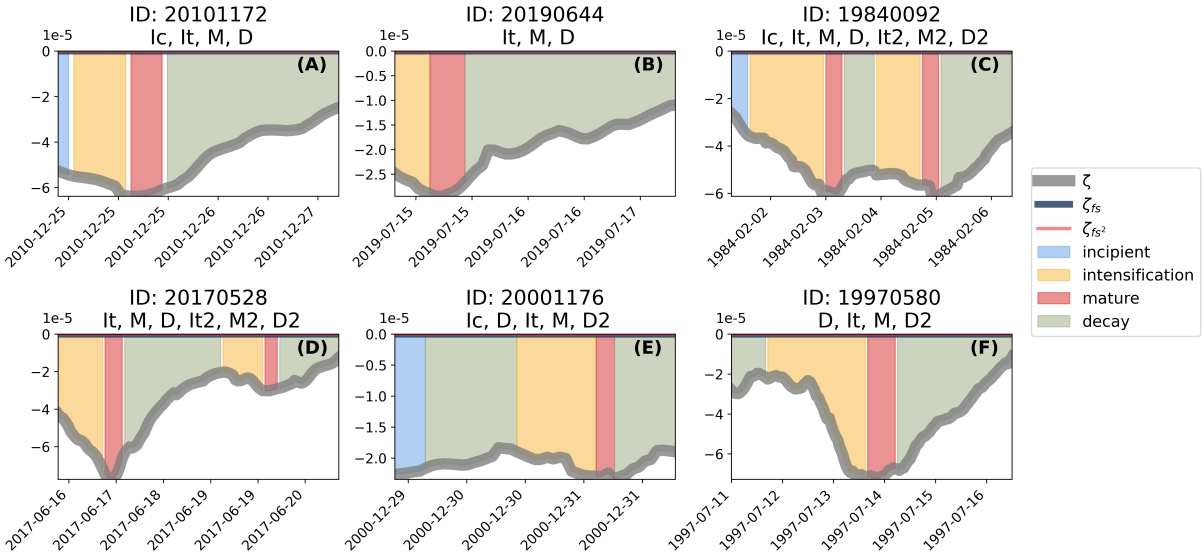


Figure 4.4: Representative examples of cyclone life cycles for configurations shown in Figure 4.3b. Panels A to F illustrate the central relative vorticity  $\zeta_{850}$  and its first ( $\zeta_{fs}$ ) and second ( $\zeta_{fs^2}$ ) smoothed derivatives. Background colors indicate different life cycle phases: : incipient (Ic), intensification (It), mature (M) and decay (D). Lines represent the original vorticity series ( $\zeta$ ), the first ( $\zeta_{fs}$ ), and the second ( $\zeta_{fs^2}$ ) smoothed relative vorticity series.

the seasonal variability of cyclone behavior, analysis is focused on the winter (JJA) and summer (DJF) months. This approach is chosen because the transitional seasons (MAM and SON) generally display characteristics that are intermediate to those observed in JJA and DJF, aligning with findings from previous climatologies of the SESA region (Gan and Rao, 1991; Reboita et al., 2010; Crespo et al., 2021, e.g.).

On average, cyclones exhibit longer lifespans during DJF, with a duration of  $97.6 \pm 66.2$

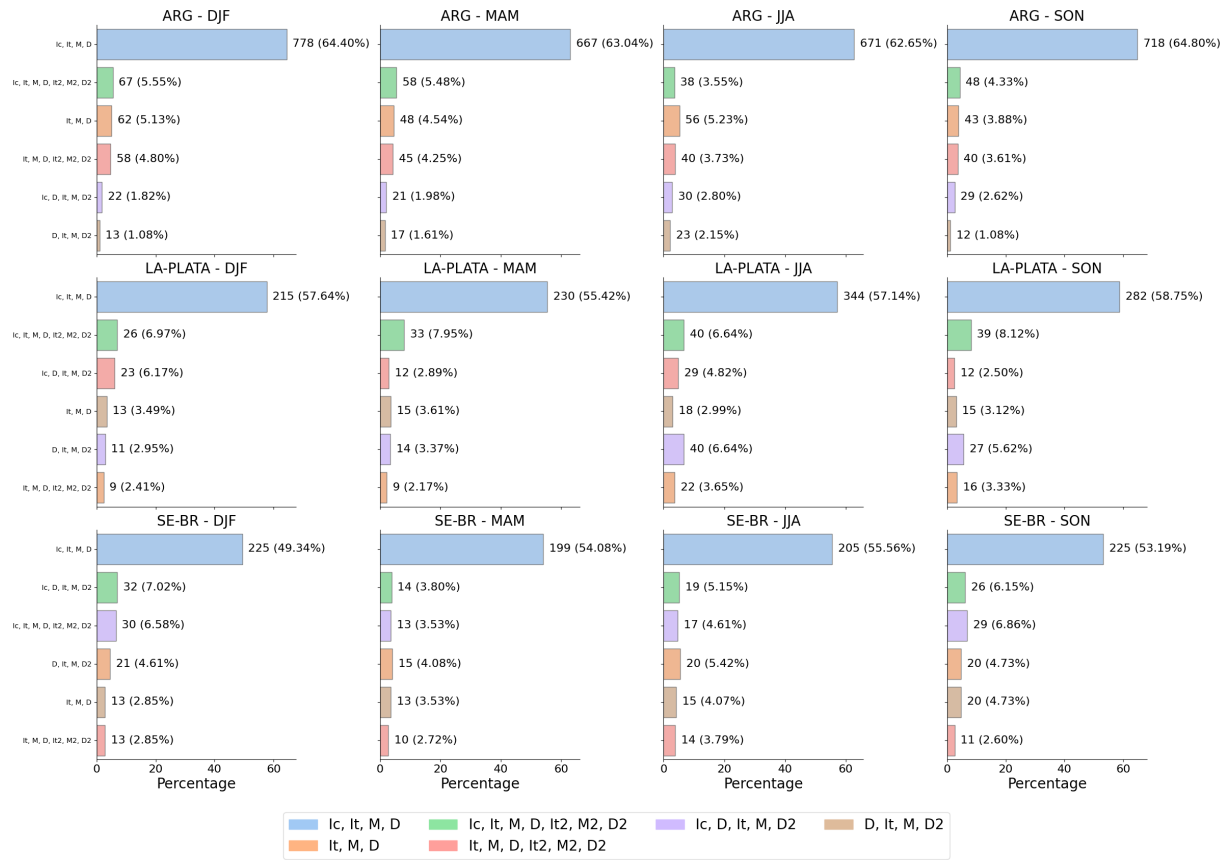
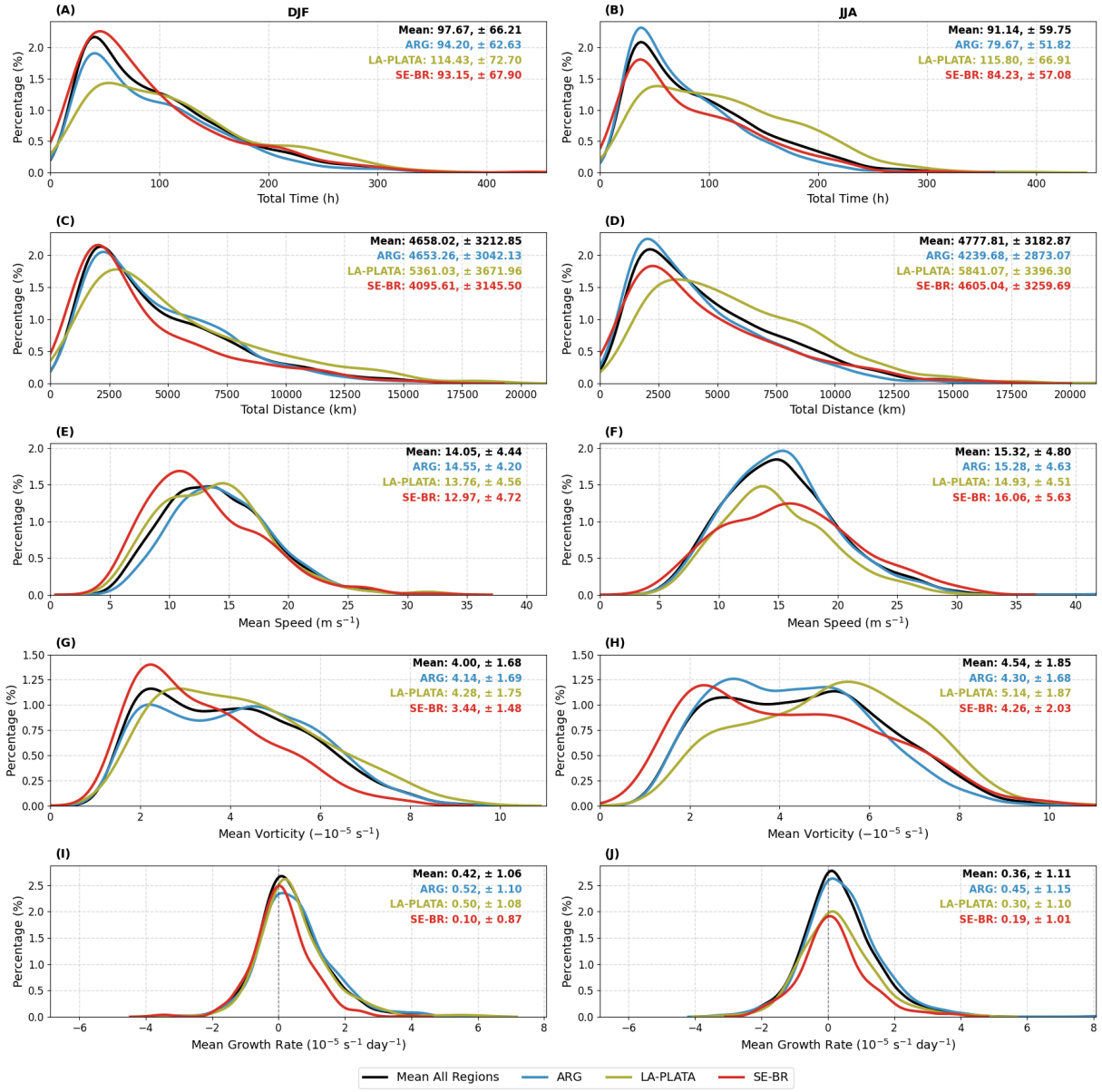


Figure 4.5: Similar to Figure 4.3, but separated by genesis region (ARG, LA-PLATA and SE-BR) and season.

hours (Figure 4.6a) compared to  $91.1 \pm 59.7$  hours during JJA (Figure 4.6b). Conversely, the average total distance traveled by cyclones is slightly greater during JJA, amounting to  $4777 \pm 3182$  km (Figure 4.6d), versus  $4658 \pm 3212$  km in DJF (Figure 4.6c). This is reflected in the mean propagation speed, which is higher in JJA at  $15.3 \pm 4.8$  m/s (Figure 4.6f) compared to DJF at  $14.0 \pm 4.4$  m/s (Figure 4.6e).

These results largely corroborate those by Gramcianinov et al. (2019, 2020); Hoskins and Hodges (2005) and exceed the mean duration, traveled distance, and propagation speed reported by Simmonds and Keay (2000), Mendes et al. (2010), and Reboita et al. (2010). The disparities likely stem from differing tracking methodologies, data sets, and the exclusion of systems without a mature phase in our analysis. Particularly, the exclusion of continental systems may inflate displacement statistics during austral summer when quasi-stationary lows are prevalent over the continent (Mendes et al., 2010). Furthermore, Reboita et al. (2010) focused on oceanic systems, which might have overlooked early deve-



*Figure 4.6:* Probability density functions (PDF) comparing cyclone lifecycle metrics across different genesis regions (ARG, LA-PLATA, SE-BR) for DJF and JJA. Each panel displays the density distributions for a specific metric: total time (A and B), total distance (C and D), mean speed (E and F), mean vorticity (G and H), and mean growth rate (I and J). The lines in each graph represent the mean values for all regions combined (black), ARG (blue), LA-PLATA (green), and SE-BR (red), while the annotations represent the mean and standard deviation values.

lopment stages, and their use of relative vorticity at 10m, impacted by surface drag, could account for variations in propagation speed.

The analysis reveals notable inter-regional variability in cyclone behavior, with trends predominantly mirroring those observed in the ARG region, which accounts for the highest frequency of cyclone occurrences within the SESA region (Figure 4.1). When examining to-

tal cyclone duration, distinct seasonal patterns emerge: both the ARG and SE-BR regions exhibit significantly shorter lifespans during JJA compared to DJF, with the probability density functions (PDFs) peaking at approximately 50 hours. In contrast, the LA-PLATA region shows slightly longer durations during JJA, with a mean difference of about 1.5 hours. Additionally, the distribution of cyclone durations in the LA-PLATA region is more right-skewed than in ARG and SE-BR, indicating greater variability in the lifespan of cyclones originating from LA-PLATA. Across all regions, the standard deviation decreases from DJF to JJA, suggesting a higher occurrence of longer-lasting cyclones during the summer months.

In terms of displacement, the ARG region displays shorter average distances during DJF compared to JJA, whereas LA-PLATA and SE-BR exhibit increases, particularly notable in SE-BR. Similar to the trends in duration, the displacement patterns in ARG and SE-BR exhibit distinct peaks at approximately 2500 km, while LA-PLATA shows a more right-skewed distribution, especially during JJA, indicating greater variability in cyclone travel distances. These regional differences in displacement are also mirrored in the average propagation speeds of the cyclones: during DJF, cyclones in ARG generally move faster than those in LA-PLATA and SE-BR. This changes in JJA, with SE-BR exhibiting the highest increases in speed, making it the region with the most mobile cyclones during this season, followed by ARG and then LA-PLATA. This variation is reflected in the PDFs for each region: during DJF, SE-BR's propagation speed peaks at approximately  $10 \text{ m s}^{-1}$  and ARG at  $13 \text{ m s}^{-1}$ , while LA-PLATA displays a bimodal distribution with peaks at approximately  $10 \text{ m s}^{-1}$  and  $15 \text{ m s}^{-1}$ . During JJA, the peak for ARG shifts to approximately  $16 \text{ m s}^{-1}$ , and LA-PLATA's distribution changes to peak at around  $14 \text{ m s}^{-1}$ , while SE-BR assumes a bimodal shape, peaking at roughly  $10 \text{ m s}^{-1}$  and  $16 \text{ m s}^{-1}$ .

The PDFs for the mean vorticity values of the examined systems display a bimodal, right-skewed distribution with peaks near  $2 \times 10^{-5} \text{ s}^{-1}$  and  $4 \times 10^{-5} \text{ s}^{-1}$ , with a higher occurrence percentage near the first peak and an average value of  $4 \pm 1.68 \times 10^{-5} \text{ s}^{-1}$  during DJF (Figure 4.6g). In JJA, the peaks are positioned near  $2 \times 10^{-5} \text{ s}^{-1}$  and  $5 \times 10^{-5} \text{ s}^{-1}$ , but with a higher occurrence percentage at the second peak, reflecting an overall increase in mean vorticity, especially in the LA-PLATA region (Figure 4.6h). The ARG region presents a PDF mirroring the mean cyclone behavior, and SE-BR peaks near  $2 \times 10^{-5} \text{ s}^{-1}$  in both seasons, being more right-skewed in JJA, which reflects the occurrence of weaker

systems in this region. Meanwhile, LA-PLATA shifts from being right-skewed in DJF to left-skewed in JJA, reflecting a significant increase in the intensity of systems in this region. These results highlight the previous findings that LA-PLATA presents the most intense systems in the SESA regions, while SE-BR, the weakest (Simmonds and Keay, 2000; Reboita et al., 2010; Gramcianinov et al., 2019). Although the regional and seasonal variability largely corroborates findings from Gramcianinov et al. (2019), the intensity of cyclones reported here is somewhat smaller, possibly due to the ERA5 dataset be able to detect less intense systems (Gramcianinov et al., 2020).

The mean growth rate distribution, is symmetric around zero with a low standard deviation, indicating a dynamic equilibrium in system intensity throughout the life cycle, marked by neither consistent intensification nor weakening, which will be later discussed for each individual phase. It is important to note that these values were computed from normalized relative vorticity data, where positive values suggest system intensification ( $\zeta_{850}$  increasing in magnitude), while negative values indicate a decay ( $\zeta_{850}$  decreasing in magnitude). Overall, although the differences are minimal, the results suggest slightly more intense intensification during DJF (Figure 4.6i) compared to JJA (Figure 4.6j), with the latter exhibiting higher mean values.

#### 4.1.3 Life Cycle Phase Statistics

This section examines the statistical characteristics of cyclones, exploring various metrics describing cyclonic behavior throughout distinct lifecycle phases. This unique approach is enabled by the Cyclophaser program, offering a more granular analysis than previously available in the literature. As shown in Section 4.1.2, the region mean results predominantly reflect the ARG region's behavior and hence, region-specific results are detailed here.

Figure 4.7 displays the PDFs for the mean total time spent in each development phase. These PDFs are right-skewed, indicating high variability across different phases but smaller seasonal and regional differences. Typically, the incipient, mature, and second mature phases show the shortest average durations, often peaking between 3 and 5 hours. The intensification, second intensification, and decay phases often exhibit longer tails, suggesting a wide variability in their durations. In the ARG region, all phases show a slight reduction in mean duration from DJF (Figure 4.7a) to JJA (Figure 4.7b), with decay and second

decay stages exhibiting the most significant reductions, indicating that shorter average total durations in JJA are primarily due to these phases (Figure 4.6). For LA-PLATA and SE-BR, notable changes include particularly variations in the standard deviations of the second intensification and decay phases, and in the decay phase for SE-BR, suggesting that seasonal differences in total mean durations for these regions are largely attributable to fluctuations in extreme values.

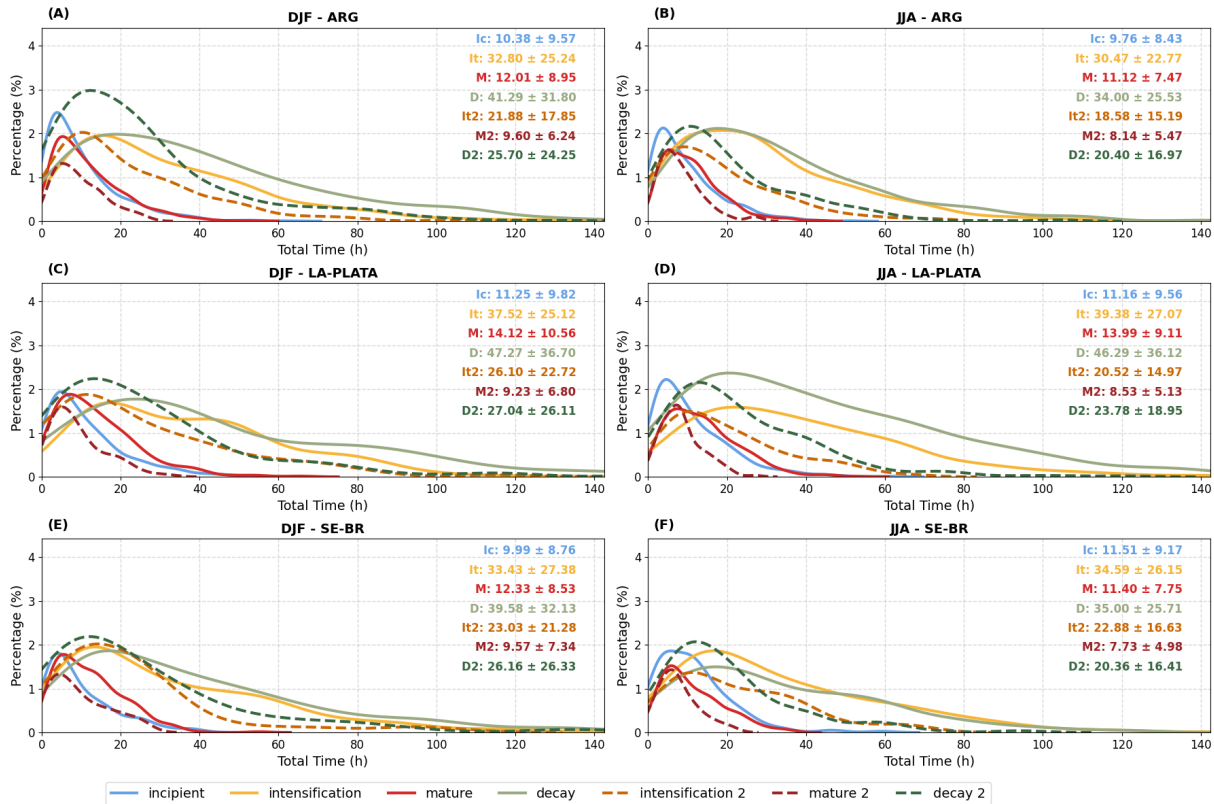


Figure 4.7: Probability density functions (PDF) comparing the mean total duration of each cyclone phase, across all regions combined and for each genesis region (ARG, LA-PLATA, SE-BR) for DJF and JJA. Annotations display mean and standard deviation values for each phase.

The total traveled distance for each phase is depicted in Figure 4.8, which mirrors the overall behavior observed for total time (Figure 4.7). All PDFs are right-skewed, and across all regions and seasons, the incipient, mature, and second mature phases peak approximately between 300 and 400 km, while the other phases present long tail distributions. In the ARG region, there is an overall reduction in traveled distance across all phases from DJF to JJA. Conversely, for LA-PLATA and SE-BR, there is a general increase, reflecting the seasonal behavior for the entire lifecycle's total distance (Figure 4.6).

The results for mean speed (Figure 4.9) aggregate the results for total time and traveled

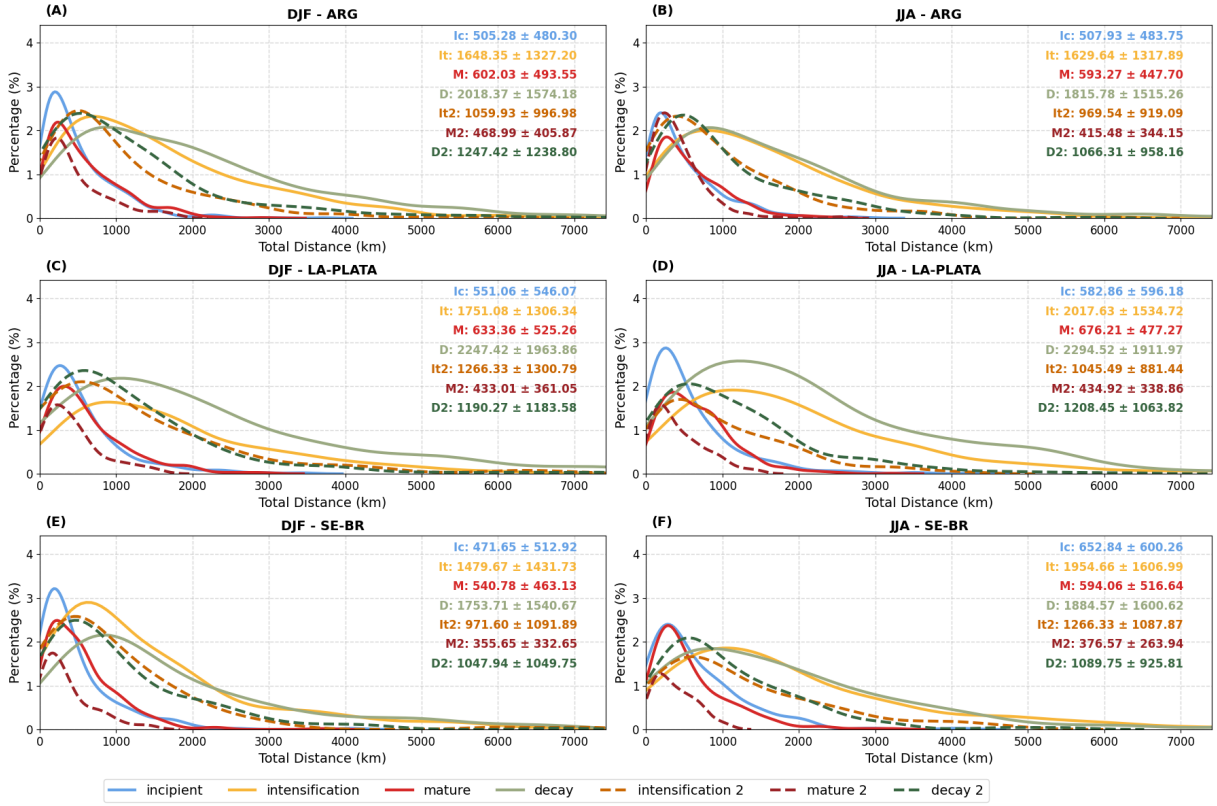


Figure 4.8: Similar to Figure 4.7, but for total traveled distance.

distance. There is less variability across distinct phases for this metric when compared to the total time and distance, with the PDFs for distinct phases, regions, and seasons often presenting a Gaussian-like shape centered between  $10$  and  $15 \text{ ms}^{-1}$ . These values align with those found in previous studies (Gramcianinov et al., 2019, 2020; Hoskins and Hodges, 2005), although slightly higher, likely due to the constraints adopted in this analysis. Additionally, this study's ability to account for distinct developmental phases provides a foundation for further research into the dynamical mechanisms that could be linked to the systems' varying speeds across different periods. In the ARG region, the largest increases in mean propagation speed from DJF to JJA are found in the secondary development phases, accompanied by increases in standard deviation values, with slightly right-skewed PDFs for these phases. LA-PLATA displays a similar behavior, especially for intensification and mature decay, which shifts their peaks from near  $10\text{ms}^{-1}$  in DJF to near  $15\text{ms}^{-1}$  in JJA. For SE-BR, the major change is in the shape of the PDFs, which change from a Gaussian-like shape in DJF to a more right-skewed shape in JJA. Overall, although the differences are only marginal, the cyclones tend to be faster in the incipient stage and in

the intensification stage, being slower at the mature phase, speeding up again in the decay phase. Also, the systems tend to be slower in the second development cycle than in the first one, especially slower at the second mature phase. Therefore, cyclones in the SESA region are slower at their mature phases. The slower propagation speed of cyclones is related to extreme wave occurrence (Gramcianinov et al., 2023) and therefore the positioning of these systems during that phase are of importance for coastal management in the South American Southeastern coast.

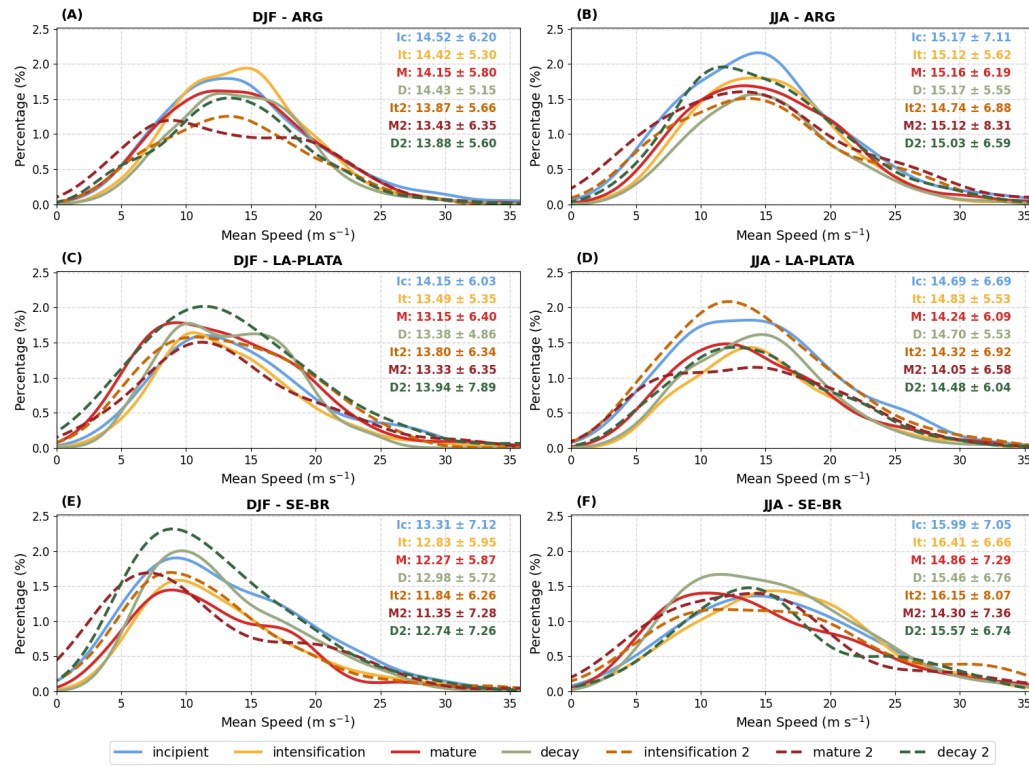


Figure 4.9: Similar to Figure 4.7, but for mean propagation speed.

The PDFs for mean central  $\zeta_{850}$  across various cyclone phases exhibit bimodal and right-skewed distributions, with a general increase in mean vorticity from DJF to JJA (Figure 4.10). This trend reflects the heightened intensity of cyclonic systems during JJA compared to DJF (Figure 4.6). It is important to note that these vorticity values are derived from the raw output of the TRACK program, and as such, they may include some level of noise that can influence the statistical results. Notably, the mature phase is characteristically the most intense during the first developmental cycle across all regions, demonstrating a wide range of vorticity values and highlighting the variability in peak intensities of mature

cyclones. Meanwhile, the second mature phase typically records the highest vorticities among all phases, suggesting a tendency for systems to intensify further during subsequent cycles. In contrast, the incipient phase generally exhibits the lowest mean vorticities, reflecting the nascent stages of cyclone development. However, in the SE-BR region, this phase shows unusually high mean vorticities during JJA, occasionally surpassing other phases, indicating exceptionally conducive conditions for early cyclone formation. The intensification and decay phases generally present similar mean vorticities, aligning with their respective roles in modifying system intensity: intensification increases vorticity from a baseline state, while decay reduces it back towards this baseline. Secondary intensification and decay phases often exhibit higher mean vorticities than their initial counterparts, reflecting the dynamics of re-intensification in the lifecycle, particularly marked by the higher mean values observed during the second mature phase.

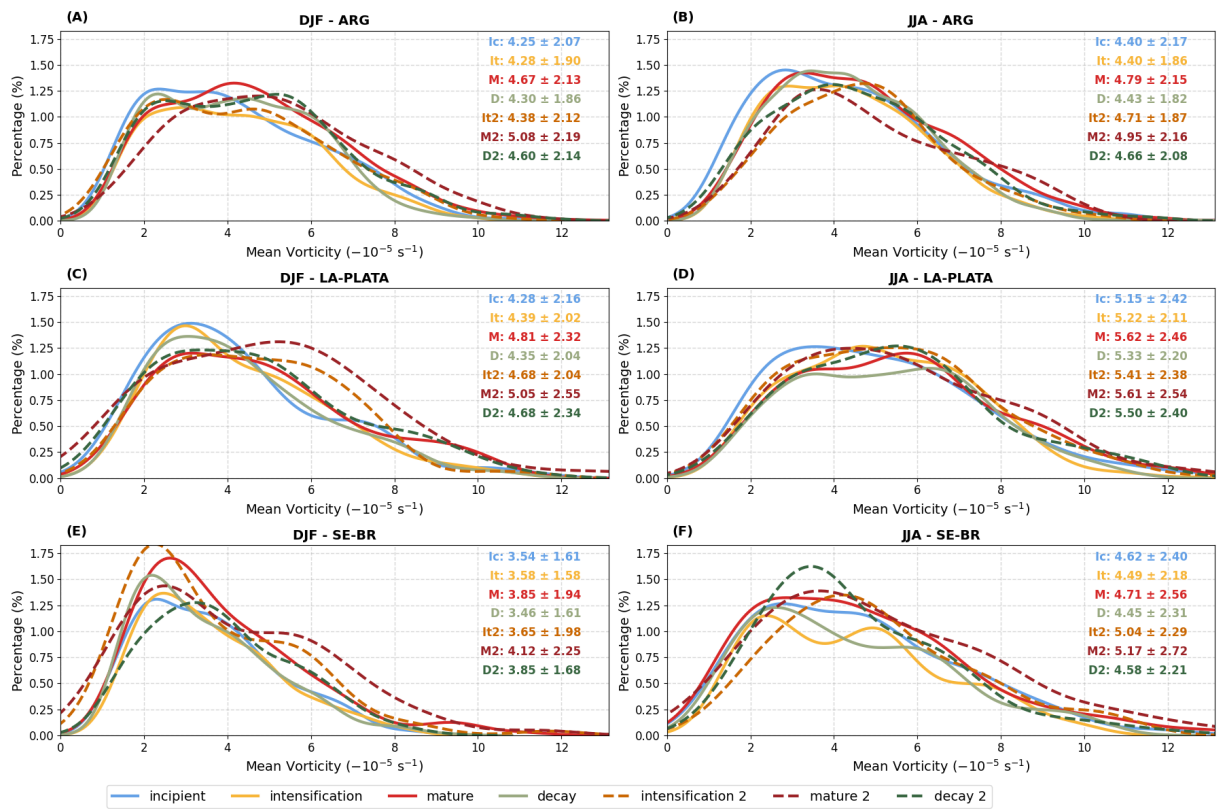


Figure 4.10: Similar to Figure 4.7, but for mean central relative vorticity at cyclone center ( $\zeta_{850}$ ).

The results found here for the incipient stage exhibit higher vorticities compared to the initial vorticities reported by Reboita et al. (2010), Gramcianinov et al. (2019), and Gramcianinov et al. (2020). This discrepancy may be attributed to our exclusion criteria,

which likely excluded weaker and underdeveloped systems, coupled with the observed tendency for vorticity to increase (becoming more negative) when an incipient stage is followed by an intensification phase (e.g., Figure 4.4a and c), potentially resulting in a bias toward higher values for this phase. Additionally, Sinclair (1995), in their analysis focusing on the first time step, the time step of minimum vorticity, and the last time step, reported higher vorticity values compared to our findings for the incipient, mature, and decay stages. However, these authors omitted the influence of topography by using geostrophic relative vorticity, which justifies the difference in vorticity distribution observed in their study.

There are complexities in interpreting the results for the mean growth rate due to the use of raw vorticity data from the TRACK algorithm, which introduces additional noise to the findings (Figure 4.11). This metric exhibits considerable variability across different regions, with most PDFs centered around zero yet displaying wide variations, where standard deviations significantly exceed the mean values. The incipient stage often shows the highest or second-highest growth rates, typically skewing more to the right. These observations are consistent with previously reported mean growth rates for cyclogenesis regions by Hoskins and Hodges (2005) and Gramcianinov et al. (2019). A similar pattern is observed in the intensification phase, which alternates with the incipient stage in displaying the greatest growth rates. Despite positive average values, the decay and second decay phases predominantly peak at negative values, reflecting their role in diminishing system vorticity.

While most regions and seasons show the mature phase peaking at zero — expected due to its position near local vorticity minima — the positive mean suggests that the increase in vorticity preceding the peak is more pronounced than the subsequent decline. This assertion is supported by the lower mean values observed during the decay phase compared to the intensification phase. Moreover, the detection of the mature phase often occurs between the peaks and valleys of vorticity derivatives (Section 3.3.1), potentially shifting its center of mass toward either the intensification or decay stages, as depicted in Figure 4.12. During JJA in LA-PLATA, the mature phase peaks positively, whereas in SE-BR during DJF, it peaks negatively. Determining whether these shifts are due to greater increases in intensity, displacement of the phase's center of mass, or residual data noise is beyond this study's scope.

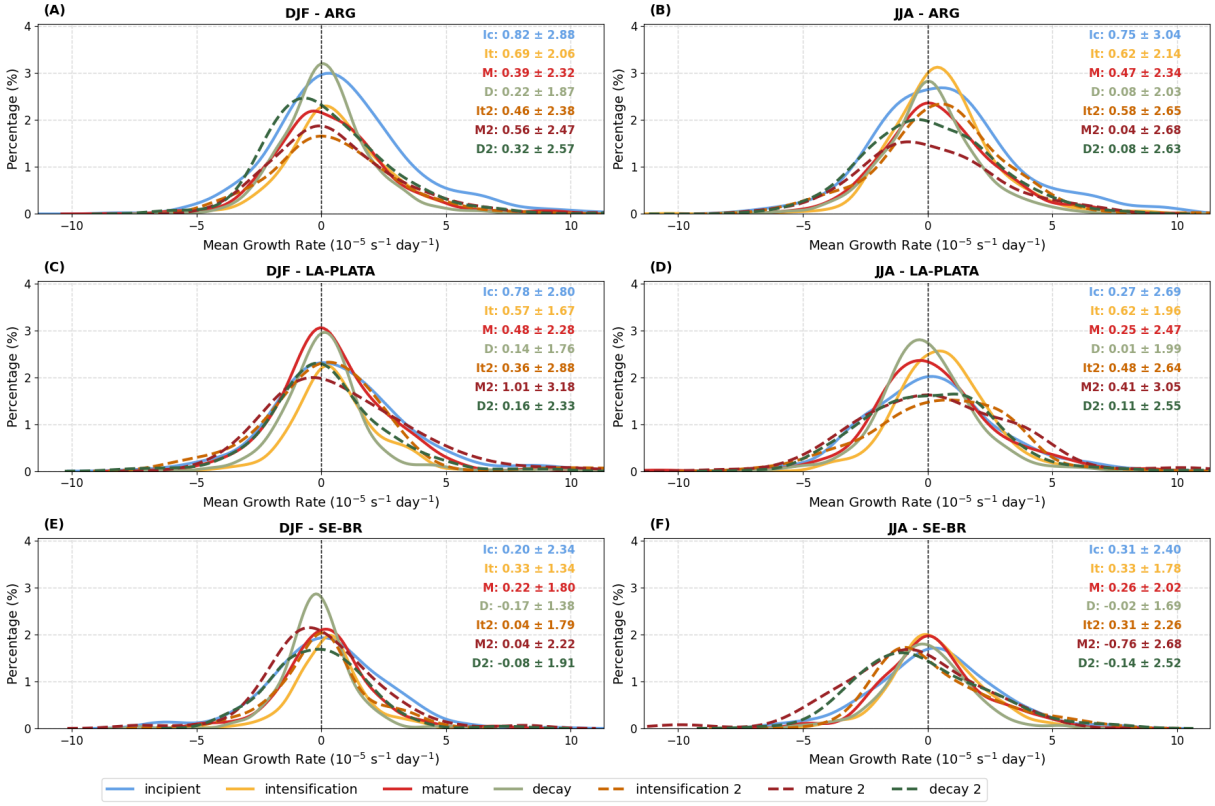
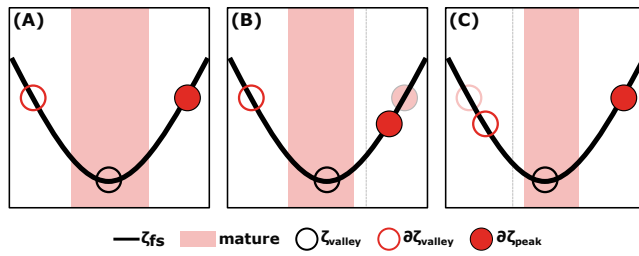


Figure 4.11: Similar to Figure 4.7, but for mean growth rate.

Figure 4.12: Illustrative example of how the center of mass of the mature phase can be displaced: (A) Symmetrically around the vorticity valley ( $\zeta_{valley}$ ) when distances to the first derivative valley ( $\partial\zeta_{valley}$ ) and peak ( $\partial\zeta_{peak}$ ) are equal. (B) Displacement towards the previous phase when  $\partial\zeta_{peak}$  is closer to  $\zeta_{valley}$ . (C) Displacement towards the subsequent phase when  $\partial\zeta_{valley}$  is closer to  $\zeta_{valley}$ .

## 4.2 Spatial Distribution of Cyclone Life Cycle Phases

The current section explores the spatial distribution across the SESA region of the distinct phases of cyclone development: incipient (Section 4.2.1), intensification (Section 4.2.2), mature (Section 4.2.3), decay (Section 4.2.4) and the secondary development cycle, as well the residual phase (Section 4.2.5). The analysis focuses only on systems that presented a mature phase to avoid including underdeveloped systems, those that might not have exhibited a mature phase before leaving the tracking domain, or cases where the maturation stages were shorter than the CycloPhaser's threshold for detecting this phase (as discussed in Section 4.1.1). The track density ranges differ from one figure to the other as does not make sense to compare track density between distinct phases, as those differ in duration and in total displacement (Section 4.1.3).

### 4.2.1 Incipient Phase

Figure 4.13 illustrates cyclone track density (cyclones per  $10^6 \text{ km}^2$  per month) during the incipient phase for DJF and JJA in the SESA region. Given that transitional seasons display intermediate characteristics between these extremes (Gan and Rao, 1991; Reboita et al., 2010; Crespo et al., 2021, e.g.,), our analysis primarily focuses on DJF and JJA, encompassing the cyclogenesis regions of ARG, LA-PLATA, and SE-BR. As expected, the track density for the incipient phase correlates with these genesis regions (Figure 4.13a and b).

The ARG region consistently shows similar track densities in both DJF (Figure 4.13c) and JJA (Figure 4.13d), exceeding 30 cyclones per  $10^6 \text{ km}^2$  per month. In contrast, LA-PLATA and SE-BR regions exhibit noticeable seasonal patterns. LA-PLATA sees increased activity in JJA (Figure 4.13f) compared to DJF (Figure 4.13e), with densities rising above 20 and 10 cyclones per  $10^6 \text{ km}^2$  per month, respectively. Conversely, SE-BR demonstrates higher activity in DJF (Figure 4.13g) than in JJA (Figure 4.13h), with densities exceeding 10 and 8 cyclones per  $10^6 \text{ km}^2$  per month, respectively. This seasonality is consistent with findings from previous studies (Gan and Rao, 1991; Hoskins and Hodges, 2005; Mendes et al., 2010; Reboita et al., 2010; Gramcianinov et al., 2019; Crespo et al., 2021). Variations in reported track density values by (Gramcianinov et al., 2020, 2019) may arise from different methodologies; those studies analyzed only the initial time step of the system life

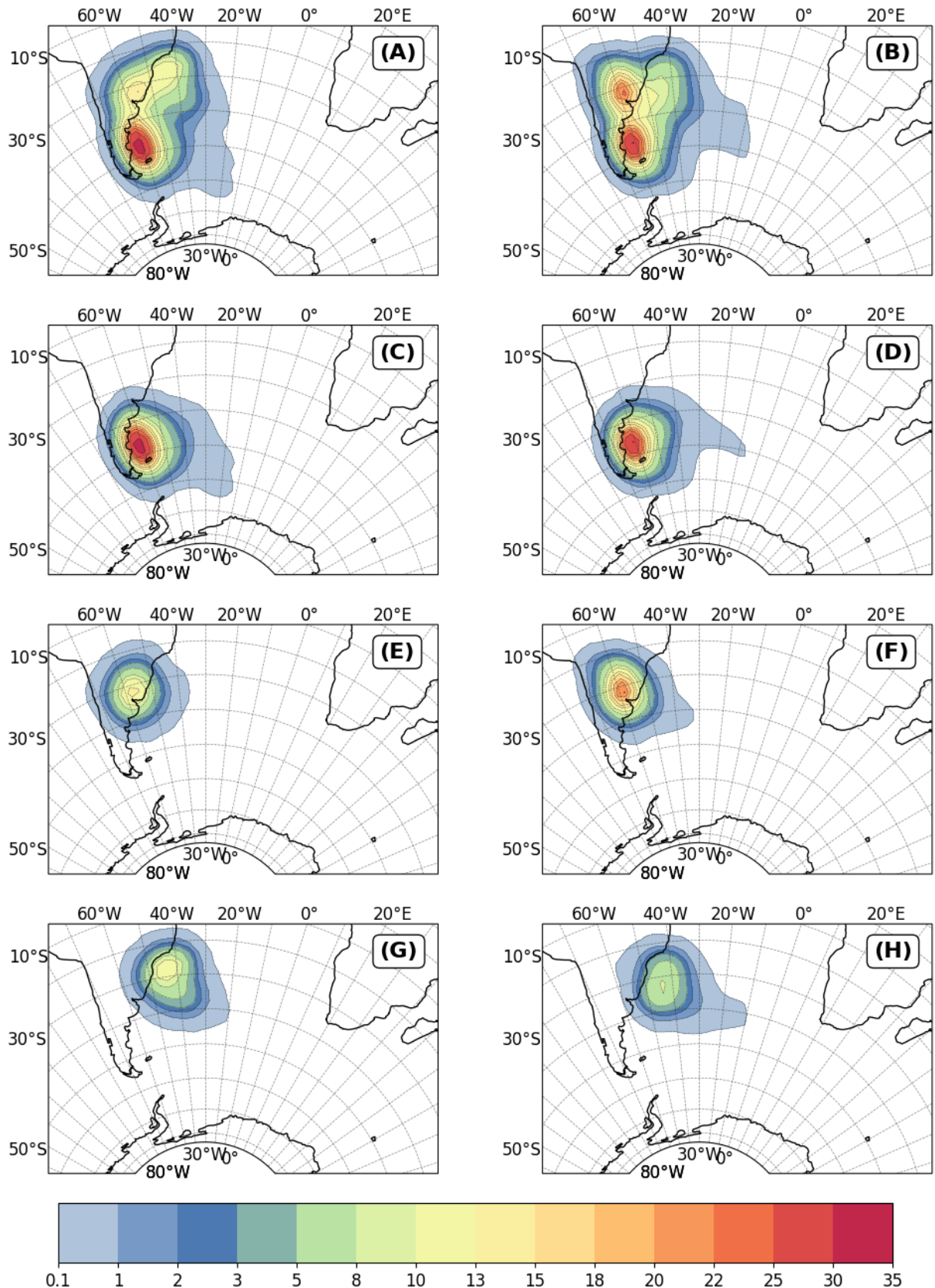


**Figure 4.13:** Cyclone track density during the incipient phase for all systems with genesis in the ARG, LA-PLATA and SE-BR regions. Panels A and B show the aggregate density across all regions for DJF and JJA, respectively. Panels C to H depict individual genesis regions: ARG (C and D), LA-PLATA (E and F), and SE-BR (G and H) for DJF (left panels) and JJA (right panels). The unit is cyclones per  $10^6 \text{ km}^2$  per month.

cycle, while this study considers all periods classified as the incipient stage. Additionally, Gramcianinov et al. (2019) utilized the NCEP-CFSR reanalysis database for tracking, in contrast to the ERA5 dataset employed here.

#### 4.2.2 Intensification Phase

The track densities during the intensification phase (Figure 4.14) exhibit significantly higher values compared to the incipient stage. This is expected due to the longer duration of the intensification phase, as discussed in Section 3.3.1. Across all genesis regions, during both DJF (Figure 4.14a) and JJA (Figure 4.14b), the maximum track density extends from approximately 60°W to 20°W. The central concentration around 50°S, particularly during both seasons, is primarily composed of systems originating in the ARG region (Figure 4.14c and d). During DJF, the maximum density region, extending eastward/southeastward from the incipient stage, reaches up to 100 cyclones per  $10^6 \text{ km}^2$  per month, while in JJA, it shows a slight decrease to 80 cyclones per  $10^6 \text{ km}^2$  per month, with a predominantly eastward orientation. The higher track density and the cyclones reaching further east in DJF can be attributed to the longer mean duration of the intensification phase for systems from ARG, as shown in Figure 4.7, and the overall greater displacement distances during this phase across all genesis regions, as indicated in Figure 4.8.

Moreover, the maximum track density at around 50°S for the ARG region connects with the track densities for the LA-PLATA and SE-BR regions. LA-PLATA shows higher activity during JJA (Figure 4.14f), with track densities reaching 50 cyclones per  $10^6 \text{ km}^2$  per month, compared to 40 during DJF (Figure 4.14e). Conversely, SE-BR exhibits higher activity during DJF (Figure 4.14g), with densities reaching 40 cyclones per  $10^6 \text{ km}^2$  per month, compared to 20 during JJA (Figure 4.14h). This seasonality for both LA-PLATA and SE-BR regions reflects the seasonality in cyclogenesis (Figure 4.1) and consequently, of the incipient phase (Figure 4.13). Consequently, in the aggregate densities for all regions during DJF (Figure 4.14a), the SE-BR region's signal is more apparent near 30°S and 40°W. In JJA (Figure 4.14b), the track density associated with LA-PLATA is evident as the maximum track region extends southeastward from near 35°S and 55°W (Figure 4.14f). Furthermore, for the LA-PLATA region, it can be seen that during JJA, the systems tend to reach further southeast, associated with higher mean displacements (Figure 4.8).

Notably, the track densities for the intensification phase across all genesis regions show

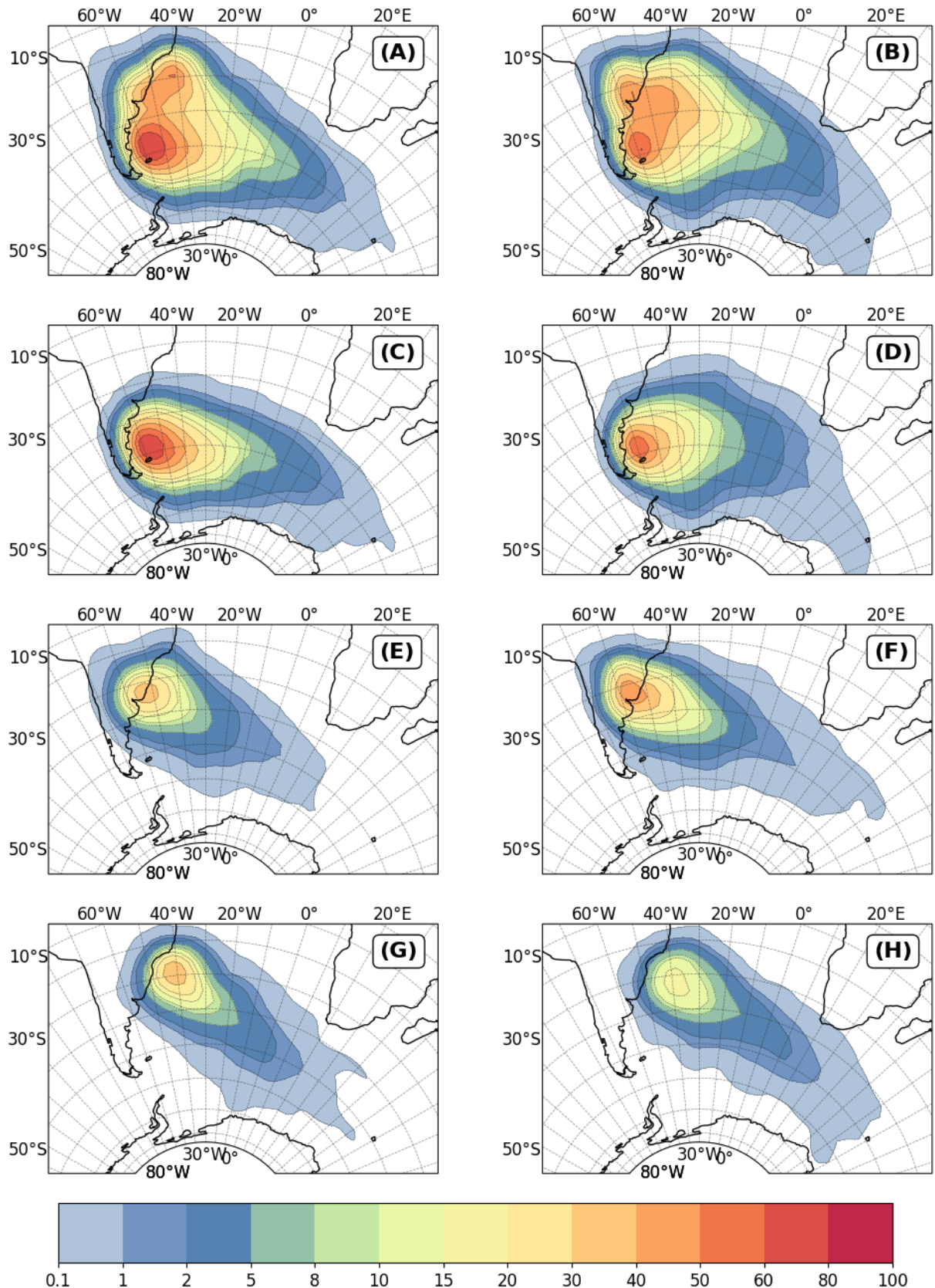


*Figure 4.14:* Cyclone track density during the intensification phase for all systems with genesis in the ARG, LA-PLATA and SE-BR regions. Panels A and B show the aggregate density across all regions for DJF and JJA, respectively. Panels C to H depict individual genesis regions: ARG (C and D), LA-PLATA (E and F), and SE-BR (G and H) for DJF (left panels) and JJA (right panels). The unit is cyclones per  $10^6 \text{ km}^2$  per month.

far-reaching systems that intensify throughout the entire South Atlantic basin, extending as far as 30°E or even 60°E. While the orientation of the track density for the ARG region is predominantly eastward, for LA-PLATA and SE-BR, the tracks are southeastward oriented. This results in a concentration of track densities between 40°S and 60°S, displaced more northward during JJA than DJF, indicating a preference for systems to intensify in this region, which corresponds to the storm track path for the South Atlantic (Hoskins and Hodges, 2005; Gramcianinov et al., 2019).

#### 4.2.3 Mature Phase

In the mature phase, there is a notable reduction in track densities compared to the intensification phase, with maximum values decreasing from 100 to 20 cyclones per  $10^6 \text{ km}^2$  per month. During DJF, the aggregate for all genesis regions shows two principal maximum track density areas (Figure 4.15a). The first area, centered near 35°S and 45°W, exhibits a lower maximum track density reaching 14 cyclones per  $10^6 \text{ km}^2$  per month, predominantly associated with cyclones originating in the LA-PLATA and SE-BR regions (Figures 4.15e and 4.15g). The second area, located near 55°S and 30°W, reaches up to 18 cyclones per  $10^6 \text{ km}^2$  per month and is primarily associated with systems from the ARG region (Figure 4.15c). During this season, maximum track densities for ARG, LA-PLATA, and SE-BR peak at 16, 9, and 10 cyclones per  $10^6 \text{ km}^2$  per month, respectively.

In JJA, the primary track density maximum for the aggregate is located near 45°S and 45°W, slightly westward compared to the DJF maximum, with secondary maxima to the north and northeast, each reaching 12 cyclones per  $10^6 \text{ km}^2$  per month (Figure 4.15b). This lower density compared to DJF reflects shorter mature phase durations and reduced mobility of systems from the ARG region during JJA, as shown in Figures 4.7 and 4.8. Notably, the track density center for the ARG region shifts from near 45°W during DJF to around 55°W during JJA (Figure 4.15d), indicating a tendency for systems to mature closer to their intensification locations, which is also indicated by the lower mobility of these systems when compared to the other genesis regions for this period (Figure 4.8). Secondary maxima near 35°S and 45°S result from overlaps in tracks from all regions, with LA-PLATA contributing significantly (Figure 4.15f). Although this overlaps with a center from SE-BR, the track density maximum for SE-BR during JJA remains low, not exceeding 5 cyclones per  $10^6 \text{ km}^2$  per month (Figure 4.15h), while for LA-PLATA, it reaches up to 7

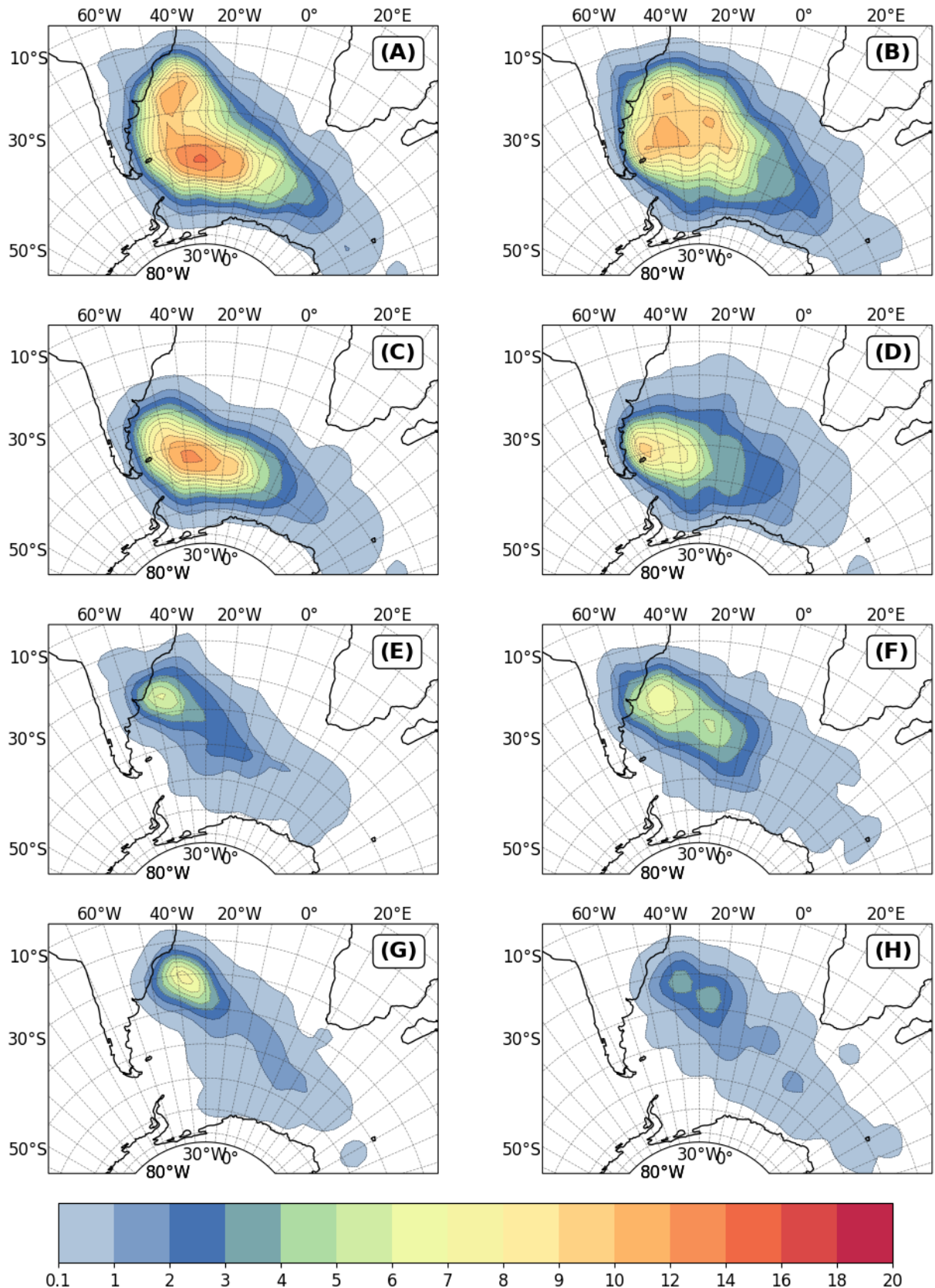


*Figure 4.15:* Cyclone track density during the mature phase for all systems with genesis in the ARG, LA-PLATA and SE-BR regions. Panels A and B show the aggregate density across all regions for DJF and JJA, respectively. Panels C to H depict individual genesis regions: ARG (C and D), LA-PLATA (E and F), and SE-BR (G and H) for DJF (left panels) and JJA (right panels). The unit is cyclones per  $10^6 \text{ km}^2$  per month.

near 55°W and 6 near 45°W.

Overall, the density maximum centers for the mature phase are displaced southeastward from those for the intensification phase for DJF and east/southeastward for JJA. Tracks are typically found between 40°S and 60°S, aligning with the storm track path for the South Atlantic. For DJF, most tracks are located below 50°S, while for JJA, they are predominantly above 50°S. This pattern is more pronounced during the mature phase than during the intensification phase, with the southward shift during DJF largely associated with cyclones originating in the ARG region, while a maximum density region closer to Uruguay and Southern/Southeastern Brazil is mostly linked with LA-PLATA and SE-BR genesis regions.

#### 4.2.4 Decay Phase

The decay phase generally exhibits increased track densities compared to the mature phase, with maximum values reaching 40 cyclones per  $10^6 \text{ km}^2$  per month, but still lower than observed during the intensification phase. During DJF, two primary centers of maximum track density are observed: one near 35°S, close to Uruguay and South/Southeastern Brazil (Figure 4.16a), and another near 55°S, west of the Weddell Sea (Figure 4.16a). The latter, primarily influenced by cyclones from the ARG region, reaches up to 35 cyclones per  $10^6 \text{ km}^2$  per month (Figure 4.16c). The former, influenced by the LA-PLATA and SE-BR regions, records densities of up to 13 and 30 cyclones per  $10^6 \text{ km}^2$  per month, respectively (Figures 4.16e and 4.16g).

For JJA, two primary density maxima are identified: one centered at 45°S, spanning from 60°W to 20°W, and another near 35°S and 40°W, with both areas achieving track densities up to 35 cyclones per  $10^6 \text{ km}^2$  per month (Figure 4.16b). The former is predominantly linked to systems from the ARG region, where densities reach 30 cyclones per  $10^6 \text{ km}^2$  per month (Figure 4.16d), while the latter is influenced by the SE-BR and especially the LA-PLATA regions, showing densities of 10 and 15 cyclones per  $10^6 \text{ km}^2$  per month, respectively (Figures 4.16h and 4.16f). Additionally, a notable center of density, although less pronounced, emerges in the LA-PLATA region, associated with systems that enter an early decay phase (Section 4.2.5).

For the ARG region, the decay phase densities are typically shifted southeastward from those of the mature phase during DJF and mostly southeastward/eastward during JJA,

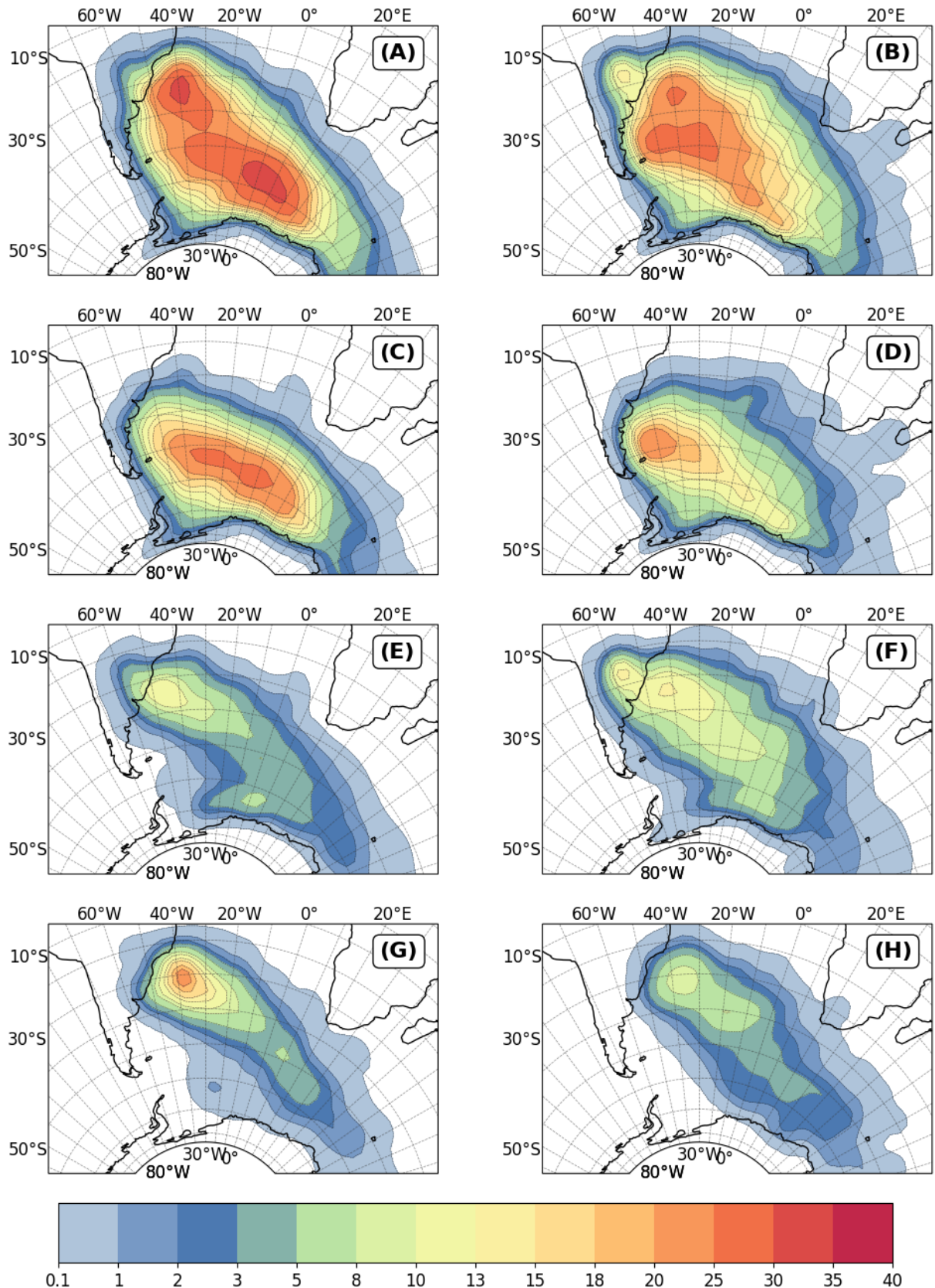


*Figure 4.16:* Cyclone track density during the decay phase for all systems with genesis in the ARG, LA-PLATA and SE-BR regions. Panels A and B show the aggregate density across all regions for DJF and JJA, respectively. Panels C to H depict individual genesis regions: ARG (C and D), LA-PLATA (E and F), and SE-BR (G and H) for DJF (left panels) and JJA (right panels). The unit is cyclones per  $10^6 \text{ km}^2$  per month.

with some systems extending westward to the Weddell Sea. This pattern highlights a seasonal variation in the decay behaviors of systems within the SESA region. Moreover, for both LA-PLATA and SE-BR, decay densities are generally proximate to those of the mature phase but extend further southeastward, reaching as far south as 70°S and as far east as 30°E. This expansive spread into the southern Atlantic aligns with findings by Hoskins and Hodges (2005), who identify the region south of 60°S and west of the Weddell Sea as the primary dissolution area for cyclones in the South Atlantic.

#### 4.2.5 Secondary Development Phases

For analyzing the track densities for the phases related to the systems' secondary development, the results are shown as yearly values rather than by seasonal variability, as done in previous sections. This approach is due to the lower frequency of systems undergoing secondary development compared to those that do not (Figure 4.3). Additionally, as shown in Section 4.1.1, the number of systems presenting early intensification or decay phases is comparable to those with secondary development stages. Therefore, the analysis here focuses on systems that exhibited a complete secondary development cycle: incipient, intensification, mature, decay, intensification 2, mature 2, and decay 2. Figure 4.17 illustrates the track density differences when other life cycle configurations are included in the analysis. The occurrence of early intensification and decay phases impacts the overall track density distribution, with maximum density centers between 30°S and 40°S, centered near 45°W (Figures 4.17a and 4.17c). These centers disappear when the analysis focus only on the systems with a complete secondary development (Figures 4.17b and 4.17d).

For the second intensification phase, there is a maximum track density region south of South Africa, with 30 cyclones per  $10^6 \text{ km}^2$  per month (Figure 4.18a). This maximum density region is related to the aggregate occurrence of systems from all genesis regions and closely matches the SE-SAO cyclogenesis region reported by Gramcianinov et al. (2019). Gramcianinov et al. (2019) highlighted a potential link between this region and secondary cyclogenesis. It is possible that some of the detected re-intensifications might stem from secondary cyclogenesis events or spurious links by the TRACK algorithm, which could mix weak decaying systems with incipient secondary cyclones. While secondary cyclogenesis generally follows a frontal wave post an extratropical cyclone's passage (Mailier et al., 2006; Shapiro et al., 1997; Ford et al., 1990; Rivals et al., 1998), the CycloPhaser program

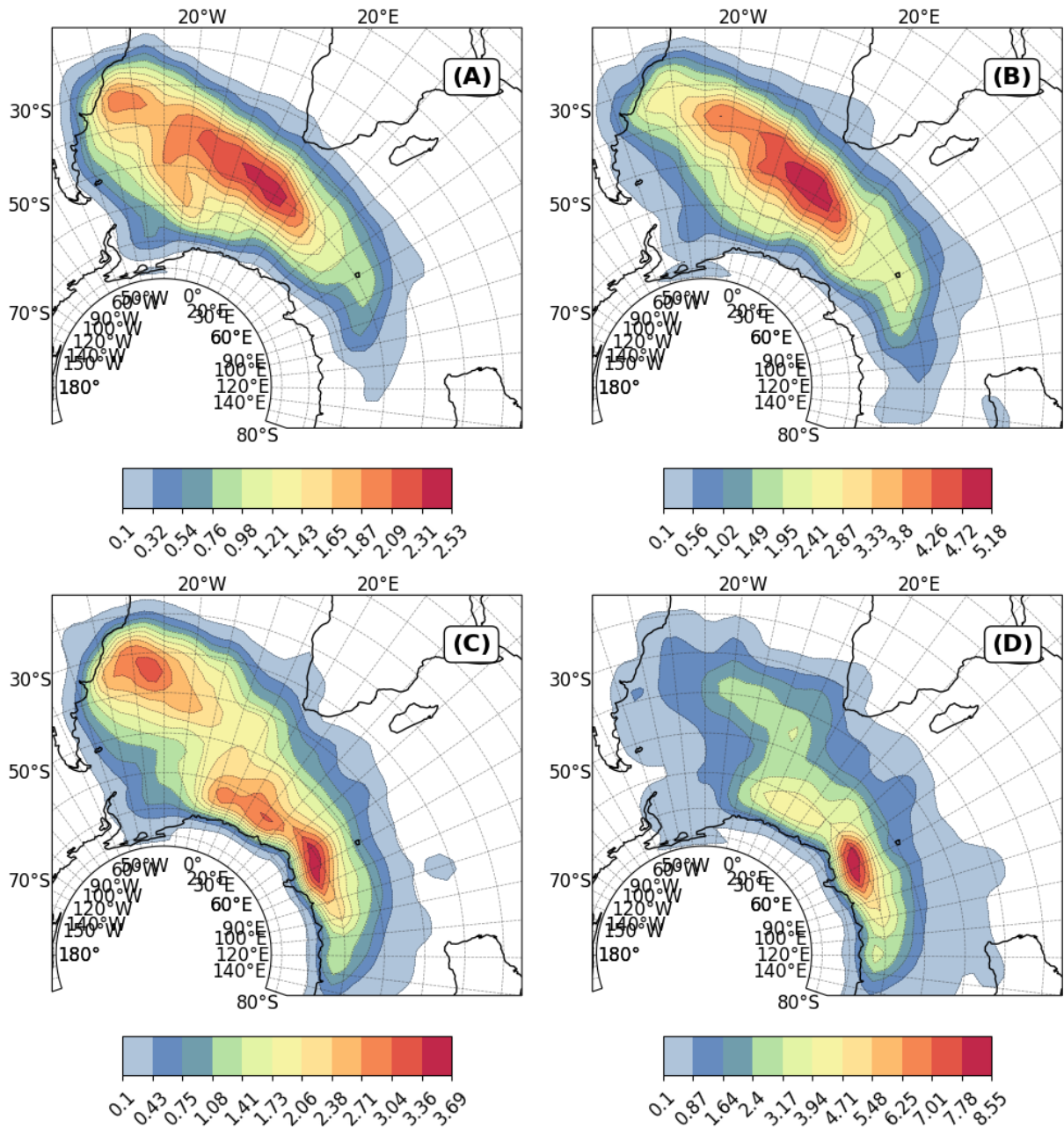


Figure 4.17: Cyclone track density for the secondary development stages. Panels A and B display the phase intensification 2, while panels C and D, phase decay 2. Panels A and C show the results when all life cycle configurations are included in the analysis, while panels B and D show the results when only the systems that exhibited a complete secondary development cycle - incipient, intensification, mature, decay, intensification 2, mature 2, and decay 2 - are analysed. The unit is cyclones per  $10^6 \text{ km}^2 \text{ per month}$ .

classifies a phase as "intensification 2" whenever the  $\zeta_{850}$  series indicates a pattern of increases in its magnitude, followed by subsequent mature and decay phases. This secondary intensification could result from a decaying wave at 850 hPa finding favorable conditions for subsequent intensification. Alternatively, the surface cyclone might have already dissipated, but there is still a signal of it in the  $\zeta_{850}$  field, causing the TRACK algorithm to continue tracking a weak decaying trough at 850 hPa. In these instances, the CycloPhaser may classify this weak intensification as 'residual' should it not progress to a mature stage (Section 3.3.1). Conversely, if the TRACK algorithm mistakenly associates this decaying wave with a newly forming cyclone nearby, the CycloPhaser would label this transition as "intensification 2," introducing potential analysis errors. However, distinguishing between true secondary genesis and re-intensification remains beyond this study's scope. Furthermore, notably, there is a track density maxima near Uruguay and South Brazil associated with LA-PLATA systems.

The second mature phase, characterized by its overall low track density, presents a diffuse spatial distribution. This low track density is primarily due to the infrequent occurrence of secondary development in SESA systems (Figure 4.3) and the fact that it exhibits the lowest displacement and duration across all phases (Figures 4.8 and 4.7). However, a notable maximum track density is centered at 60°S and 50°E, with 2 cyclones per  $10^6 \text{ km}^2$  per month (Figure 4.19a). This peak is mainly associated with systems from ARG and SE-BR (Figures 4.19b and 4.19d). A weaker density maximum is found to the west, between 10°E and 20°E, predominantly linked to systems from LA-PLATA (Figure 4.19c). For all regions, the track density regions are mostly displaced southeastward compared to the intensification 2 phase.

The second decay phase displays the systems in their southernmost and easternmost positions, with track densities extending up to 140°E and bordering the Antarctic continent. All three genesis regions present a track density maximum centered between 60°E and 110°E, with the resulting aggregate displaying up to 8.5 cyclones per  $10^6 \text{ km}^2$  per month (Figure 4.20a). Individually, each genesis region has a track maximum of approximately 2 to 3 cyclones per  $10^6 \text{ km}^2$  per month, with LA-PLATA displaying a second weaker maximum between 20°E and 40°E, with up to 2 cyclones per  $10^6 \text{ km}^2$  per month (Figure 4.20c). This region also presents the highest density values northwestwards, contributing to the track densities near 40°S.

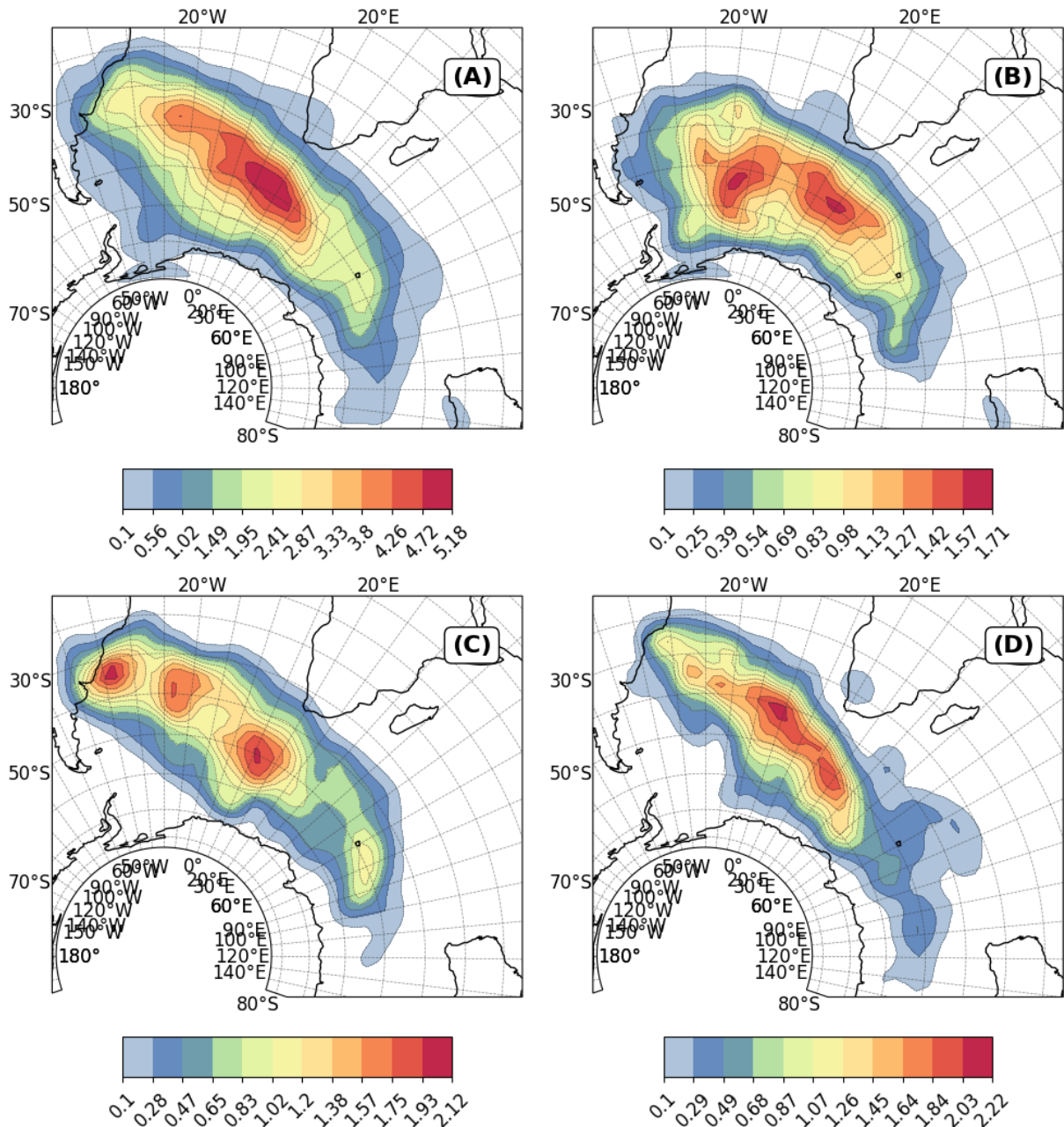


Figure 4.18: Cyclone track density during the second intensification phase for all systems with genesis in the ARG, LA-PLATA and SE-BR regions that display a complete secondary development cycle. Panel A shows the aggregate density across all regions. Panels B to D depict individual genesis regions: ARG (B), LA-PLATA (C), and SE-BR (D). The unit is cyclones per  $10^6 \text{ km}^2 \text{ per month}$ .

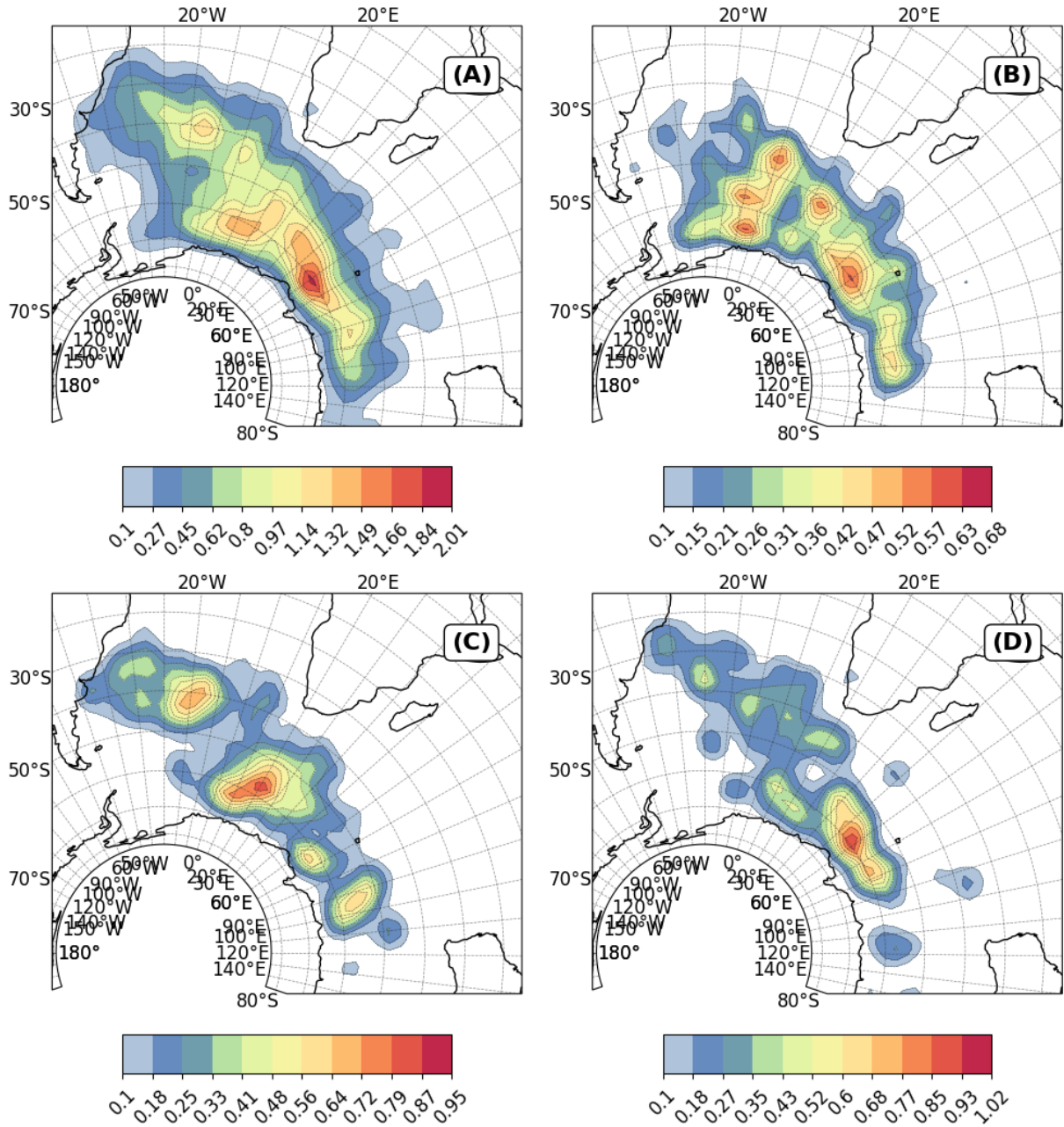


Figure 4.19: Cyclone track density during the second mature phase for all systems with genesis in the ARG, LA-PLATA and SE-BR regions that display a complete secondary development cycle. Panel A shows the aggregate density across all regions. Panels B to D depict individual genesis regions: ARG (B), LA-PLATA (C), and SE-BR (D). The unit is cyclones per  $10^6 \text{ km}^2$  per month.

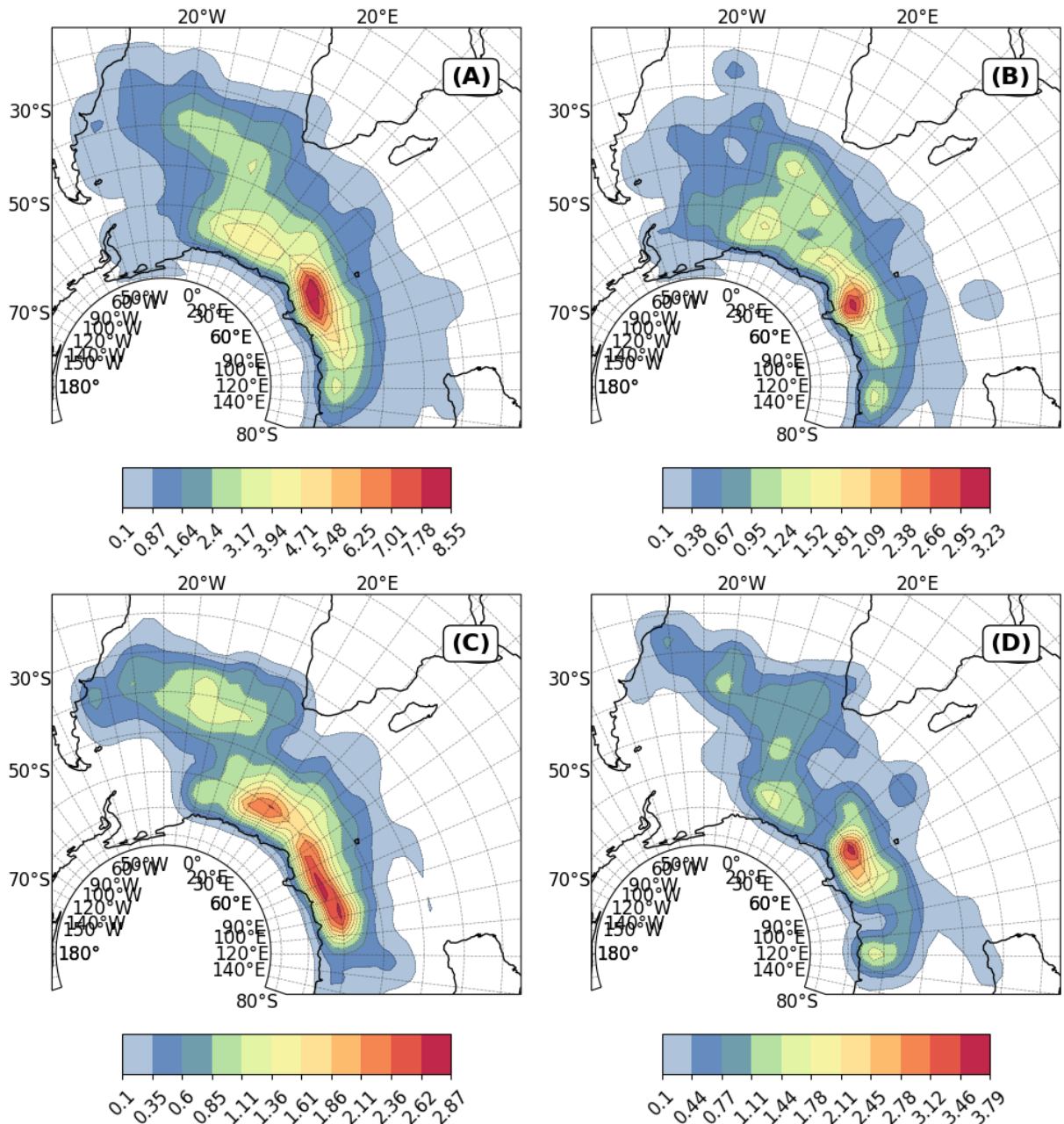


Figure 4.20: Cyclone track density during the second decay phase for all systems with genesis in the ARG, LA-PLATA and SE-BR regions that display a complete secondary development cycle. Panel A shows the aggregate density across all regions. Panels B to D depict individual genesis regions: ARG (B), LA-PLATA (C), and SE-BR (D). The unit is cyclones per  $10^6 \text{ km}^2 \text{ per month}$ .

Across all second development phases, a weaker albeit noticeable track density region is present near the SE-BR genesis area. This region also shows occurrences of subtropical cyclones Evans and Braun (2012); de Jesus et al. (2022); Cardoso et al. (2022), especially during DJF months, where approximately 30% of the systems exhibit hybrid characteristics Gozzo et al. (2014). Previous works analyzing case studies of such systems that have genesis in the SE-BR region reveal that they present complex life cycles, often transitioning between different types of cyclonic systems and presenting multiple stages of intensification, maturation, and decay (Dias Pinto et al., 2013; Veiga et al., 2008; Reboita et al., 2022; Dutra et al., 2017; Reboita et al., 2021, e.g.,). Consequently, one can speculate that some of the systems related to these track density regions near SE-BR might be subtropical. However, further analysis would be needed for confirm this assertion, which is beyond the scope of the current work.

#### 4.2.6 Residual Phase

The residual phase, though not representing a physical stage of cyclone development, plays an important role in identifying tracking and detection inconsistencies, highlighting potential areas for methodological improvement. This phase typically includes systems that experience temporary intensification due to favorable environmental factors but fail to progress into mature cyclones. Identifying the residual phase involves detecting situations where a system's central vorticity increases outside the standard development cycle, often influenced by nearby systems or localized atmospheric conditions that promote brief intensification (Section 3.3.1).

Figure 4.21 shows the track densities across all regions and seasons. A noticeable track density maximum is present near Uruguay and South Brazil, over the Brazil-Malvinas confluence (Gordon, 1989). The confluence region presents low-level baroclinicity, which can be transferred upwards in the atmosphere (Sanders and Gyakum, 1980; Vera et al., 2002, e.g.,). Systems passing over the confluence might experience brief intensification due to favorable conditions but not achieve maturity. This could also be important for systems with genesis in SE-BR, which are often weaker (Sinclair, 1995; Hoskins and Hodges, 2005). Furthermore, the track density maximum near 40°E and 55°S indicates that upper-level jet support (Swart et al., 2015, e.g.,) and a baroclinic environment (Hoskins and Hodges, 2005, e.g.,) could similarly drive marginal intensification, leading to a residual classification.

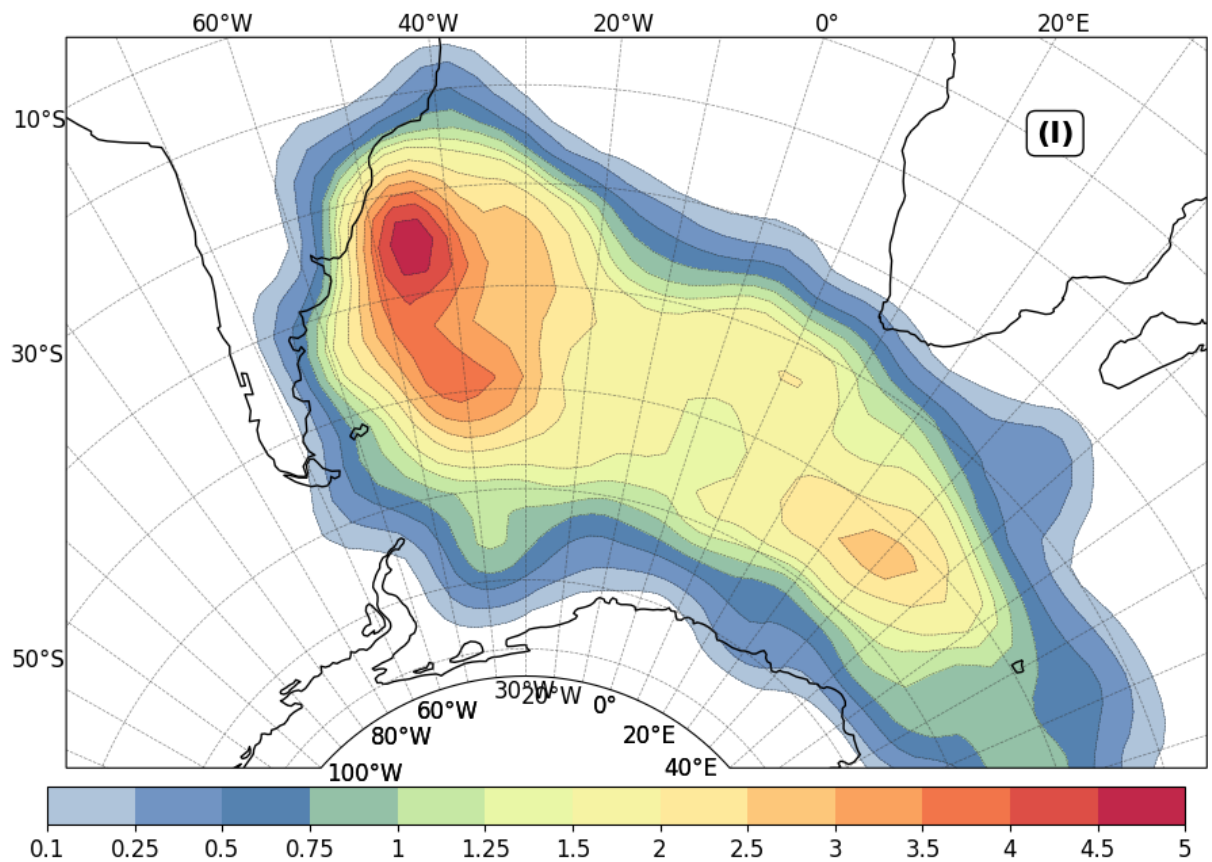


Figure 4.21: Cyclone track density during the residual phase for all systems with genesis in the ARG, LA-PLATA and SE-BR regions. The unit is cyclones per  $10^6 \text{ km}^2$  per month.

### 4.3 Summary and Concluding Remarks

This chapter introduced CycloPhaser, a novel, open-source Python package for automated cyclone life cycle detection, available on the PyPI repository. Its low memory footprint, flexibility, and rapid deployment capabilities make it a valuable asset for climatological studies or even operational forecasts. The TRACK program identified a total of 7,931 systems from 1979 to 2020 for the cyclogenesis regions near South America. These results were narrowed down to life cycle configurations that accounted for at least 1% of the overall life cycle types count and presented at least one mature phase. These configurations represented approximately 95% of the total systems, amounting to 7,531 systems in total. The most common cyclone type followed a four-phase configuration: incipient, intensification, mature, and decay, accounting for about 60% of the analyzed systems. The results from the CycloPhaser program align well with previous studies regarding cyclone behavior in the South Atlantic region, confirming known cyclogenesis regions and providing statistical insights into cyclone lifetimes and paths. The CycloPhaser program calculated an average cyclone lifetime of approximately 97.6 and 91.1 hours (4 and 3.7 days) for austral summer (DJF) and winter (JJA), respectively, and an average displacement of 4,658 and 4,777 km for DJF and JJA. The mean displacement speed ranged from 14 to 15  $ms^{-1}$  from DJF to JJA, while the mean vorticity ranged from 4 to  $4.5 - 10^{-5}s^{-1}$ . These findings largely corroborate those of previous studies for the regions and indicate a broad range of cyclone behaviors (Simmonds and Murray, 1999; Hoskins and Hodges, 2005; Mendes et al., 2010; Reboita et al., 2010; Gramcianinov et al., 2019, 2020; Crespo et al., 2023).

The analysis of spatial distributions revealed distinct patterns across various phases of the cyclone life cycle:

- **Incipient Phase:** The overall pattern matches the genesis regions described in the literature.
- **Intensification Phase:** The seasonal differences in track densities are mostly related to seasonal differences in genesis. Two maxima are present in both seasons: one mostly associated with ARG and the other with either LA-PLATA or SE-BR. However, other patterns include ARG systems being more eastward-oriented during JJA than DJF and reaching further east during DJF, while LA-PLATA systems tend to reach further southeast during JJA. Overall, the tracks are more displaced northward

during JJA than DJF.

- **Mature Phase:** The maximum track densities are southeast of the intensification centers during DJF and east/southeast during JJA. During JJA, cyclones from the ARG region mature close to the intensification. There is a higher positioning of cyclones close to Uruguay and Southern/Southeastern Brazil during DJF than JJA.
- **Decay Phase:** The track density regions elongate southeastward compared to the mature phase, with a maximum density east of the Weddell Sea, mainly related to systems from ARG. Systems with an early decay phase appear as density centers in LA-PLATA. During DJF, there are more tracks positioned near Uruguay and South/Southeast Brazil than JJA.
- **Second Intensification Phase:** There is a high concentration of tracks south of South Africa, which might be linked to secondary cyclogenesis processes (Mailier et al., 2006; Shapiro et al., 1997; Ford et al., 1990; Rivals et al., 1998).
- **Second Mature Phase:** This phase generally occurs southeastward of the second intensification phase.
- **Second Decay Phase:** This phase occurs bordering Antarctica, predominantly east of 40°E.

Figure 4.22 provides an illustrative representation of the life cycle of systems with genesis in the South American cyclogenesis regions. This figure highlights the systems' path through their lifecycle, showing that after genesis, the systems follow the usual storm tracks in the South Atlantic or, in the case of systems with genesis in ARG and LA-PLATA, the subtropical storm path branch. Although systems from ARG and SE-BR tend to have their genesis and intensification over the ocean, LA-PLATA systems tend to start intensifying close to the continent, which can impact coastal communities (de Souza and da Silva, 2021). Moreover, systems from SE-BR and LA-PLATA have their mature phases — where they are most intense and, therefore, transfer more momentum from the atmosphere to the ocean — near oceanic regions close to South and Southeast Brazil. These regions host large urban centers and significant economic activities, such as oil drilling.

The results presented here contribute significantly to the climatology of South Atlantic cyclones. CycloPhaser's detailed analysis of cyclone life cycle types, particularly focusing

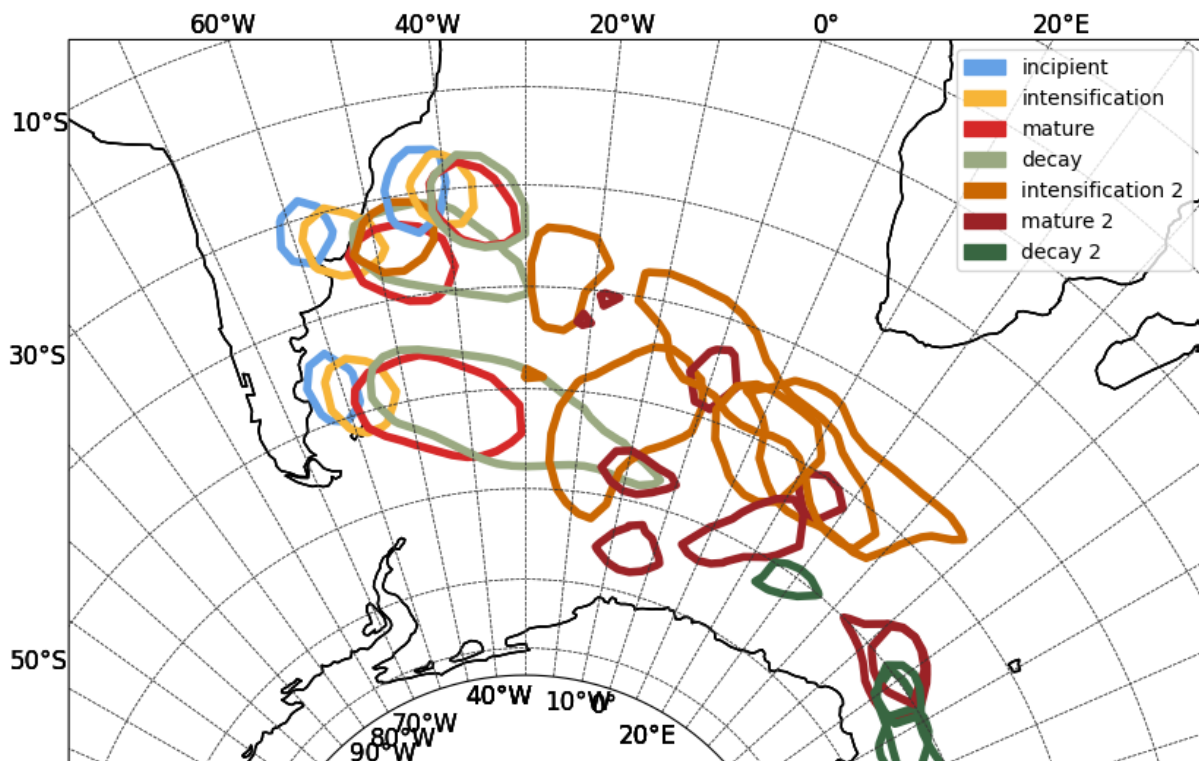


Figure 4.22: Track densities normalized for each region, using yearly values for all phases. For computing the track densities for the secondary development phases, only systems that display a complete secondary development cycle were used. Contours representing normalized track densities above 0.8 were plotted for each region individually.

on configurations accounting for significant proportions of cyclone activity, enhances our understanding of the spatial distribution of cyclone phases. This analysis reaffirms the common four-phase configuration (incipient, intensification, mature, and decay) and sheds light on variations in cyclone development cycles, contributing to a better understanding of how different regions within the South Atlantic influence the formation and evolution of distinct cyclone types. These insights are valuable for improving weather forecasting and developing effective mitigation strategies in the region.

Despite the valuable contributions of the CycloPhaser program, it is important to acknowledge the study's limitations. The analysis at a single atmospheric level offers a concentrated but partial view of the cyclone life cycle. Consequently, our conclusions about cyclone characteristics throughout their life cycle predominantly reflect the processes observable at the 850 hPa level. This methodological choice inherently limits our ability to fully explore the cyclones' vertical development and the complex interactions occurring at different atmospheric altitudes. Future research could benefit from incorporating a multi-level approach, providing a more holistic understanding of cyclone dynamics across the troposphere.

One of the unique contributions of this research is the assessment of cyclone life cycle stages along their storm tracks, a perspective not commonly explored in existing cyclone track climatologies. This first application has highlighted the complexity of cyclone systems and opened several avenues for future research. The approach presented here allows for the analysis of distinct dynamical mechanisms linked to the development of cyclonic systems at different stages of their life cycle. Investigating cyclonic life cycles in climate projections might be particularly relevant for coastal management in South America, posing questions such as: Will future cyclones intensify and mature closer to or further from coastal regions? Will these phases last longer? Furthermore, using the method presented here, future studies can delve deeper into the primary processes associated with each development stage in cyclone life cycles, including the secondary development stages reported herein, and determine whether some of these cases represent secondary genesis.



# Chapter 5

---

## Southwestern Atlantic Cyclones Energetics Climatology

This chapter delves into the energetics of cyclones in the Southwestern Atlantic. The Lorenz Energy Cycle (LEC) was computed for all 7,531 systems with genesis in the ARG, LA-PLATA, and SE-BR regions, as described in Chapter 2.14. This extensive dataset, the first of its kind for the South Atlantic region, provides a comprehensive view of the energetics of cyclonic systems near South America. Section 5.1 explores the climatology of these systems over their complete life cycle, while Section 5.2 examines the energetics across each development phase, offering a unique perspective on the energy cycle of cyclonic systems in the region.

### 5.1 Complete Life Cycle Climatology

#### 5.1.1 Descriptive Statistics

This section provides exploratory statistics for each term of the LEC, covering the systems' complete life cycle. The aim is to offer a comprehensive view of the systems' energetics while identifying the main differences among the terms. Table 5.1 contains exploratory statistical metrics for these terms. Figure 5.1 presents the boxplots for all LEC components, where each panel depicts a distinct group of terms: (A) energy, (B) conversion, (C) boundary, (D) generation/dissipation terms, and (E) budgets. Figures 5.2, 5.3, 5.4, 5.5, and 5.6 display these groups of terms' density distributions, respectively.

For the energy terms, the values for  $K_Z$  are an order of magnitude higher than the others for all metrics analyzed (Table 5.1). Despite the high standard deviation (std) and quantile (Q) values indicating substantial variability, this can be attributed to the presence of numerous outliers (Figure 5.1a). Most values for  $K_Z$  peak between 15 and 17

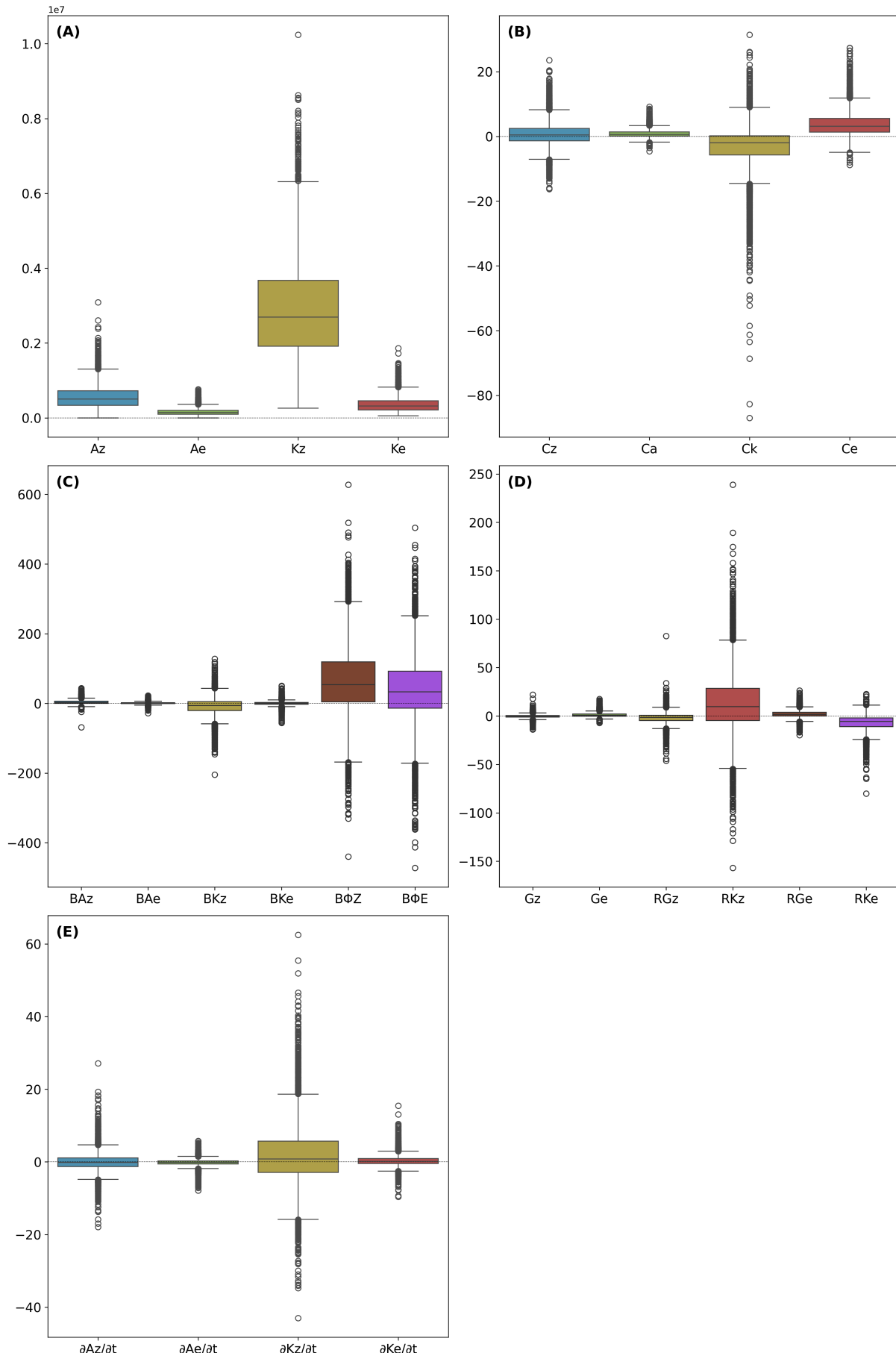


Figure 5.1: Box plots of each group of energetic terms, for the systems complete lifecycle. Each subplot represents a different group of terms: (A) Energy Terms, (B) Conversion Terms, (C) Boundary Terms, (D) Generation/Dissipation Terms, (E) Budgets. The box plots display the distribution of values for each term within the specified group, with the horizontal line indicating the median, the box representing the interquartile range (IQR), and the whiskers extending to the full range. Outliers are shown as individual points.

$\times 10^5 \text{ J m}^{-2}$  (Figure 5.2c). In contrast,  $A_Z$  presents relatively moderate mean and median values, with a right-skewed distribution and significant spread (Figure 5.2a). The notable outliers (Figure 5.1a) suggest periods of unusually high energy values.

Overall, the eddy energy terms ( $A_E$  and  $K_E$ ) exhibit less variability and fewer outliers compared to the zonal energy terms ( $A_Z$  and  $K_Z$ ) (Figure 5.1a). They also have smaller mean and median values (Table 5.1). Although both eddy energy terms peak close to each other, the distribution of  $A_E$  is more concentrated around the median (Figure 5.2b), with a narrower interquartile range (IQR) and lower standard deviation, suggesting it is more stable and consistent over time. In contrast,  $K_E$  presents a more right-skewed distribution than  $A_E$  (Figure 5.2d).

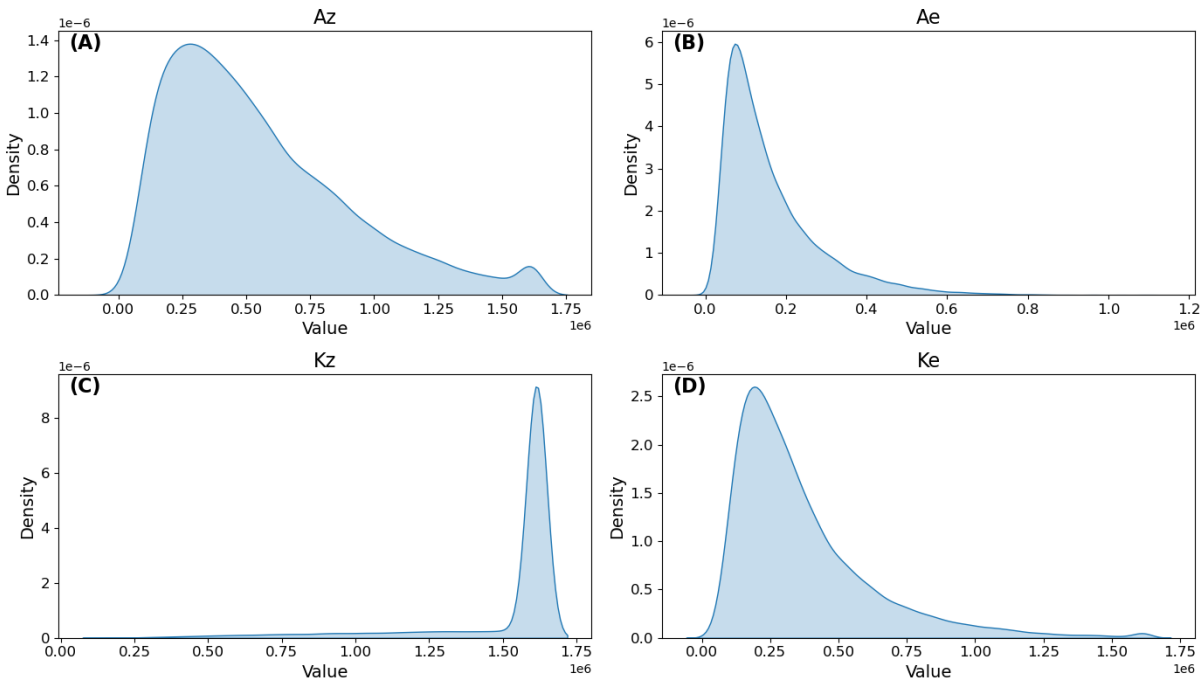


Figure 5.2: Density plots for energy terms  $A_Z$  (A),  $A_E$  (B),  $K_Z$  (C), and  $K_E$  (D). The units are  $\text{J m}^{-2}$ .

While the mean values of  $A_E$  and  $K_E$  are generally in agreement with previous studies, the values of  $K_Z$  and  $A_Z$  differ significantly (Michaelides et al., 1999; Veiga et al., 2008; Dias Pinto and Rocha, 2011; Pezza et al., 2014, e.g.). Li et al. (2007) and Veiga et al. (2013), analyzing global LEC values, found mean  $K_Z$  values for the Southern Hemisphere of approximately  $10$  and  $15.8 \times 10^5 \text{ J m}^{-2}$  and mean  $A_Z$  values of approximately  $40$  and  $16 \times 10^5 \text{ J m}^{-2}$ , respectively. Analyzing the LEC of extratropical cyclones primarily in the Northern Hemisphere, Smith (1980) found mean  $K_Z$  and  $A_Z$  values of  $15$  and  $25 \times$

$10^5 \text{ J m}^{-2}$ , respectively. Meanwhile, Black and Pezza (2013), for explosive cyclogenesis in the Northwest Pacific region, found mean  $A_Z$  and  $K_Z$  values of approximately 30 and  $48 \times 10^5 \text{ J m}^{-2}$ , respectively. Here,  $K_Z$  and  $A_Z$  presented mean values of 28.55 and  $5.55 \times 10^5 \text{ J m}^{-2}$ , respectively.

**Table 5.1** - Summary Statistics of Lorenz Energetics Components: mean, median, standard deviation (std), 20th percentile (Q20), 80th percentile (Q80), interquartile range (IQR), and range. The IQR measures the range within which the central 50% of the values fall, while the range is computed as the difference between the maximum and minimum values. The units for the energy terms ( $A_Z$ ,  $A_E$ ,  $K_Z$ , and  $K_E$ ) are  $10^5 \text{ J m}^{-2}$  and  $\text{W m}^{-2}$  for the remaining terms.

Term	Mean	Median	Std	Q20	Q80	IQR	Range
Az	5.55	4.68	3.71	2.41	8.30	5.89	36.46
Ae	1.62	1.24	1.20	0.69	2.37	1.68	11.07
Kz	28.55	26.19	15.10	15.52	40.16	24.64	114.55
Ke	3.70	2.95	2.62	1.73	5.22	3.49	24.81
Cz	0.52	0.38	4.85	-2.69	3.72	6.41	86.70
Ca	0.93	0.46	1.57	-0.06	1.79	1.84	19.78
Ck	-3.56	-1.63	9.51	-7.41	1.11	8.52	206.43
Ce	3.84	2.47	4.92	0.33	6.97	6.64	54.74
BAz	3.54	2.03	7.67	-1.35	8.23	9.57	175.05
BAe	0.58	0.16	4.40	-1.62	2.75	4.37	75.72
BKz	-7.93	-5.53	31.75	-29.51	12.06	41.57	445.63
BKe	0.47	0.08	8.59	-3.67	4.40	8.07	146.87
BΦZ	63.87	49.25	128.05	-24.60	156.65	181.25	1419.08
BΦE	39.66	31.19	126.50	-46.44	132.10	178.54	1353.99
Gz	-0.31	-0.17	2.66	-1.82	1.14	2.96	68.74
Ge	1.17	0.56	3.14	-0.47	2.79	3.26	58.39
$\frac{\partial A_Z}{\partial t}$	-0.07	-0.14	4.46	-2.66	2.31	4.97	106.39
$\frac{\partial A_E}{\partial t}$	-0.23	-0.10	1.92	-1.14	0.74	1.88	48.19
$\frac{\partial K_Z}{\partial t}$	1.59	0.75	13.38	-7.13	10.40	17.53	251.24
$\frac{\partial K_E}{\partial t}$	0.28	0.12	3.18	-1.53	2.09	3.62	61.50
RGz	-2.17	-1.00	7.60	-6.69	2.31	9.01	220.06
RKz	12.56	8.69	40.49	-13.89	40.08	53.96	561.24
RGe	2.10	1.20	5.15	-0.84	5.28	6.12	97.25
RKe	-7.59	-4.63	10.62	-13.68	-0.45	13.23	138.42

The scarcity of results for a comprehensive set of systems hinders drawing decisive conclusions about the behavior of the  $A_Z$  and  $A_E$  terms in cyclonic occurrences, while

individual cases offer high variability, as indicated by case studies (Brennan and Vincent, 1980; Dias Pinto and Rocha, 2011; Pezza et al., 2014, e.g.,) and the higher variability in the data (Table 5.1). However, several observations can be made: 1) When compared to global energetics, cyclonic systems present higher  $K_Z$  values. This is expected because  $K_Z$  involves a zonal average of the wind components (Equation 2.34), and global averages would yield smaller values than those for limited areas closer to the cyclonic center, often associated with high-level jets; 2) Limited areas provide smaller  $A_Z$  values than hemispheric averages, due to the reduced meridional temperature and static stability gradients (Equation 2.32). These effects are even more evident in the current study, as the computational domain following the system focuses on the environmental dynamics surrounding it, thus capturing overall higher wind speeds through the atmosphere and smaller meridional temperature gradients. A similar effect is noted in Michaelides et al. (1999); 3) Furthermore, the literature shows that the magnitude and sign of the conversion, boundary, generation, and dissipation terms exhibit high variability across different systems and development phases (Brennan and Vincent, 1980; Smith, 1980; Michaelides, 1987; Bulic, 2006; Dias Pinto and Rocha, 2011; Black and Pezza, 2013, e.g.,), complicating comparisons of the overall values presented here with individual cases.

For the conversion terms, while  $C_Z$ ,  $C_A$ , and  $C_E$  are positive on average and in median values,  $C_K$  is negative (Table 5.1). For  $C_A$  and  $C_E$ , there is a relatively narrow spread around the median, with some significant outliers (Figure 5.1b).  $C_A$ , showing a distribution centered around zero with both negative and positive values (Figure 5.3b), indicates alternating periods of energy transfer in both directions, predominantly from  $A_Z$  to  $A_E$ . Meanwhile,  $C_E$  has a left-skewed distribution (Figure 5.3d) and higher Q20 and IQR values, suggesting a more consistent positive net conversion.

The  $C_K$  term exhibits a wide distribution peaking at negative values (Figure 5.3c), with a significant negative mean and median, indicating a dominant net conversion from  $K_Z$  to  $K_E$ . The large range and standard deviation, along with the presence of significant outliers, suggest substantial variability in this conversion process. Lastly,  $C_Z$  presents the most distinctive behavior, with values centered around zero but peaking at both positive and negative values (Figure 5.3a). However, the higher peak at positive values along with the positive mean and median values indicate a preference for conversion from  $A_Z$  to  $K_Z$ .

The overall values presented here indicate that, throughout the systems' complete li-

fecycle,  $K_E$  tends to receive energy from  $A_E$  and, in most cases, from  $K_Z$  as well, although there are instances where  $C_K$  tends to be positive. There is also a general tendency for  $A_Z$  to be converted to  $A_E$ , albeit with a lower magnitude. Meanwhile, although  $C_Z$  can be positive, negative, or neutral, the predominant tendency is for conversion from  $A_Z$  to  $K_Z$ .

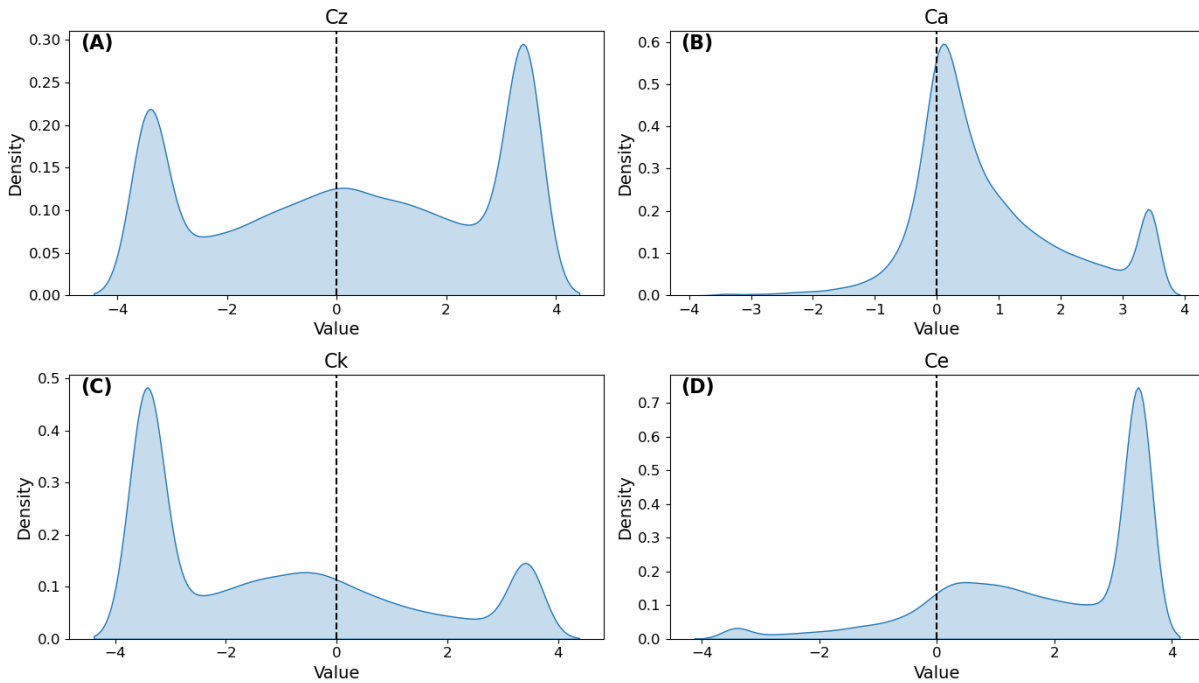


Figure 5.3: Density plots for conversion terms  $C_Z$  (A),  $C_A$  (B),  $C_K$  (C), and  $C_E$  (D). The units are  $Wm^{-2}$ .

There is a notable difference between the boundary flux terms ( $BA_Z$ ,  $BA_E$ ,  $BK_Z$ ,  $BK_E$ ) and the boundary pressure work terms ( $B\Phi_Z$  and  $B\Phi_E$ ) (Table 5.1). For the boundary flux terms,  $BA_Z$  presents the highest mean and median values, while  $BK_Z$  has the lowest.  $BA_E$  and  $BK_E$  have mean and median values closer to zero. The  $BA_Z$  term exhibits moderate variability, with a wide distribution around the median (Figure 5.4a) and few outliers (Figure 5.1c), a similar pattern to  $BK_E$  (Figure 5.4d).  $BA_E$ , in turn, displays the lowest variability among the boundary terms, with most values peaking near zero (Figure 5.4b). Meanwhile,  $BK_Z$  presents the most distinctive behavior, exhibiting high variability, with a wide distribution (Figure 5.4c) and numerous outliers. Its values range from the most negative to the most positive among the boundary terms, indicating an overall tendency for the exportation of zonal kinetic energy, supported by its negative mean and median values.

On the other hand, the boundary pressure work terms present similar behavior, with

very high mean and median values, especially  $B\Phi Z$ , and displaying two peaks: one on negative values (with a higher peak for the  $B\Phi E$  term) and another, which displays higher densities, on positive values (Figure 5.4e and 5.4f). Both terms present low Q20 and high Q80 values, indicating that although they generally contribute to the appearance of energy in the  $K_Z$  and  $K_E$  terms, there are instances where they contribute negatively. For all metrics presented, they exhibit the highest values in magnitude across all terms. As Brennan and Vincent (1980) argued, these high values are associated with minor errors in the geopotential height field that can escalate. Although ERA5 presents the most modern reanalysis product offering homogeneous high-resolution data, systematic errors might be present, especially in regions with low data coverage, such as over the oceans and high altitudes (Hersbach et al., 2020). As most studies do not compute these terms as residuals and thus do not present the values (for instance, none of the studies presented in Section 2.4.3 do so), direct comparison of the values obtained here with the literature is hindered.

Although the energy budgets are computed using residuals (which include the boundary pressure work terms), the generation terms are also analyzed as they serve both as an overall evaluation of the generation residual terms and because, in future sections, they will be used for understanding the systems' dynamics. Both  $G_Z$  and  $G_E$  present a similar distribution, displaying low variability (Figure 5.4), with most values peaking near zero and with minor peaks on both positive and negative values (Figures 5.5a and 5.5b). However,  $G_E$  presents a higher density of positive values, which is reflected in its higher mean and median values than  $G_Z$  and higher Q80 values (Table 5.1).

For the generation residual terms, both present three peaks - at positive, neutral, and negative values - but while  $RG_Z$  has the highest density around negative values,  $RG_E$  peaks at positive values (Figures 5.5c and 5.5e). This results in  $RG_E$  presenting positive mean and median values, despite a minor peak at negative values - which reflects in a negative Q20 value - indicating that its contribution to  $\frac{\partial A_E}{\partial t}$  is mainly positive, with situations where this term contributes negatively. For  $RG_Z$ , the opposite is noted, with negative mean and median values, but a minor peak at positive values - reflected in a positive Q80 - indicating it mainly contributes negatively to  $\frac{\partial A_Z}{\partial t}$ , with situations where this term contributes positively.

Furthermore, while  $RK_Z$  presents higher positive mean and median values, it also shows high variability and numerous outliers (Figure 5.1d). It presents a distinctive density

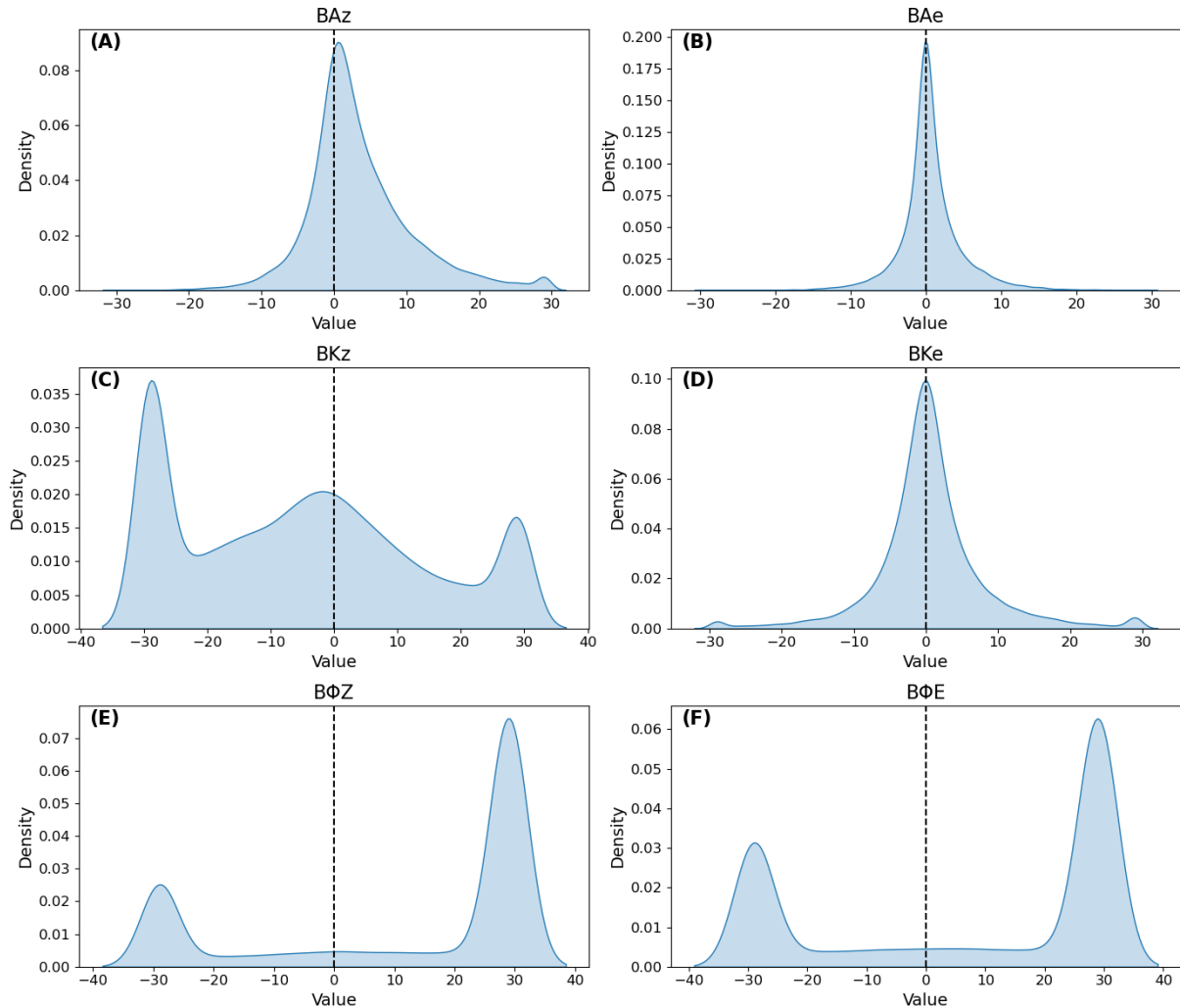


Figure 5.4: Density plots for boundary terms  $BA_Z$  (A),  $BA_E$  (B),  $BK_Z$  (C),  $BK_E$  (D),  $B\Phi_Z$  (E), and  $B\Phi_E$  (F). The units are  $Wm^{-2}$ .

distribution, with two marked peaks, one for positive and the other for negative values (Figure 5.5d). This is reflected in its negative Q20 and positive Q80 values, with a high IQR. Therefore, although it mostly contributes positively to  $\frac{\partial K_Z}{\partial t}$ , there are also significant instances where it contributes negatively.  $RK_E$ , on the other hand, presents mean and median values peaking at negative values (Figure 5.5f). Therefore, it mostly contributes negatively to  $\frac{\partial K_E}{\partial t}$ , acting as a sink for  $K_E$ .

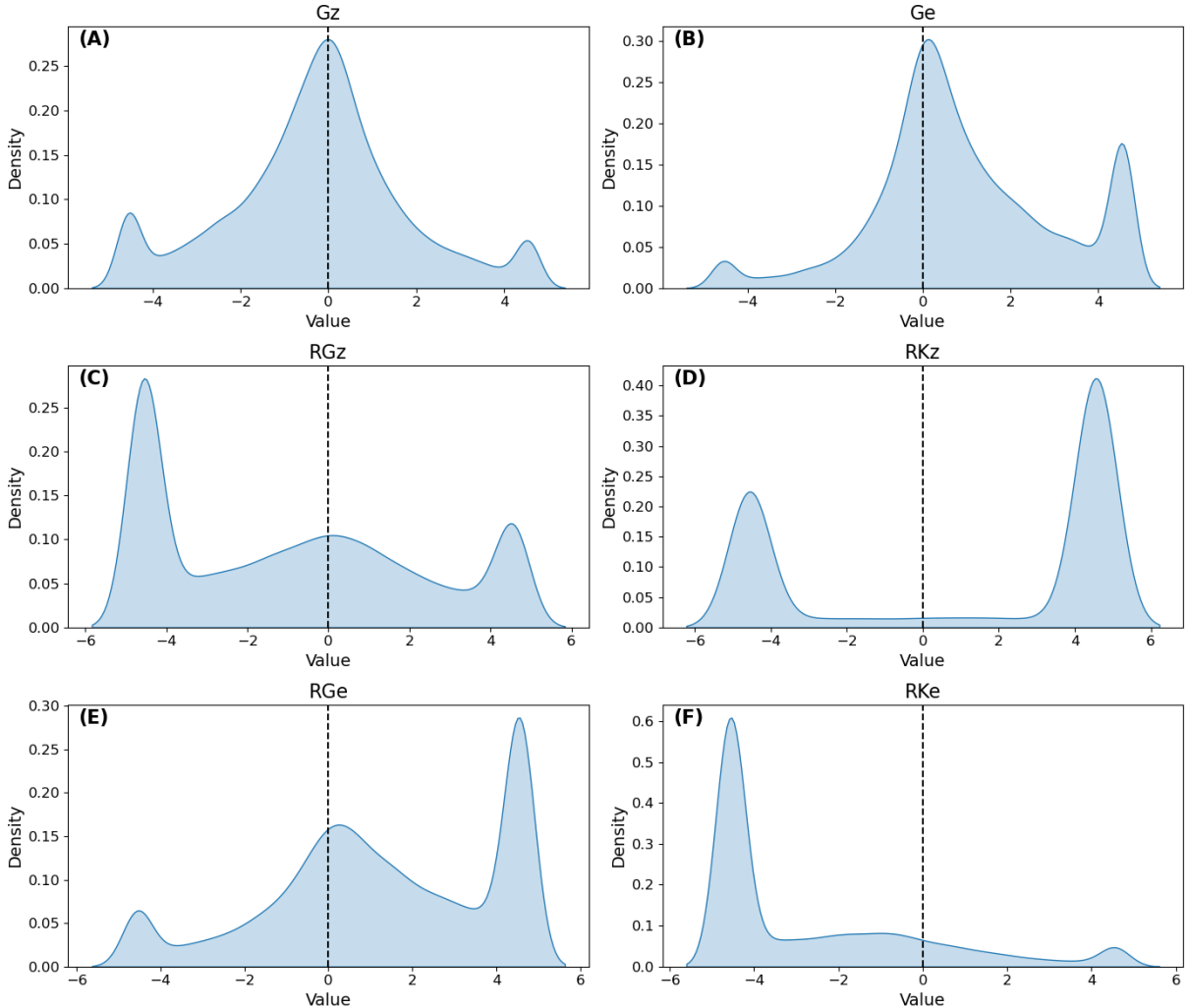


Figure 5.5: Density plots for generation terms  $G_Z$  (A) and  $G_E$  (B); and residual terms  $RG_Z$  (C),  $RK_Z$  (D),  $RG_E$  (E), and  $RK_E$  (F). The units are  $Wm^{-2}$ .

Among the budget terms, APE terms ( $\frac{\partial A_Z}{\partial t}$  and  $\frac{\partial A_E}{\partial t}$ ) present negative mean and median values, while the kinetic energy terms ( $\frac{\partial K_Z}{\partial t}$  and  $\frac{\partial K_E}{\partial t}$ ) are positive, although all of them exhibit negative Q20 values and positive Q80 values, indicating variability among the analyzed systems (Table 5.1).  $\frac{\partial A_E}{\partial t}$  has the lowest variability, with the smallest IQR and range values, fewest outliers (Figure 5.1), and the highest peak density centered around

zero (Figure 5.6b). This indicates that while in most cases there is an overall tendency for  $A_E$  to be neutral, there are also occurrences of positive and negative increments.

In contrast,  $\frac{\partial A_Z}{\partial t}$  and  $\frac{\partial K_E}{\partial t}$  display similar density distributions (Figure 5.6a and 5.6d), with peaks at negative, neutral, and positive values.  $\frac{\partial A_Z}{\partial t}$  has a higher peak at negative values, indicating a tendency for  $A_Z$  to decrease, while  $\frac{\partial K_E}{\partial t}$  peaks at positive values, reflecting a tendency for  $K_E$  to increase. However, both terms also show instances of neutrality and opposite trends. Lastly,  $\frac{\partial K_Z}{\partial t}$  exhibits a unique behavior with two prominent peaks at opposite extremes (Figure 5.6c). This term has the lowest Q20 and the highest Q80, IQR, and range values, indicating that  $K_Z$  tends to exhibit extreme changes — either significant increases or decreases — with a smaller tendency to remain neutral.

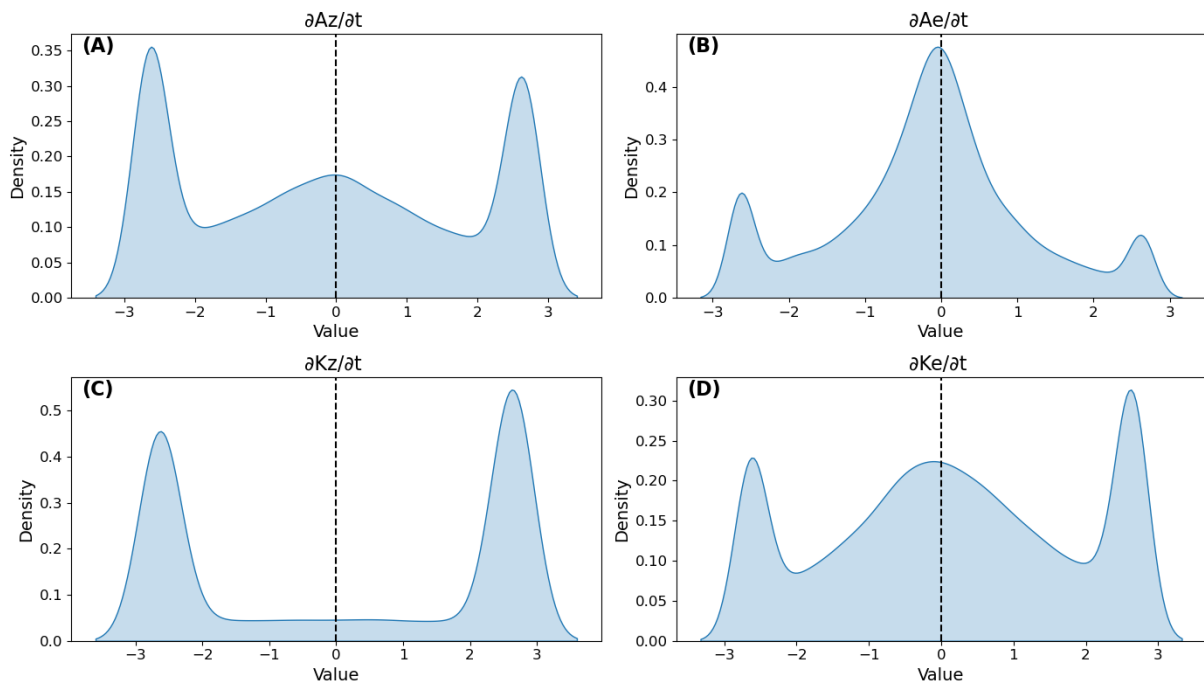


Figure 5.6: Density plots for budget terms  $\frac{\partial A_Z}{\partial t}$  (A) and  $\frac{\partial A_E}{\partial t}$  (B);  $\frac{\partial K_Z}{\partial t}$  (C), and  $\frac{\partial K_E}{\partial t}$  (D). The units are  $Wm^{-2}$ .

### 5.1.2 Mean Energy Cycle

Figure 5.7 illustrates the LEC for the mean values of each term. Although, due to the high variability presented for the distinct terms, as shown previously, such result should be looked upon with care, it can provide an overview of the mean energy fluxes on the analyzed systems. Additionally,  $G_Z$  and  $G_E$  terms are used for a more physically based interpretation, although the budgets were computed using their respective residuals. Since

the residual terms integrated these components, the presented budgets may not perfectly balance positive and negative energy fluxes due to the finite differences method used, which also incorporates numerical errors.

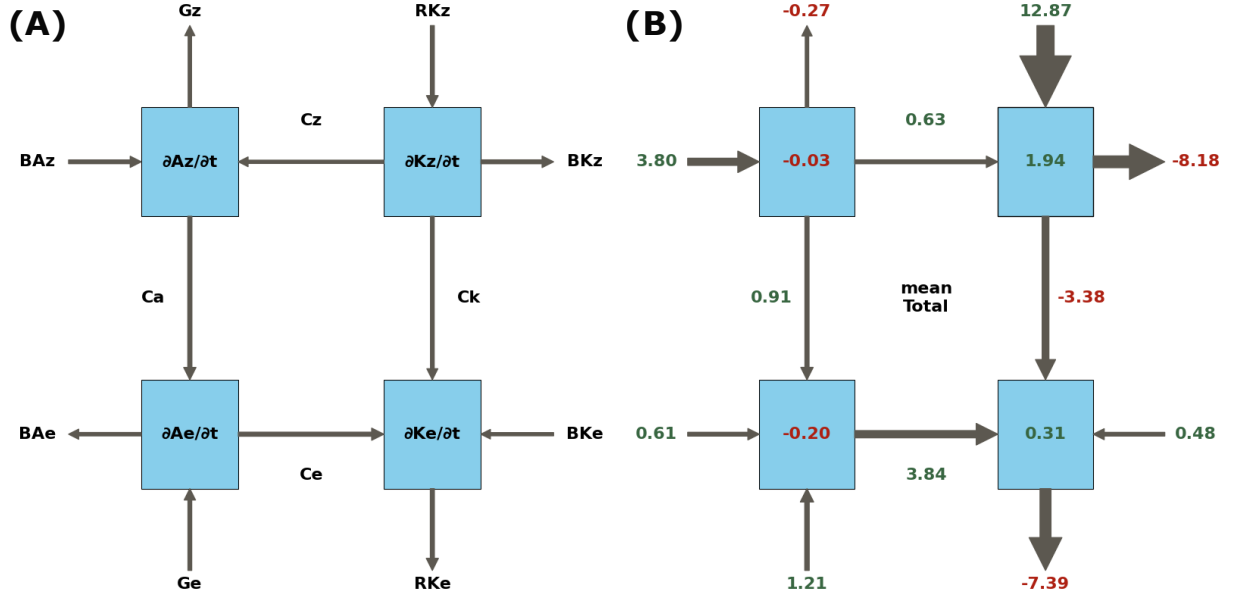


Figure 5.7: Representation of the LEC, with arrows denoting positive energy conversions (A) and mean values of the Lorenz Energy Cycle (LEC) terms (B). Each blue box represents an energy component, with arrows showing the direction of energy flow. The numbers adjacent to the arrows indicate the magnitude and direction of the energy flux, with green indicating positive values and red indicating negative values.

The mean values indicate an overall tendency for both APE terms to decrease over time. The decreases in  $A_Z$  are primarily due to conversions to  $A_E$  ( $C_A > 0$ , Figure 2.24), which is an expected result. As discussed in Section 3.2.2, most cyclones in the dataset are extratropical, which have the final cause of diminishing Equator-Pole temperature gradients (Section 2.1.4), i.e., reducing  $A_Z$ . Additionally, there are overall losses of  $A_Z$  due to the  $G_Z$  term, indicating either anomalous heating in cool regions or anomalous cooling in warm regions caused by the eddy's meridional heat transport. Imports of  $A_Z$  are also observed through the  $B_{Az}$  term. For the  $A_E$  term, there are decreases over time. Despite influxes from  $C_A$ , diabatic processes ( $G_E > 0$ ) and imports of energy ( $B_{Ae} > 0$ ), most of its energy is converted to  $K_E$  ( $C_E > 0$ ) due to enhanced zonal temperature gradients.

The mean values indicate both forms of kinetic energy increasing over time. The increase in  $K_Z$  - which is the greatest among the budget terms - primarily stems from influxes from the residual term ( $R_{KZ} > 0$ ). Although the inclusion of numerical errors hinders the interpretation of the residual term, Section 5.1 indicates that  $B\Phi_Z$  often presents large va-

lues, suggesting that this energy influx might be related to the generation of kinetic energy - by the zonal jets - towards the cyclone's central low pressure. Meanwhile, a great part of  $K_Z$  energy is exported outside the domain ( $BK_Z < 0$ ), while a minor part is converted to  $K_E$  through the barotropic conversion term ( $C_K < 0$ ). Only negligible amounts are converted from  $A_Z$ . Finally,  $K_E$  displays increases over time, driven mostly by conversion from  $A_E$ , but also with significant contributions from  $C_K$ . Notably,  $RK_E$  presents high magnitudes, possibly indicating the dissipation of this energy. The importation of  $K_E$  is almost negligible.

In summary, for the mechanisms related to eddy growth, it can be seen that the mean environment energetics related to the cyclones in the SESA region indicate that both the baroclinic and barotropic chains are active. This indicates that the eddies gain energy from both meridional temperature gradients as well as from horizontal wind shear. Moreover, diabatic processes contribute to increasing the eddy APE, thus supporting the moist baroclinic chain. Finally, the main sink for eddy energy is the residual term, possibly associated with dissipation by frictional forces.

### 5.1.3 EOFs

The results presented in Section 5.1.1 demonstrate that the LEC terms exhibit high variability. Even a view of the LEC for the mean values can be problematic, as each term spans a wide range of possible values, often with varying signs. Therefore, delineating an overall picture of the LEC for the analyzed systems is not a trivial task. To help address this issue, an empirical orthogonal function (EOF) analysis is used. It is important to note that the values represent anomalies rather than the actual magnitudes of the energy cycle components.

Figure 5.8 illustrates the proportion of variance in the dataset that is explained by each of the first eight Empirical Orthogonal Functions (EOFs). The first EOF accounts for the largest share of the variance, explaining 28.3%, indicating it captures the most significant pattern in the data. The second and third EOFs both explain around 11% of the variance, showing that they also represent notable patterns but with less influence compared to the first EOF. The subsequent EOFs explain progressively smaller proportions of the variance: 8.2% for the fourth, 7.4% for the fifth, 5.9% for the sixth, 5.2% for the seventh, and 4.4% for the eighth. Together, these eight EOFs capture the primary modes of variability within

the dataset. Usually, the principal components (PCs, not shown) represent the temporal evolution of the signal magnitude of each EOF. However, in this context, they would merely represent the signal magnitude across the distinct cyclones and therefore do not represent any physical feature.

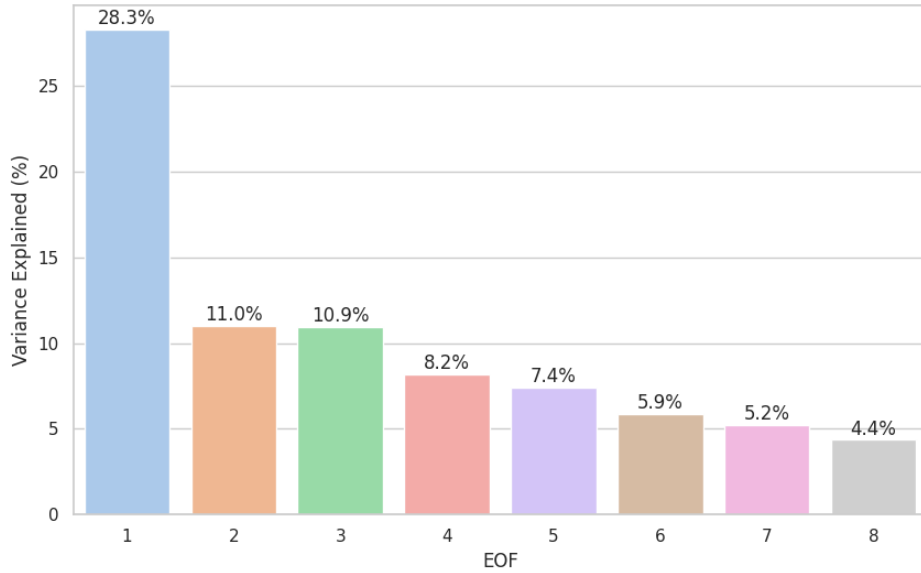


Figure 5.8: Proportion of variance in the dataset explained by the first eight Empirical Orthogonal Functions (EOFs).

For the EOF1 (Figure 5.9), most terms are in general agreement with the signal for mean values presented in Figure 5.7, indicating an enhancement of the average behavior. The exceptions to this are the  $C_Z$ ,  $BA_E$  and  $A_E$  budget terms; however, the anomaly signal magnitude is lower than what is found in the mean values, indicating that for the first variability mode, there is no reversal in the sign of the observed values. In general, this result confirms the observation that the overall behavior of the environmental energetics related to the cyclones in the SESA region is associated with the moist baroclinic chain, acting together with barotropic conversions.

For the EOF2, although many terms present anomalies with a reversed sign compared to the mean values, the magnitude of most of them is not high enough to signal a reversal in the energy flux direction or represent significant changes in the overall behavior. However, some significant changes can be noted in certain terms. For instance, the terms  $\frac{\partial A_Z}{\partial t}$  and  $\frac{\partial K_E}{\partial t}$  present an enhancement of the mean behavior. For  $\frac{\partial A_Z}{\partial t}$ , this is mostly linked to the further diminishing of  $G_Z$  in the EOF2, while for  $\frac{\partial K_E}{\partial t}$ , this is primarily associated with

enhanced imports from  $BK_E$ , with minor contributions from the enhanced moist baroclinic chain. Although the signal is weak, EOF2 also presents a small weakening of the barotropic conversions.

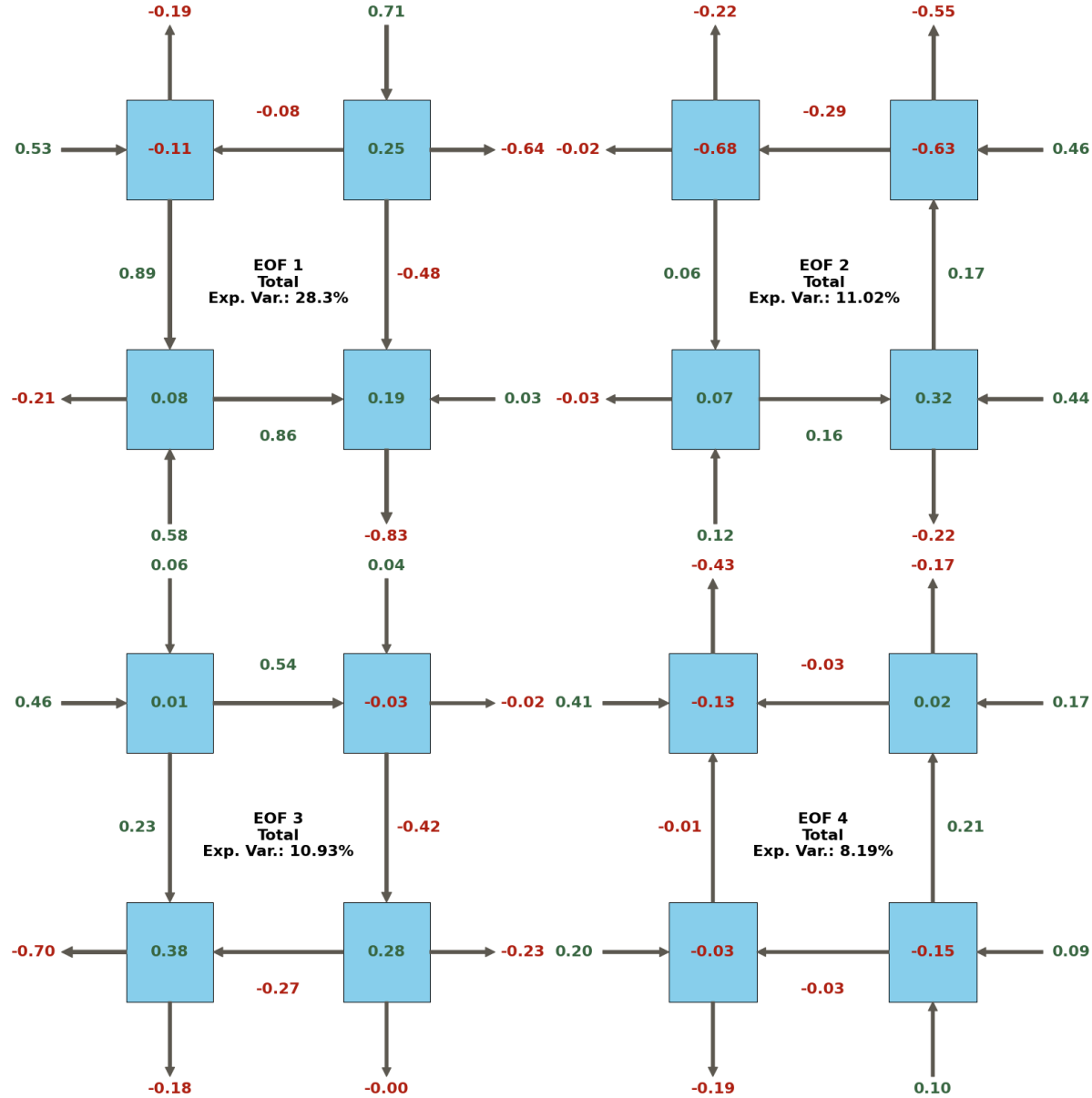


Figure 5.9: EOF Analysis of Lorenz Energy Cycle (LEC) Terms, illustrating the anomalies in energy fluxes: EOF1 (A), EOF2 (B), EOF3 (C) and EOF4 (D). The numbers adjacent to the arrows denote the magnitude and direction of the anomaly, with green indicating positive values and red indicating negative values.

For the EOF3, it is evident that the signal for  $\frac{\partial A_E}{\partial t}$  has a higher magnitude and opposite sign compared to the mean value. The positive budget for  $A_E$  is mostly associated with enhanced conversion from  $A_Z$  and a reduction in the conversions to  $K_E$ , although there are strong reductions in the  $BA_E$ , which indicate a reversal in this term's sign. For  $\frac{\partial K_E}{\partial t}$ , there

is also a significant signal for the enhancement of the positive budget, primarily associated with the enhancement of the barotropic conversion by the  $C_K$  term.

In general, while the EOF2 presents an enhancement of the moist baroclinic chain, with a diminishment of barotropic conversions, the EOF3 presents the opposite behavior. The EOF4, in turn, presents a reversal in sign for most terms compared to the mean values. However, for most of them, the signal is not high enough to represent a significant reversal of the mean values. The most notable distinction is in the  $G_Z$  term, which becomes even more negative.

The following EOFs continue to exhibit such small signals, presenting only minor deviations from the mean behavior of the LEC. Therefore, they will not be further discussed. The EOF analysis presented here demonstrates that, although there is high variability in the dataset, with individual cases presenting overall energetics deviating from the mean values, the mean energetics or the mean state of the cyclones is much stronger than the fluctuations or variations captured by the EOFs (Appendix C contains the reconstructed EOFs). This might be intrinsically linked to the EOFs being calculated for the entire life cycle of the systems, with distinct dynamical processes acting at different development stages. Next sections will explore to what extent the results presented can be applied to each development phase or if the distinct phases will reveal further details about the energetics of the cyclones in SESA region.

## 5.2 Climatology Across Life Phases

### 5.2.1 Descriptive Statistics

Although Sections 5.1.1 and 5.1.3 provide an overview of the systems' energetics, their results apply to the complete life cycle. As distinct dynamical processes might act at different development stages, it is expected that different phases of the cyclone's life cycle will present different overall energy cycles. Here, the cyclones' lifecycle was dissected using the Cyclophaser program to investigate the LEC for each phase individually, aiming to understand which processes dominate in each of them.

The first step was to assess whether the different development phases exhibit statistically significant differences among themselves. Table 5.2 presents the p-values for the normality, homogeneity, and significance tests employed. Normality was assessed using

the Shapiro-Wilk test, and homogeneity was assessed using Levene's test. For all terms, the p-values were well below the 0.05 threshold, indicating that the data significantly deviate from normality and that their variances differ significantly across the phases. Therefore, to determine statistically significant differences between the phases, we employed the non-parametric Kruskal-Wallis (KW) test. The results indicated that the differences in the LEC terms among the phases are statistically significant. While post-hoc Dunn's tests could be conducted to identify which specific phases differ if the Kruskal-Wallis test is significant, this would involve a combinatorial analysis of pairs among seven phases for all 17 terms in the LEC. Such an analysis would be impractical. Consequently, the statistically significant results from the KW test were deemed sufficient for proceeding with the analysis.

The next step is to investigate the overall behavior of each term across distinct development phases through their density distributions. Beyond energy terms, the focus will be on the overall energy flux direction, providing a proxy for understanding the dynamical forcing related to the development of cyclonic systems throughout their life cycle. Finally, a summary of the main findings along with interpretations drawn from the results is presented at the end of this section.

Figure 5.10 displays the density plots for the energy terms for each development phase. It can be observed that the overall shapes of the distributions within the same term are similar, mirroring the distribution for the complete life cycle (Section 5.1.1), with minor differences across each specific phase. For  $A_Z$  (Figure 5.10a), every phase presents maximum densities centered between 2 and  $3 \times 10^5 Jm^{-2}$ , but displays right-skewed distributions, indicating high variability and the occasional occurrence of extremely high values. Mature phases (1 and 2) exhibit sharper peaks, while intensification (1 and 2) and incipient phases present broader peaks. An overall trend, indicated by both mean and median values, shows  $A_Z$  decreasing from the incipient to the mature phase and increasing again through the decay phase. The same trend is observed during secondary development: it decreases from intensification 2 to mature 2 and then increases again at decay 2. Notably, despite this increase during the decay phase, the mean and median values are lower than the initial values, and even lower during the secondary development. This overall trend displayed by  $A_Z$  throughout the cyclone's life cycle aligns with the discussion at the end of Section 5.1.1 and in Section 2.1.4: extratropical cyclones aim to balance global temperature, diminishing

*Table 5.2 - Statistical Analysis Results for Different Phases.* The table shows the p-values for the Kruskal-Wallis (KW) test, the Shapiro-Wilk normality test, and Levene's test for homogeneity of variances. The Kruskal-Wallis test is used here due to non-normality or heterogeneity of variances in the data, indicating significant differences among phases if the p-value is less than 0.05.

Term	KW p-value	Normality p-value	Homogeneity p-value
Az	5.16e-273	2.86e-50	5.54e-67
Ae	6.51e-283	1.24e-57	3.49e-111
Kz	2.30e-22	3.08e-36	1.80e-46
Ke	0.00e+00	3.05e-55	6.78e-269
Cz	1.01e-48	1.79e-34	1.14e-134
Ca	7.46e-192	5.32e-57	5.71e-85
Ck	1.64e-92	5.90e-62	0.00e+00
Ce	0.00e+00	6.43e-52	1.84e-189
BAz	6.58e-79	1.14e-54	8.02e-39
BAe	1.66e-282	1.92e-51	5.02e-137
BKz	7.56e-05	1.71e-38	2.54e-54
BKe	2.03e-118	6.67e-60	1.92e-76
BΦZ	2.30e-45	4.71e-28	5.33e-105
BΦE	6.89e-39	2.31e-27	3.23e-94
Gz	1.50e-48	9.91e-50	0.00e+00
Ge	0.00e+00	2.70e-58	6.95e-256
RGz	7.43e-164	5.41e-54	1.09e-148
RKz	5.09e-06	1.22e-35	2.78e-69
RGe	1.27e-179	4.83e-47	1.77e-122
RKe	1.84e-267	9.33e-54	7.03e-205
$\frac{\partial A_Z}{\partial t}$	2.58e-221	2.52e-50	0.00e+00
$\frac{\partial A_E}{\partial t}$	3.85e-212	1.51e-53	0.00e+00
$\frac{\partial K_Z}{\partial t}$	1.33e-108	3.36e-44	3.67e-194
$\frac{\partial K_E}{\partial t}$	0.00e+00	2.65e-55	0.00e+00

temperature gradients (i.e.,  $A_Z$ ).

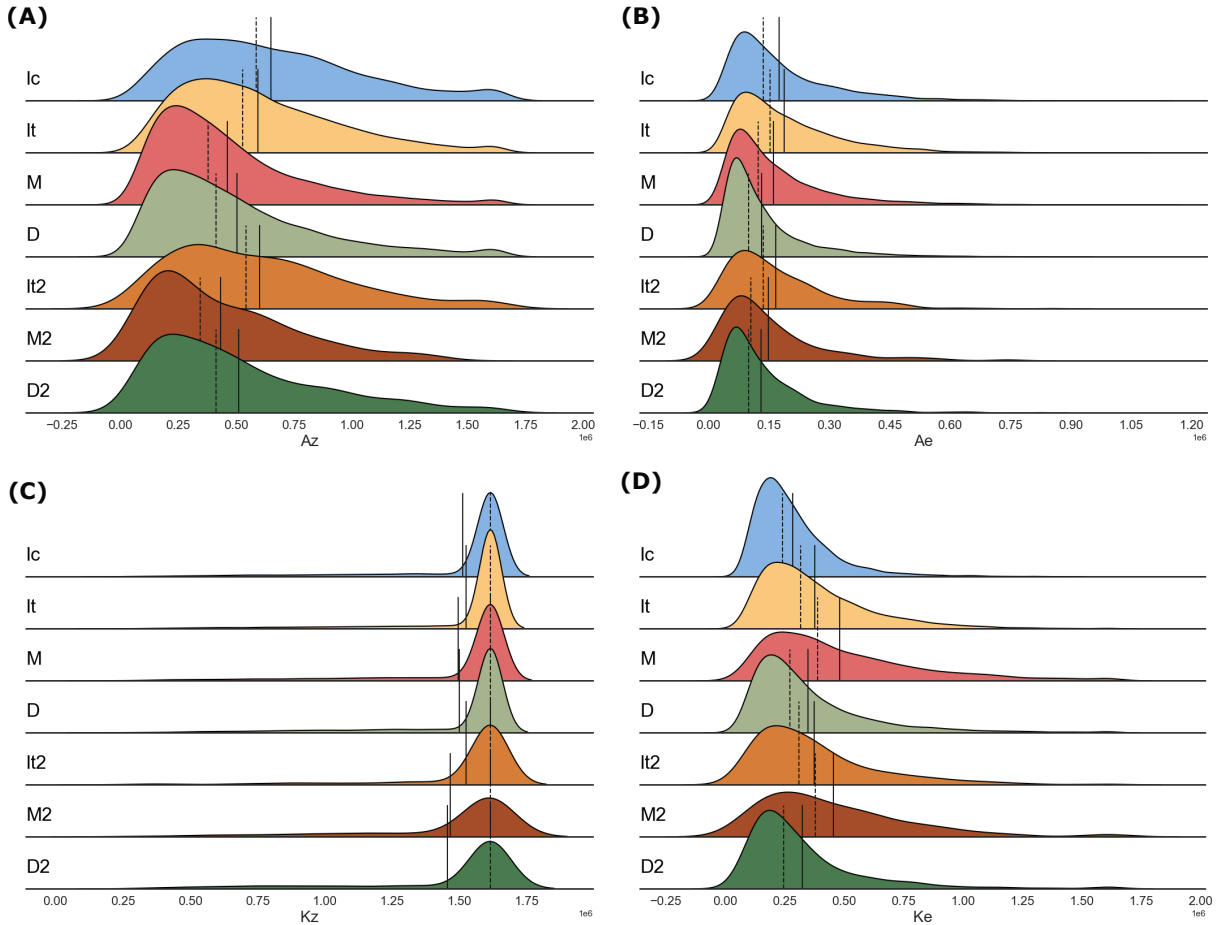


Figure 5.10: Density plots for energy terms  $A_Z$  (A),  $A_E$  (B),  $K_Z$  (C), and  $K_E$  (D), for each development phase: incipient (Ic), intensification (It), mature (M), decay (D) and the secondary development phases (indicated by "2"). The solid vertical lines indicate the mean values for a given phase while the dashed lines, the median values. The units are  $Wm^{-2}$ .

For  $A_E$  (Figure 5.10b), the densities are less skewed, with sharper peaks compared to  $A_Z$ , indicating lower variability and fewer extreme values. Most values peak between 0.5 and  $1.15 \times 10^5 Jm^{-2}$ , and the mean and median values show an overall increase from the incipient to the intensification phase, where  $A_E$  reaches its highest values, followed by a consistent decrease until the decay phase.  $A_E$  increases again during the second intensification phase and then decreases from the second mature phase to the decay phases. This pattern suggests that after genesis, the eddies initiate the conversion from meridional to zonal temperature gradients, which peak during intensification and diminish afterward. The lower mean and median values at the decay phases compared to the beginning of each life cycle indicate that the eddies not only diminish the zonal temperature gradients but also

reduce them to levels lower than their initial states.

The  $K_Z$  term densities present narrow peaks with long tails towards low values, mirroring the distribution for the total phase (Figure 5.10c). For all phases, the distributions peak at nearly  $16 \text{ } 15^5 Jm^{-2}$ , with sharper peaks for the initial development phases and broader peaks for the secondary development phases. Unlike the other terms, the median values remain constant across all phases, while only the mean values vary. The mean values are higher during the intensification phases (1 and 2) and lower during the remaining phases of the same life cycle.

The densities for  $K_E$  are similar to those for  $A_E$ , with left-skewed distributions peaking at approximately  $2 \text{ } 15^5 Jm^{-2}$  (Figure 5.10d). However, the densities for the mature phases (1 and 2) present broader peaks. The mean and median values for this term follow the overall trend for the relative vorticity series (Chapter 4), showing behavior opposite to that of  $A_Z$ : it increases from the incipient to the mature phase, decreases at the decay stage, increases again during the second intensification and mature phases, and finally decreases during the second decay phase. As expected, this term serves as a proxy for the overall intensity of the cyclonic systems, starting with lower energy states and gaining energy up to their maturity, then losing energy as they decay.

Figure 5.11 displays the density plots for the conversion terms for each development phase. All terms present density shapes with multiple peaks:  $C_A$  and  $C_E$  for neutral and positive values, while  $C_Z$  and  $C_K$  also present peaks for negative values. This behavior indicates significant variability within the terms and suggests that the energy can flow in both directions (positive and negative peaks) or that energy fluxes can be active or inactive (neutral peaks).

The  $C_Z$  term exhibits high variability in its density distribution across the different development phases (Figure 5.11a). During the incipient phase, there are two distinct peaks: one at negative values and a sharper peak at positive values, with a broad distribution in between, resulting in positive mean and median values. In contrast, the intensification and mature phases display symmetric peaks at both ends of the spectrum, with a broader peak at neutral values. For the decay phase, the peak at negative values diminishes, while the peaks at neutral and positive values become sharper, pushing the mean and median to positive values. The second intensification phase, despite having peaks at neutral, positive, and negative values, shows a wide distribution in the positive range, reflected in its positive

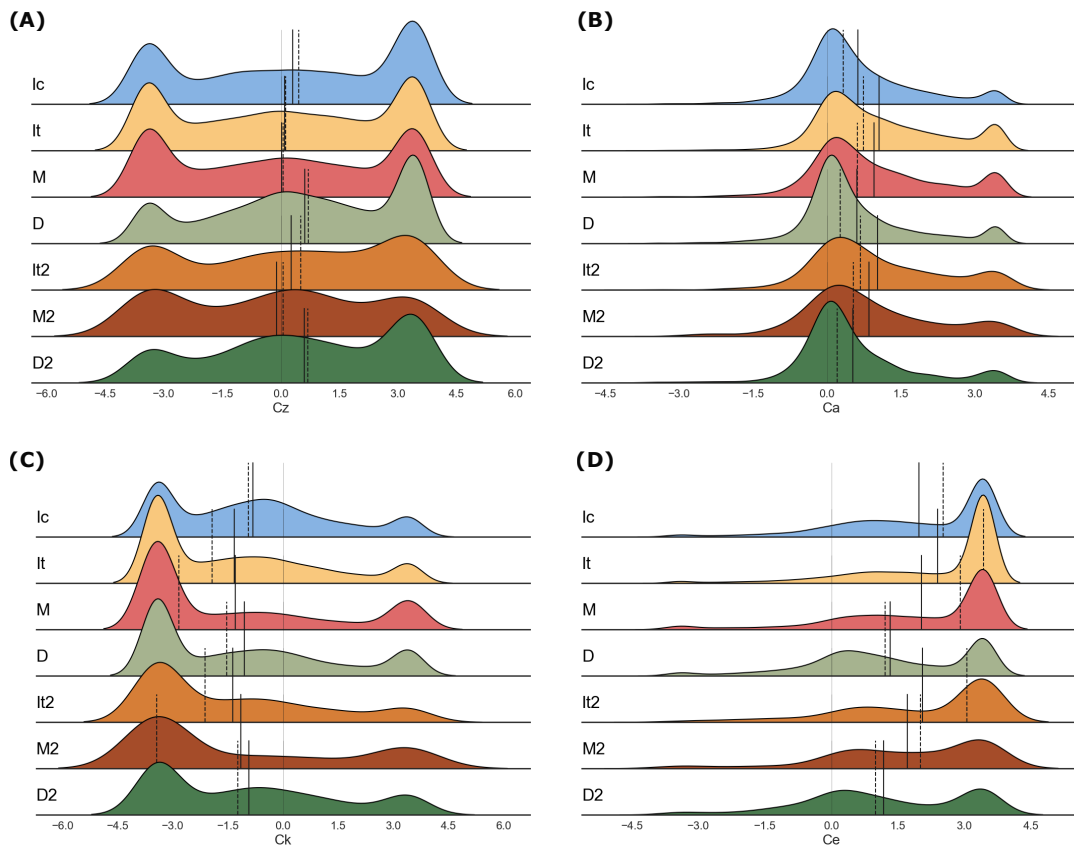


*Figure 5.11:* Density plots for conversion terms  $C_Z$  (A),  $C_A$  (B),  $C_K$  (C), and  $C_R$  (D), for each development phase: incipient (Ic), intensification (It), mature (M), decay (D) and the secondary development phases (indicated by "2"). The solid vertical lines indicate the mean values for a given phase while the dashed lines, the median values. The units are  $Wm^{-2}$ .

mean and median values. Lastly, the second mature and decay phases present opposite shapes: the former has a sharper peak at negative values, while the latter has a sharper peak at positive values. For the second mature phase, the mean and median values are on opposite sides of the spectrum. Therefore, while the initial and final phases of each development cycle tend to have overall positive values and the intermediate phases tend toward neutrality, the high variability makes it difficult to define a definitive behavior for the  $C_Z$  term. This high variability (across systems and phases) is also noted in previous studies (Michaelides, 1987; Veiga et al., 2008; Dias Pinto and Rocha, 2011; Dias Pinto et al., 2013, e.g.).

For the  $C_A$  term, each phase presents a peak near neutral values, right-skewed with a long tail distribution extending towards positive values (Figure 5.11b). There are also minor peaks near  $3Ws^{-2}$ , which are sharper for the phases of the first development cycle. Furthermore, the distributions become more right-skewed in the intensification phases (1 and 2) and less skewed in the later phases. Consequently, the mean and median values increase from the beginning of each development cycle, peak during each intensification phase, and then decrease afterward. This indicates an overall tendency for energy to be converted from  $A_Z$  to  $A_E$  during the development cycle, which aligns with the overall trend observed for the  $A_E$  term (Figure 5.10b).

The  $C_K$  term, across all phases, presents a peak at negative values, right-skewed towards positive values with a minor peak at positive values (Figure 5.11c). During the first development cycle, the incipient stage shows a sharp peak near  $-3.5Ws^{-2}$  and a minor peak near  $-1Ws^{-2}$ . As the systems intensify, the minor peak becomes broader and the sharp peak becomes more pronounced. Meanwhile, the peak at positive values, near  $3.5Ws^{-2}$ , also becomes sharper. Consequently, the median values become significantly more negative from the incipient to the mature phase and less negative during the decay phase. Although the mean values follow a similar pattern, the sharper peak at positive values during the mature phase results in mean values for the mature phase that are similar to — or even less negative than — those of the intensification phase. The secondary development cycle shows a similar behavior to the first one. These results indicate an overall tendency for conversion from  $K_Z$  to  $K_E$  throughout the cyclone's life cycle, but with a significant number of systems where the energy flows in the opposite direction. The tendency for  $C_K$  to be negative and most intense during mature phases is consistent with the overall behavior of

the  $K_E$  term. However, this analysis does not clarify whether there are instances where the energy flow reverses direction during the life cycle. This will be investigated in the next sections, as previous studies have suggested that such reversals might occur, especially in systems transitioning from one type to another (Brennan and Vincent, 1980; Michaelides, 1987; Wahab et al., 2002; Veiga et al., 2008; Pezza et al., 2010, e.g.,).

The density distributions for all phases of the  $C_E$  term present peaks at positive values, near  $3.5 W s^{-2}$ , with left-skewed distributions and long tails extending into negative values, albeit with low densities (Figure 5.11d). The peaks tend to become sharper during the intensification phases and decrease afterward. Additionally, for the decay phases (1 and 2), a broad peak near neutral values emerges. As a result, the mean and median values are higher during the intensification phases and closer to zero during the decay phases (1 and 2). Since the peaks in conversion from  $A_E$  to  $K_E$  coincide with the phases where  $A_E$  is on average highest, it can be inferred that a significant amount of the energy content in this term is being converted to  $K_E$ .

The density plots for the boundary terms are displayed in Figure 5.12. The  $BA_Z$  term presents a right-skewed distribution peaking at values close to zero (Figure 5.12a). There are also long tail distributions towards high positive values, indicating the occurrence of unusually extreme values. This behavior is reflected in the overall positive mean and median values. Across the phases, there is a tendency for the imports of  $A_Z$  to decrease from the intensification to mature phases (1 and 2), increasing again for the decay phases (1 and 2). This behavior is consistent with the values for the  $A_Z$  term (Figure 5.10).

The  $BA_E$  and  $BK_E$  terms present similar distributions, with sharp peaks near zero and long tails extending towards both negative and, especially, positive values (Figures 5.12b and 5.12d). Consequently, the mean and median values are often positive. Despite the similarities in the density distributions, the overall behavior across the distinct phases among these terms differs. For  $BA_E$ , there is a tendency for the mean and median values to decrease from the beginning of each development cycle to the mature phase, becoming negative in the latter and increasing again during decay, but with mean and median values near zero. This behavior indicates imports of  $A_E$  in the systems' early life stages but exports as they mature. Meanwhile, for  $BK_E$ , the mean and median values tend to increase from the incipient to the intensification phases and then decrease from the intensification (1 and 2) to the decay phases (1 and 2), displaying negative mean and median values at

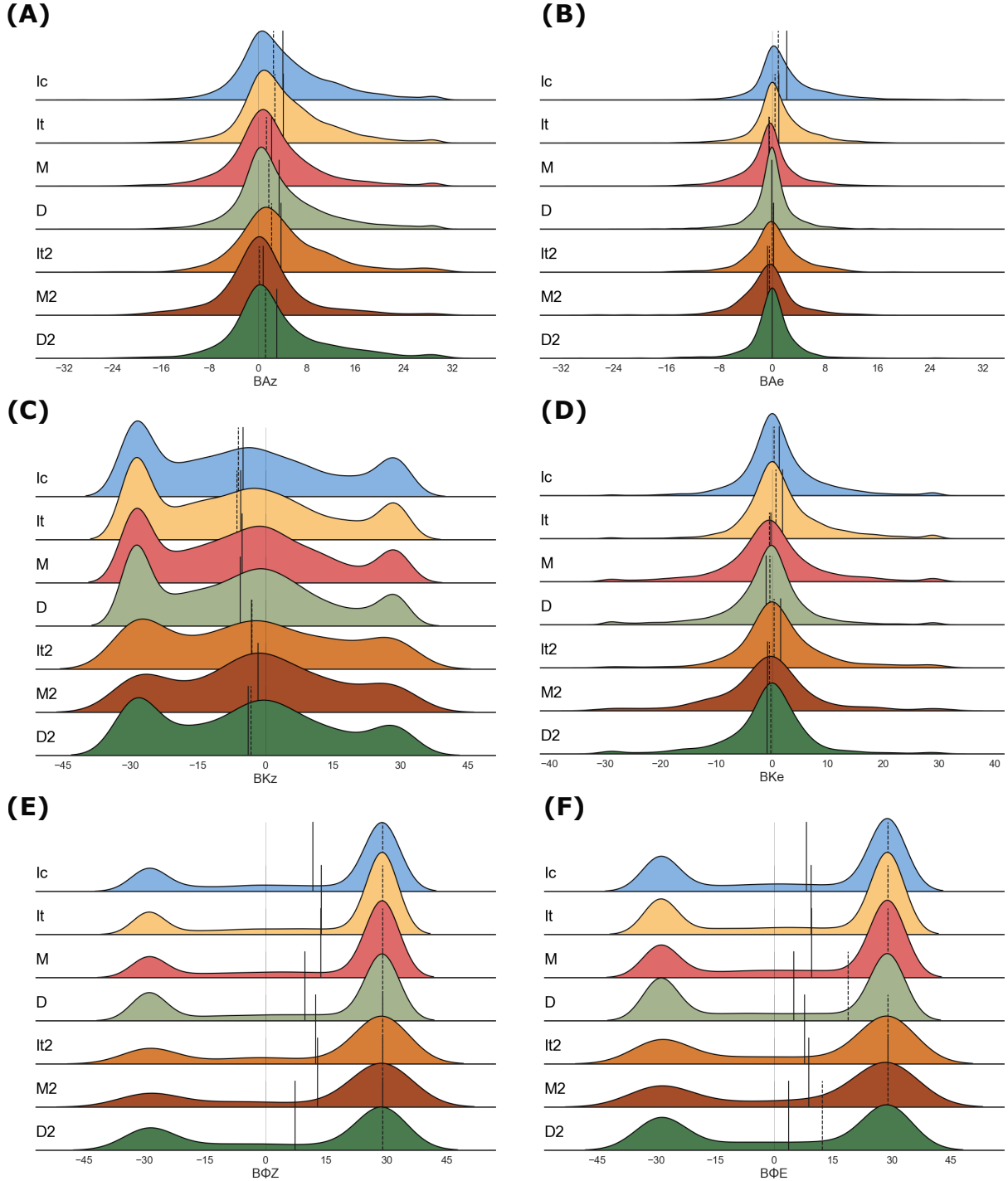


Figure 5.12: Density plots for boundary terms  $BA_Z$  (A),  $BA_E$  (B),  $BK_Z$  (C),  $BKE$  (D) and boundary pressure work terms  $B\Phi Z$  and  $B\Phi E$ , for each development phase: incipient (Ic), intensification (It), mature (M), decay (D) and the secondary development phases (indicated by "2"). The solid vertical lines indicate the mean values for a given phase while the dashed lines, the median values. The units are  $Wm^{-2}$ .

the mature and decay phases. This indicates that after intensification, the systems overall export  $K_E$  outside the computational domain.

The  $BK_Z$  term presents densities peaking at positive, neutral, and negative values (Figure 5.12c). Across all phases, the peaks are often sharpest at negative values, but the peaks at neutral values tend to become sharper throughout the systems' life cycles. The mean and median values are similar for the first development cycle phases, while the differences are more marked for the second development cycle phases, with mean and median values becoming more positive from intensification 2 to mature 2 and then decreasing in the decay 2 phase. Overall, this pattern indicates a tendency for systems to consistently export  $K_Z$  through their life cycles, although there is significant variability in the data.

Lastly,  $B\Phi Z$  and  $B\Phi E$  display nearly identical distributions, presenting peaks at both positive and negative values, but with sharper peaks at the former (Figures 5.12e and 5.12f). As a result, the median values are often aligned across all phases in the positive range. However, during the decay phase, the peaks at negative values become sharper, especially for  $B\Phi E$ , which causes the median values to decrease. As discussed in Section 2.4.2, the physical interpretation of these terms is difficult and can be hindered by small errors in the geopotential field, which might lead to unusually high values.

Figure 5.13 displays the densities for the generation and the residuals of the dissipation terms. Here, the generation terms will be explored instead of their residuals as they allow for a physical interpretation, while the residuals account for numerical errors that escalate from the other terms in the  $A_Z$  and  $A_E$  budgets. For the  $G_Z$  term, each phase often displays distributions with peaks at neutral values and minor peaks at positive and negative values (Figure 5.13a). During the incipient stage, the peak at neutral values is broader, resulting in negative mean and median values. As the systems evolve, the peak at neutral values becomes sharper, causing the mean and median values to approach zero by the decay phase. Notably, for the second mature phase, the minor peak at positive values diminishes, causing the mean and median values to become negative again.

Surprisingly, the  $G_E$  term presents an identical distribution to the  $G_Z$  term for the incipient phase, while the other phases display peaks at both neutral and positive values, with high inter-phase variability (Figure 5.13b). During the intensification phase, there is a broad right-skewed peak at neutral values, followed by a sharper peak at positive values.

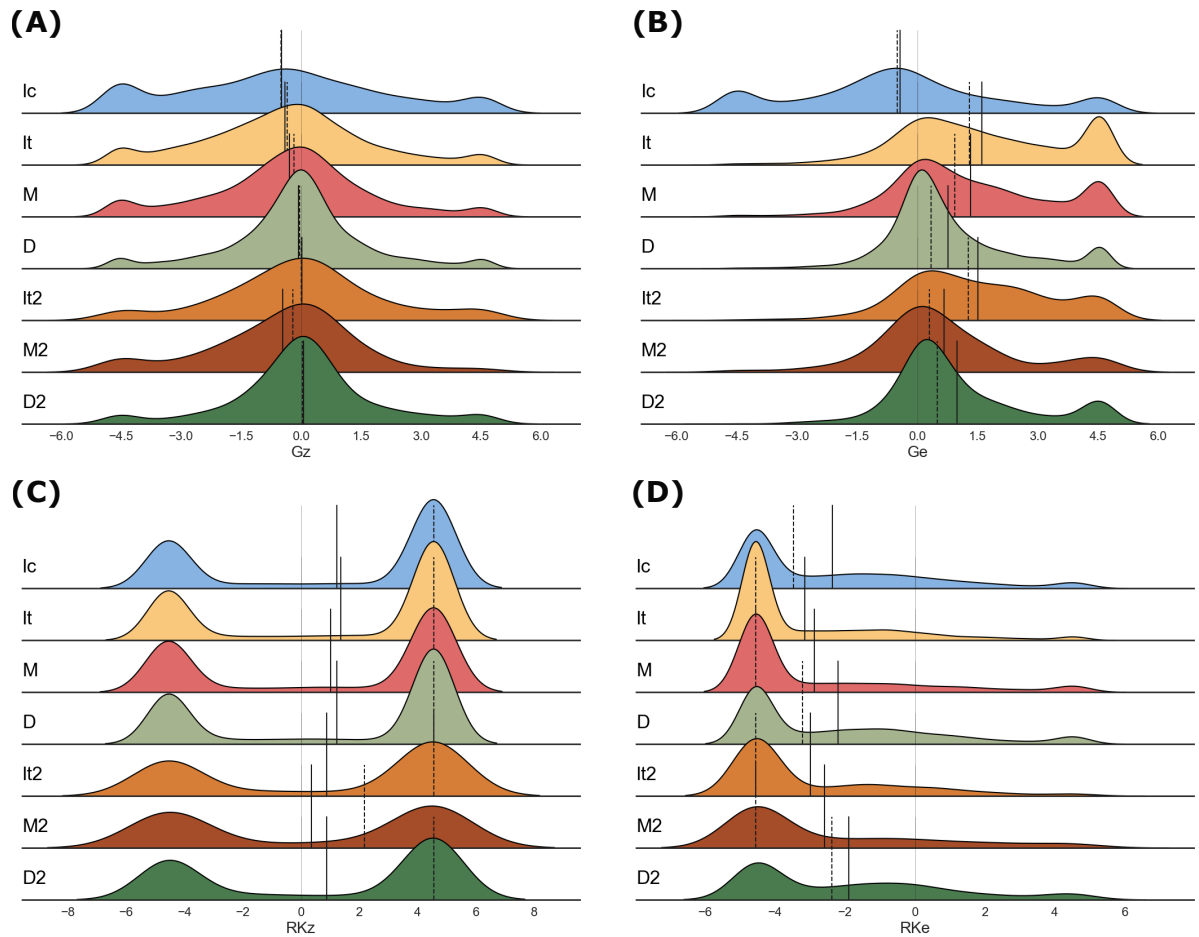


Figure 5.13: Density plots for generation and dissipation residual terms  $G_Z$  (A),  $G_E$  (B),  $RK_Z$  (C), and  $RK_E$  (D), for each development phase: incipient (Ic), intensification (It), mature (M), decay (D) and the secondary development phases (indicated by "2"). The solid vertical lines indicate the mean values for a given phase while the dashed lines, the median values. The units are  $Wm^{-2}$ .

As the systems transition to the mature and decay phases, the peak at positive values decreases and the peak at neutral values becomes broader. Overall, there are negative mean and median values during the incipient stage, reaching the largest positive values in the intensification phase and decreasing through the mature and decay phases. The second development cycle, in turn, presents a distinctive behavior: while the values are largest for intensification 2 and decrease during the mature 2 phase, they increase again during the decay 2 phase. Overall, these results indicate a generation of  $A_E$  especially during the intensification phases, which decreases afterward, consistent with the overall  $A_E$  behavior (Figure 5.10).

The  $RK_Z$  term displays distributions with peaks at both negative and positive values, but with small inter-phase variability, similar to the  $B\Phi Z$  term (Figure 5.13c). This suggests an influence of the latter on the former term, although the magnitudes are much smaller. Due to the sharper peak at positive values compared to the one at negative values, the mean and median values are positive across all phases, with median values being identical. Meanwhile,  $RK_E$  presents right-skewed peaks at negative values, with long tail distributions extending towards positive values (Figure 5.13d). The mean and median values for this term increase from the intensification to decay phases. Although it is tempting to associate the positive values of  $RK_Z$  with either the upscaling of energy and generation of  $K_Z$  through zonal jet fluxes towards the low-pressure system, and the negative values of both  $RK_Z$  and  $RK_E$  with kinetic energy dissipation, the assimilation of numerical errors and boundary pressure work terms prevents drawing such conclusions.

Finally, the budget terms result from the aggregate contributions of each energy cycle term. The density distributions for these terms are illustrated in Figure 5.14. Due to the high variability often present in each individual term, the budget terms also exhibit high variability, with modest inter-phase variations in shape distribution (i.e., although the overall behavior is preserved among the distinct phases, the magnitude of the peaks changes).

The  $\frac{\partial A_Z}{\partial t}$  term often presents three peaks across the distinct phases: one at positive, negative, and neutral values (Figure 5.14a). For the incipient phase, the peak at positive values is more prominent, while for the intensification and mature phases, the peak at negative values is more significant. The decay phase displays an increase in the peaks at neutral and positive values. A similar behavior is seen for the secondary development

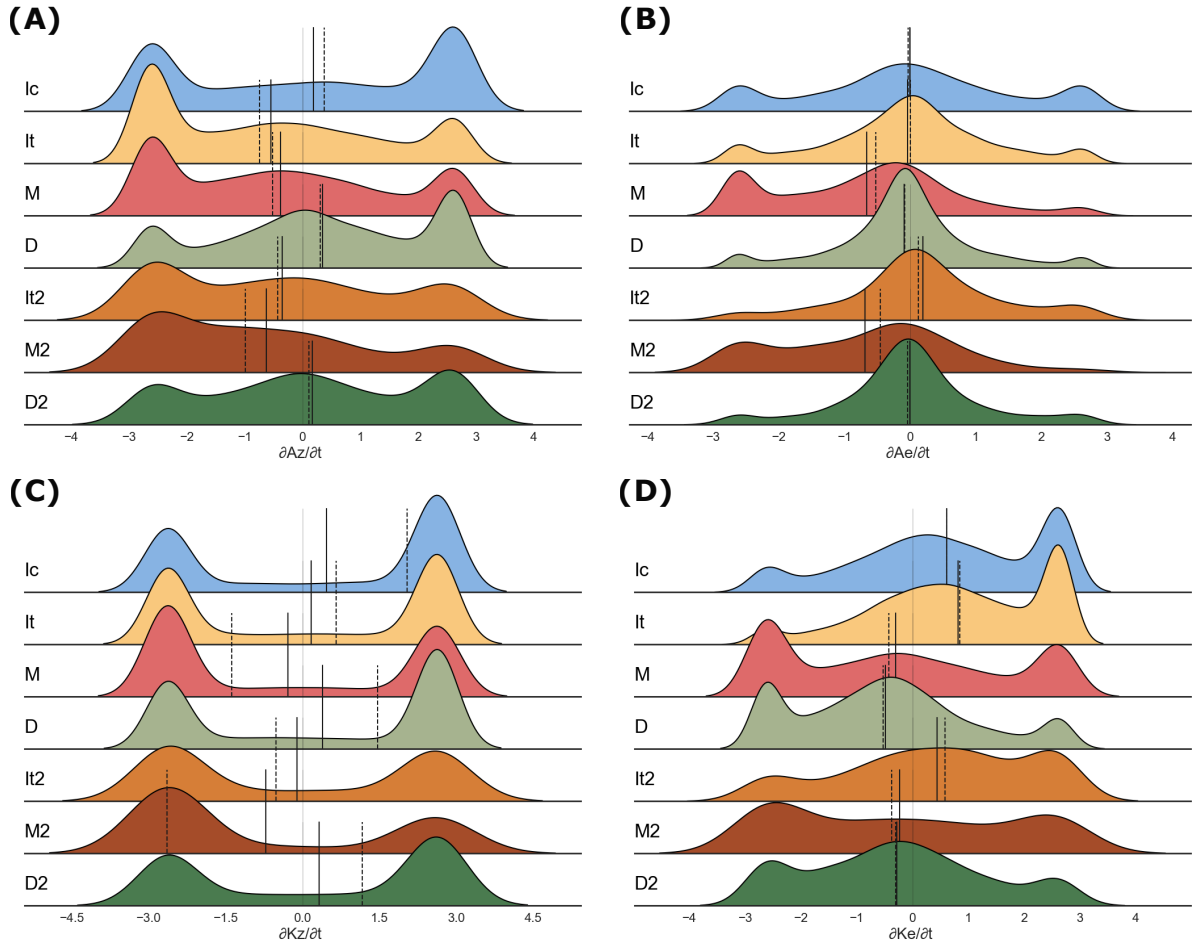


Figure 5.14: Density plots for energy budget terms  $\frac{\partial A_Z}{\partial t}$  (A),  $\frac{\partial A_E}{\partial t}$  (B),  $\frac{\partial K_Z}{\partial t}$  (C), and  $\frac{\partial K_E}{\partial t}$  (D), for each development phase: incipient (Ic), intensification (It), mature (M), decay (D) and the secondary development phases (indicated by "2"). The solid vertical lines indicate the mean values for a given phase while the dashed lines, the median values. The units are  $Wm^{-2}$ .

phases. As indicated by the mean and median values,  $A_Z$  usually increases during incipient and decay phases, displaying decreases during the other phases.

Meanwhile, the  $\frac{\partial A_E}{\partial t}$  term often displays a sharp peak at neutral values, with long tail distributions towards both positive and negative values. The exceptions are the mature phases (1 and 2), which are left-skewed and present broad peaks at negative values. As a result, while most phases tend towards neutrality for the  $A_E$  term, the mature phases tend to decrease this term.

For the  $\frac{\partial K_Z}{\partial t}$  term, a distribution with peaks at opposite sides of the spectrum can be seen (Figure 5.14c). The differences among each phase lie in the positioning of the sharpest peak. Overall, for the first development cycle, there is a tendency for  $K_Z$  to increase over the incipient and intensification phases, decrease during the mature phase, and then increase again during the decay phase. Despite the tendency for decreases during the second intensification, the peaks at each end of the spectrum are nearly symmetrical. The second mature phase presents an overall tendency for decreases in  $K_Z$ , which is reversed during the second decay. These results suggest that  $K_E$  is often increasing or decreasing but rarely neutral, and despite the overall trends noted here, there is high variability in behavior among the systems.

Lastly, for  $\frac{\partial K_E}{\partial t}$ , the distributions present peaks at positive, neutral, and negative values, with large inter-phase differences (Figure 5.14d). For the incipient and intensification phases, the peaks are sharper at positive values, which is reversed during the mature and decay phases. This behavior is reflected in the mean and median values. A similar behavior can be noted for the secondary development phases. These results indicate a tendency for  $K_E$  to increase during its initial development for each cycle, peaking during the intensification phases (1 and 2), while the tendency in subsequent phases is a decrease.

### 5.2.2 Mean Energy Cycle

Figure 5.15 illustrates the LEC for the mean values of each term for the first development cycle. As noted in Section 4.1.1, due to the high variability presented for the distinct terms, the results should be interpreted with caution. However, they can provide an overview of the mean energy fluxes in the analyzed systems across the different development phases and their respective dynamical evolution. Additionally, similarly to Figure 5.7, the  $G_Z$  and  $G_E$  terms are used instead of their respective residuals for a more physically based

interpretation, although the budgets were computed using the residuals. Since the residual terms were integrated into the budgets, the presented budgets may not perfectly balance positive and negative energy fluxes due to the finite differences method used, which also incorporates numerical errors.

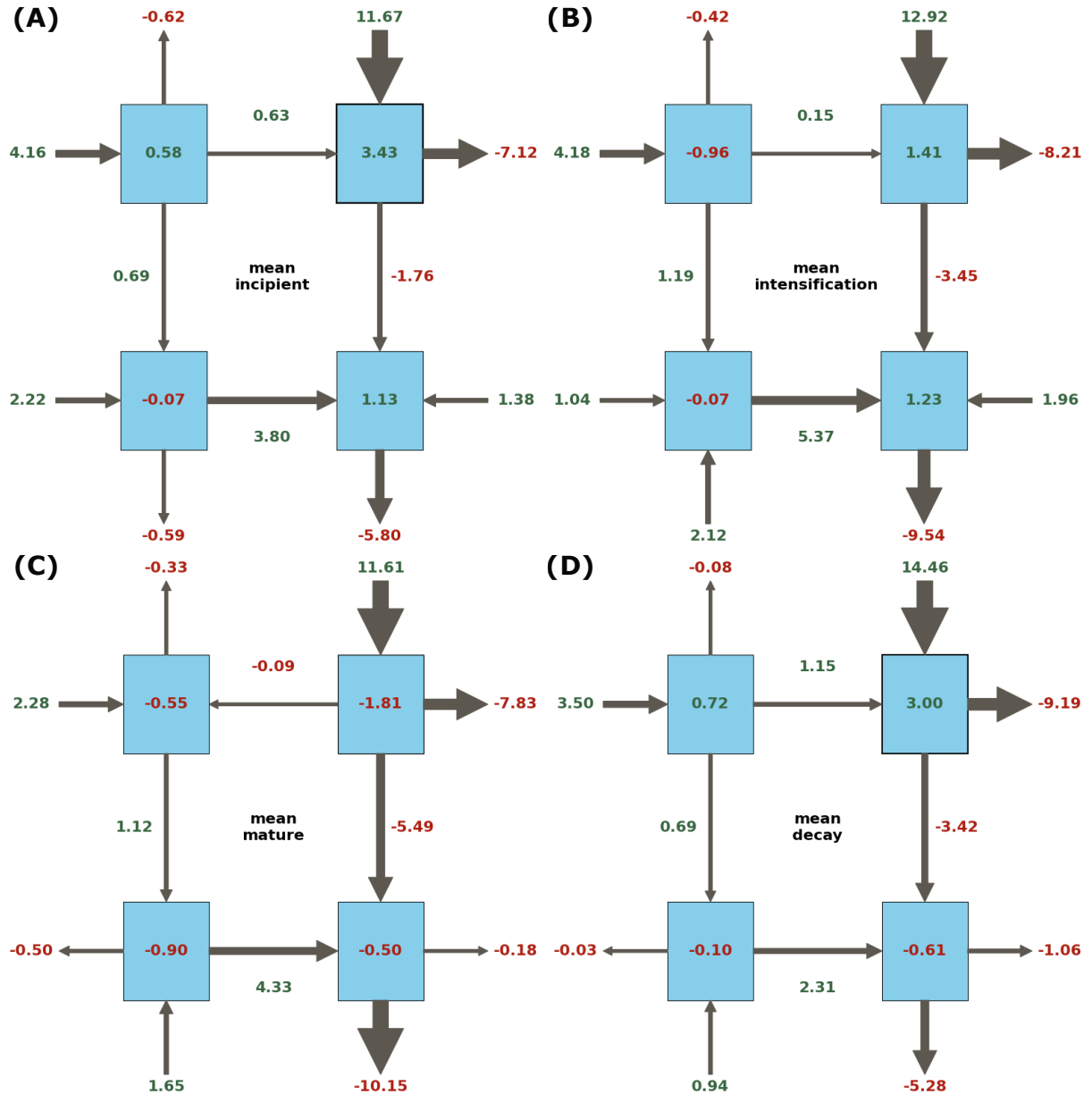


*Figure 5.15:* Mean values of the Lorenz Energy Cycle (LEC) terms for each life cycle phase: incipient (A), intensification (B), mature (C), and decay (D). Each blue box represents an energy component, with arrows showing the direction of energy flow. The numbers adjacent to the arrows indicate the magnitude and direction of the energy flux, with green indicating positive values and red indicating negative values. A representation of the complete cycle, with the positioning of each term can be found at Figure 5.7.

The incipient stage is confirmed as the development stage where the cyclone is not fully formed and the eddy-related environmental energetics are still responding to large-scale

dynamics. This is mostly indicated by the  $A_Z$  term, which is increasing due to heating at low latitudes and diabatic cooling at higher latitudes. However, this increase is not driven by  $G_Z$ , but rather from imports of  $A_Z$ . Such behavior (both  $G_Z < 0$  and  $BA_Z > 0$ ) has been observed in study cases, but often the  $\frac{\partial A_Z}{\partial t}$  is negative in the initial phases (Brennan and Vincent, 1980; Dias Pinto and Rocha, 2011; Dias Pinto et al., 2013, e.g.,). The excess  $A_Z$  is being converted into both  $K_Z$  and  $A_E$  as, in this phase, while a meridional temperature gradient is still present, there are also eddy meridional heat transports.

The  $K_Z$  term experiences the largest increases during this phase, driven mainly by  $RK_Z$ , although a significant portion of this energy is exported outside the domain, with some of it converted to  $K_E$ . In contrast,  $A_E$  experiences modest decreases. The negative  $\frac{\partial A_E}{\partial t}$  indicates that the initial  $A_E$  reservoir must be large enough to sustain the eddy development. As Figure 5.10 demonstrated, this is indeed the case. The existence of a zonal temperature gradient drives the conversion of  $A_E$  into  $K_E$ . This initial conversion chain of  $A_Z \rightarrow K_Z$  and  $A_Z \rightarrow A_E \rightarrow K_E$  is observed in the initial stages of most LECs of baroclinic disturbances previously reported (Michaelides, 1992; Pezza et al., 2010; Dias Pinto and Rocha, 2011; Black and Pezza, 2013, e.g.,).

While  $A_E$  receives energy from  $A_Z$  and there are some imports of  $A_E$  through the boundaries, this energy is mostly converted to  $K_E$ . Additionally, during this stage,  $G_E$  is negative, possibly due to the lower convective activity at the cyclone's initial development. The  $K_E$  term then experiences increases in energy, driven by the barotropic conversion term, imports of energy, and mainly conversions from  $A_E$ , although a significant portion of this energy is lost through  $RK_E$ .

During the intensification phase, although the loss of  $A_Z$  energy from the  $G_Z$  term and the conversion to  $K_Z$  diminish, the enhancement in conversion to  $A_E$  causes an overall decrease in this term. This indicates a weakening of the meridional temperature gradient, driven by the eddy-induced meridional heat transport. For the  $K_Z$  term, the enhanced  $RK_Z$  is balanced by increased export of energy and conversion to  $K_E$ , leading to a decrease in the magnitude of  $\frac{\partial K_Z}{\partial t}$ .

In this phase, enhanced eddy-related convective processes are evident, indicated by the positive  $G_E$ . This process, in conjunction with the increased meridional heat transport, creates zonal temperature and  $\omega$  gradients, enhancing  $A_E \rightarrow K_E$  conversions. With reduced  $A_E$  imports, the magnitude of  $\frac{\partial A_E}{\partial t}$  remains consistent with the incipient phase. For

the  $K_E$  term, despite increases in all energy influxes, the increased activity of  $RK_E$  results in only modest increments in  $\frac{\partial K_E}{\partial t}$ .

In the mature phase, most LEC terms present an overall reduction in magnitude as the system's energetics become less active and begin to equalize with the environment. The exception is the barotropic term  $C_K$ , which increases in magnitude. As a result, the  $K_Z$  term begins to experience decreases, indicating an overall weakening of the zonal jets. The  $\frac{\partial A_E}{\partial t}$  term becomes significantly more negative, primarily due to the reduction in convective activity, as indicated by the  $G_E$  term, and because this term starts to export energy outside the domain.

The  $\frac{\partial K_E}{\partial t}$  term also experiences decreases, presenting a reversal in sign, despite the enhanced barotropic conversions ( $C_K$  term), indicating a weakening of the eddy activity. This is due to the combined effect of the reduced conversion from  $A_E$  — indicating an overall reduction in zonal temperature gradients — and the reversal in sign of  $BK_E$ , as the eddy begins to export energy outside the domain, alongside further increases in the magnitude of the  $RK_E$  term.

Lastly, in the decay phase following the mature phase, most terms present a further overall reduction in magnitude. The  $\frac{\partial A_Z}{\partial t}$  reverts to its original positive values, driven by the enhanced imports of energy. A similar behavior is observed for  $\frac{\partial K_Z}{\partial t}$ , presenting comparable magnitudes to their values during the incipient phase. This scenario suggests that as the eddy decays, the atmosphere regains its original behavior, with the equator-to-pole temperature gradients increasing and the zonal jets strengthening.

The  $\frac{\partial A_E}{\partial t}$  term also presents a magnitude comparable to the incipient stage. However, the  $A_E$  boundary and generation terms present opposite signs during the decay phase compared to the incipient phase, with  $G_E$  being positive due to residual convective activity, although less vigorous than in previous phases, and minimal exports of  $A_E$  through the boundaries. Despite the decrease in magnitude of  $RK_E$ , the reduced contributions from  $C_E$  — due to weakened zonal gradients — and  $C_K$  — due to reduced barotropic conversions — along with the enhanced export of energy, result in the  $K_E$  term presenting its largest decreases across all phases.

Notably, the energy fluxes often maintain the same direction across all development phases, although the terms exhibit notable variations in magnitude. For instance, both the baroclinic chain and the barotropic conversion term are active throughout the entire

life cycle. For baroclinic disturbances, this consistency in the baroclinic chain is expected (Pezza et al., 2010; Dias Pinto and Rocha, 2011; Black and Pezza, 2013, e.g.,), although high variability is present and this behavior can vary from case to case (Figure 5.11). Regarding barotropic conversions, some studies report its predominance in extratropical cyclone development (Michaelides, 1987; Wahab et al., 2002; Bulic, 2006; Cavicchia et al., 2018, e.g.,), while others do not (Pezza et al., 2010; Dias Pinto and Rocha, 2011, e.g.,). Here, it is believed that the choice of computational domain as well as the use of a Semi-Lagrangian framework might aid in making barotropic conversions more evident (Michaelides et al., 1999). The next sections will explore this more deeply.

The contributions from  $G_E$  are negative during the incipient phase, peaking during intensification, and diminishing afterward, which is consistent with previous studies (Michaelides, 1987; Dias Pinto and Rocha, 2011; Wahab et al., 2002, e.g.,), although those studies analyze the  $RG_E$  term, making direct comparisons difficult. While the moist baroclinic chain is most intense during the intensification phase, the barotropic conversion is most intense during the mature phase. The  $RK_Z$  and  $RK_E$  terms are also consistent across all phases:  $RK_Z$  provides energy to  $K_Z$ , while  $RK_E$  acts as a sink of energy. Although both residuals aggregate a combination of terms, making it difficult to attribute the overall behavior to a specific term, the results presented here align with Smith (1980), which indicated high generation of kinetic energy by cross-contour flow and high dissipation of  $K_E$  throughout the system's life cycle. Moreover, the overall paradox related to the negative sign of the term  $\frac{\partial A_E}{\partial t}$  might be attributed to the inclusion of numerical errors in the energy budget.

Figure 5.16 displays the Lorenz Energy Cycle (LEC) for the mean values of each term for the second development cycle. The overall energy flux for each LEC term remains the same as for the first development cycle: the baroclinic chain is most active during the second intensification phase, while the barotropic conversion term is most active during the second mature phase, along with higher  $RK_E$ . Notably, the  $\frac{\partial A_E}{\partial t}$  term presents positive values during the second intensification, while, for the same phase, the  $RK_Z$  shows its lowest values and  $C_K$  its highest values across all phases. Furthermore, the values of  $C_A$  and  $C_E$  are lower than their respective counterparts in the first development cycle. These results suggest that distinct dynamical processes are related to the development during the second cycle.

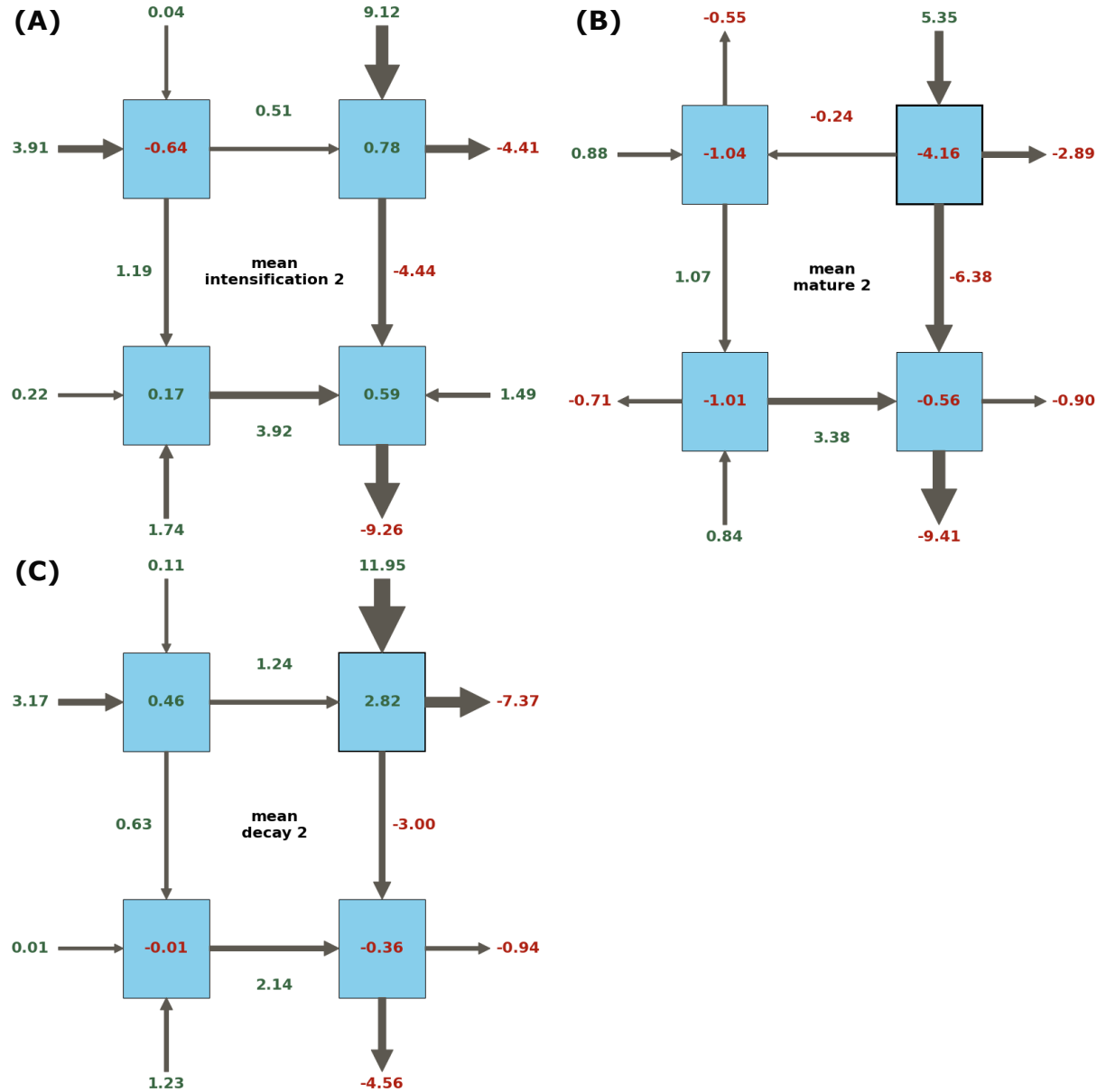


Figure 5.16: Mean values of the Lorenz Energy Cycle (LEC) terms for each phase of the cyclones secondary development: intensification 2 (A), mature 2 (B), and decay 2 (C). Each blue box represents an energy component, with arrows showing the direction of energy flow. The numbers adjacent to the arrows indicate the magnitude and direction of the energy flux, with green indicating positive values and red indicating negative values. A representation of the complete cycle, with the positioning of each term can be found at Figure 5.7.

The analysis of the LEC across different development phases reveals significant insights into the energy dynamics of cyclonic systems. During the incipient phase, there is a notable increase in  $A_Z$ , primarily due to imports rather than generation, with conversions to  $K_Z$  and  $A_E$  occurring. The intensification phase sees enhanced eddy-related convective processes and thermally direct circulation, leading to increased conversions from  $A_E$  to  $K_E$ . The mature phase is characterized by a reduction in overall energy magnitudes and a weakening of zonal jets. In the decay phase, the system's energetics further diminish, suggesting a reversion to the atmosphere's original state.

The second development cycle exhibits similar energy flux patterns, with distinct variations in the intensity of key energy fluxes, indicating an enhanced importance of barotropic conversions. These findings underscore the importance of both baroclinic and barotropic processes in different phases. The baroclinic chain is especially important during the intensification phase, consistent with previous studies on extratropical cyclone development, while barotropic conversions become more evident in the mature phase and in the secondary development cycle. The observed high variability and the integration of residual terms into the budgets suggest that numerical errors and domain choices significantly influence the interpretation of these energy cycles.

### 5.2.3 EOFs

Similar to the mean behavior presented in Section 5.1.2, the results for the mean behavior across each life phase exhibit high variability. Therefore, each term can span a wide range of possible values, possibly resulting in reversals of energy fluxes. To delineate an overall picture of the LEC across each phase for cyclones in the SESA region, unlike the presentation in Section 5.9, the reconstructed EOFs will be analyzed. These were computed by reversing the normalization process and adding back the mean to each EOF. Here, the analysis is limited to the first developmental cycle for simplicity, justified by the higher prevalence of systems that only present one developmental cycle.

Figure 5.17 illustrates the proportion of variance in the dataset that is explained by each of the first four Empirical Orthogonal Functions (EOFs) for each life phase. As shown for the EOFs representing the mean LEC behavior, the first four EOFs explain the main modes of variability contained in the data. For practical reasons, only the first four EOFs will be explored. Similar to the total life cycle, the first EOF accounts for the largest

portion of the variance for all phases, explaining approximately 26% to 30%, indicating it captures the most significant pattern in the data. The exception is the incipient phase, where EOF1 explains approximately 21% of the variance in the data. Meanwhile, the subsequent EOFs explain progressively smaller proportions of the variance. Furthermore, as discussed in Section 5.9, the PCs will not be presented as they would merely represent the signal magnitude across the distinct cyclones rather than any physical feature.

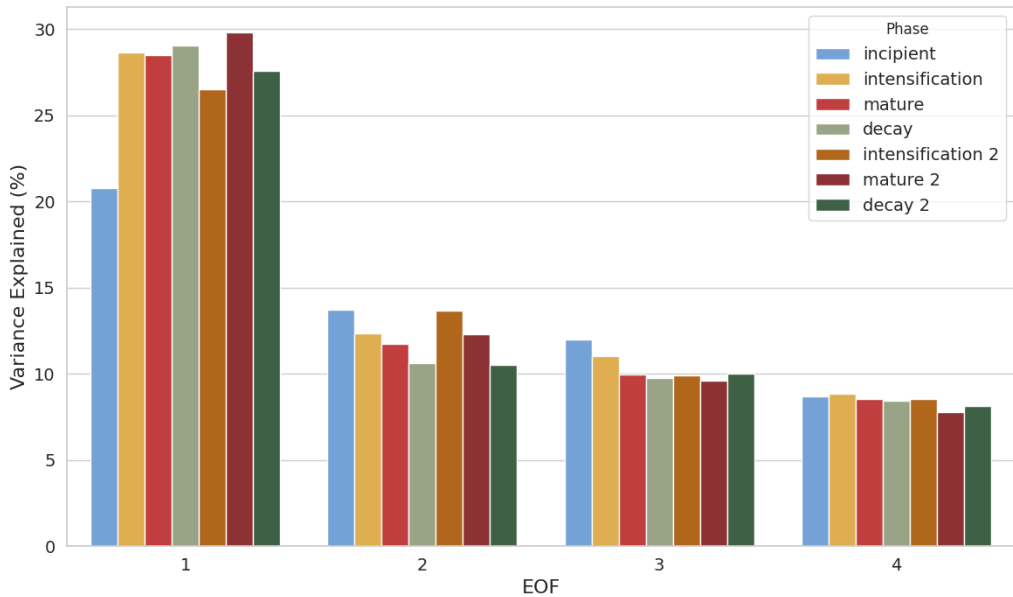


Figure 5.17: Proportion of variance in the dataset explained by the first four Empirical Orthogonal Functions (EOFs), for each development phase.

For EOF1 (Figure 5.18), most terms reinforce the overall behavior presented for the mean values across each phase (Figure 5.15). An enhancement of both the baroclinic chain and the barotropic conversion from  $K_Z$  to  $K_E$  is consistent across all phases. Both instabilities increase in activity during the life cycle, decreasing at the onset of the decay phase: the baroclinic chain presents higher values during the incipient phase and peaks during the intensification phase, while the barotropic conversion peaks during the mature phase. Notably, the  $G_E$  term is enhanced and positive throughout all phases, peaking during intensification, indicating overall enhanced convective activity for this EOF.

Furthermore,  $RK_Z$  is highly enhanced, resulting in positive tendencies for  $\frac{\partial K_Z}{\partial t}$ . However, this positive tendency is not significantly above the average, as most of the excess energy is exported outside the domain via the  $BK_Z$  term. A similar behavior is found for

$\frac{\partial K_E}{\partial t}$ . Despite the increased energy influxes for  $K_E$ , they are accompanied by significant increases in  $RK_E$ , which sinks that extra energy. Additionally, despite the enhanced imports of  $K_E$  during the incipient and intensification phases, the mature and decay phases observe enhanced exports.

Other distinctions from the mean behavior are found in the budgets for  $A_Z$  and  $A_E$  terms. For  $A_Z$ , there is a negative tendency during the incipient phase, indicating a weakening of the meridional temperature gradients during the cyclone's initial development. Meanwhile, for the  $A_E$  budget, an enhancement above the mean conditions is observed, resulting in a positive budget for the incipient and intensification phases. This indicates that the negative values found in the mean behavior might be attributed to the presence of outliers.

In EOF2, the overall mean behavior is weakened for most terms (Figure 5.19). Notably, during the incipient stage, there is a deviation in the energy flux from  $K_Z$ : a reversal in the sign of the  $C_Z$  term and a reduction in barotropic conversions are observed. The negative  $C_Z$ , accompanied by negative  $G_Z$  and positive  $C_A$ , indicates an overall weakening of the meridional gradient in vertical motions. During this stage, there is also a stronger than average negative  $G_E$  but a strengthening of  $C_E$ , which is explained by imports of  $A_E$  through the boundaries.

For the remaining phases, the import of  $A_E$  reduces, the barotropic conversion progressively increases, and the  $G_E$  term is similar to the mean behavior. Despite this,  $\frac{\partial K_E}{\partial t}$  presents a below-average tendency. This can be explained by the enhancement of sinks via the  $RK_E$  term during the intensification and mature phases, and the progressively increased exports of  $K_E$ . During the decay phase, although the sink from the  $RK_E$  term reduces significantly while  $C_K$  is strongest, this is compensated by the highest exports of energy and the weakest conversions from  $A_E$ .

Furthermore, from the intensification phase onwards, an enhancement of  $RK_Z$  can be seen, which, similar to EOF1, is followed by an enhancement of exports of  $K_Z$ . During the decay phase,  $\frac{\partial A_Z}{\partial t}$  presents significant increases, followed by a reversal in the sign of  $C_Z$  compared to previous states. These combined processes result in an enhancement of  $\frac{\partial K_Z}{\partial t}$ , making it twice the average mean.

For EOF3, the inter-phase variability is less marked (Figure 5.20). Across all phases, there are high values of  $RK_Z$ , which — similarly to the previous EOFs — are almost

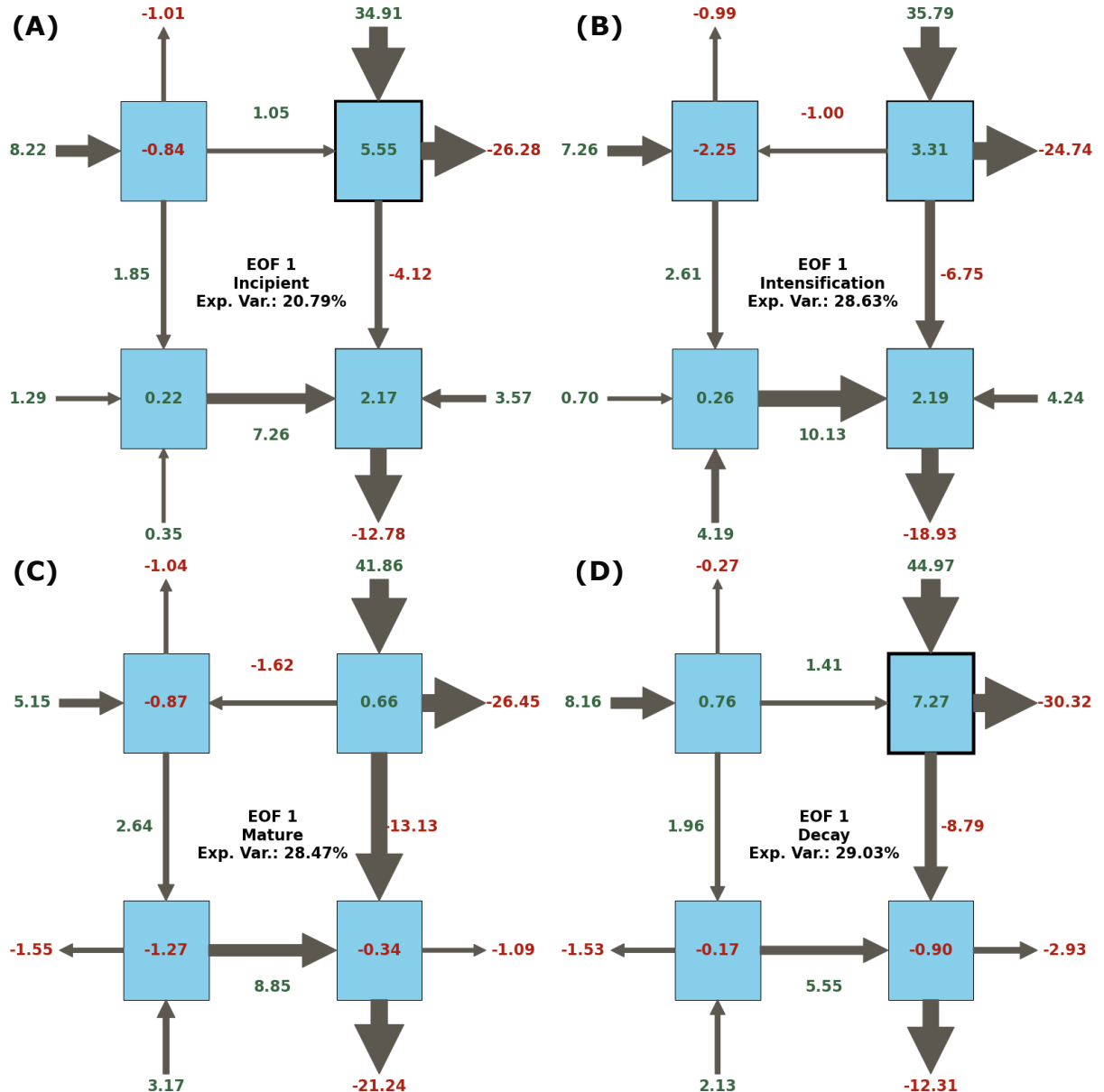


Figure 5.18: Reconstructed first EOF (EOF1) of Lorenz Energy Cycle (LEC) Terms, illustrating energy fluxes across each phase of the first development cycle: incipient (A), intensification (B), mature (C) and decay (D). The numbers adjacent to the arrows denote the magnitude and direction of the anomaly, with green indicating positive values and red indicating negative values.

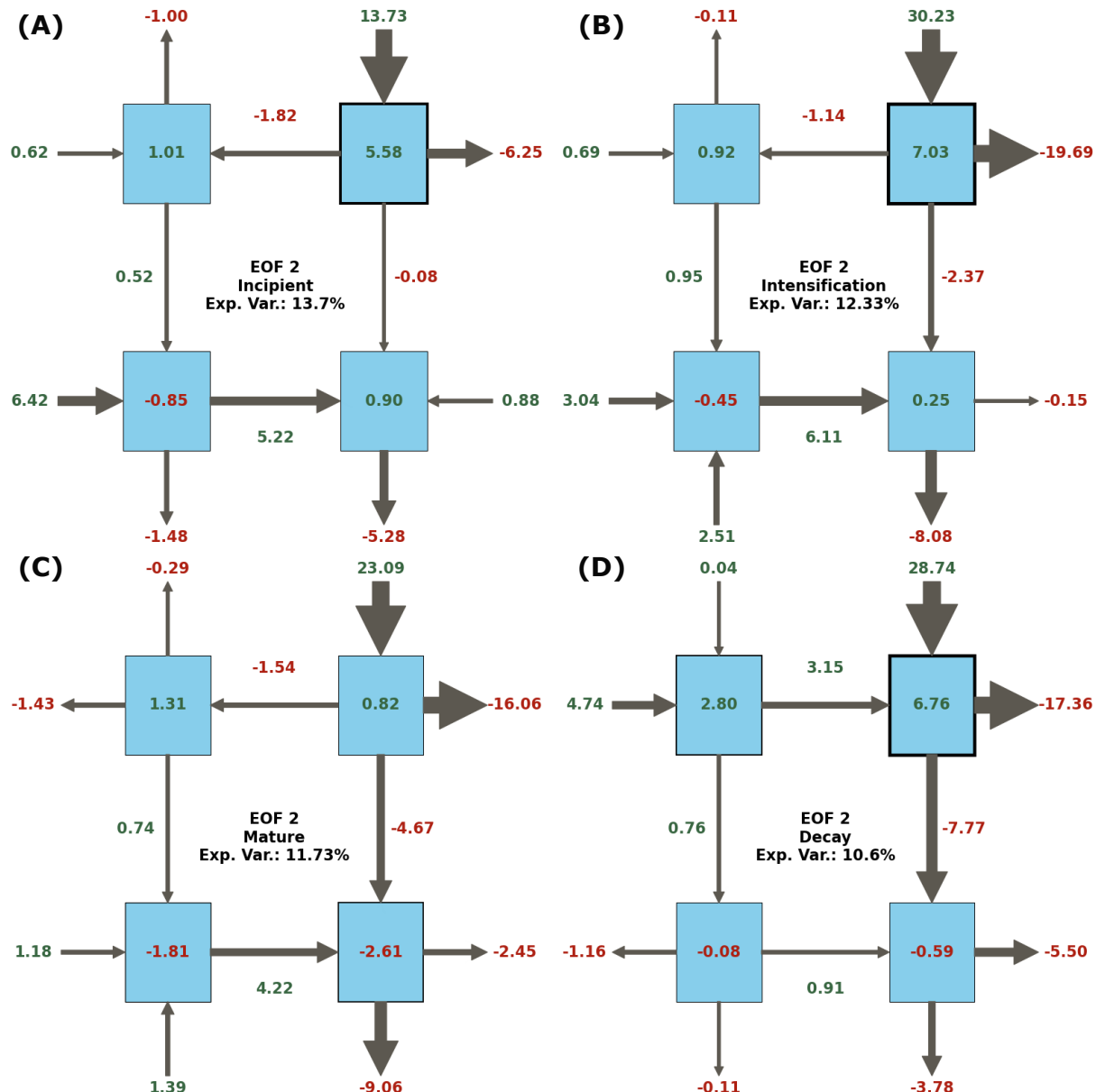


Figure 5.19: Reconstructed second EOF (EOF2) of Lorenz Energy Cycle (LEC) Terms, illustrating energy fluxes across each phase of the first development cycle: incipient (A), intensification (B), mature (C) and decay (D). The numbers adjacent to the arrows denote the magnitude and direction of the anomaly, with green indicating positive values and red indicating negative values.

compensated by exports of  $K_Z$ . There is also a consistent conversion from  $A_Z$  to  $K_Z$  and imports of  $A_Z$ . During the incipient phase, positive  $\frac{\partial A_Z}{\partial t}$  is found due to the importation of energy and positive generation ( $G_Z$ ). There is then a conversion of  $A_Z$  into  $A_E$  and  $K_Z$ .  $\frac{\partial A_Z}{\partial t}$  is unusually high due to the enhanced  $RK_Z$  and thus provides above-average energy to  $K_E$ . Meanwhile,  $\frac{\partial A_E}{\partial t}$  is increasing — due to the combined effects of  $C_A$ , imports, and enhanced convective activity — and is providing energy to  $K_E$ . This term, in turn, is exporting energy and losing it via  $RK_E$ . During the intensification and mature phases, the imports of  $A_E$  become exports of energy, while the barotropic conversion becomes the highest contributor to  $K_E$ . Meanwhile, the  $RK_E$  term peaks at the mature phase, decreasing afterward. Lastly, during the decay phase, most LEC terms are below average, indicating a weaker eddy at later stages.

In EOF4, most terms generally present lower magnitudes across all phases than in the mean behavior, indicating that this EOF corresponds to weaker systems development (Figure 5.21). The  $RK_Z$  presents above-mean values only during the incipient phase, where both  $C_K$  and  $C_E$  contribute equally to  $K_E$ . However, during this phase,  $G_E$  is negative and  $C_A$  is low, with the main contributor to  $A_E$  being the imports of energy. As the system develops,  $G_E$  becomes positive, peaking during the mature phase, and  $C_A$  increases, peaking during the intensification phase. Notably, for the first time,  $C_K$  is positive during the decay phase.

In summary, EOF1 displays a strengthening of the mean behavior — a scenario where the moist baroclinic chain and barotropic conversions sustain the eddy throughout its entire life cycle. The former is most intense during the incipient and intensification phases, while the latter is strongest during the mature and decay phases. In EOF2, cyclogenesis and initial development are triggered mostly by imports of  $A_E$  and  $K_E$  and the import of the former continue until the mature phase. Meanwhile, there is a consistent increase in barotropic conversions through the life cycle. In this case it seems that instead of intensifying the cyclone, the barotropic conversion acts as impeding it to decay earlier.

For EOF3, although the initial development is fueled by the moist baroclinic chain in conjunction with imports of  $A_E$ , barotropic conversions dominate during the intensification and mature periods. In the decay phase, all terms are weakest. For all EOFs 1, 2, and 3, during later development stages, high barotropic conversions are typically observed. However, they are not sufficient to surpass the loss of energy from exports and the  $RK_E$

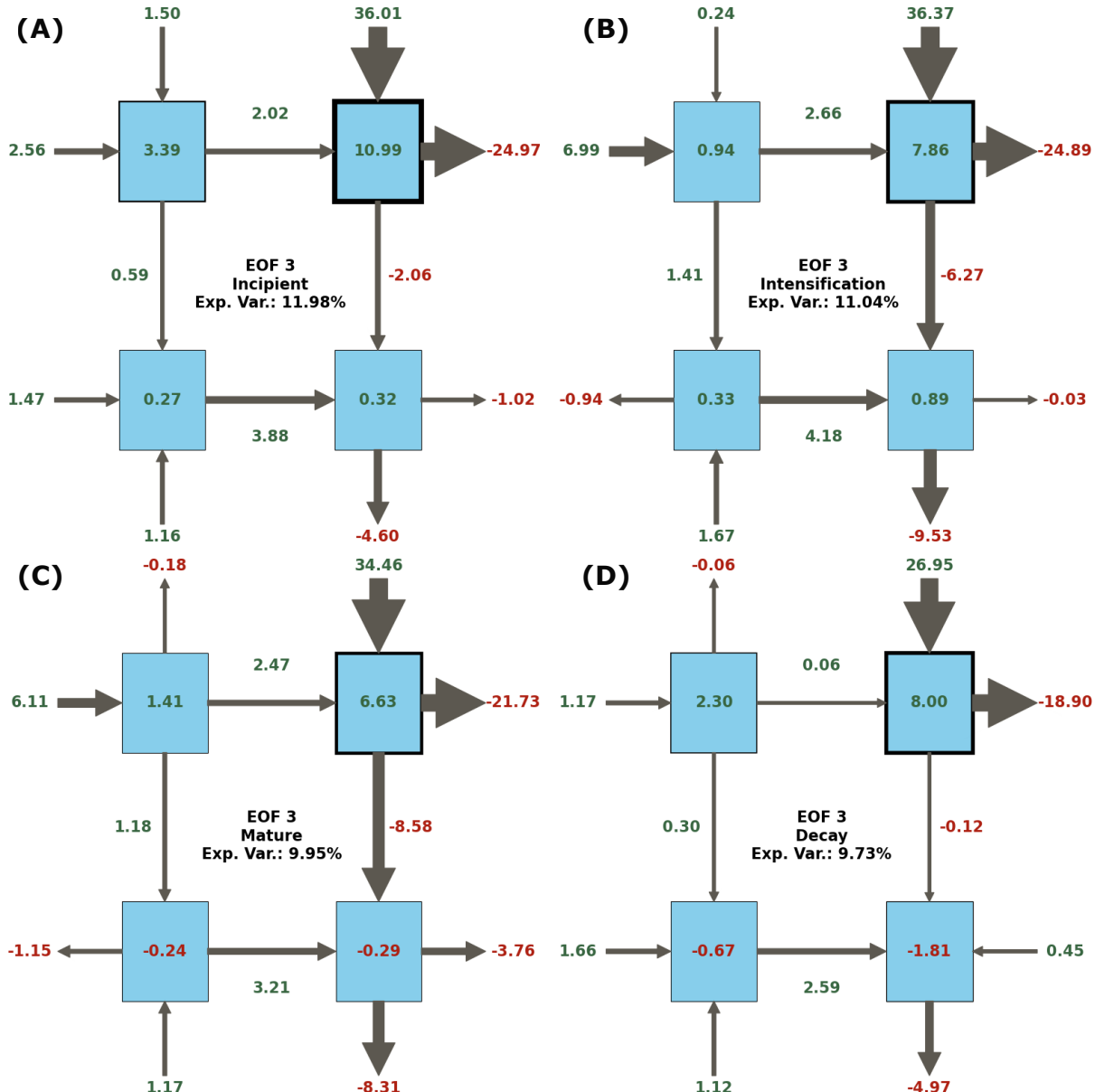


Figure 5.20: Reconstructed third EOF (EOF3) of Lorenz Energy Cycle (LEC) Terms, illustrating energy fluxes across each phase of the first development cycle: incipient (A), intensification (B), mature (C) and decay (D). The numbers adjacent to the arrows denote the magnitude and direction of the anomalies, with green indicating positive values and red indicating negative values.

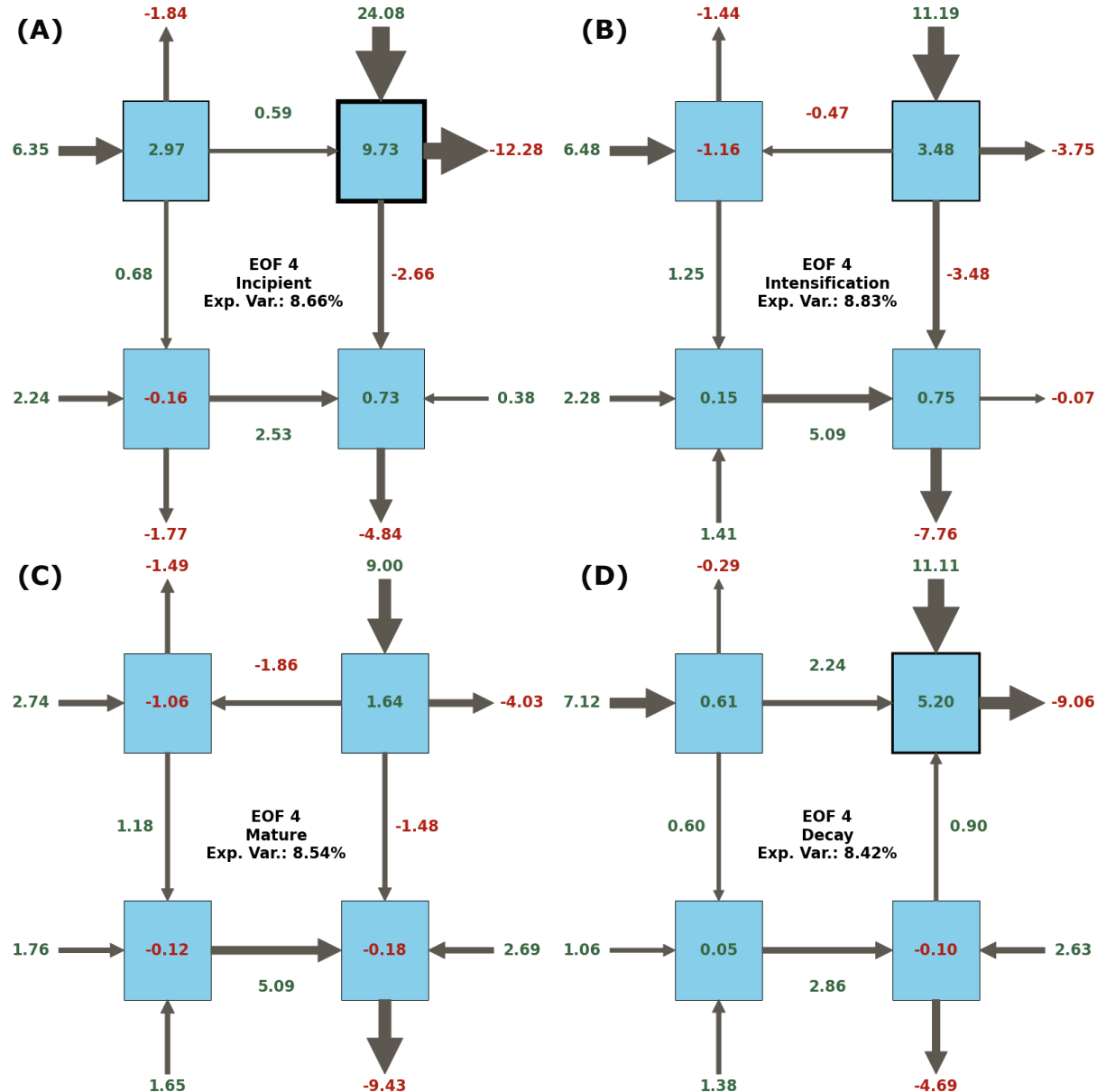


Figure 5.21: Reconstructed fourth EOF (EOF4) of Lorenz Energy Cycle (LEC) Terms, illustrating energy fluxes across each phase of the first development cycle: incipient (A), intensification (B), mature (C) and decay (D). The numbers adjacent to the arrows denote the magnitude and direction of the anomaly, with green indicating positive values and red indicating negative values.

term, resulting in  $\frac{\partial A_E}{\partial t} < 0$ . Lastly, for EOF4, while the initial development is related to imports of both  $A_E$  and  $K_Z$ , the barotropic and especially the moist baroclinic chain lead to eddy growth. Nonetheless, the lower than average values indicate that this EOF is related to the development of weaker systems.

### 5.3 Summary and Concluding Remarks

This chapter delves into the energetics of cyclones in the Southwestern Atlantic, focusing on the Lorenz Energy Cycle (LEC) for 7,531 cyclonic systems originating in the ARG, LA-PLATA, and SE-BR regions. It presents the first comprehensive dataset for the South Atlantic, offering insights into the energetics of these systems over their complete life cycles and development phases. The LEC was computed using limited-area energetics through a Semi-Lagrangian approach, following the method proposed by Michaelides et al. (1999). Therefore, some limitations might be recognized: the results presented represent the limited-area contributions to the global energetics (Smith, 1969), while the formulations used do not account for the displacement related to the moving domain (Michaelides et al., 1999). However, we advocate that by adopting the snapshot approach, where each computational domain represents a fixed domain individually, each contribution can be treated individually for each time-step. For small time-steps, the aggregate contribution would represent the evolution of the eddy environment energetics.

The results presented in this chapter demonstrate that the LEC terms exhibit high variability and many outliers, explaining the differences in results found among previous studies. The Semi-Lagrangian framework overall results in higher mean values for  $K_Z$  and smaller mean  $A_Z$  than those reported by previous studies. This effect is attributed to the isolation of the jet features in the domain plus the reduced meridional temperature gradients compared to when large domains are adopted. For the remaining terms, their variable behavior hinders direct comparison with the literature. However, the mean LEC behavior, presenting an overall importance of the baroclinic chain in consonance with the barotropic conversion term, corroborates previous findings.

Here, the LEC is accessed from cyclogenesis until the moment the tracking methodology stops following a given system. This moment is then considered the cyclolysis. How the environmental energetics behave pre-cyclogenesis or post-lysis remains an open question

and is beyond the scope of the current study. The EOF analysis demonstrates that for both the mean behavior and across each life cycle phase, the main variability is related to the enhancement of the moist baroclinic chain and barotropic conversions from the zonal jets to the eddies. This reinforces the conclusion that the main contributions to the eddy environmental energetics come from the moist baroclinic chain in consonance with barotropic conversions. These indicate that most cyclones' life cycles are modulated by the meridional temperature gradients, which are converted into kinetic energy by eddy motion. At the same time, the cyclones are also receiving momentum from the zonal jets. This mean behavior is observed across all life phases, from cyclogenesis, often strengthened during the intensification and mature phases, and weakened during the decay.

While these processes initiate and contribute to eddy growth, in later life stages, the  $RK_E$  term and exports of  $K_E$  result in the eddy's decay and dissipation. Although the  $RK_E$  term also aggregates numerical errors and the  $B\Phi E$  term, whose physical interpretation is not obvious, the presented results suggest that most of this term's signal is related to the dissipation of energy, which is consistent with Smith (1980). Nevertheless, there are also a smaller, although significant number of cases where the mechanisms leading to eddy growth are distinct, such as imports of either or both eddy forms of energy ( $A_E$  and  $K_E$ ). Michaelides et al. (1999) previously associated imports of  $K_E$  with downstream development (Simmons and Hoskins, 1979), a mechanism previously noted in some cases of cyclone development in the South America region (Piva et al., 2010; Rosa et al., 2013). Meanwhile, the  $A_E$  imports have not been thoroughly discussed previously and will be further explored in the next chapter. Additionally, the results indicate distinct mechanisms related to the secondary development phases, but these were not fully explored as they represent a minority of cyclones in the dataset.

Meanwhile, ubiquitous high values of  $RK_E$  are found across distinct phases and LEC configurations. Again, this term's interpretation is difficult. However, as the zonal circulation is often providing kinetic energy to the eddy circulation ( $C_K < 0$ ), it is possible to infer that the positive values of  $RK_Z$  are not related to upscaling of energy from smaller scales ( $D_Z > 0$ ). Thus, it might seem that the positive values of  $RK_Z$  are associated with the  $B\Phi K$  term, which is further supported by the high values computed for this term. Future research on elucidating this term's physical interpretation and post-processing methods to ensure its validity against small errors in the geopotential field would further reveal new

insights into cyclonic dynamics.

The high values of  $RK_Z$  throughout the systems' entire life cycle indicate that this methodology may not be ideal for studying large-scale circulation, which is understandable given its focus on individual systems. However, the results are consistent and provide new perspectives on cyclone energetics. Due to the high variability in the data, it was not possible to analyze seasonality and temporal trends: while analyzing the mean would reveal little about the seasonality and/or long-term trends in the energetics of the systems in general, using EOFs would make such an analysis impractical. The next chapter attempts to use a different perspective, enabling such analyses to be performed.

# Chapter 6

---

## Energetic Patterns of Cyclones in the Southwestern Atlantic

Chapter 5 investigated the LEC climatology for the cyclones with genesis in the South American sector. Although the mean behavior across all systems was discussed, the results exhibited high variability, which hindered a deeper analysis of patterns that deviated from the norm. This chapter will employ clustering analysis to determine patterns in the LEC — energy patterns — related to eddy development, so this variability can be further assessed.

### 6.1 Lorenz Phase Space and Energy Patterns

#### 6.1.1 Introducing the Lorenz Phase Space

The first step in constructing the energy patterns (EP) involves devising a visualization that could facilitate the understanding of the environmental energetics related to cyclonic systems. As demonstrated in Chapter 5, the usual LEC visualization (where arrows representing energy fluxes connect the distinct energy terms) is a powerful tool for understanding the atmospheric dynamics associated with atmospheric systems and their evolution. However, it is not practical for large datasets and considering multiple phases denoting the systems' evolution over time, as is the case here. Therefore, the goal of this section is to devise a new visualization tool that simplifies this process while maintaining the focus on displaying the dynamics related to eddy development, i.e., related to their Efficient and Final Causes (Sections 2.1.3 and 2.1.4).

Figures 6.1 and 6.2 contain Phase Diagrams, inspired by the Cyclone Phase Space created by Hart (2003), in which distinct sets of the LEC terms are represented. These

representations are called Lorenz Phase Space (LPS) diagrams. As mentioned, they focus on the mechanisms related to eddy growth, so there is a trade-off between representing as many terms as possible but keeping some degree of simplicity, while still providing an intuitive visualization.

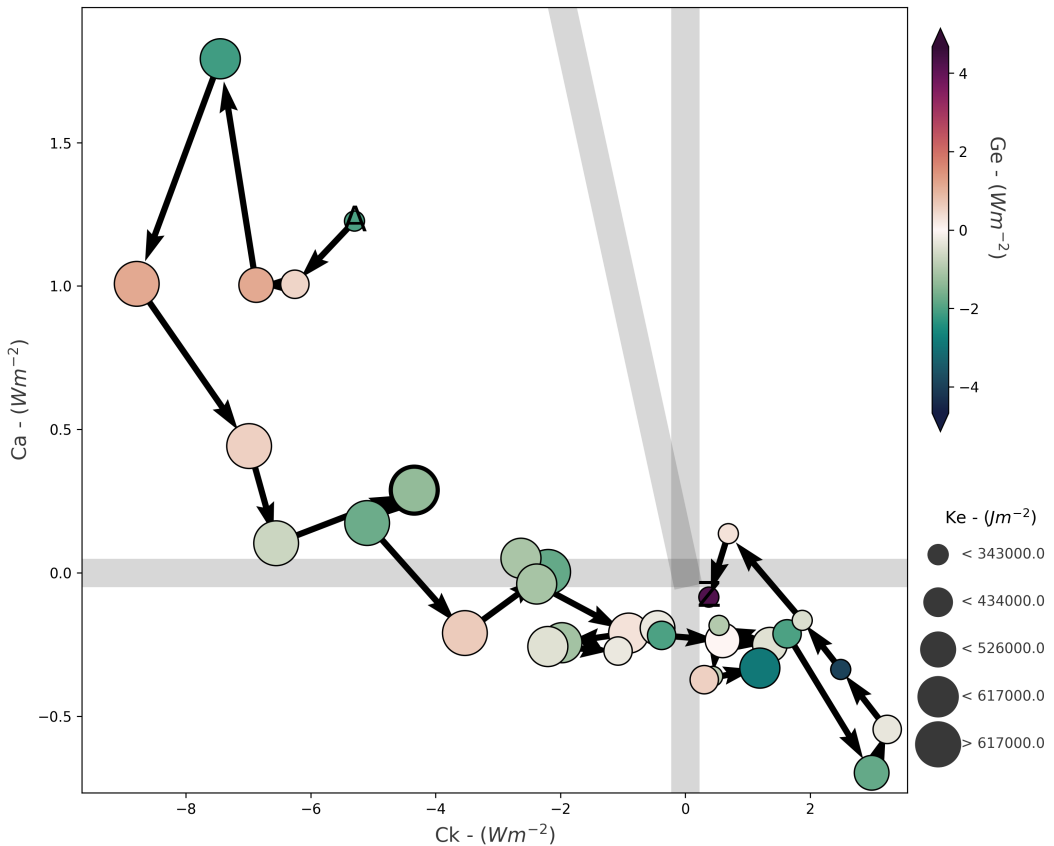


Figure 6.1: Lorenz Phase Space (LPS) diagram 1 for "Reg1" cyclone (Dias Pinto and Rocha, 2011). The x-axis represents the barotropic conversion term ( $C_K$ ), which indicates the conversion from zonal to eddy kinetic energy, while the y-axis shows the baroclinic conversion term ( $C_A$ ). The color shading denotes the generation of eddy potential energy ( $G_E$ ), with warmer colors indicating higher convective activity and cooler colors representing lower activity. The size of the circles correlates with the system intensity, measured by  $K_E$ . The letters "A" and "Z" mark the system's initial and final positions, respectively. The point where the system reaches its peak intensity is highlighted by a thick circle border.

Figure 6.1 displays the LPS representing the main terms related to dynamical instabilities in the atmosphere. The x-axis represents the barotropic conversion term ( $C_K$ ), the y-axis the baroclinic conversion term ( $C_A$ ), while the color shading represents the convective activity ( $G_E$ ) and the circle sizes represent the system intensity ( $K_E$ ). There is

also an "A" and a "Z" representing the system's initial and final positions, and the moment where the system is most intense is marked by a thick circle border. Meanwhile, Figure 6.2 illustrates the LPS related to imports of Eddy Energy. This diagram is similar to Figure 6.1, but here the x-axis represents importation and exportation of eddy APE across the system boundaries ( $BA_E$ ), while the y-axis shows the importation and exportation of eddy kinetic energy across the system boundaries ( $BK_E$ ).

The choice for using the  $C_A$  term in the LPS diagram (Figure 6.1) is justified by its high correlation with the  $C_E$  term (Appendix D). Thus, when positive conversions from  $A_Z$  to  $A_E$  occur, there is a high probability that conversions from  $A_E$  to  $K_E$  are also happening, indicating an active baroclinic chain. Additionally, since the second LPS diagram (Figure 6.2) represents the imports of  $A_E$  and both LPS diagrams indicate  $G_E$ , the  $C_E$  signal can be inferred. Meanwhile, the  $K_E$  was chosen to represent the system's intensity because it generally increases from genesis to the mature phase and decreases during the decay phase (Section 5.2). It also correlates well with central relative vorticity at 850 hPa (Appendix D).

On Figures 6.1 and 6.2, the energetics of the "Reg1" system from Dias Pinto and Rocha (2011) are analyzed using the LPS diagrams. Here, for comparison with the original results, the same computational procedure as from Dias Pinto and Rocha (2011) is used (Eulerian framework), for the same domain, as well as the same dataset (NCEP-R2 reanalysis). The computational domain and time series for energy and conversion terms are presented in Appendix E. The only difference is that here  $G_E$  is used instead of  $RG_E$ , in order to allow for a physical interpretation of this term's contributions.

Using the LPS diagrams, one can easily identify the dynamical mechanisms inciting eddy development during the occurrence of this system. For instance, Figure 6.1 indicates that during the system's early life stages, baroclinic and barotropic conversions provided support for its development, as well as contributions from convective processes (evidenced by  $G_E$ ). As the system's life progresses, the importance of baroclinic conversions and convective processes diminishes, with both terms becoming negative and the eddy being sustained only by barotropic conversions. During later periods,  $G_E$  is negative, indicating a predominance of descending movements, and the eddy is feeding the zonal circulation, as well as  $K_E$  being converted to  $A_E$ . Meanwhile, Figure 6.2 shows that in the initial development stages, there were exports of both  $A_E$  and  $K_E$  outside the domain, but as

the system developed, both boundary terms reverted to imports of energy, with higher magnitudes than the conversion terms displayed in Figure 6.1. Also, in later development stages, as the summed magnitudes of  $C_A$  and  $BA_E$  were lower than  $G_E$ , it can be inferred that  $C_E < 0$ , so the eddy-driven thermal circulation had stopped, and the Equator-to-pole temperature gradients were being reestablished.

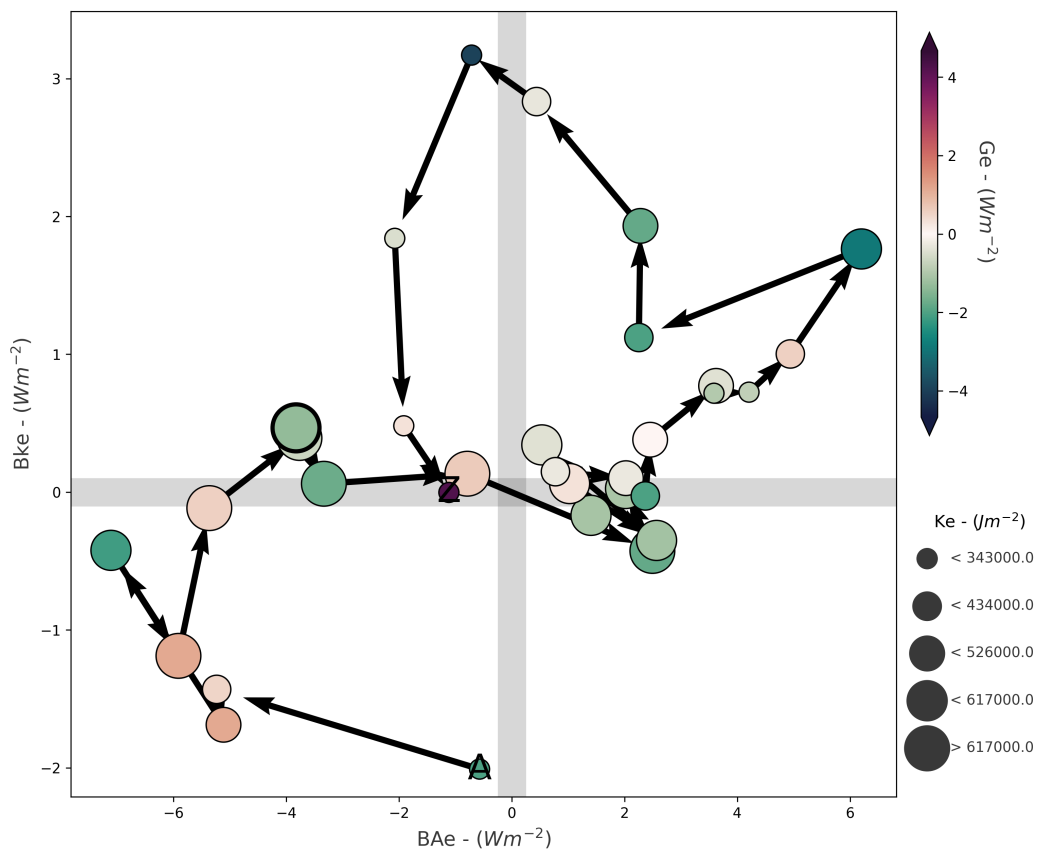


*Figure 6.2:* Lorenz Phase Space (LPS) diagram 2 for "Reg1" cyclone (Dias Pinto and Rocha, 2011). The x-axis represents importation and exportation of eddy APE across the system boundaries ( $BA_E$ ), while the y-axis shows the importation and exportation of eddy kinetic energy across the system boundaries ( $BKE$ ). The color shading denotes the generation of eddy potential energy ( $G_E$ ), with warmer colors indicating higher convective activity and cooler colors representing lower activity. The size of the circles correlates with the system intensity, measured by  $K_E$ . The letters "A" and "Z" mark the system's initial and final positions, respectively. The point where the system reaches its peak intensity is highlighted by a thick circle border.

### 6.1.2 Energetic Patterns for All Life Cycle Configurations

The LPS diagrams containing all systems for the SESA region for the 1979-2020 period can be found in Appendix F. Due to the large amount of data and the presence of outliers, it is not possible to discern the relative importance of the LEC terms for smaller groups of systems precisely. Therefore, the K-means algorithm is employed to group the energy cycles into distinct representative clusters.

The first attempt at clustering all cyclones' energetics in the dataset is performed for all major lifecycle configurations, presented in Chapter 4 (Figure 4.3b). For this, the LEC terms were averaged for each life cycle phase, and each life cycle configuration was clustered independently. For all life cycle configurations analyzed, the elbow method returned an ideal number of clusters as 3, as represented in Figure 6.3. This figure corresponds to the "Incipient, Intensification, Mature, Decay" life cycle configuration, but the plots for each configuration were nearly identical.

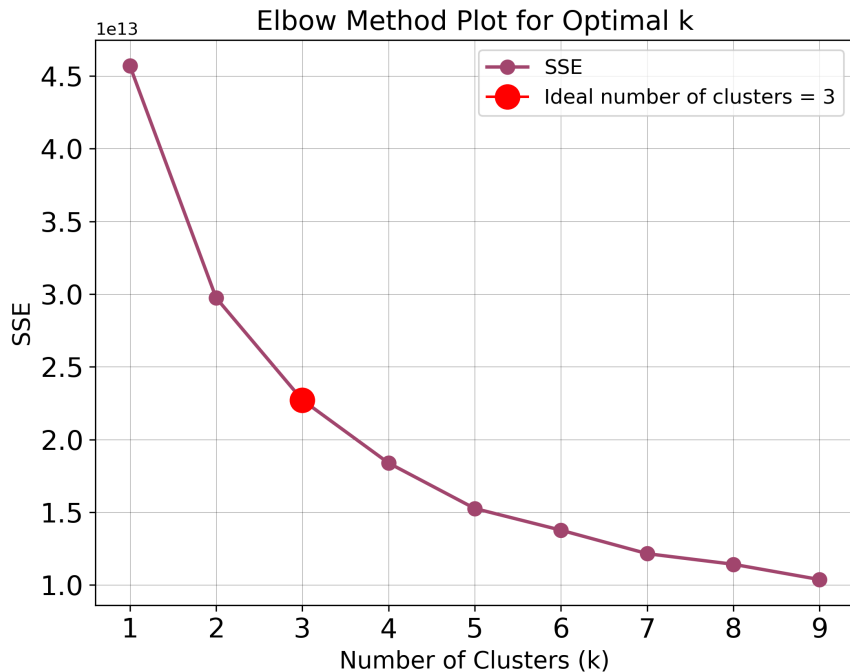


Figure 6.3: Elbow method plot for determining the optimal number of clusters. The x-axis represents the number of clusters (k), while the y-axis indicates the Sum of Squared Errors (SSE). The purple line shows the SSE for each k value. The red dot highlights the optimal number of clusters (k=3), where the SSE begins to decrease at a slower rate, forming an "elbow." This point suggests that three clusters provide a good balance between minimizing variance within clusters and model simplicity.

Figures 6.4 and 6.5 present the LPS diagrams for the centroids of the three clusters

for each life cycle configuration. On these diagrams, each circle represents the energetics corresponding to a distinct life cycle phase, initiating on the incipient phase (A) and ending of either the first or second decay phases (Z). The centroids, which represent the mean positions of all data points within a cluster, serve as representative profiles of the LEC terms for the respective clusters. These centroids are not actual data points from the dataset but synthetic constructs that encapsulate the average characteristics of the LEC terms within each cluster. Consequently, they provide a generalized yet insightful depiction of the typical energy dynamics observed in the cyclonic systems classified within each cluster. This clustering approach allows us to identify and characterize distinct energetic patterns (EPs), facilitating a deeper understanding of the underlying physical processes driving the variability in cyclonic energetics.

The LPS 1 diagram (Figure 6.4) indicates similar patterns emerging for all life cycle configurations, with systems often initiating in low energy states. As they intensify, both baroclinic and barotropic conversions, as well as convective activity, become more vigorous. Meanwhile, when the systems are decaying, they tend to revert back to lower energy states. The EPs within the same life cycle group usually differentiate from each other by the magnitude of the conversion and generation terms in each phase. It is notable that  $C_K$  is usually higher than the other forms of energy, while  $G_E$  and  $C_A$  present comparable magnitudes. This reinforces the conclusion in Chapter 5 that barotropic conversions are one of the main mechanisms driving cyclone development in the SESA region.

There are some exceptions to the overall energetic development pattern described above. For example, for the "intensification, mature, decay" configuration (Figure 6.4b), there is an EP which already initiates with relatively high conversion levels and convective activity, decreasing in later stages, while another pattern starts with the highest  $G_E$  values for this life cycle configuration EPs. Enhanced convective activity in the initial stages can also be noted for the configuration where "intensification, mature, decay" repeats twice (Figure 6.4d). This enhancement of energy conversion and/or generation is expected for these configurations, as they lack an incipient stage. In the Cyclophaser program, the incipient stage is not detected if the system's life starts with a relatively steep increase in relative vorticity (becoming more negative, i.e., becoming more intense) and if this process is fast enough that the duration criteria for phase detection are not met. Therefore, the LPS diagram 1 suggests that for these cases, the enhanced conversions/generation in earlier

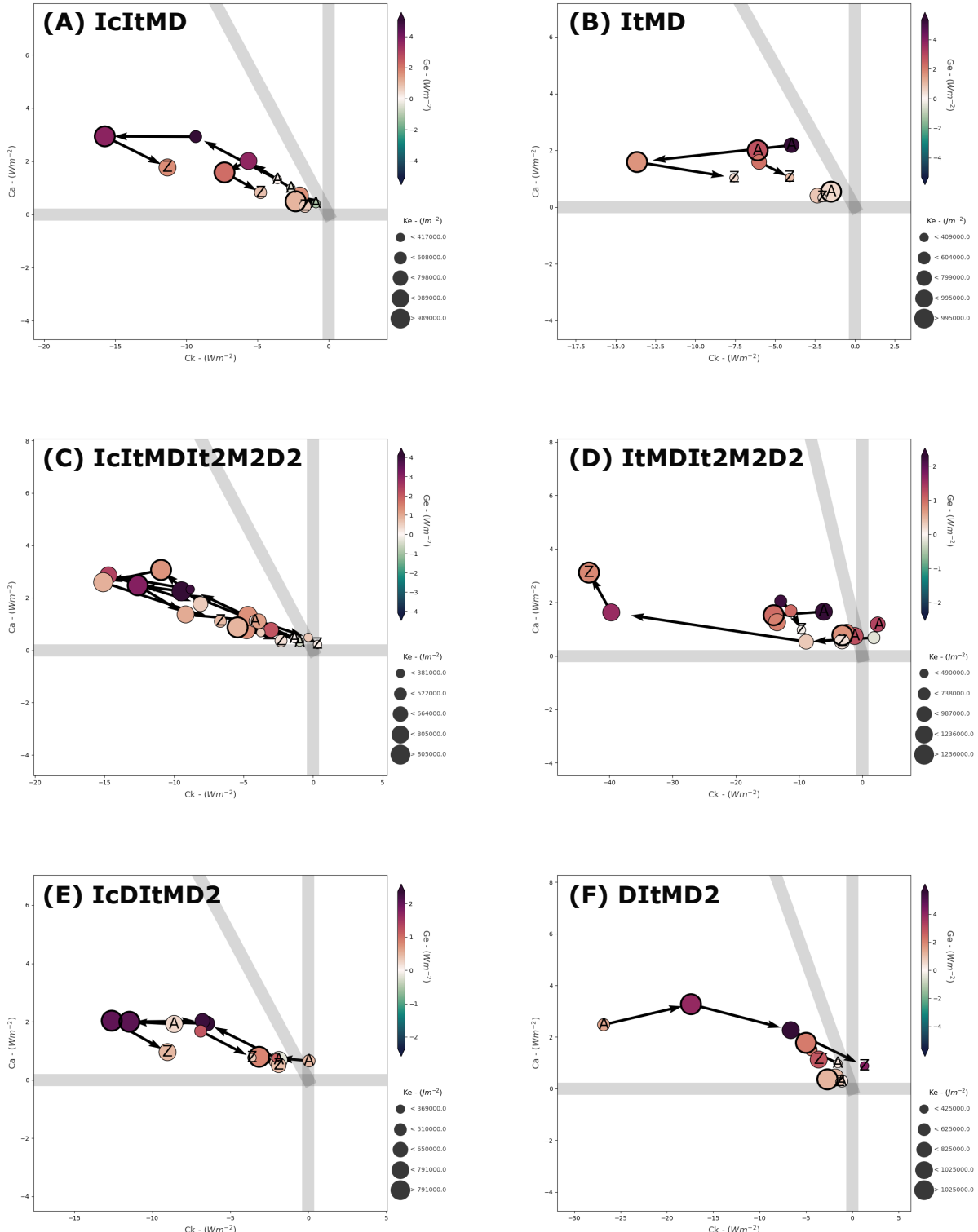


Figure 6.4: Lorenz Phase Space (LPS) diagram 1 for all main life cycle configurations (Figure 4.3b). "Ic", "It", "M," and "D" denote incipient, intensification, mature, and decay phases, respectively, while a "2" is used to denote their second occurrence within the same life cycle configuration.

life periods are responsible for an abrupt intensification phase and the lack of an incipient phase.

Furthermore, another exception can be found in systems presenting an early decay phase (Figure 6.4f). In this case, one EP starts with a high energy state and then reverts to lower energy states as the system evolves. This EP, which roughly corresponds to only 3% of the variability for this life cycle, representing less than 3% of the cyclones in the total dataset, is composed of only four systems. Further examination revealed that this high energy state is linked to an outlier within this EP, while the other systems start in lower energy states (Appendix G). Although further examination of the dynamics related to this outlier is of interest, it is beyond the scope of the current study.

The LPS 2 diagram (Figure 6.5) presents a more heterogeneous behavior, although an overall pattern can still be observed. Systems often initiate with imports of  $A_E$ , which decrease as they develop. During the intensification phase, imports of  $K_E$  increase, diminish in the mature phase, and revert to exports of  $K_E$  during decay. As with LPS 1, the clusters for each life cycle configuration tend to differentiate from each other by the magnitude of the boundary and generation terms in each phase. The magnitude of the boundary terms is often comparable to  $C_A$  and  $G_E$ , and for some EPs at specific phases, they present higher values, comparable to  $C_K$  values. Similarly, as noted for LPS 1, the EPs lacking an incipient stage often initiate in higher energy states, reinforcing the argument that rapid intensification in these cases is related to an enhanced energy cycle. Meanwhile, the outlier for the life cycle configuration with an early decay can still be noted (Figure 6.5f).

Given that the behavior presented by the EPs shows low variability among distinct life cycle configurations, the next sections will focus on the EPs for the "incipient, intensification, mature, decay" configuration for simplicity (Figure 6.4a). This choice is also justified by the prevalence of this life cycle configuration within the dataset, representing nearly 60% of all systems (Figure 4.3b). This approach allows for more detailed analysis while maintaining the potential for generalizing the results.

### 6.1.3 Energetic Patterns - Seasonality and Spatial Variability

While Section 6.1.2 focused on the differences of the EPs among the distinct life cycle configurations, the present section will investigate their seasonality and spatial variability. As previously discussed, the focus will be on the EPs for the "incipient, intensification,

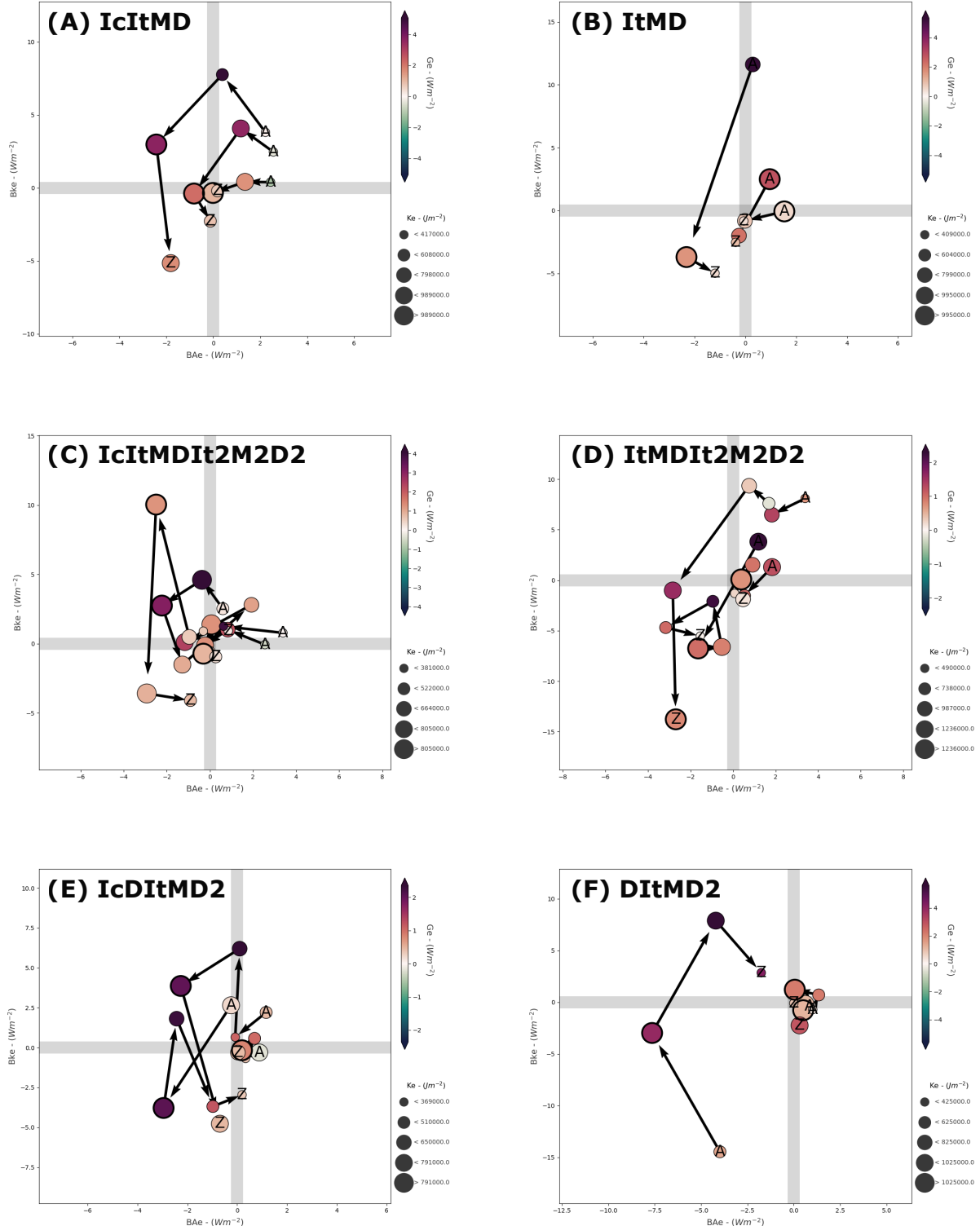
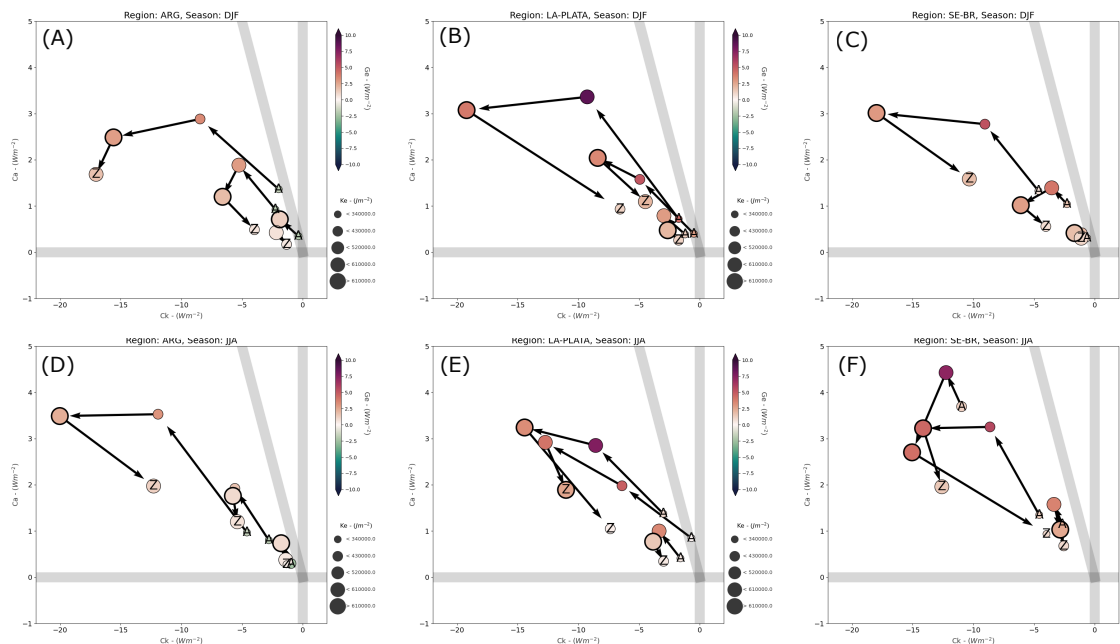


Figure 6.5: Lorenz Phase Space (LPS) diagram 2 for all main life cycle configurations (Figure 4.3b). "Ic", "It", "M," and "D" denote incipient, intensification, mature, and decay phases, respectively, while a "2" is used to denote their second occurrence within the same life cycle configuration.

mature, decay”life cycle configuration. The spatial and seasonal variability is assessed by employing the clustering technique for the distinct seasons and genesis regions in the Southwestern Atlantic region: ARG, LA-PLATA, and SE-BR, as delineated in Chapter 4. For this analysis, the K-means algorithm was initialized for each region and season separately. As in Chapter 4, only austral summer (DJF) and winter (JJA) are assessed.

Figure 6.6 presents the LPS 1 diagram for the EPs related to each region, for JJA and DJF. Notably, for each season-region group, the elbow method detected an optimal number of clusters as three, similarly to the EPs for all systems. It can be seen that the overall behavior is preserved across the distinct seasons and regions: the systems often initiate in lower energy states, and as they develop, the energy conversions, as well as convective activity, become more intense. Within each group, each distinct EP represents an overall higher energy state: one EP presents more neutrality for  $C_A$ ,  $C_K$ , and  $G_E$  for all life phases, while the second and third EP progressively present higher conversions and often higher generation of  $A_E$ .



*Figure 6.6:* Lorenz Phase Space (LPS) diagram 1 for the EPs related to the ”incipient, intensification, mature, decay”life cycle configuration, across DJF (a, b, c) and JJA months (c, d, e) and for each genesis region in Southwestern Atlantic Region: ARG (a, d), LA-PLATA (b, e) and SE-BR (c, f).

Despite the apparent similarity across the distinct groups, some seasonality and inter-regional variability can be noted. The most notable distinction is in the  $G_E$  term: LA-PLATA EPs tend to present lower  $G_E$  values compared to the other regions, with ARG

presenting relatively high values for both seasons. For both cases, there is no distinction between each season. Meanwhile, for SE-BR, JJA systems present overall higher  $G_E$  than DJF systems. For the conversion terms, each group consistently presents EPs that can be interpreted as having lower, medium, and higher energy states, which are very similar among the groups. However, for LA-PLATA and SE-BR during JJA, there are two groups with higher energy states instead.

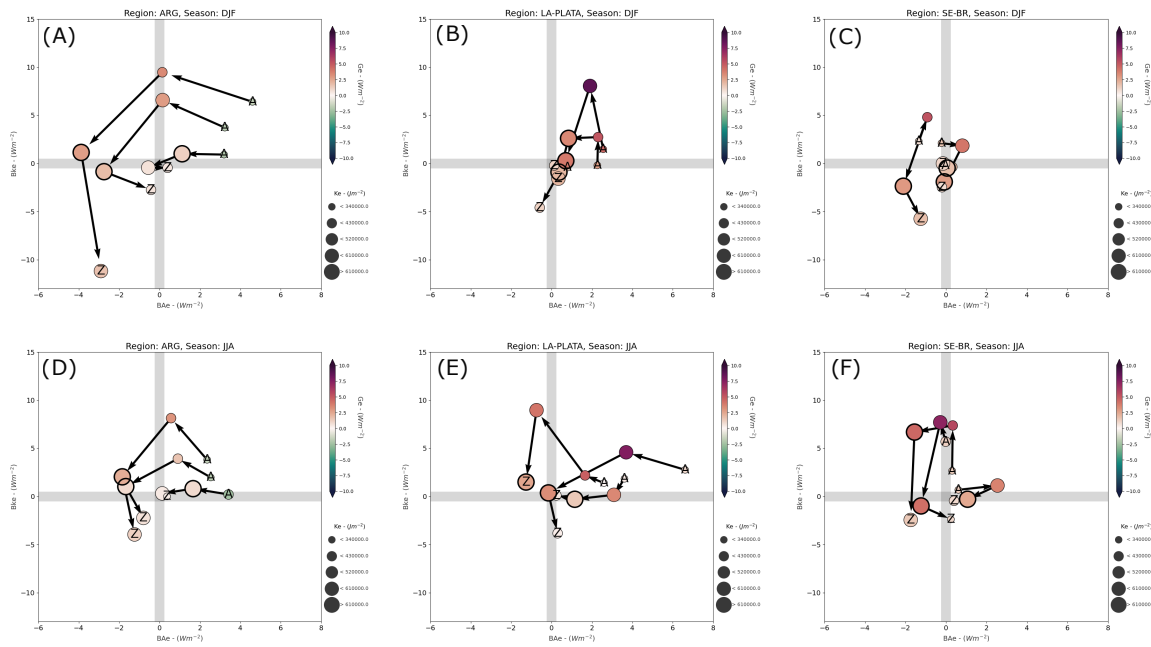


Figure 6.7: Lorenz Phase Space (LPS) diagram 2 for the EPs related to the "incipient, intensification, mature, decay" life cycle configuration, across DJF (a, b, c) and JJA months (c, d, e) and for each genesis region in Southwestern Atlantic Region: ARG (a, d), LA-PLATA (b, e) and SE-BR (c, f).

Meanwhile, for the LPS 2 diagram, the seasonal and inter-regional variability is more evident. For ARG, during both seasons, all EPs initiate with similar imports of  $A_E$ , with the magnitude of  $K_E$  imports increasing in the distinct EPs. During the intensification phase,  $K_E$  imports increase, while  $A_E$  imports tend to neutrality. In the mature phase,  $K_E$  tends to neutrality, while the systems start to export  $A_E$ . Lastly, in the decay stage, the boundary terms tend to neutrality, except for one cluster, where there are relatively high exports of  $K_E$ , accompanied by lesser exports of  $A_E$ .

For LA-PLATA during DJF, two clusters initiate importing  $A_E$ , with  $K_E$  imports increasing during the intensification phase. These imports are higher for one of the EPs. For the remaining phases and the other EP, the boundary terms tend to neutrality. For JJA, one cluster begins with  $A_E$  imports, tending to neutrality in later phases. Meanwhile,

another cluster starts with high imports of  $A_E$ , with  $K_E$  imports increasing but still moderate in the intensification phase, and both terms tending to neutrality later. For the remaining EP, there are initial imports of  $A_E$ , high  $K_E$  imports in the mature phase, and then finishing near neutrality.

Lastly, for SE-BR, the imports, especially of  $A_E$ , seem to be of lesser importance. For DJF, all but one EP present neutrality for the import of both forms of energy, with the exception related to imports of  $K_E$  in the initial phases and exports in the mature and decay phases. For JJA, one of the EPs presents neutrality for the boundary terms, except during the intensification phase, which shows modest contributions of  $A_E$  imports. The remaining EPs start with neutral  $A_E$  imports, with increasing  $K_E$  imports during the intensification phase. While for one of the EPs, both terms tend to neutrality after the intensification, for the other,  $BA_E$  becomes negative during the mature phase, though it remains small, and  $BK_E$  becomes negative during decay.

In conclusion, utilizing K-means clustering, the analysis for different regions — ARG, LA-PLATA, and SE-BR — during austral summer (DJF) and winter (JJA) demonstrates that while overall cyclonic systems generally follow a progression from lower to higher energy states through genesis and intensification, there are regional and seasonal variations. The  $G_E$  term showed distinct regional characteristics, with LA-PLATA exhibiting higher values and ARG showing lower values irrespective of the season, whereas SE-BR systems displayed higher  $G_E$  during winter. Additionally, each region-season group had EPs representing low, medium, and high energy states, with specific variations observed in LA-PLATA and SE-BR during winter. The LPS 2 diagram further highlighted regional differences in energy import/export behaviors, with ARG displaying varied import/export dynamics across life cycle phases, LA-PLATA showing differing patterns between DJF and JJA, and SE-BR generally presenting neutral energy imports/exports with some phase-specific deviations. These findings emphasize the importance of baroclinic and especially barotropic conversions for cyclone development on the SESA region, while imports of both eddy energy forms presents a more pronounced seasonal and inter-regional variability.

#### 6.1.4 Energy Patterns - Characteristics

In this section, the main characteristics of the EPs for the "incipient, intensification, mature, decay" life cycle configuration will be analyzed (Figure 6.8). As in Section 6.1.2,

these EPs were devised by initializing the K-means algorithm for the LEC results for systems in the dataset. EP1 presented the highest occurrence probability, relating to 52% of all systems, while EP2 and EP3 present progressively lesser probabilities of 36% and 11%, respectively. Surprisingly, even when the K-means algorithm was initialized for only the systems where the minimum relative vorticity is lower than the 0.9 quantile, the detected EPs were very similar to EP1. This indicates a consistency in the energy cycle for the systems within the dataset (Appendix H).

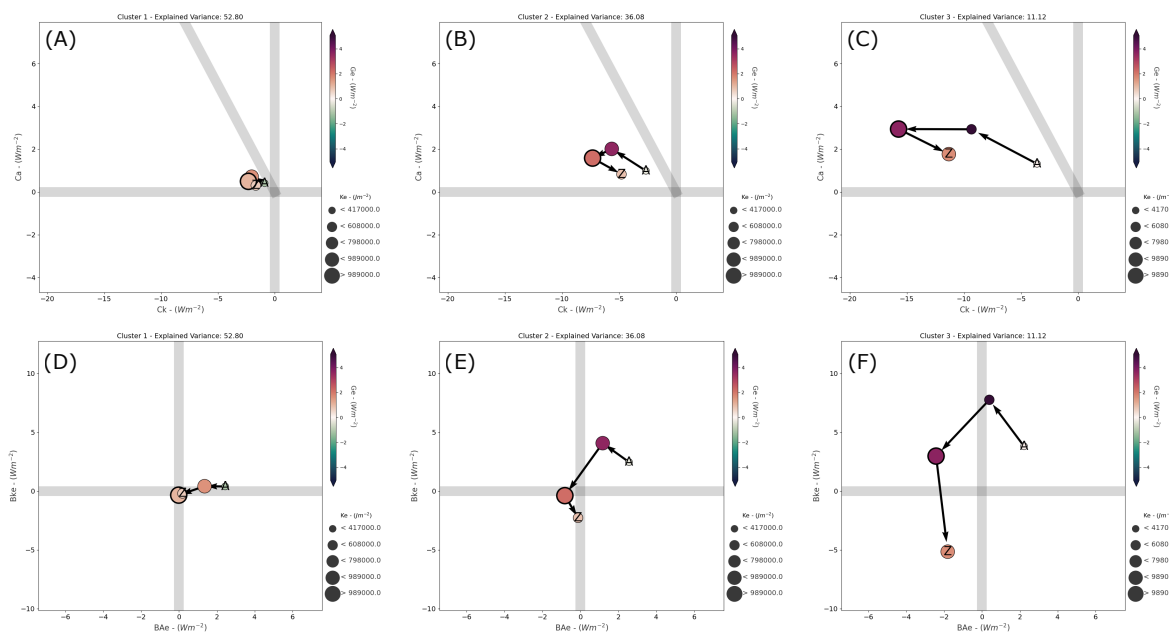
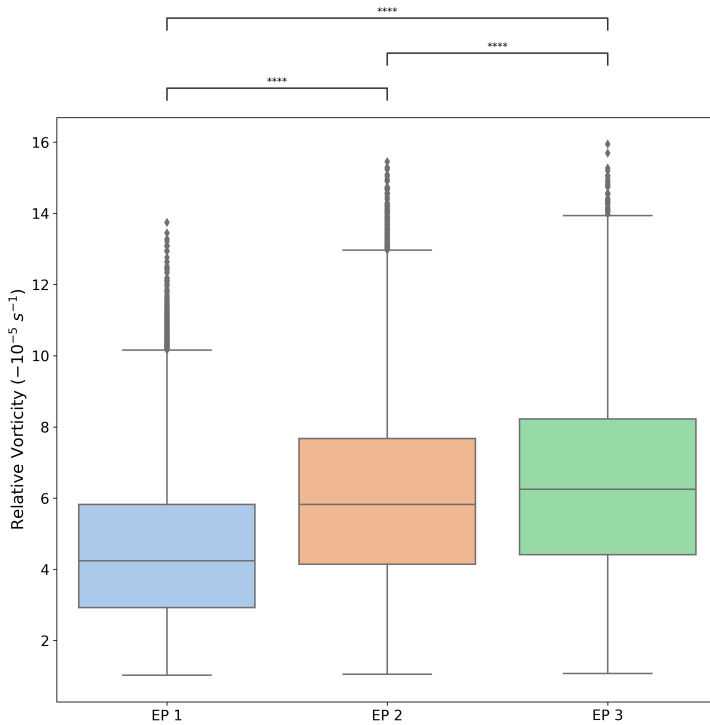


Figure 6.8: Lorenz Phase Space (LPS) diagrams 1 (a, b, c) and 2 (d, e, f) for EPs 1 (a, d), 2 (b, e), and 3 (c, f), related to the "incipient, intensification, mature, decay" life cycle configuration.

As indicated in Sections 6.1.2 and 6.1.3, the differences found in the EPs are related to their energy states. For the three EPs detected, EP1 has a low energy state, with EPs 2 and 3 presenting progressively higher energy states. Figure 6.9 compares the vorticity distributions across each EP to confirm whether the higher/lower energy states correlate with higher/lower system intensity. The Kruskal-Wallis test was used to assess overall differences in vorticity among the clusters, revealing significant disparities. Subsequently, pairwise comparisons using the Mann-Whitney U test identified specific clusters with significantly different vorticity values. The plot illustrates that the EPs exhibit significantly different vorticity values, as indicated by the stars, which represent p-values from the pairwise comparisons. Therefore, the hypothesis that each EP represents a distinct intensity cyclone category is confirmed.



*Figure 6.9:* Box plot comparing the vorticity distributions among different energy patterns (EPs). The Kruskal-Wallis test was used to determine if there were statistically significant differences in the vorticity distributions across the clusters. Significant differences identified by pairwise Mann-Whitney U tests are annotated on the plot.

In Figure 6.10, the relative frequency of each EP for each genesis region is represented. For ARG and SE-BR, the regional behavior is similar to the overall frequencies, with the most intense systems (EP3) presenting lower frequencies and relative frequencies increasing progressively for EP2 and EP1. However, for LA-PLATA, EP2 presents a higher relative frequency than EP1. Additionally, this region shows the highest relative frequencies for EP2 and EP3, indicating that it often generates more intense systems than the others.

Figure 6.11 displays the seasonality of each EP, represented as the counts of the cyclogenesis events associated with each EP. These events were defined as the first time step of the track for each system in the dataset. The results presented here differ from those presented in Section 6.1.3, as there the EPs for each region-season group were determined independently, while here, the seasonal behavior of the mean EPs is observed.

Overall, there is a higher occurrence of EP1 in DJF, followed by SON. EP2 presents a more homogeneous distribution across seasons, while EP3 is especially active during JJA, with low activity in DJF. This indicates a higher occurrence of stronger cyclonic systems, with more active energy conversion and convective activity during JJA, and weaker systems

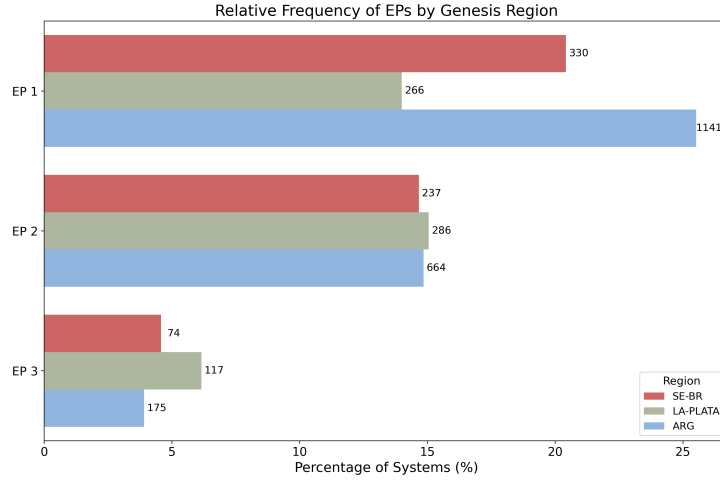


Figure 6.10: Relative regional variability of each energy pattern (EP) for each genesis region in the Southwestern Atlantic. The annotations alongside each bar represent the total count for each EP for the given region.

during DJF. This result is corroborated by Chapter 4 (Figure 4.10), which indicates the occurrence of stronger systems during JJA than DJF.

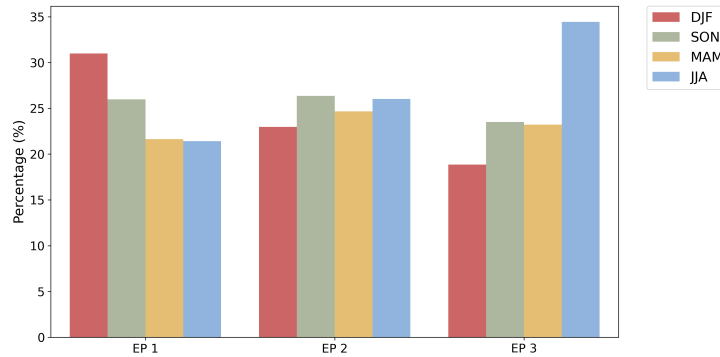


Figure 6.11: Box plot comparing the Seasonality of energy patterns (EPs) in the Southwestern Atlantic region, with the y-axis representing the percentage of cyclones occurring in each season within the respective EP.

Figure 6.12 illustrates the interannual variability of each EP from 1979 to 2020. While the results do not indicate clear trends in EP occurrence over the years, they do reflect significant interannual differences. Notably, EP3 exhibits higher variability, with relative yearly frequencies ranging from 1% to 5%, whereas EPs 1 and 2 demonstrate more homogeneous behavior, typically with relative frequencies between 2% and 3%. Exceptionally high frequencies of EP1 were observed in 1996 and 2013, with particularly low frequencies in 2016. The relative importance of EP1 is noteworthy due to the impacts caused by strong cyclonic systems in coastal regions (de Souza and da Silva, 2021; Cardoso et al.,

2022; Leal et al., 2023). This variability could suggest low-frequency climate influences on cyclone genesis and development in the South Atlantic region, such as those from the El Niño-Southern Oscillation and the Southern Annular Mode, which will be explored in future studies.

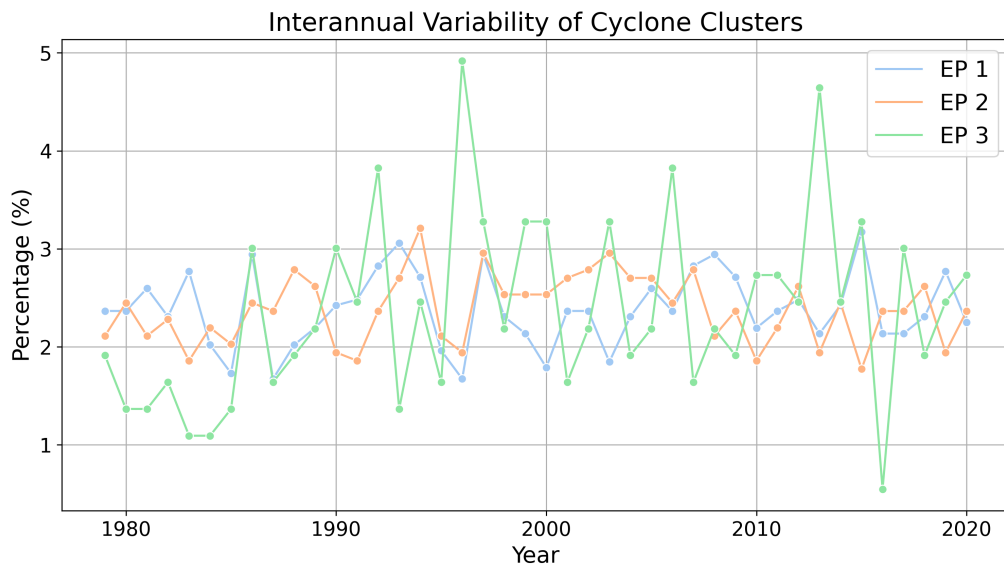


Figure 6.12: Interannual variability of energy patterns (EPs) from 1979 to 2020. The y-axis represents the percentage of cyclones each year for different EPs, normalized to total cyclones numbers for each EP.

## 6.2 Physical Mechanisms

### 6.2.1 Barotropic and Baroclinic Instability

Through Chapter 5 and Section 6.1 the results for the LEC for all systems forming on the cyclogenesis regions located near South America, for the period ranging from 1979 and 2020 were explored and discussed. The results indicates an ominous importance of baroclinic and barotropic conversions for the development of the cyclonic systems analysed. The role of baroclinic instability on mid-latitude cyclogenesis, and the further development of these systems, is deeply established on the literature (Bjerknes and Solberg, 1922; Eady, 1949; Charney, 1947; Petterssen and Smebye, 1971; Hoskins and Valdes, 1990). However, the relationship of barotropic instability and extratropical cyclogenesis and development is not often explored.

Given that the relationship between extratropical cyclones and barotropic instability might challenge the common notions in the scientific literature, the current section aims

to demonstrate the validity of the presented results. An analysis of the Rayleigh-Kuo criterion will be performed to determine if barotropic instability is indeed occurring in the systems analyzed (Section 3.6). For this, only the systems associated with EP1 will be used, as they present the highest energy states (Figure 6.8). These systems tracks are represented on Appendix I. Also, only data for the intensification phase will be used, as these conversions are often strong during this phase and for ensuring the dynamics related to the system intensification is captured.

Firstly, the vertical levels where the baroclinic and barotropic conversions are most intense are assessed. Figure 6.13 displays the vertical distribution of  $C_A$  and  $C_E$  terms for EP1 systems. It can be seen that for  $C_A$ , the most positive values (indicating baroclinic conversions) are found near the surface, at 1000 hPa. This agrees with the Polar Front Theory, which suggests that low-level baroclinicity initiates cyclogenesis and maintains cyclone development (Bjerknes and Solberg, 1922), as well as with Petterssen type A cyclones (Petterssen and Smebye, 1971). Positive mean values can also be seen for  $C_A$  on the upper troposphere, but with smaller overall magnitudes. For barotropic conversions, however, the lowest values ( $K_Z \rightarrow K_E$  conversions) are found in the upper troposphere, with the lowest mean values at 300 hPa. This vertical distribution of  $C_K$  is consistent with the mean jet vertical positioning, indicating the importance of upper-level jet streams in providing kinetic energy to the eddy motions.

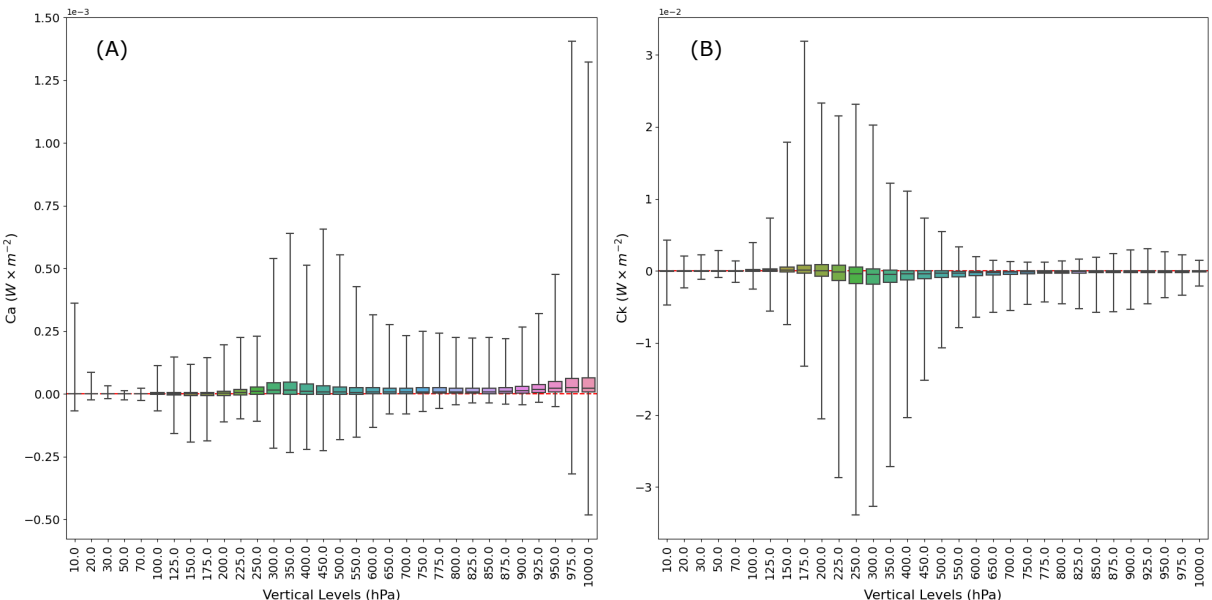


Figure 6.13: Boxplots for each vertical level, for (A)  $C_A$  and (B)  $C_E$  terms, for energy pattern (EP) 1 systems.

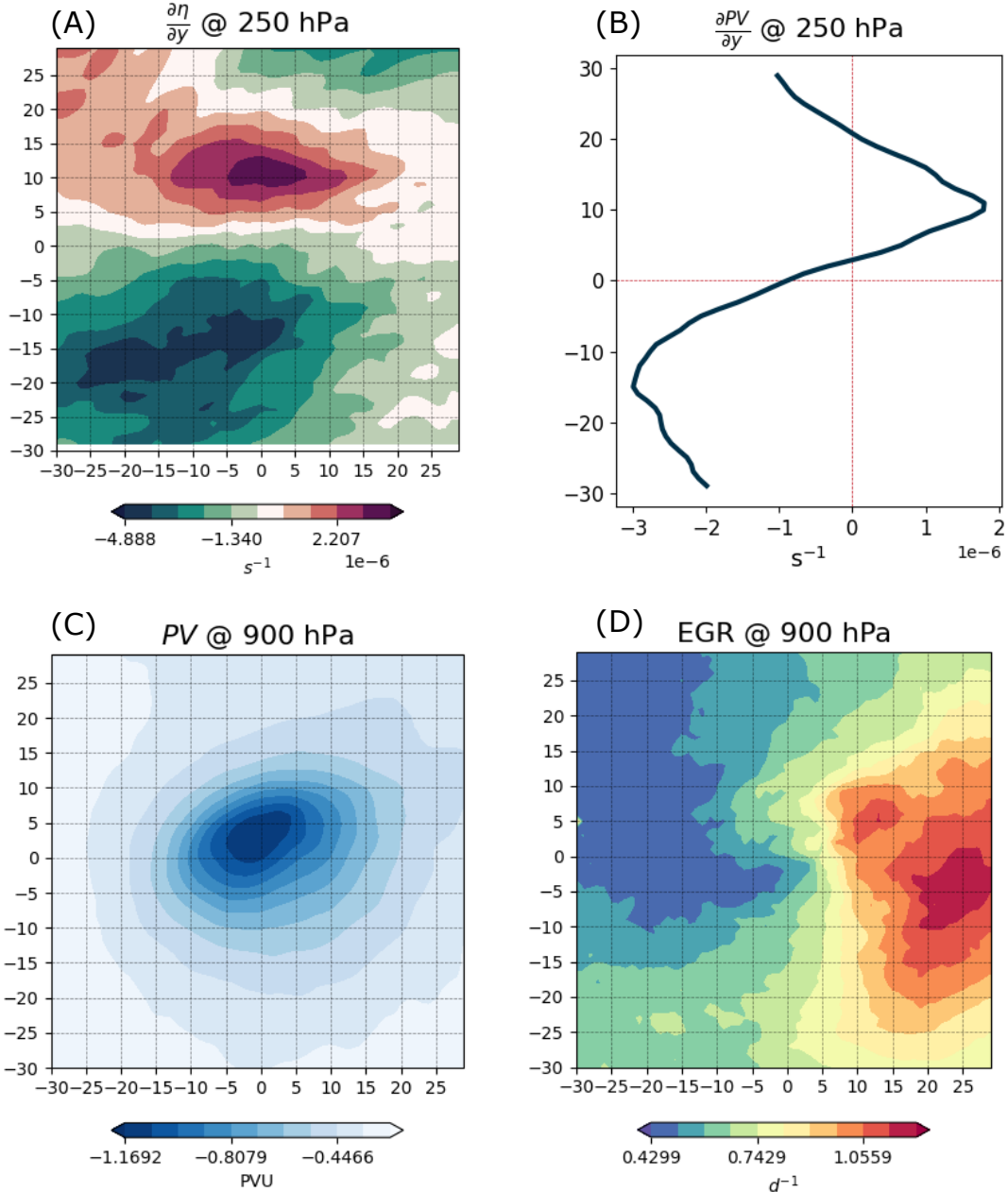
Given such vertical distributions for  $C_A$  and  $C_K$  terms, composites of meteorological fields were prepared to assess the occurrence of baroclinic and barotropic instabilities at these distinct levels. For this purpose, the maximum Eady Growth Rate (EGR) fields were evaluated and the Rayleigh-Kuo (RK) criterion was applied. These metrics are shown in Figure 6.14, for the composites of all systems related to EP1, across the mean fields during the intensification phase.

Figure 6.14a demonstrates the RK criterion, showing the derivative of absolute vorticity ( $\eta$ ) at 250 hPa with respect to latitude. A strong meridional gradient of  $\eta$  is evident, with a sign reversal near the cyclone center, satisfying the RK criterion and indicating that barotropic instability might indeed be occurring. Figure 6.14b shows the zonally averaged meridional derivative of  $\eta$ , providing a clearer illustration of the RK criterion.

Meanwhile, Figure 6.14c shows the potential vorticity composites. Here, the 900 hPa level was used instead of 1000 hPa due to artifacts related to the vertical coordinate interpolation from height to isobaric levels when computing the EGR fields. This figure reveals an area of intense cyclonic activity in the middle of the Semi-Lagrangian domain, associated with low-pressure systems and significant vorticity. Figure 6.14d shows the EGR composites, demonstrating a strong baroclinic region east/southeast of the cyclone centers, indicating regions susceptible to baroclinic instability, which is in agreement with mean cyclone displacement on SESA region (Hoskins and Hodges, 2005; Gramcianinov et al., 2019). These areas coincide with sharp PV gradients observed in Figure 6.14c, reinforcing these areas as susceptible to cyclonic development.

These presented results reinforce the conclusions from Chapter 5 and Section 6.1 that both baroclinic and barotropic instabilities act in consonance for cyclone genesis and development in the SESA region. While barotropic instability acts in the upper troposphere, extracting energy from the jets for cyclonic development, baroclinic instability in the lower troposphere transforms the meridional temperature gradients into eddy potential energy, ultimately feeding eddy kinetic energy.

Hoskins et al. (1985) described the general situation where an upper-level PV cyclone acting over a low-level baroclinic region triggers surface cyclogenesis. The results shown here indicate that the baroclinic chain is initially stronger, with barotropic conversions increasing afterward and peaking at the cyclone's mature phase (Section 5.2.3). If these baroclinic conversions occur at lower levels, while barotropic conversions occur at upper



*Figure 6.14:* Composite Analysis of Barotropic and Baroclinic Instabilities. (a) The derivative of absolute vorticity ( $\eta$ ) at 250 hPa with respect to latitude, illustrating the Rayleigh-Kuo (RK) criterion. (b) Zonally averaged meridional derivative of  $\eta$ . (c) Potential vorticity (PV) composites at 900 hPa. (d) Maximum Eady Growth Rate (EGR) composites at 900 hPa.

levels, this suggests a distinct mechanism as proposed by Hoskins et al. (1985), although this requires further exploration.

It is important to recognize, however, that the approach adopted has its limitations. Firstly, the Rayleigh–Kuo criterion is derived from a linear stability analysis, which assumes small perturbations to the basic flow and does not account for the nonlinear processes that can become significant as instabilities grow and evolve. It is also based on idealized conditions, such as an inviscid (non-viscous) and incompressible flow, whereas real atmospheric and oceanic flows are neither purely inviscid nor incompressible. Furthermore, it is a necessary but insufficient criterion for instability (see Read et al. (2020)). However, the overall  $K_Z \rightarrow K_E$  conversions, in consonance with satisfying the RK criterion, provide strong evidence for barotropic instability being related to cyclone development in the SESA region.

### 6.2.2 Comparing with the Fixed Framework

The results shown so far indicate that barotropic instability plays an important role in extratropical cyclone development. But why haven't previous studies detected this phenomenon? As the use of the Semi-Lagrangian framework is rarely seen in the literature, the answer might lie in the intrinsic differences between the Semi-Lagrangian and the more commonly used Fixed framework.

This section aims to explore this dichotomy. Here, the same systems analyzed in Section 6.2.1 (the systems related to EP1) are analyzed, but now using the Fixed framework. In Figure 6.15 it is shown the LPS diagram 1 for EP1 systems mean values. In this case, the LEC of EP1 systems were computed using the Fixed framework and then, for each development phase (incipient, intensification, mature and decay), the mean values were computed, excluding outliers. The LPS indicates a mean behaviour where the cyclones have genesis and intensify with shared contributions from moist baroclinic and barotropic conversions, with the barotropic conversions becoming more important on the mature and decay phases. These results indicate that the Fixed methodology also evidences the importance of barotropic conversions on cyclonic systems in SESA region, but with lower mean magnitude than the Semi-Lagrangian method. Also, caution should be taken into examining the results form the Fixed approach, as, for EP1 cases there were systems with high displacement (Appendix I), therefore their computational domain encompassed

almost entirely the Southern Atlantic region and most certainly more than one cyclonic system was acting on that domain during the analysis.

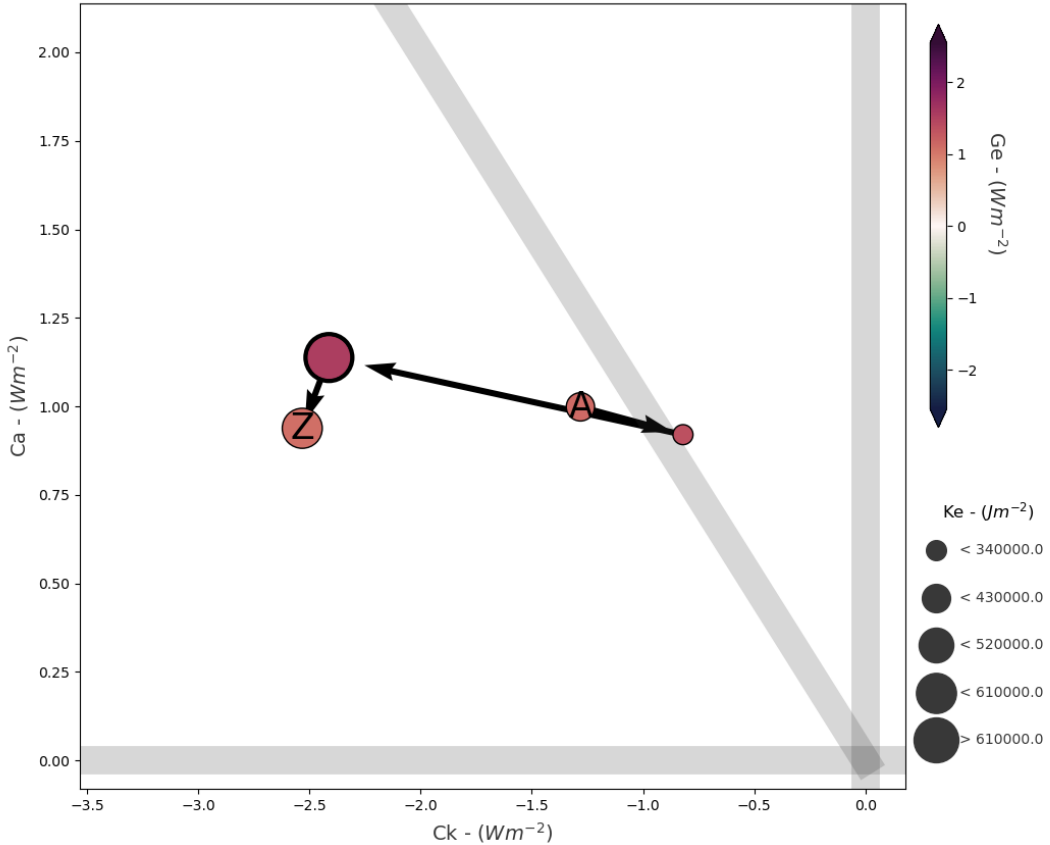


Figure 6.15: Lorenz Phase Space (LPS) diagram 1 for energy pattern (EP) 1 systems mean values for each phase (incipient, intensification, mature and decay), computed using a fixed framework.

The following step was to investigate the role of the LEC methodology in affecting the magnitude of the barotropic and baroclinic conversions. Figure 6.16 displays the same analysis as Figure 6.14, but for the composites using the Fixed framework. Although there are sign reversals in the meridional  $\eta$  derivative zonally averaged values, the spatial field displays a less cohesive spatial field compared to the Semi-Lagrangian results. For the PV field, an increase in its magnitude can be seen poleward, which is the expected behavior. Additionally, for EGR, a modest baroclinic region can be seen from the central to eastern parts of the domain. This is again the expected behavior for this region, with magnitudes comparable to the climatological values (de Souza and Piva, 2023). There is also a spot of

high baroclinicity to the west, near the interpolated domain area equivalent to the ARG cyclogenesis region. Although this high baroclinic region in the west might be related to cyclogenesis in the Southwestern region, the composites do not show a clear signature of cyclonic development as in Figure 6.14.

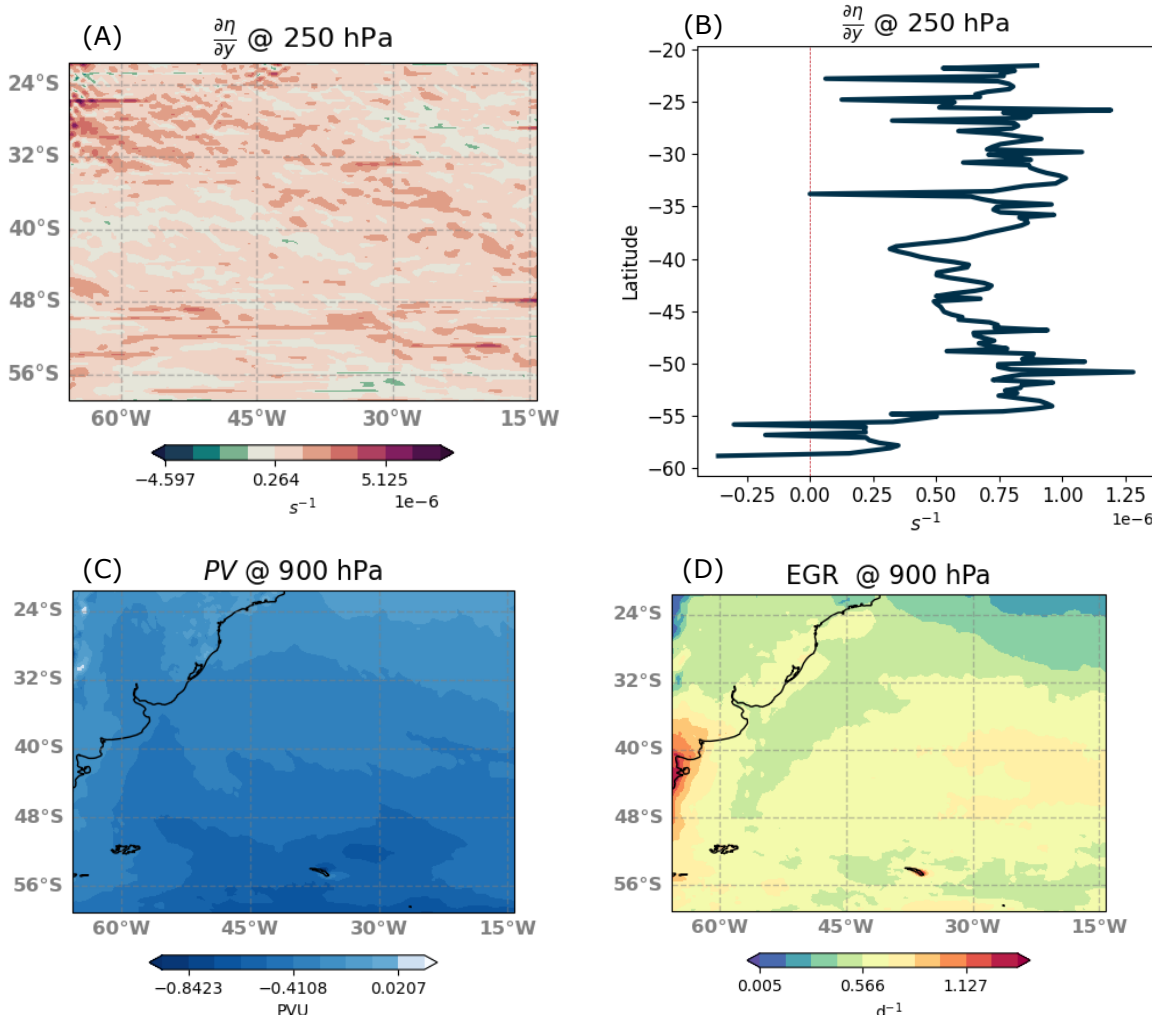


Figure 6.16: Composite Analysis of Barotropic and Baroclinic Instabilities using the Fixed framework. (a) The derivative of absolute vorticity ( $\eta$ ) at 250 hPa with respect to latitude, illustrating the Rayleigh-Kuo (RK) criterion. (b) Zonally averaged meridional derivative of  $\eta$ . (c) Potential vorticity (PV) composites at 900 hPa. (d) Maximum Eady Growth Rate (EGR) composites at 900 hPa.

To better illustrate the effect of the methodology on the results, let us examine a case study, comparing the results for both methodologies. Figure 6.17 showcases the results for system 19820099, for the time period where the barotropic conversions were most intense. Figure 6.17a illustrates the computational domain used for running the Fixed framework, while its track is displayed in Figure 6.17b, together with the Semi-Lagrangian domain defined for that given time step.

The EGR fields for the Fixed domain display a maximum in the southern parts of South America, near  $70^{\circ}W$  (Figure 6.17c), while the cyclonic center is at  $36^{\circ}W$  (Figure 6.17d). Here, the EGR fields for 875 hPa are displayed due to the occurrence of artifacts related to the vertical interpolation in the 900 hPa fields. Thus, despite the mean EGR values for the Fixed domain being higher ( $0.55 \text{ day}^{-1}$ ) than those for the Semi-Lagrangian domain ( $0.45 \text{ day}^{-1}$ ), these values are related to the maximum away from the cyclone center. This reinforces the reasoning that the use of the Fixed framework captures dynamics unrelated to cyclonic system development. For the meridional derivative of  $\eta$ , regions inside the Fixed domain satisfying the RK criterion can be seen, such as in Southern Argentina (Figure 6.17e). However, inside the Semi-Lagrangian domain, near the cyclone center, this effect is more pronounced (Figure 6.17f).

The results presented here suggest that the Semi-Lagrangian framework better represents the process of barotropic instability compared to the Fixed framework. When Fixed domains are used for computing the LEC of cyclonic systems, they have to be large enough to capture the system's total displacement, which is on average approximately 5,000 km for the South Atlantic, but can reach up to 10,000 km (Figure 4.8). Therefore, such domains would definitely capture the baroclinic regions in the mid-latitudes. However, barotropic conversions occur more localized in specific areas and thus can be overshadowed when analyzing larger domains using the Fixed framework. For the Semi-Lagrangian framework, however, the computational domain is centered on the cyclonic system, where the barotropic conversions are well represented. Nevertheless, it was shown that the use of Fixed domains captures energetics of regions not associated with the eddy development, which could potentially lead to misleading results.

Furthermore, the use of the Fixed framework for computing the LEC for EP1 systems demonstrated that even with this framework, the importance of barotropic conversions is still evident. Thus, the apparent underestimation of the role of barotropic instability in extratropical cyclone development is not a methodological issue. It can be argued that either the role of barotropic conversions is more pronounced in this methodology only for the most intense systems, whose energetics might not have been analyzed previously, or that this issue might arise from the lack of studies investigating the energetics of such a large number of systems.

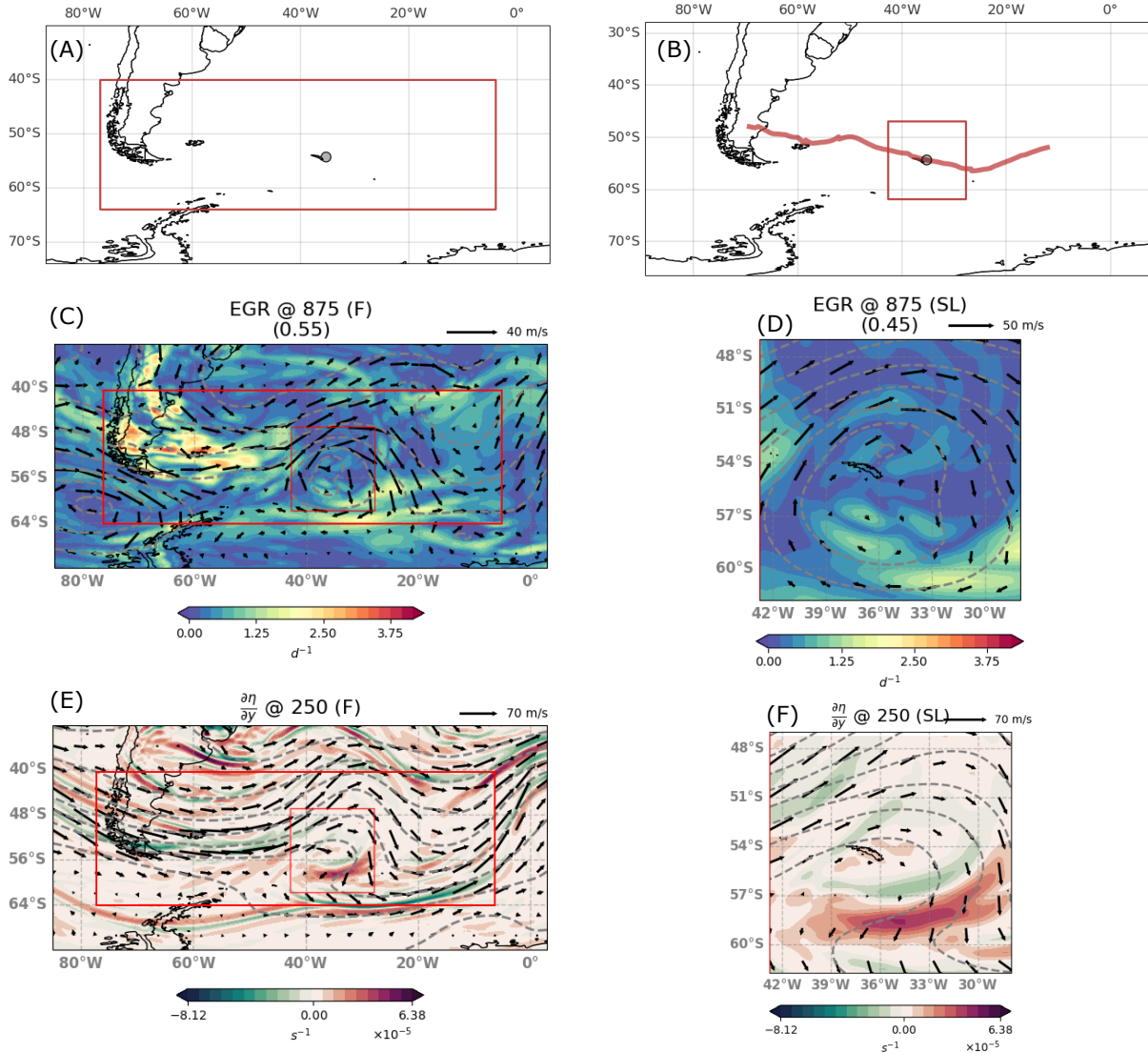


*Figure 6.17:* Comparison of barotropic and baroclinic instability analysis between the Fixed and Semi-Lagrangian frameworks for system 19820099, during the time step of most intense  $K_Z \rightarrow K_E$  conversions. (a) Computational domain for the Fixed framework, indicated by the larger rectangle. (b) Track of the system with the Semi-Lagrangian domain, indicated by the smaller rectangle. (c) EGR fields for the Fixed domain, with the averaged EGR value in the domain shown in parentheses ( $0.55 \text{ day}^{-1}$ ). (d) EGR fields for the Semi-Lagrangian domain, with the averaged EGR value in the domain shown in parentheses ( $0.45 \text{ day}^{-1}$ ). (e) Meridional derivative of  $\eta$  for the Fixed domain. (f) Meridional derivative of  $\eta$  for the Semi-Lagrangian domain.

### 6.3 Summary and Concluding Remarks

This chapter presented the Lorenz Phase Space (LPS) diagrams, a visualization tool aimed at providing a diagnostic of the eddy-related energetics inspired by the Hart (2003) Cyclone Phase Space. This tool allows for a quick assessment of the dynamical mechanisms related to cyclone development, such as baroclinic and barotropic energy conversions, imports of both eddy kinetic and available potential energy, as well as the generation of eddy available potential energy due to diabatic processes (convective activity).

The energy cycle of all systems with genesis in the Southwestern Atlantic and Southeast America (SESA) region was dissected for each life cycle phase and then clustered using the K-means algorithm to determine their energy patterns (EP). Three EPs were found, and the differences among them were defined by their energy states. EP1 represents the most common cyclones in the SESA region, presenting low energy states and the lowest maximum relative vorticity values. Meanwhile, EPs 2 and 3 display progressively increased energy states and higher maximum vorticity values.

The identified EPs indicate the following behavior for the energy cycle of cyclones in the SESA region:

- During cyclogenesis and incipient development, the systems present low baroclinic and barotropic conversions, but with imports of eddy APE. The imports of eddy kinetic energy are initially neutral, but more intense systems present progressively higher levels of imports of such energy.
- In the intensification phase, the baroclinic conversions and imports of eddy kinetic energy are often at their maximum, with their relative magnitude increasing from EP1 to 3. During this phase, imports of eddy APE become neutral.
- Both baroclinic conversions and imports of eddy kinetic energy tend to diminish in the mature phase. Meanwhile, barotropic conversions become more intense and the systems begin to export eddy APE, with progressively higher values for both terms from EPs 1 to 3.
- The baroclinic and barotropic conversion terms, as well as boundary fluxes of eddy APE, tend to become more neutral during the decay phase, while the export of eddy kinetic energy tends to intensify.

Significant variability in this mean behavior across different life cycle configurations or genesis regions and seasons was not found, although the overall magnitude of the terms tends to vary, with some exceptions noted.

The importance of barotropic conversions for cyclone development was not evidenced by previous studies. To determine whether barotropic instability was occurring near the cyclone systems, it was investigated if the Rayleigh-Kuo criterion was being satisfied, which was confirmed by the analysis for EP1 systems. These results were replicated using the Fixed framework, revealing that even with a different methodology, the signal of barotropic conversions was still noted, although weakened.

Nevertheless, the barotropic conversion term  $C_K$  is composed of five distinct terms: meridional advection of zonal momentum, meridional shear of meridional wind, interaction of eddy zonal wind with zonal meridional wind, and vertical advection of zonal momentum. Only the first three terms are strictly related to the classical view of barotropic instability (Rayleigh, 1895; Kuo, 1949; Holton, 1973). Meanwhile, the last two terms involve vertical transports of momentum, which are intimately related to the presence of vertical wind shear and, therefore, due to the thermal-wind relationship, baroclinicity. A future study will be conducted to assess which terms dominate in the barotropic conversions. The author believes this can help to better understand the dynamical processes presented here and will open avenues for further research.

In conclusion, the results shown here indicate barotropic instability as an important dynamical mechanism for cyclone development in the SESA region. The lack of previous indication of such behavior is due to either a lack of analysis of such a large dataset or due to methodological limitations, or both.

It is proposed here to use the LPS diagrams as the visual representation of the dynamic processes related to cyclone development, similarly to how Hart (2003) is a representation of the cyclones' thermal structure and symmetry. In Figure 6.18, LPS diagram 1 is represented along with the dynamical processes related to each of its quadrants. Cyclones in the top-right quadrant are said to be related to baroclinic instability, while in the bottom-left, barotropic instability, and in the top-left, both instabilities are occurring. Lastly, in the bottom-right, the eddy is feeding the zonal circulation.

While this research contributed to understanding the mechanisms related to each quadrant in LPS diagram 1, this is not the case for LPS diagram 2 (Figure 6.19). While the

imports of eddy kinetic energy have been suggested to be related to downstream development (Michaelides et al., 1999), this relationship was not further investigated. Also, for imports of eddy APE, from the mathematical expression for such term, it is tentative to relate it to thermal advection or heat fluxes, previously related as important mechanisms for cyclone development on SESA region (Gozzo et al., 2014; Dutra et al., 2017; Gramcianinov et al., 2019). It is then suggested here for future research to investigate such relationships.

Nevertheless, the LPS diagrams are  not yet ready to be used as a diagnostic tool for cyclone classification. For this, future research should be conducted on examining the EPs for distinct cyclonic systems, such as tropical and subtropical cyclones. It is the author's best wish to continue with this research, providing an integrated framework for cyclone classification, alongside with Hart (2003) diagrams, which will account for cyclones' Material, Formal, Efficient, and Final Causes.

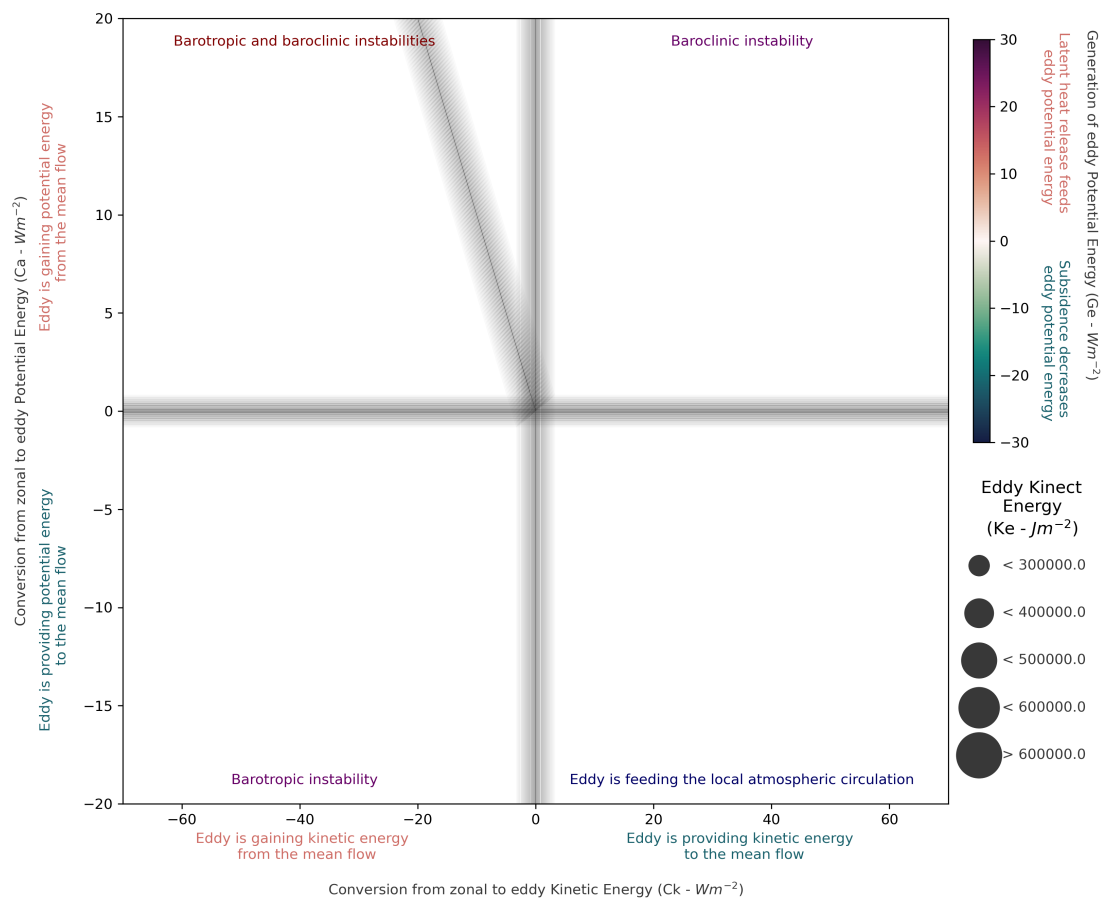


Figure 6.18: Lorenz Phase Space (LPS) diagram 1 representation with each dynamical process related to each quadrant represented.

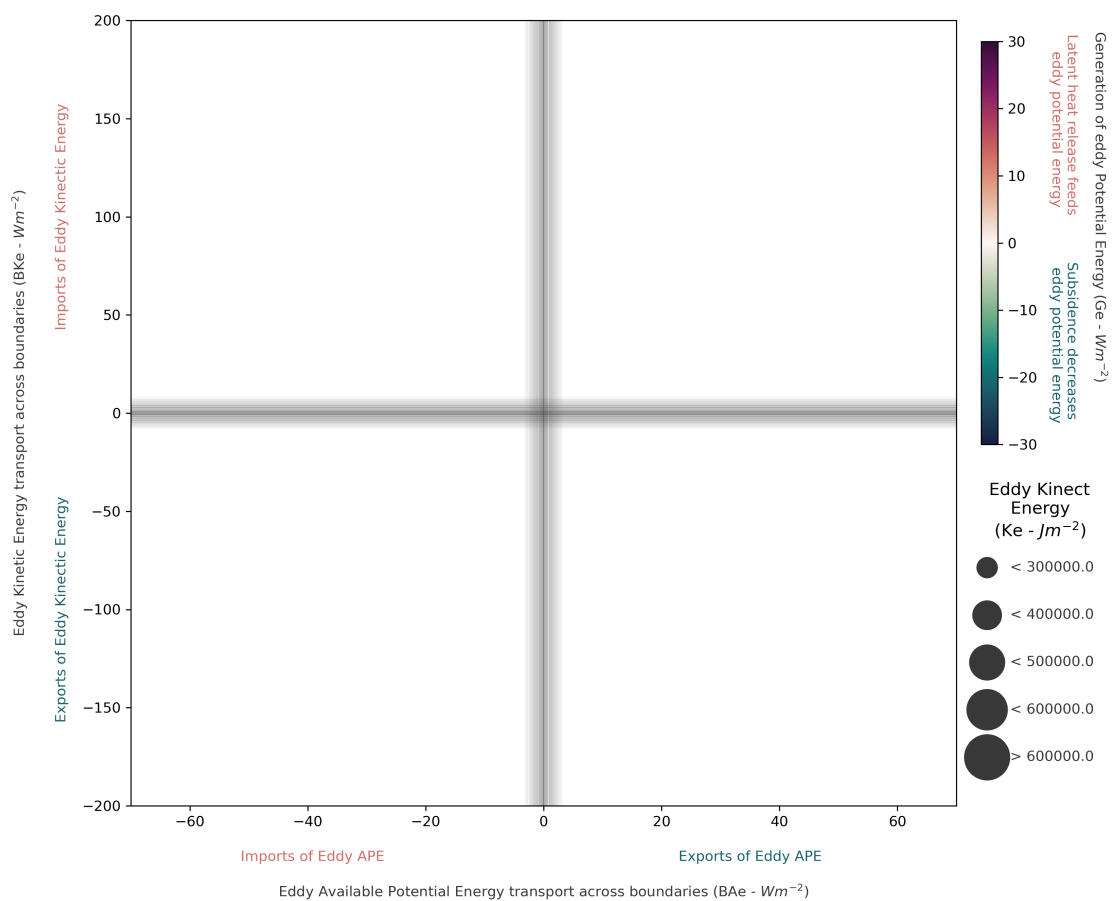


Figure 6.19: Lorenz Phase Space (LPS) diagram 2 representation with each dynamical process related to each quadrant represented.



## Chapter 7

---

# Conclusions

The main goal of this thesis was to determine the primary dynamical mechanisms related to cyclone development in the Southwestern Atlantic and Southeast American regions during each of their development phases. For this, a database of cyclonic system tracks with genesis in this region was utilized. This database was constructed by detecting cyclones from their central relative vorticity at 850 hPa and includes all systems in the South Atlantic region from 1979 to 2020. Subsequently, a program called CycloPhaser was created to dissect the relative vorticity series into distinct life phases, based on its maximum, minimum, and derivative values. The CycloPhaser was then used to construct a climatology of cyclone life cycle phases from the original track database, which also allowed for investigating the mean characteristics of cyclones across each phase.

The next step involved programming an application to compute the Lorenz Energy Cycle and using it to analyze the energetics of all cyclones in the database. The mean characteristics of the systems' energy cycles were investigated and dissected for each life cycle phase. Afterward, the K-means algorithm was employed to determine the energy patterns. Finally, the dynamical mechanisms related to cyclonic system development, as indicated by the energy cycle analysis, were further investigated.

### 7.1 *Summary of Main Findings*

This thesis provides significant insights into the detection, analysis, and energetics of 7,531 cyclonic systems in the Southwestern Atlantic region through the development and application of new methodologies.

First, the CycloPhaser's ability to detect and analyze cyclone life cycles was demons-

trated, highlighting key patterns in cyclone behavior. The analysis confirmed known cyclogenesis regions, cyclone paths, and statistical properties such as average lifetime and displacement, providing new insights related to each development phase. It was revealed that cyclonic systems exhibit multiple life phase configurations, with some configurations including secondary life cycle development. The analysis of spatial distributions across various phases of the cyclone life cycle reveals that systems often intensify and mature near their genesis regions, decaying over a broader area.

Second, the thesis delved into the Lorenz Energy Cycle (LEC) to assess the energetics of the selected cyclonic systems in the Southwestern Atlantic. Using a Semi-Lagrangian approach, the study revealed high variability in LEC terms, highlighting the importance of the baroclinic chain, convective activity, and barotropic conversions in cyclone development. The main mode of variability emphasized the significance of these processes throughout the cyclone life cycle, from cyclogenesis to decay, with the moist baroclinic chain peaking during the intensification phase and the barotropic conversions peaking during the mature phase. Nevertheless, these conversions continue even during the decay phase, where exports and especially dissipation of eddy kinetic energy lead to the eventual dissipation of the eddy. Furthermore, there is a relevant group of systems for which the imports of eddy APE are important during the cyclones' initial life stages.

Third, the Lorenz Phase Space (LPS) diagrams were introduced as a diagnostic tool for eddy-related energetics. These diagrams provided a visual representation of the dynamic mechanisms in cyclone development, including baroclinic and barotropic conversions and imports of eddy kinetic and available potential energy. The analysis identified three energy patterns (EPs) with distinct energy states and vorticity values, providing new perspectives on cyclone energetics. Furthermore, the occurrence of barotropic and baroclinic instabilities was further indicated through the application of the Rayleigh-Kuo criterion and the analysis of the maximum Eady Growth Rate for composites and case studies.

## 7.2 Final Remarks and Recommendations for Future Work

The Lorenz Energy Cycle of cyclonic systems in the Southwestern Atlantic and Southeast America region indicates that barotropic instability plays a pivotal role in extratropical cyclone development, which is commonly associated with baroclinic instability. Although

the occurrence of such instabilities was not directly assessed, the indications from the energy cycle and the Rayleigh-Kuo criterion provide strong evidence for this argument. It is also demonstrated that the use of the Fixed framework for computing the Lorenz Energy Cycle underestimates the role of barotropic conversions while capturing baroclinic effects unrelated to cyclone development, which might produce misleading results.

The findings presented here lead to the following research questions, left as suggestions for future work:

- Why do cyclones have distinct life cycle configurations? For example, why do some systems not present an incipient stage, and why do others present a secondary life cycle? To answer these questions, the energy cycle (as done in the current study) as well as vorticity and heat budgets (Dutra et al., 2017, e.g.) can be employed, and the different life cycle configurations can be assessed.
- How does climate change affect the spatial distribution of cyclone phases in the South Atlantic region? Will cyclones mature closer to the coast? Will phase characteristics (duration, displacement, etc.) change? This could be evaluated using climate models, as has already been done in the literature (Reboita et al., 2018; de Jesus et al., 2022, e.g.), but using the CycloPhaser program to diagnose differences in life cycle phases.
- Which terms of the barotropic conversion term  $C_K$  present the dominant magnitude for the cyclones in the current dataset? Do their behaviors change across distinct life cycles? This could be evaluated by modifying the Lorenz-cycle program to export the results for each distinct term and comparing the results.
- What are the actual physical mechanisms related to the imports of eddy APE and kinetic energy? To investigate the former, vorticity and heat budgets can be employed (Dutra et al., 2017, e.g.), while for the latter, an initial point could be investigating whether it can be attributed to downstream development (Piva et al., 2010, e.g.).



## Bibliography

- Acevedo O. C., Pezzi L. P., Souza R. B., Anabor V., Degrazia G. A., Atmospheric boundary layer adjustment to the synoptic cycle at the Brazil-Malvinas Confluence, South Atlantic Ocean, *Journal of Geophysical Research: Atmospheres*, 2010, vol. 115
- Albuquerque M. d. G., Leal Alves D. C., Espinoza J. M. d. A., Oliveira U. R., Simões R. S., Determining shoreline response to meteo-oceanographic events using remote sensing and unmanned aerial vehicle (UAV): case study in southern Brazil, *Journal of Coastal Research*, 2018, pp 766–770
- American Meteorological Society, 2012 Cyclone <https://glossary.ametsoc.org/wiki/Cyclone>
- Aristotle A., Aristotle Metaphysics. vol. 1, Harvard University Press Cambridge, MA, 1933
- Arthur D., Vassilvitskii S., K-Means++: The Advantages of Careful Seeding. In Soda , vol. 8, 2007, p. 1027
- Azad R., Sorteberg A., The vorticity budgets of North Atlantic winter extratropical cyclone life cycles in MERRA reanalysis. Part I: Development phase, *Journal of the Atmospheric Sciences*, 2014a, vol. 71, p. 3109
- Azad R., Sorteberg A., The vorticity budgets of North Atlantic winter extratropical cyclone life cycles in MERRA reanalysis. Part II: Decaying phase, *Journal of the Atmospheric Sciences*, 2014b, vol. 71, p. 3129
- Balmaceda Huarte R., Olmo M. E., Bettolli M. L., Poggi M. M., Evaluation of multiple re-analyses in reproducing the spatio-temporal variability of temperature and precipitation indices over southern South America, *International Journal of Climatology*, 2021

Bembenek E., Merlis T. M., Straub D. N., Influence of latitude and moisture effects on the barotropic instability of an idealized ITCZ, *Journal of the Atmospheric Sciences*, 2021, vol. 78, p. 2677

Bengtsson L., Hodges K. I., Keenlyside N., Will extratropical storms intensify in a warmer climate?, *Journal of Climate*, 2009, vol. 22, p. 2276

Bjerknes J., On the structure of moving cyclones, *Monthly Weather Review*, 1919, vol. 47, p. 95

Bjerknes J., Holmboe J., On the theory of cyclones, *Journal of Atmospheric Sciences*, 1944, vol. 1, p. 1

Bjerknes J., Solberg H., Life cycle of cyclones and the polar front theory of atmospheric circulation. Grondahl, 1922

Black M. T., Pezza A. B., A universal, broad-environment energy conversion signature of explosive cyclones, *Geophysical Research Letters*, 2013, vol. 40, p. 452

Bluestein H. B., *Synoptic-dynamic Meteorology in Midlatitudes: Observations and theory of weather systems.* vol. 2, Taylor & Francis, 1992

Booth J. F., Naud C. M., Jeyaratnam J., Extratropical cyclone precipitation life cycles: A satellite-based analysis, *Geophysical Research Letters*, 2018, vol. 45, p. 8647

Brennan F. E., Vincent D. G., Zonal and eddy components of the synoptic-scale energy budget during intensification of hurricane Carmen (1974), *Monthly Weather Review*, 1980, vol. 108, p. 954

Brown Jr J. A., A diagnostic study of tropospheric diabatic heating and the generation of available potential energy, *Tellus*, 1964, vol. 16, p. 371

Bulic I., Limited area energy budget during a life cycle of Genoa cyclone (18-21 November 1999), NUOVO CIMENTO-SOCIETA ITALIANA DI FISICA SEZIONE C, 2006, vol. 29, p. 167

Burpee R. W., The origin and structure of easterly waves in the lower troposphere of North Africa, *Journal of the Atmospheric Sciences*, 1972, vol. 29, p. 77

- Campos R. M., Gramcianinov C. B., de Camargo R., da Silva Dias P. L., Assessment and calibration of ERA5 severe winds in the Atlantic Ocean using satellite data, *Remote Sensing*, 2022, vol. 14, p. 4918
- Cao X., Huang P., Chen G., Chen W., Modulation of western North Pacific tropical cyclone genesis by intraseasonal oscillation of the ITCZ: A statistical analysis, *Advances in Atmospheric Sciences*, 2012, vol. 29, p. 744
- Cardoso A. A., da Rocha R. P., Crespo N. M., Synoptic Climatology of Subtropical Cyclone Impacts on Near-Surface Winds Over the South Atlantic Basin, *Earth and Space Science*, 2022, vol. 9, p. e2022EA002482
- Cavicchia L., Dowdy A., Walsh K., Energetics and dynamics of subtropical australian east coast cyclones: Two contrasting cases, *Monthly Weather Review*, 2018, vol. 146, p. 1511
- Chan J. C. L., Kepert J. D., eds, *Global Perspectives on Tropical Cyclones: From Science to Mitigation*. vol. 4 of *World Scientific Series on Asia-Pacific Weather and Climate*, World Scientific Singapore, 2010
- Chang E. K., Lee S., Swanson K. L., Storm track dynamics, *Journal of climate*, 2002, vol. 15, p. 2163
- Charney J. G., The dynamics of long waves in a baroclinic westerly current, *Journal of the Atmospheric Sciences*, 1947, vol. 4, p. 136
- Charney J. G., Eliassen A., On the growth of the hurricane depression, *Journal of the Atmospheric Sciences*, 1964, vol. 21, p. 68
- Craig G. C., Gray S. L., CISK or WISHE as the mechanism for tropical cyclone intensification, *Journal of Atmospheric Sciences*, 1996, vol. 53, p. 3528
- Crespo N. M., da Rocha R. P., Sprenger M., Wernli H., A potential vorticity perspective on cyclogenesis over centre-eastern South America, *International Journal of Climatology*, 2021, vol. 41, p. 663
- Crespo N. M., Reboita M. S., Gozzo L. F., de Jesus E. M., Torres-Alavez J. A., Lagos-Zúñiga M. Á., Torrez-Rodriguez L., Reale M., da Rocha R. P., Assessment of the

- RegCM4-CORDEX-CORE performance in simulating cyclones affecting the western coast of South America, Climate Dynamics, 2023, vol. 60, p. 2041
- Da C., Shen B., Yan P., Ma D., Song J., The shallow water equation and the vorticity equation for a change in height of the topography, Plos one, 2017, vol. 12, p. e0178184
- da Rocha R. P., Reboita M. S., Gozzo L. F., Dutra L. M. M., de Jesus E. M., Subtropical cyclones over the oceanic basins: a review, Annals of the New York Academy of Sciences, 2019, vol. 1436, p. 138
- da Silva Dias P. L., da Silva Dias M. A. F., Seluchi M., de Assis Diniz F., O ciclone Catarina: Análise preliminar da estrutura, dinâmica e previsibilidade. In CONGRESSO BRASILEIRO DE METEOROLOGIA , 2004
- Dacre H. F., Gray S. L., The spatial distribution and evolution characteristics of North Atlantic cyclones, Monthly Weather Review, 2009, vol. 137, p. 99
- Daniel J., Data science with Python and Dask. Simon and Schuster, 2019
- de Jesus E. M., da Rocha R. P., Crespo N. M., Reboita M. S., Gozzo L. F., Future climate trends of subtropical cyclones in the South Atlantic basin in an ensemble of global and regional projections, Climate Dynamics, 2022, vol. 58, p. 1221
- de Souza D., da Silva R. R., Ocean-Land Atmosphere Model (OLAM) performance for major extreme meteorological events near the coastal region of southern Brazil, Climate Research, 2021, vol. 84, p. 1
- de Souza D. C., Crespo N. M., da Silva D. V., Harada L. M., de Godoy R. M. P., Domingues L. M., Luiz R., Bortolozo C. A., Metodiev D., de Andrade M. R. M., et al., Extreme rainfall and landslides as a response to human-induced climate change: a case study at Baixada Santista, Brazil, 2020, Natural Hazards, 2024, pp 1–26
- de Souza D. C., da Silva Dias P. L., Gramcianinov C. B., da Silva M. B. L., de Camargo R., New perspectives on South Atlantic storm track through an automatic method for detecting extratropical cyclones' lifecycle, International Journal of Climatology, 2024, vol. 1, p. 1

- de Souza D. C., Ramos da Silva R., Gomes da Silva P., Fetter Filho A. F. H., Mendez F. J., Werth D., A hybrid regional climate downscaling for the southern Brazil coastal region, International Journal of Climatology, 2022, vol. 42, p. 6753
- de Souza M. R., Piva E. D., Storm tracks and cyclogenesis over the Southern Ocean: An overview with the HadGEM3-GC3.1 model, International Journal of Climatology, 2023, vol. 43, p. 7565
- Deveson A., Browning K., Hewson T., A classification of FASTEX cyclones using a height-attributable quasi-geostrophic vertical-motion diagnostic, Quarterly Journal of the Royal Meteorological Society: A journal of the atmospheric sciences, applied meteorology and physical oceanography, 2002, vol. 128, p. 93
- Dias Pinto J. R., Reboita M. S., da Rocha R. P., Synoptic and dynamical analysis of subtropical cyclone Anita (2010) and its potential for tropical transition over the South Atlantic Ocean, Journal of Geophysical Research: Atmospheres, 2013, vol. 118, p. 10
- Dias Pinto J. R., Rocha R. P., The energy cycle and structural evolution of cyclones over southeastern South America in three case studies, Journal of Geophysical Research: Atmospheres, 2011, vol. 116
- Donald Ahrens C., Henson R., Meteorology Today: An introduction to weather, climate and the environment. Brooks/Cole, 2015
- Duchon C. E., Lanczos filtering in one and two dimensions, Journal of Applied Meteorology and Climatology, 1979, vol. 18, p. 1016
- Dutra L. M. M., da Rocha R. P., Lee R. W., Peres J. R. R., de Camargo R., Structure and evolution of subtropical cyclone Anita as evaluated by heat and vorticity budgets, Quarterly Journal of the Royal Meteorological Society, 2017, vol. 143, p. 1539
- Dutton J. A., Johnson D. R., The theory of available potential energy and a variational approach to atmospheric energetics, Advances in geophysics, 1967, vol. 12, p. 333
- Eady E. T., Long waves and cyclone waves, Tellus, 1949, vol. 1, p. 33

Edmon H. J., Vincent D. G., Large-scale atmospheric conditions during the intensification of Hurricane Carmen (1974) II. Diabatic heating rates and energy budgets, *Monthly Weather Review*, 1979, vol. 107, p. 295

Emanuel K. A., An air-sea interaction theory for tropical cyclones. Part I: Steady-state maintenance, *Journal of Atmospheric Sciences*, 1986, vol. 43, p. 585

Emanuel K. A., The dependence of hurricane intensity on climate, *Nature*, 1987, vol. 326, p. 483

Emanuel K. A., Rotunno R., Polar lows as arctic hurricanes, *Tellus A: Dynamic Meteorology and Oceanography*, 1989, vol. 41, p. 1

Evans J. L., Braun A., A climatology of subtropical cyclones in the South Atlantic, *Journal of Climate*, 2012, vol. 25, p. 7328

Evans J. L., Hart R. E., Objective indicators of the life cycle evolution of extratropical transition for Atlantic tropical cyclones, *Monthly Weather Review*, 2003, vol. 131, p. 909

Ferreira R. N., Schubert W. H., Barotropic aspects of ITCZ breakdown, *Journal of the Atmospheric Sciences*, 1997, vol. 54, p. 261

Flaounas E., Kotroni V., Lagouvardos K., Flaounas I., CycloTRACK (v1. 0)—tracking winter extratropical cyclones based on relative vorticity: sensitivity to data filtering and other relevant parameters, *Geoscientific Model Development*, 2014, vol. 7, p. 1841

Ford R., Ford R. P., Moore G. W. K., Moore G. W. K., Moore G. W. K., Secondary Cyclogenesis—Comparison of Observations and Theory, *Monthly Weather Review*, 1990

Frank N. L., Atlantic tropical systems of 1969, *Monthly Weather Review*, 1970, vol. 98, p. 307

Frank W. M., The structure and energetics of the tropical cyclone I. Storm structure, *Monthly Weather Review*, 1977a, vol. 105, p. 1119

Frank W. M., The structure and energetics of the tropical cyclone II. Dynamics and energetics, *Monthly Weather Review*, 1977b, vol. 105, p. 1136

- Fukuoka A., A Study of 10-day Forecast (A Synthetic Report), *The Geophysical Magazine*, 1951, vol. XXII, p. 177
- Gall R., The effects of released latent heat in growing baroclinic waves, *Journal of the Atmospheric Sciences*, 1976, vol. 33, p. 1686
- Gan M. A., Rao V. B., Surface cyclogenesis over south America, *Monthly Weather Review*, 1991, vol. 119, p. 1293
- Gan M. A., Rao V. B., The influence of the Andes Cordillera on transient disturbances, *Monthly Weather Review*, 1994, vol. 122, p. 1141
- Gibbs J. W., Fourier's series, *Nature*, 1898, vol. 59, p. 200
- Gordon A. L., Brazil-malvinas confluence—1984, *Deep Sea Research Part A. Oceanographic Research Papers*, 1989, vol. 36, p. 359
- Gozzo L., Da Rocha R., Gimeno L., Drumond A., Climatology and numerical case study of moisture sources associated with subtropical cyclogenesis over the southwestern Atlantic Ocean, *Journal of Geophysical Research: Atmospheres*, 2017, vol. 122, p. 5636
- Gozzo L. F., da Rocha R. P., Reboita M. S., Sugahara S., Subtropical cyclones over the southwestern South Atlantic: Climatological aspects and case study, *Journal of Climate*, 2014, vol. 27, p. 8543
- Gramcianinov C., Campos R., De Camargo R., Hodges K., Soares C. G., da Silva Dias P., Analysis of Atlantic extratropical storm tracks characteristics in 41 years of ERA5 and CFSR/CFSv2 databases, *Ocean Engineering*, 2020, vol. 216, p. 108
- Gramcianinov C., Campos R., Soares C. G., de Camargo R., Extreme waves generated by cyclonic winds in the western portion of the South Atlantic Ocean, *Ocean Engineering*, 2020, vol. 213, p. 107745
- Gramcianinov C., Hodges K., Camargo R. d., The properties and genesis environments of South Atlantic cyclones, *Climate Dynamics*, 2019, vol. 53, p. 4115
- Gramcianinov C. B., Campos R. M., de Camargo R., Hodges K. I., Guedes Soares C., da Silva Dias P. L., Atlantic extratropical cyclone tracks in 41 years of ERA5 and CFSR/CFSv2 databases, *Mendeley Data*, 2020, vol. V4

Gramcianinov C. B., de Camargo R., Campos R. M., Guedes Soares C., da Silva Dias P. L., Impact of extratropical cyclone intensity and speed on the extreme wave trends in the Atlantic Ocean, *Climate dynamics*, 2023, vol. 60, p. 1447

Gray S. L., Dacre H. F., Classifying dynamical forcing mechanisms using a climatology of extratropical cyclones, *Quarterly Journal of the Royal Meteorological Society: A journal of the atmospheric sciences, applied meteorology and physical oceanography*, 2006, vol. 132, p. 1119

Gray W. M., Global view of the origin of tropical disturbances and storms, *Monthly Weather Review*, 1968, vol. 96, p. 669

Gray W. M., The formation of tropical cyclones, *Meteorology and atmospheric physics*, 1998, vol. 67, p. 37

Grise K. M., Son S.-W., Gyakum J. R., Intraseasonal and interannual variability in North American storm tracks and its relationship to equatorial Pacific variability, *Monthly Weather Review*, 2013, vol. 141, p. 3610

Guimarães P., Farina L., Toldo Jr E., Analysis of extreme wave events on the southern coast of Brazil, *Natural Hazards and Earth System Sciences*, 2014, vol. 14, p. 3195

Gutowski W. J., Branscome L. E., Stewart D. A., Life cycles of moist baroclinic eddies, *Journal of the atmospheric sciences*, 1992, vol. 49, p. 306

Hadley G., VI. Concerning the cause of the general trade-winds, *Philosophical Transactions of the Royal Society of London*, 1735, vol. 39, p. 58

Hamming R. W., *Digital Filters*. Prentice Hall, 1989

Hannachi A., Jolliffe I. T., Stephenson D. B., et al., Empirical orthogonal functions and related techniques in atmospheric science: A review, *International journal of climatology*, 2007, vol. 27, p. 1119

Harris F. J., On the use of windows for harmonic analysis with the discrete Fourier transform, *Proceedings of the IEEE*, 1978, vol. 66, p. 51

Harrold T., Browning K., The polar low as a baroclinic disturbance, *Quarterly Journal of the Royal Meteorological Society*, 1969, vol. 95, p. 710

- Hart R. E., A cyclone phase space derived from thermal wind and thermal asymmetry, Monthly weather review, 2003, vol. 131, p. 585
- Held I. M., The macroturbulence of the troposphere, Tellus A, 1999, vol. 51, p. 59
- Hersbach H., Bell B., Berrisford P., Hirahara S., Horányi A., Muñoz-Sabater J., Nicolas J., Peubey C., Radu R., Schepers D., et al., The ERA5 global reanalysis, Quarterly Journal of the Royal Meteorological Society, 2020, vol. 146, p. 1999
- Hodges K., Feature tracking on the unit sphere, Monthly Weather Review, 1995, vol. 123, p. 3458
- Hodges K., Spherical nonparametric estimators applied to the UGAMP model integration for AMIP, Monthly Weather Review, 1996, vol. 124, p. 2914
- Hodges K. I., A general method for tracking analysis and its application to meteorological data, Monthly Weather Review, 1994, vol. 122, p. 2573
- Holopainen E. O., Investigation of friction and diabatic processes in the atmosphere. vol. 29, na, 1964
- Holton J. R., An introduction to dynamic meteorology. vol. 41, American Association of Physics Teachers, 1973, 752
- Hoskins B. J., Theory of extratropical cyclones. Springer, 1990, 63
- Hoskins B. J., Hodges K. I., New perspectives on the Northern Hemisphere winter storm tracks, Journal of the Atmospheric Sciences, 2002, vol. 59, p. 1041
- Hoskins B. J., Hodges K. I., A new perspective on Southern Hemisphere storm tracks, Journal of Climate, 2005, vol. 18, p. 4108
- Hoskins B. J., McIntyre M. E., Robertson A. W., On the use and significance of isentropic potential vorticity maps, Quarterly Journal of the Royal Meteorological Society, 1985, vol. 111, p. 877
- Hoskins B. J., Valdes P. J., On the existence of storm-tracks, Journal of Atmospheric Sciences, 1990, vol. 47, p. 1854

- Jensen C. E., Energy transformation and vertical flux processes over the northern hemisphere, *Journal of Geophysical Research*, 1961, vol. 66, p. 1145
- Johnson D. R., The available potential energy of storms, *Journal of Atmospheric Sciences*, 1970, vol. 27, p. 727
- Jorgensen D. P., Zipser E. J., LeMone M. A., Vertical motions in intense hurricanes, *Journal of the atmospheric sciences*, 1985, vol. 42, p. 839
- Knutson T. R., McBride J. L., Chan J., Emanuel K., Holland G., Landsea C., Held I., Kossin J. P., Srivastava A., Sugi M., Tropical cyclones and climate change, *Nature geoscience*, 2010, vol. 3, p. 157
- Kuo H.-l., Dynamic instability of two-dimensional nondivergent flow in a barotropic atmosphere, *Journal of Atmospheric sciences*, 1949, vol. 6, p. 105
- Lavers D. A., Simmons A., Vamborg F., Rodwell M. J., An evaluation of ERA5 precipitation for climate monitoring, *Quarterly Journal of the Royal Meteorological Society*, 2022, vol. 148, p. 3152
- Leal K. B., Robaina L. E. d. S., Körting T. S., Nicolodi J. L., da Costa J. D., Souza V. G., Identification of coastal natural disasters using official databases to provide support for the coastal management: the case of Santa Catarina, Brazil, *Natural Hazards*, 2023, pp 1–18
- Li L., Ingersoll A. P., Jiang X., Feldman D., Yung Y. L., Lorenz energy cycle of the global atmosphere based on reanalysis datasets, *Geophysical Research Letters*, 2007, vol. 34
- Lorenz E., The nature and theory of the general circulation of the atmosphere, *World meteorological organization*, 1967, vol. 161
- Lorenz E. N., Available Potential Energy and the Maintenance of the General Circulation, *Tellus*, 1955, vol. 7, p. 157
- Lorenz E. N., Empirical orthogonal functions and statistical weather prediction. vol. 1, Massachusetts Institute of Technology, Department of Meteorology Cambridge, 1956
- McLennan N., , 1988 Technical report Marine Bombs Program: Phase II. Pacific Weather Centre

MacQueen J., et al., Some methods for classification and analysis of multivariate observations. In Proceedings of the fifth Berkeley symposium on mathematical statistics and probability , 1967, p. 281

McTaggart-Cowan R., Bosart L. F., Davis C. A., Atallah E. H., Gyakum J. R., Emanuel K. A., Analysis of hurricane Catarina (2004), Monthly Weather Review, 2006, vol. 134, p. 3029

Mailier P., Mailier P. J., Stephenson D. B., Stephenson D. B., Ferro C. A. T., Ferro C. A. T., Hodges K. I., Hodges K. I., Serial Clustering of Extratropical Cyclones, Monthly Weather Review, 2006

Maloney E. D., Hartmann D. L., The Madden–Julian oscillation, barotropic dynamics, and North Pacific tropical cyclone formation. Part I: Observations, Journal of the atmospheric sciences, 2001, vol. 58, p. 2545

Margules M., Über die Energie der Stürme, Jahrb. kair-kon Zent, 1903

Marquet P., On the concept of exergy and available enthalpy: Application to atmospheric energetics, Quarterly Journal of the Royal Meteorological Society, 1991, vol. 117, p. 449

Marquet P., The last paper "On the theory of storm" (Zur Sturmtheorie) published by Max Margules in 1906, arXiv preprint arXiv:1704.06128, 2017

Marrafon V. H., Reboita M. S., da Rocha R. P., de Jesus E. M., Classificação dos tipos de ciclones sobre o Oceano Atlântico Sul em projeções com o RegCM4 E MCGs, Revista Brasileira de Climatologia, 2022, vol. 30, p. 1

May R. M., Goebbert K. H., Thielen J. E., Leeman J. R., Camron M. D., Bruick Z., Bruning E. C., Manser R. P., Arms S. C., Marsh P. T., MetPy: A meteorological Python library for data analysis and visualization, Bulletin of the American Meteorological Society, 2022, vol. 103, p. E2273

Mendes D., Souza E. P., Marengo J. A., Mendes M. C., Climatology of extratropical cyclones over the South American–southern oceans sector, Theoretical and applied climatology, 2010, vol. 100, p. 239

Michaelides S. C., Limited area energetics of Genoa cyclogenesis, *Monthly Weather Review*, 1987, vol. 115, p. 13

Michaelides S. C., A spatial and temporal energetics analysis of a baroclinic disturbance in the Mediterranean, *Monthly weather review*, 1992, vol. 120, p. 1224

Michaelides S. C., Prezerakos N. G., Flocas H. A., Quasi-Lagrangian energetics of an intense Mediterranean cyclone, *Quarterly Journal of the Royal Meteorological Society*, 1999, vol. 125, p. 139

Mitra S. K., *Digital Signal Processing: A Computer-Based Approach*. McGraw-Hill, 2001

Molinari J., Knight D., Dickinson M., Vollaro D., Skubis S., Potential vorticity, easterly waves, and eastern Pacific tropical cyclogenesis, *Monthly weather review*, 1997, vol. 125, p. 2699

Molinari J., Vollaro D., Skubis S., Dickinson M., Origins and mechanisms of eastern Pacific tropical cyclogenesis: A case study, *Monthly Weather Review*, 2000, vol. 128, p. 125

Montgomery M. T., Persing J., Smith R. K., Putting to rest WISHE-ful misconceptions for tropical cyclone intensification, *Journal of Advances in Modeling Earth Systems*, 2015, vol. 7, p. 92

Montgomery M. T., Smith R. K., Paradigms for tropical cyclone intensification, *Australian Meteorological and Oceanographic Journal*, 2014, vol. 64, p. 37

Muench H. S., On the dynamics of the wintertime stratosphere circulation, *Journal of Atmospheric Sciences*, 1965, vol. 22, p. 349

Murray R. J., Simmonds I., A numerical scheme for tracking cyclone centres from digital data. Part II: Application to January and July general circulation model simulations, *Australian Meteorological Magazine*, 1991, vol. 39, p. 167

Nordeng T. E., Rasmussen E. A., A most beautiful polar low. A case study of a polar low development in the Bear Island region, *Tellus A*, 1992, vol. 44, p. 81

Norquist D. C., Recker E. E., Reed R. J., The energetics of African wave disturbances as observed during phase III of GATE, *Monthly Weather Review*, 1977, vol. 105, p. 334

- Novak L., Tailleux R., On the local view of atmospheric available potential energy, *Journal of the Atmospheric Sciences*, 2018, vol. 75, p. 1891
- Okajima S., Nakamura H., Kaspi Y., Cyclonic and anticyclonic contributions to atmospheric energetics, *Scientific reports*, 2021, vol. 11, p. 13202
- Oort A. H., On estimates of the atmospheric energy cycle, *Monthly Weather Review*, 1964, vol. 92
- Ooyama K. V., Conceptual evolution of the theory and modeling of the tropical cyclone, *Journal of the Meteorological Society of Japan. Ser. II*, 1982, vol. 60, p. 369
- Oppenheim A. V., *Discrete-time signal processing*. Pearson Education India, 1999
- Oppenheim A. V., Schafer R. W., *Discrete-Time Signal Processing*. Prentice Hall, 2009
- Ozawa H., Shimokawa S., Thermodynamics of a tropical cyclone: Generation and dissipation of mechanical energy in a self-driven convection system, *Tellus A: Dynamic Meteorology and Oceanography*, 2015, vol. 67, p. 24216
- Palmén E. H., Newton C. W., Atmospheric circulation systems: their structure and physical interpretation. vol. 13, Academic press, 1969
- Parise C. K., Calliari L. J., Krusche N., Extreme storm surges in the south of Brazil: atmospheric conditions and shore erosion, *Brazilian Journal of Oceanography*, 2009, vol. 57, p. 175
- Parzen E., On estimation of a probability density function and mode, *The annals of mathematical statistics*, 1962, vol. 33, p. 1065
- Pedregosa F., Varoquaux G., Gramfort A., Michel V., Thirion B., Grisel O., Blondel M., Prettenhofer P., Weiss R., Dubourg V., Vanderplas J., Passos A., Cournapeau D., Brucher M., Perrot M., Édouard Duchesnay Scikit-learn: Machine Learning in Python, *Journal of Machine Learning Research*, 2011, vol. 12, p. 2825
- Pereira Filho A. J., Pezza A. B., Simmonds I., Lima R. S., Vianna M., New perspectives on the synoptic and mesoscale structure of Hurricane Catarina, *Atmospheric Research*, 2010, vol. 95, p. 157

Petterssen S., Smebye S., On the development of extratropical cyclones, *Quarterly Journal of the Royal Meteorological Society*, 1971, vol. 97, p. 457

Pezza A. B., Garde L. A., Veiga J. A. P., Simmonds I., Large scale features and energetics of the hybrid subtropical low ‘Duck’ over the Tasman Sea, *Climate dynamics*, 2014, vol. 42, p. 453

Pezza A. B., Simmonds I., The first South Atlantic hurricane: Unprecedented blocking, low shear and climate change, *Geophysical Research Letters*, 2005, vol. 32

Pezza A. B., Simmonds I., Pereira Filho A. J., Climate perspective on the large-scale circulation associated with the transition of the first South Atlantic hurricane, *International Journal of Climatology: A Journal of the Royal Meteorological Society*, 2009, vol. 29, p. 1116

Pezza A. B., Veiga J. A. P., Simmonds I., Keay K., Mesquita M. d. S., Environmental energetics of an exceptional high-latitude storm, *Atmospheric Science Letters*, 2010, vol. 11, p. 39

Pinto J. G., Spangehl T., Ulbrich U., Speth P., Sensitivities of a cyclone detection and tracking algorithm: individual tracks and climatology, *Meteorologische Zeitschrift*, 2005, vol. 14, p. 823

Piva E. D., Gan M. A., Rao V. B., Energetics of winter troughs entering South America, *Monthly Weather Review*, 2010, vol. 138, p. 1084

Plumb R. A., A new look at the energy cycle, *Journal of Atmospheric Sciences*, 1983, vol. 40, p. 1669

Proakis J. G., Manolakis D. G., *Digital Signal Processing: Principles, Algorithms, and Applications*. Prentice Hall, 2006

Ramage C. S., Hurricane development, *Journal of Atmospheric Sciences*, 1959, vol. 16, p. 227

Ramon J., Lledó L., Torralba V., Soret A., Doblas-Reyes F. J., What global reanalysis best represents near-surface winds?, *Quarterly Journal of the Royal Meteorological Society*, 2019, vol. 145, p. 3236

- Rasmussen E., The polar low as an extratropical CISK disturbance, Quarterly Journal of the Royal Meteorological Society, 1979, vol. 105, p. 531
- Rasmussen E., A case study of a polar low development over the Barents Sea, Tellus A, 1985, vol. 37, p. 407
- Rasmussen E. A., A comparative study of tropical cyclones and polar lows. vol. 47, A. Deepak Publishing, 1989, 80
- Rayleigh On the stability or instability of certain fluid motions (iii.), Proceedings of the London Mathematical Society, 1895, vol. 1, p. 5
- Read P., Kennedy D., Lewis N., Scolan H., Tabataba-Vakili F., Wang Y., Wright S., Young R., Baroclinic and barotropic instabilities in planetary atmospheres: energetics, equilibration and adjustment, Nonlinear Processes in Geophysics, 2020, vol. 27, p. 147
- Reboita M., Crespo N., Dutra L., Silva B., Capucin B., da Rocha R., Iba: the first pure tropical cyclogenesis over the western South Atlantic Ocean, Journal of Geophysical Research: Atmospheres, 2021, vol. 126, p. e2020JD033431
- Reboita M. S., Da Rocha R. P., Ambrizzi T., Sugahara S., South Atlantic Ocean cyclogenesis climatology simulated by regional climate model (RegCM3), Climate Dynamics, 2010, vol. 35, p. 1331
- Reboita M. S., da Rocha R. P., de Souza M. R., Llopis M., et al., Extratropical cyclones over the southwestern South Atlantic Ocean: HadGEM2-ES and RegCM4 projections, Int. J. Climatol, 2018, vol. 38, p. 2866
- Reboita M. S., Da Rocha R. P., Oliveira D. M. d., Key features and adverse weather of the named subtropical cyclones over the Southwestern South Atlantic Ocean, Atmosphere, 2018, vol. 10, p. 6
- Reboita M. S., Gan M. A., Rocha R. P. d., Ambrizzi T., Regimes de precipitação na América do Sul: uma revisão bibliográfica, Revista brasileira de meteorologia, 2010, vol. 25, p. 185

Reboita M. S., Gan M. A., Rocha R. P. d., Custódio I. S., Ciclones em superfície nas latitudes austrais: Parte I-revisão bibliográfica, Revista Brasileira de Meteorologia, 2017, vol. 32, p. 171

Reboita M. S., Gozzo L. F., Crespo N. M., Custodio M. d. S., Lucyrio V., de Jesus E. M., da Rocha R. P., From a Shapiro–Keyser extratropical cyclone to the subtropical cyclone Raoni: An unusual winter synoptic situation over the South Atlantic Ocean, Quarterly Journal of the Royal Meteorological Society, 2022, vol. 148, p. 2991

Reboita M. S., Oliveira D., Da Rocha R., Dutra L., Subtropical cyclone Anita's potential to tropical transition under warmer sea surface temperature scenarios, Geophysical Research Letters, 2019, vol. 46, p. 8484

Reed R. J., Norquist D. C., Recker E. E., The structure and properties of African wave disturbances as observed during phase III of GATE, Monthly Weather Review, 1977, vol. 105, p. 317

Reed R. J., Wolfe J. L., Nishimoto H., A spectral analysis of the energetics of the stratospheric sudden warming of early 1957, Journal of the Atmospheric Sciences, 1963, vol. 20, p. 256

Rennick M. A., The generation of African waves, Journal of Atmospheric Sciences, 1976, vol. 33, p. 1955

Riehl H., On the formation of typhoons, Journal of the Atmospheric Sciences, 1948, vol. 5, p. 247

Rivals H., Rivals H., Cammas J., Cammas J.-P., Renfrew I. A., Renfrew I. A., Secondary cyclogenesis: The initiation phase of a frontal wave observed over the eastern Atlantic, Quarterly Journal of the Royal Meteorological Society, 1998

Robertson F., Smith P., The impact of model moist processes on the energetics of extra-tropical cyclones, Monthly Weather Review, 1983, vol. 111, p. 723

Rosa M. B., Ferreira N. J., Gan M. A., Machado L. H. R., Energetics of cyclogenesis events over the southern coast of Brazil, Revista Brasileira de Meteorologia, 2013, vol. 28, p. 231

- Rosenblatt M., Estimation of a probability density-function and mode, Ann Math Statist, 1956, vol. 27, p. 832
- Rudeva I., Gulev S. K., Climatology of cyclone size characteristics and their changes during the cyclone life cycle, Monthly Weather Review, 2007, vol. 135, p. 2568
- Saltzman B., Fleisher A., Further statistics on the modes of release of available potential energy, Journal of Geophysical Research, 1961, vol. 66, p. 2271
- Sanders F., Gyakum J. R., Synoptic-dynamic climatology of the “bomb”, Monthly Weather Review, 1980, vol. 108, p. 1589
- Savitzky A., Golay M. J., Smoothing and differentiation of data by simplified least squares procedures., Analytical chemistry, 1964, vol. 36, p. 1627
- Schemm S., Sprenger M., Wernli H., When during their life cycle are extratropical cyclones attended by fronts?, Bulletin of the American Meteorological Society, 2018, vol. 99, p. 149
- Schneider T., The general circulation of the atmosphere, Annu. Rev. Earth Planet. Sci., 2006, vol. 34, p. 655
- Schultz D. M., Keyser D., Bosart L. F., The effect of large-scale flow on low-level frontal structure and evolution in midlatitude cyclones, Monthly weather review, 1998, vol. 126, p. 1767
- Shapiro M. A., Doyle J., Zou X., Jorgensen D. P., Jorgensen D. P., Jorgensen D. P., Extratropical Secondary Cyclones: Simulations and Observations,, null, 1997
- Shapiro M. A., Keyser D., Fronts, jet streams and the tropopause. Springer, 1990
- Shea D. J., Gray W. M., The hurricane’s inner core region. I. Symmetric and asymmetric structure, Journal of the Atmospheric Sciences, 1973, vol. 30, p. 1544
- Silva Dias P. L., Gan M., Beven J. L., Pezza A., Holland G., Pereira A., McTaggart-Cowan R., Diniz F. d. A., Seluchi M., Braga H. J., The Catarina Phenomenon. In Proceedings of the Sixth International Workshop on Tropical Cyclones , São Paulo, Brazil, 2004

- Simmonds I., Size changes over the life of sea level cyclones in the NCEP reanalysis, *Monthly Weather Review*, 2000, vol. 128, p. 4118
- Simmonds I., Keay K., Mean Southern Hemisphere extratropical cyclone behavior in the 40-year NCEP–NCAR reanalysis, *Journal of Climate*, 2000, vol. 13, p. 873
- Simmonds I., Murray R. J., Southern extratropical cyclone behavior in ECMWF analyses during the FROST special observing periods, *Weather and forecasting*, 1999, vol. 14, p. 878
- Simmons A. J., Hoskins B. J., The downstream and upstream development of unstable baroclinic waves, *Journal of the Atmospheric Sciences*, 1979, vol. 36, p. 1239
- Simpson R. H., Evolution of the Kona storm a subtropical cyclone, *Journal of Atmospheric Sciences*, 1952, vol. 9, p. 24
- Sinclair M. R., An objective cyclone climatology for the Southern Hemisphere, *Monthly Weather Review*, 1994, vol. 122, p. 2239
- Sinclair M. R., A climatology of cyclogenesis for the Southern Hemisphere, *Monthly Weather Review*, 1995, vol. 123, p. 1601
- Smith P. J., On the contribution of a limited region to the global energy budget, *Tellus*, 1969, vol. 21, p. 202
- Smith P. J., The energetics of extratropical cyclones, *Reviews of Geophysics*, 1980, vol. 18, p. 378
- Smith P. J., Vincent D. G., Edmond Jr H. J., The time dependence of reference pressure in limited region available potential energy budget equations, *Tellus*, 1977, vol. 29, p. 476
- Smith S. W., *The Scientist and Engineer's Guide to Digital Signal Processing*. California Technical Publishing, 1997
- Spiridonov V., Ćurić M., *Fundamentals of meteorology*. Springer, 2021
- Starr V. P., Note concerning the nature of the large-scale eddies in the atmosphere, *Tellus*, 1953, vol. 5, p. 494

- Starr V. P., Further statistics concerning the general circulation, *Tellus*, 1959, vol. 11, p. 481
- Steele C., Dorling S., von Glasow R., Bacon J., Modelling sea-breeze climatologies and interactions on coasts in the southern North Sea: implications for offshore wind energy, *Quarterly Journal of the Royal Meteorological Society*, 2015, vol. 141, p. 1821
- Stoll P. J., Spengler T., Terpstra A., Graversen R. G., Polar lows–moist-baroclinic cyclones developing in four different vertical wind shear environments, *Weather and Climate Dynamics*, 2021, vol. 2, p. 19
- Stull R. B., Practical meteorology: an algebra-based survey of atmospheric science. University of British Columbia, 2015
- Sutcliffe R., A contribution to the problem of development, *Quarterly Journal of the Royal Meteorological Society*, 1947, vol. 73, p. 370
- Swart N. C., Fyfe J. C., Gillett N., Marshall G. J., Comparing trends in the southern annular mode and surface westerly jet, *Journal of Climate*, 2015, vol. 28, p. 8840
- Terry J. P., Tropical cyclones: climatology and impacts in the South Pacific. Springer Science & Business Media, 2007
- Thorndike R. L., Who belongs in the family?, *Psychometrika*, 1953, vol. 18, p. 267
- Tibaldi S., Buzzi A., Malguzzi P., Orographically induced cyclogenesis: Analysis of numerical experiments, *Monthly Weather Review*, 1980, vol. 108, p. 1302
- Trenberth K. E., On the interpretation of the diagnostic quasi-geostrophic omega equation, *Mon. Wea. Rev.*, 1978, vol. 106, p. 131
- Trigo I. F., Climatology and interannual variability of storm-tracks in the Euro-Atlantic sector: a comparison between ERA-40 and NCEP/NCAR reanalyses, *Climate Dynamics*, 2006, vol. 26, p. 127
- Veiga J. A. P., Ambrizzi T., et al., A global and hemispherical analysis of the Lorenz energetics based on the representative concentration pathways used in CMIP5, *Advances in Meteorology*, 2013, vol. 2013

Veiga J. A. P., Pezza A. B., Simmonds I., Silva Dias P. L., An analysis of the environmental energetics associated with the transition of the first South Atlantic hurricane, Geophysical Research Letters, 2008, vol. 35

Vera C. S., Vigliarolo P. K., Berbery E. H., Cold season synoptic-scale waves over subtropical South America, Monthly Weather Review, 2002, vol. 130, p. 684

Vianna M., Menezes V., Pezza A., Simmonds I., Interactions between Hurricane Catarina (2004) and warm core rings in the South Atlantic Ocean, Journal of Geophysical Research: Oceans, 2010, vol. 115

Vincent D., Chang L., Some further considerations concerning energy budgets of moving systems, Tellus, 1973, vol. 25, p. 224

Virtanen P., Gommers R., Oliphant T. E., Haberland M., Reddy T., Cournapeau D., Burovski E., Peterson P., Weckesser W., Bright J., et al., SciPy 1.0: fundamental algorithms for scientific computing in Python, Nature methods, 2020, vol. 17, p. 261

Virtanen P., Gommers R., Oliphant T. E., Haberland M., Reddy T., Cournapeau D., Burovski E., Peterson P., Weckesser W., Bright J., van der Walt S. J., Brett M., Wilson J., Millman K. J., Mayorov N., Nelson A. R. J., Jones E., Kern R., Larson E., Carey C. J., Polat İ., Feng Y., Moore E. W., VanderPlas J., Laxalde D., Perktold J., Cimrman R., Henriksen I., Quintero E. A., Harris C. R., Archibald A. M., Ribeiro A. H., Pedregosa F., van Mulbregt P., SciPy 1.0 Contributors SciPy 1.0: Fundamental Algorithms for Scientific Computing in Python, Nature Methods, 2020, vol. 17, p. 261

Wahab M. A., Basset H. A., Lasheen A., On the mechanism of winter cyclogenesis in relation to vertical axis tilt, Meteorology and Atmospheric Physics, 2002, vol. 81, p. 103

Walsh K., Tropical cyclones and climate change: unresolved issues, Climate Research, 2004, vol. 27, p. 77

Walsh K. J., Camargo S. J., Knutson T. R., Kossin J., Lee T.-C., Murakami H., Patricola C., Tropical cyclones and climate change, Tropical Cyclone Research and Review, 2019, vol. 8, p. 240

- Walsh K. J., McBride J. L., Klotzbach P. J., Balachandran S., Camargo S. J., Holland G., Knutson T. R., Kossin J. P., Lee T.-c., Sobel A., et al., Tropical cyclones and climate change, *Wiley Interdisciplinary Reviews: Climate Change*, 2016, vol. 7, p. 65
- Wang D., Lin Y., Chavas D. R., Tropical cyclone potential size, *Journal of the Atmospheric Sciences*, 2022, vol. 79, p. 3001
- Waskom M. L., Seaborn: statistical data visualization, *Journal of Open Source Software*, 2021, vol. 6, p. 3021
- Weatherford C. L., Gray W. M., Typhoon structure as revealed by aircraft reconnaissance. Part I: Data analysis and climatology, *Monthly Weather Review*, 1988, vol. 116, p. 1032
- Whitaker J. S., Davis C. A., Cyclogenesis in a saturated environment, *Journal of the atmospheric sciences*, 1994, vol. 51, p. 889
- Whittaker L., Horn L., Northern Hemisphere extratropical cyclone activity for four mid-season months, *Journal of Climatology*, 1984, vol. 4, p. 297
- Wiin-Nielsen A., A study of energy conversion and meridional circulation for the large-scale motion in the atmosphere, *Monthly Weather Review*, 1959, vol. 87, p. 319
- Wiin-Nielsen A., Brown J. A., Drake M., On atmospheric energy conversions between the zonal flow and the eddies, *Tellus*, 1963, vol. 15, p. 261
- Willoughby H. E., Marks F. D., Feinberg R. J., Stationary and moving convective bands in hurricanes, *Journal of the Atmospheric Sciences*, 1984, vol. 41, p. 3189
- Wu M.-L. C., Reale O., Schubert S. D., Suarez M. J., Thorncroft C. D., African easterly jet: Barotropic instability, waves, and cyclogenesis, *Journal of Climate*, 2012, vol. 25, p. 1489
- Yanai M., A detailed analysis of typhoon formation, *Journal of the Meteorological Society of Japan. Ser. II*, 1961, vol. 39, p. 187
- Yanase W., Niino H., Hodges K., Kitabatake N., Parameter spaces of environmental fields responsible for cyclone development from tropics to extratropics, *Journal of Climate*, 2014, vol. 27, p. 652

Yano J.-I., Emanuel K., An improved model of the equatorial troposphere and its coupling with the stratosphere, *Journal of Atmospheric Sciences*, 1991, vol. 48, p. 377

Zehr R. M., , 1992 Technical Report 61 Tropical cyclogenesis in the western North Pacific. National Environmental Satellite, Data, and Information Service (NESDIS), NOAA USA

Zheng Z., , 2021 zzheng93/pyEOF: First release (v0.0.0)

## Appendix



## Appendix A

---

### Lanczos Filter

#### A.1 Formulation

The Lanczos band-pass filter is mathematically formulated as follows:

$$w(n) = \begin{cases} 2 \cdot (\text{cutoff}_{\text{high}} - \text{cutoff}_{\text{low}}) & \text{if } n = 0 \\ (\text{sinc}(2 \cdot \text{cutoff}_{\text{high}} \cdot n) - \text{sinc}(2 \cdot \text{cutoff}_{\text{low}} \cdot n)) \cdot \text{sinc}\left(\frac{n}{N}\right) & \text{if } n \neq 0 \end{cases} \quad (\text{A.1})$$

where  $n$  is the index of the weight in the filter window,  $w(n)$  is the weight at index  $n$ ,  $\text{cutoff}_{\text{low}}$  and  $\text{cutoff}_{\text{high}}$  are the specified lower and upper cutoff frequencies, respectively, and  $N$  is half the length of the filter window. The *sinc* function is defined as:

$$\text{sinc}(x) = \frac{\sin(\pi x)}{\pi x} \quad (\text{A.2})$$

#### A.2 Related Issues

The Lanczos filter, like other finite impulse response filters (FIR), can exhibit issues at discontinuities in the data. For the vorticity data series, this would be at its endpoints. These issues arise primarily due to the Gibbs phenomenon and edge effects:

1. **Gibbs Phenomenon:** The Gibbs phenomenon refers to the overshoot and ringing that occurs near discontinuities when approximating a function with a finite series of basis functions (Gibbs, 1898; Hamming, 1989). In the context of the Lanczos filter, which utilizes a sinc function, abrupt changes at the edges of the filter window can cause ringing effects at the points of discontinuity in the data.

**2. Edge Effects:** FIR filters, including the Lanczos filter, can produce artifacts at the boundaries of the data series due to the reliance on data points that may not be available at the edges (Oppenheim and Schafer, 2009; Proakis and Manolakis, 2006). Techniques such as zero-padding or reflection are often used to mitigate these effects, but they can still result in artifacts or less accurate filtering near the boundaries.

**3. Finite Window Length:** The window length of the Lanczos filter determines the number of data points used in the convolution. A finite window length means the filter may not fully capture long-term trends or low-frequency components, especially at the edges, leading to discontinuities or spurious oscillations (Smith, 1997; Oppenheim, 1999).

**4. Windowing Effect:** The Lanczos filter uses a windowed *sinc* function to perform the convolution. While windowing reduces spectral leakage by smoothing the transition at the edges of the filter, it also introduces artifacts, particularly near discontinuities where the transition from one region to another is abrupt (Harris, 1978; Mitra, 2001).

To mitigate this, a weaker low-pass Lanczos filter is applied to the initial and final 5% of the data series, ensuring smoother transitions at the endpoints (Figure 3.3b).

## Appendix B

---

### Lorenz Energy Cycle Program Description

To compute the Lorenz Energy Cycle (LEC), an open-source Python application named "lorenz-cycle" was developed and is available on GitHub. The application is designed for collaboration and transparency, allowing peers to freely use, modify, and review the computation procedures. Full documentation and a user guide with illustrative examples can be found at <https://github.com/daniloceano/lorenz-cycle>.

The lorenz-cycle application utilizes the mathematical expressions detailed in Section 2.4.2 and supports both Eulerian and Semi-Lagrangian frameworks. Additionally, it can compute the generation and dissipation terms directly or estimate them as residuals. When using the residual approach, the budget equations are estimated using finite differences: a first-order forward/backward method is applied to the endpoints, while second-order centered differences are employed for the remaining data points. Regardless of whether residuals are estimated or not, the generation terms are always computed.

In the Semi-Lagrangian framework, users can either run the program using a predefined track file or iteratively choose the computation domain step-by-step. For the Eulerian framework, users must provide a "box limits" file containing the minimum and maximum latitudes and longitudes for the desired computational domain. When using a predefined track file, the track may only contain the system's central position (latitude and longitude), in which case the program defaults to a  $15^\circ \times 15^\circ$  domain for each time step. The track file can also be adjusted to include the length and width of the computational domain for each time step.

Additionally, in the Semi-Lagrangian approach, users can provide an input file containing the required meteorological data or, by using an appropriate program flag, automatically download the matching ERA5 dataset using ECMWF's Python plugin "CDS

API” (<https://pypi.org/project/cdsapi/>). To use this option, the user must install and configure the library as instructed at <https://cds.climate.copernicus.eu/api-how-to>.

The program is not limited to the ERA5 dataset and can run with any meteorological dataset, whether it is reanalysis data or model output. It reads a namelist file specifying the variable naming conventions used in the input file. The requirements for the input file are: 1) it must be a NetCDF file, 2) the horizontal grid must be structured, and 3) it must use an isobaric vertical coordinate system. The file should also contain data for temperature, u and v wind components,  $\omega$  vertical wind component, and either geopotential or geopotential height data.

For handling meteorological constants and variable units, the lorenz-cycle program uses the MetPy package (May et al., 2022). This open-source package, initially developed and maintained by the National Science Foundation (NSF) Unidata, a member of the University Corporation for Atmospheric Research (UCAR) Community Programs, ensures correct variable assignment and unit conversion, preventing errors such as summing variables with different units.

To ensure efficient and fast computations, the program is fully parallelized using Dask, a parallel computing library that handles large datasets efficiently (Daniel, 2019). Dask allows large data arrays to be split into smaller chunks for independent processing by multiple computing cores, preventing memory overload and optimizing performance. In the lorenz-cycle program, Dask’s configuration is optimized to handle large matrices by dividing them into smaller chunks for efficient processing.

The program outputs the results for each term in comma-separated values (CSV) files. It generates one CSV file for each term, and for energy, conversion, and generation terms, it also provides results for each vertical level, enabling a two-dimensional analysis. Additionally, the program can be configured by the user to automatically generate plots. These plots include spatial representations of the computational domain defined for the analysis, time series of the system’s central minimum pressure and relative vorticity at 850 hPa, time series of each LEC term, Hovmöller diagrams, and complete energy flux boxes for the LEC.

## Appendix C

---

### Complete Life Cycle LEC EOFs Reconstructed

Figures C.1 illustrate the reconstructed EOFs for the complete life cycle. These EOFs were reconstructed by reversing the normalization process and adding the mean values to each EOF.

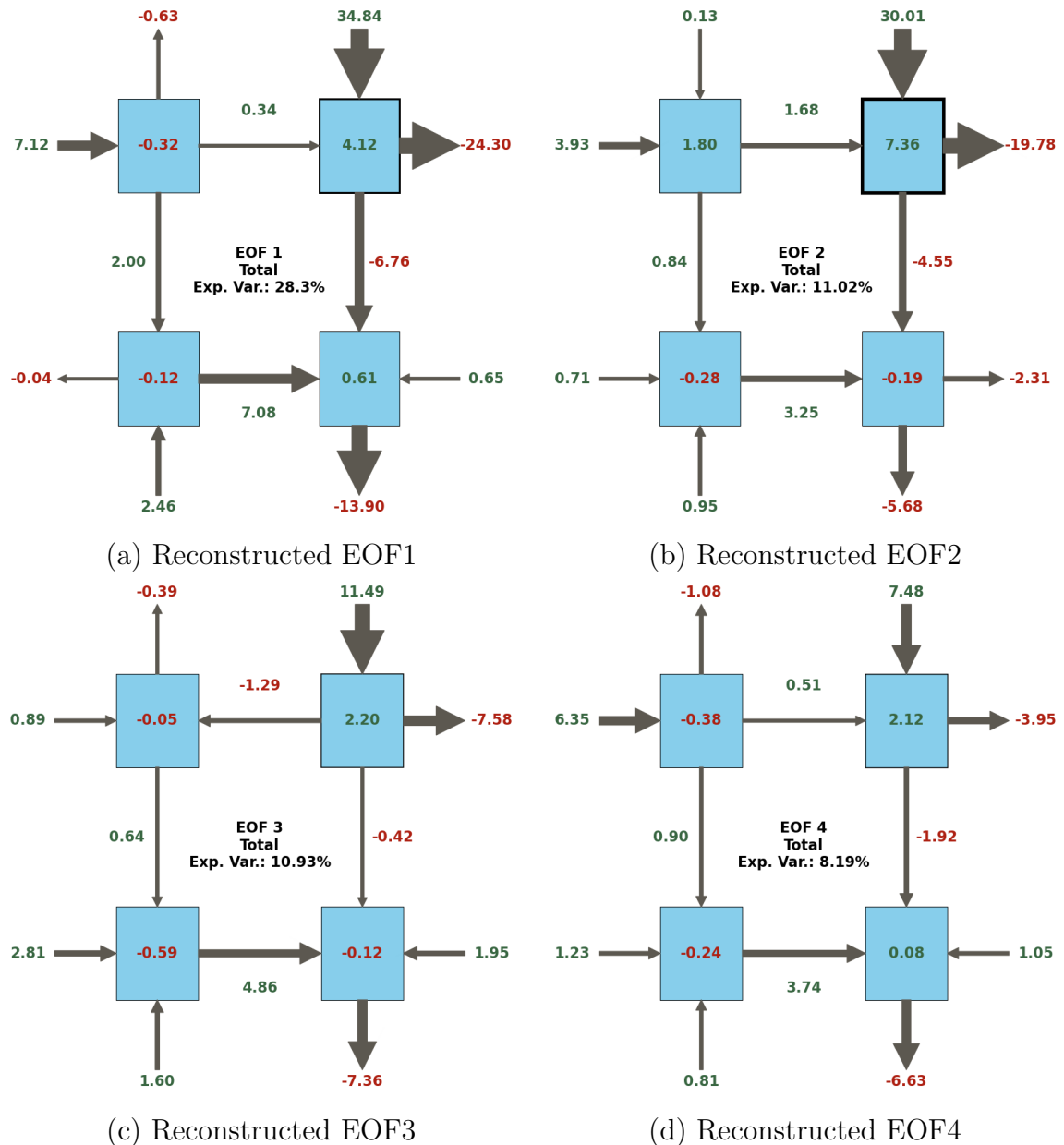


Figure C.1: Lorenz Energy Cycle (LEC) Terms EOFs reconstructed. The numbers adjacent to the arrows denote the magnitude and direction of the anomaly, with green indicating positive values and red indicating negative values.

## Appendix D

---

### LEC - Terms Correlation

Figure D.1 presents correlation plots between the conversion terms  $C_A$  and  $C_E$  (Figure D.1a) and between eddy kinetic energy  $K_E$  and relative vorticity at 850 hPa in the cyclone center (Figure D.1b).

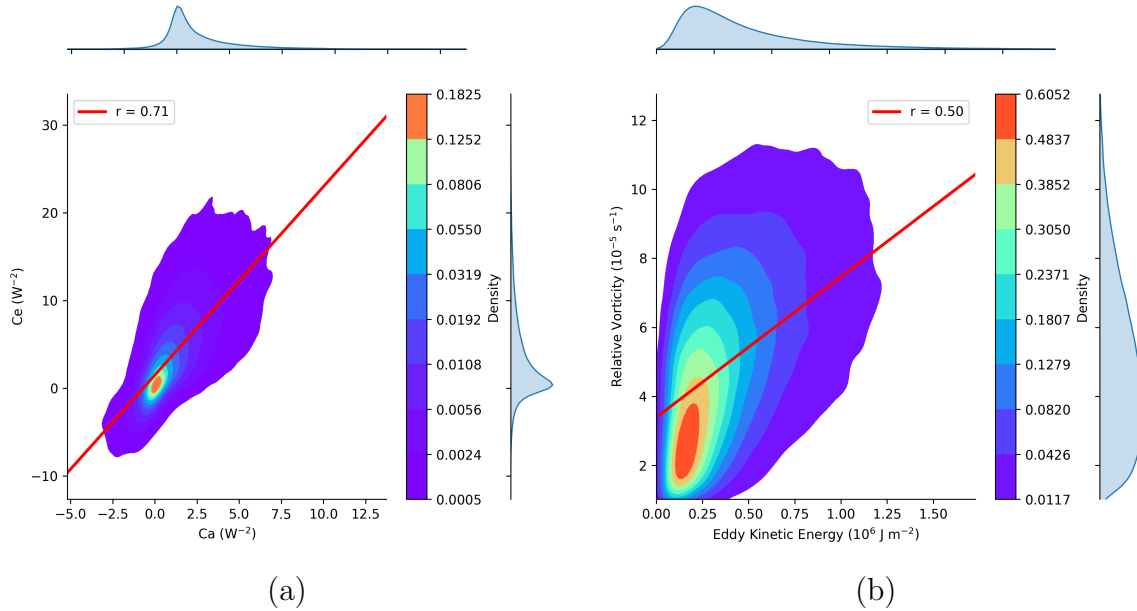


*Figure D.1:* Correlation between  $C_A$  and  $C_E$  (a), as well as between  $K_E$  and relative vorticity at 850 hPa in the cyclone center (b). The red line represents the linear regression, with the Pearson's correlation coefficient ( $r$ ) indicated in each plot.



## Appendix E

---

### LEC Results for Reg1 System

Here, the same analysis conducted by Dias Pinto and Rocha (2011) is performed for the "Reg1" system. The aim is to validate the results obtained by the "lorenz-cycle" program and provide support for the analysis performed using the Lorenz Phase Space Diagrams. Figure E.1 illustrates the computational domain used for computing the LEC for this system, while Figure E.2 displays the energy and conversion terms, matching Figure 5 from Dias Pinto and Rocha (2011).

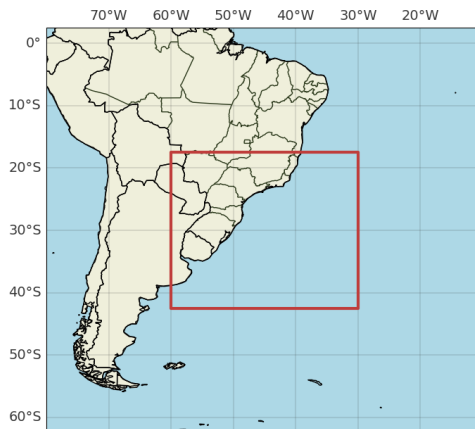


Figure E.1: Computational domain used for analyzing the "Reg1" system (Dias Pinto and Rocha, 2011).

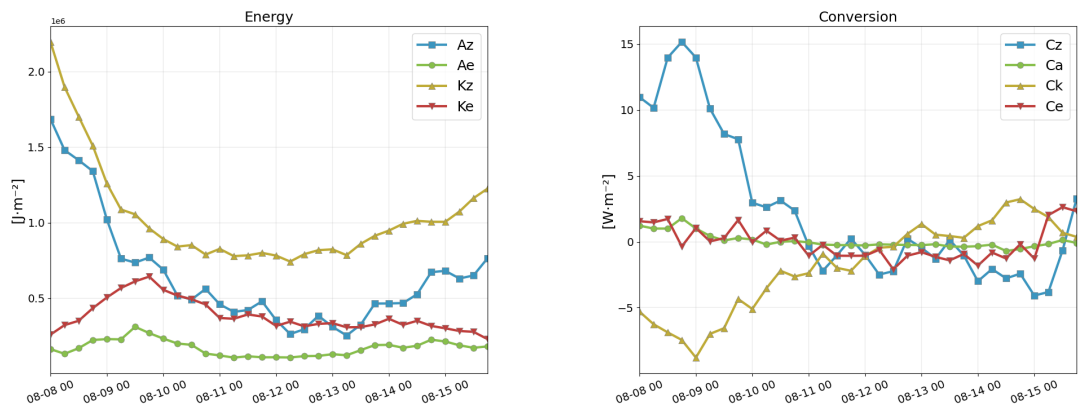


Figure E.2: Energy and conversion terms computed for the "Reg1" system (Dias Pinto and Rocha, 2011), using an Eulerian framework (Figure E.1).

## Appendix F

---

### Lorenz Phase Space - All Systems

Figures F.1 and F.2 illustrate the LPS diagrams for all systems with genesis in ARG, LA-PLATA, and SE-BR between 1979 and 2020. Due to the large amount of data and the presence of outliers, it is not possible to discern the relative importance of the LEC terms for smaller groups of systems precisely. However, the LPS visualization still provides an overview of the main mechanisms related to cyclone development in the SESA region.

For LPS diagram type 1, a cloud of data spreads primarily over the top-left quadrant. Moreover, there is a high density below the 1:1 diagonal line. This indicates that for most systems, there is a shared importance of baroclinic and barotropic conversions for eddy development, as indicated in previous chapters. For diagram type 2, a clear distinct tendency cannot be found from this analysis, indicating a high quantity of systems that either import or export both  $A_E$  and  $K_E$ .

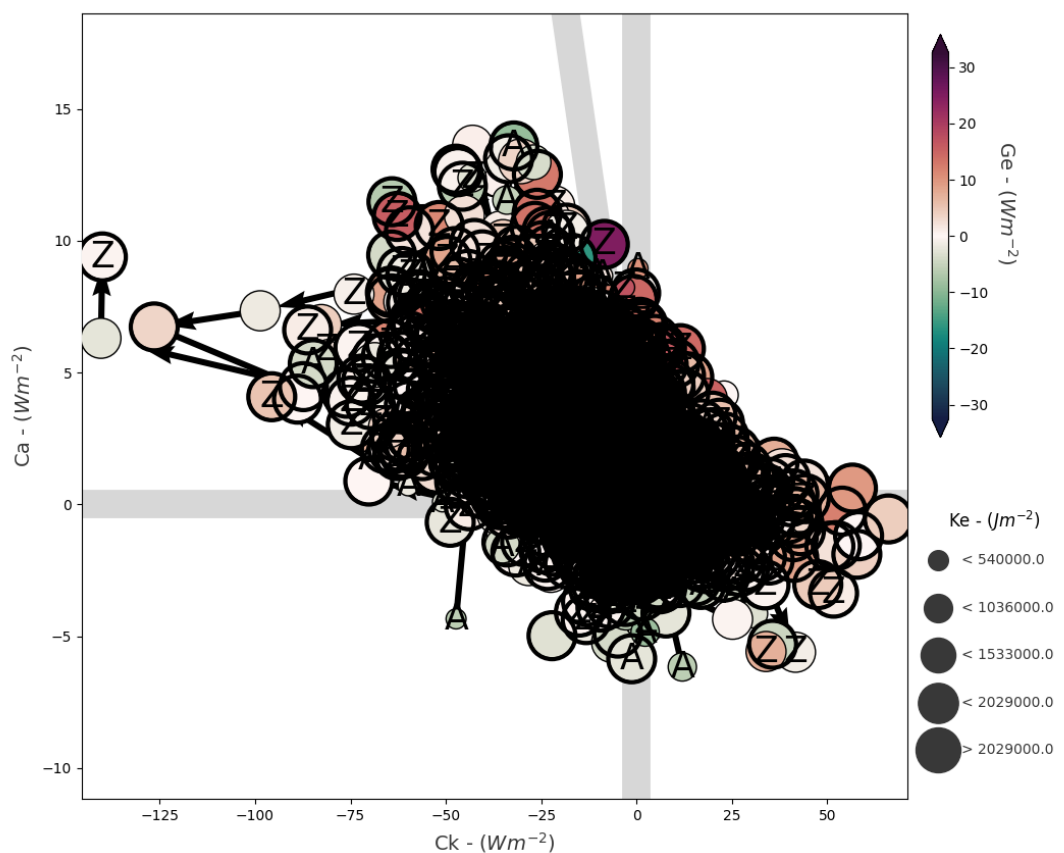


Figure F.1: Lorenz Phase Space (LPS) diagram 1 for all systems with genesis near South America.

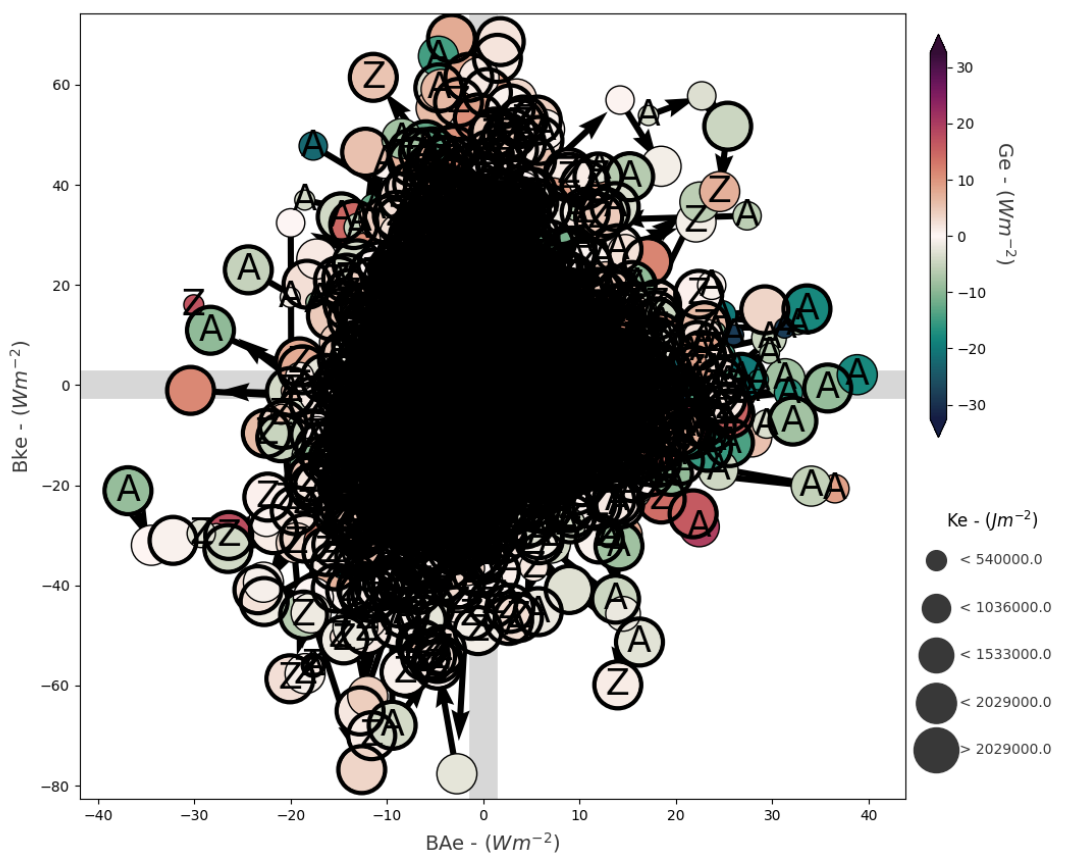


Figure F.2: Lorenz Phase Space (LPS) diagram 2 for all systems with genesis near South America.



## Appendix G

---

### Lorenz Phase Space 1 - Early Decay

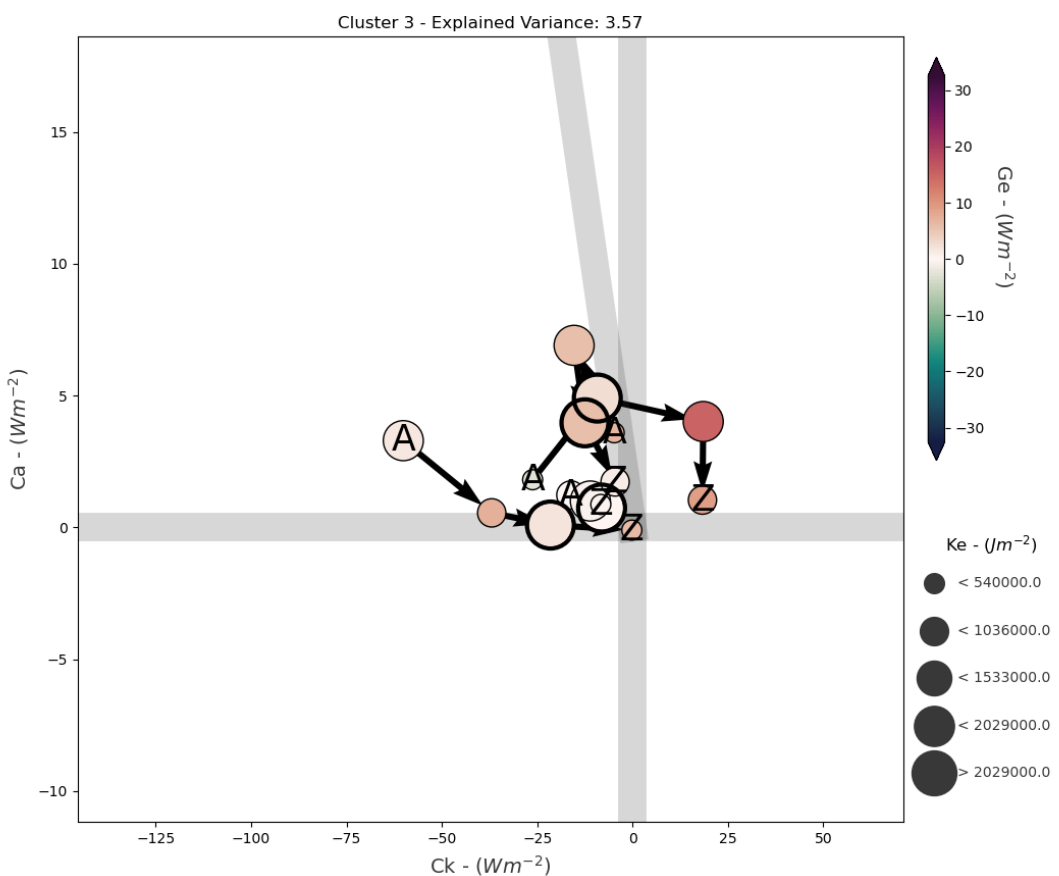


Figure G.1: Lorenz Phase Space (LPS) diagram 1 for all systems represented in cluster 3 of the "decay, intensification, matude, decay 2" life cycle.



## Appendix H

---

### Lorenz Phase Space - Most Intense Systems

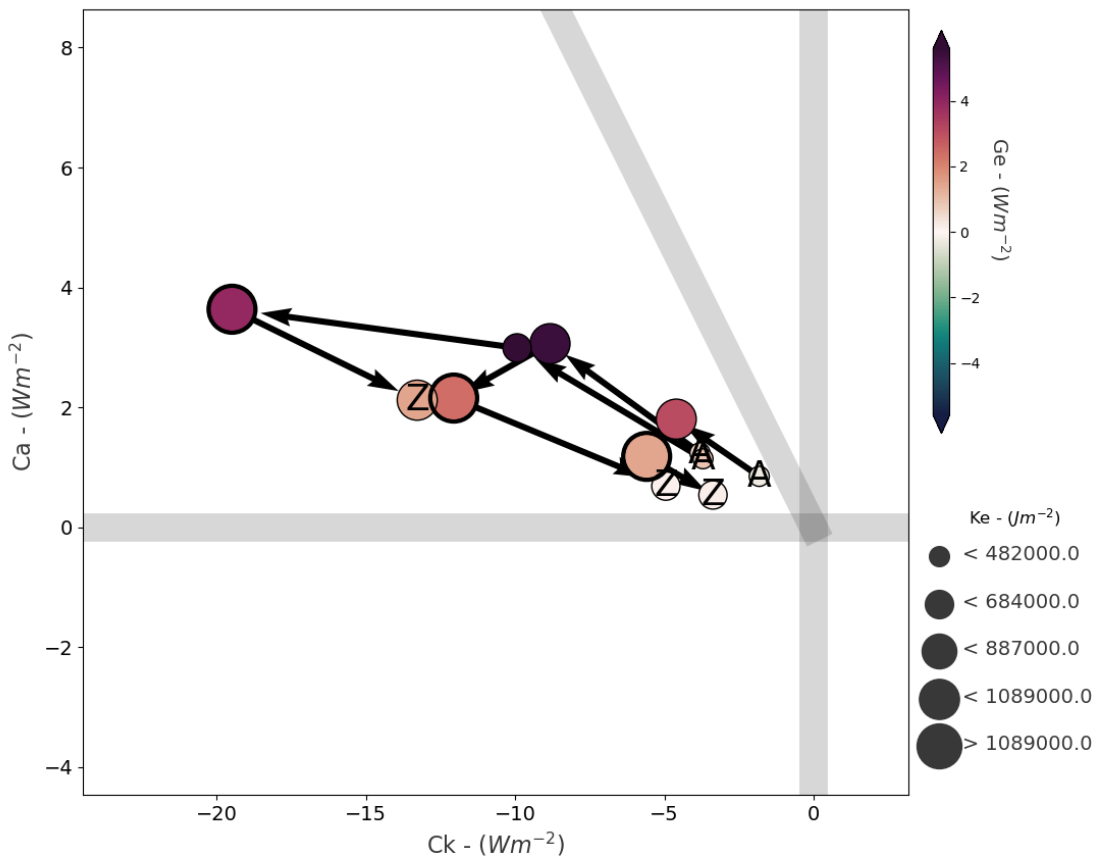


Figure H.1: Lorenz Phase Space (LPS) diagram 1 for the energy patterns of the systems presenting central relative vorticity higher than the 0.9 quantile.



## Appendix I

---

### Tracks - Energy Pattern 1

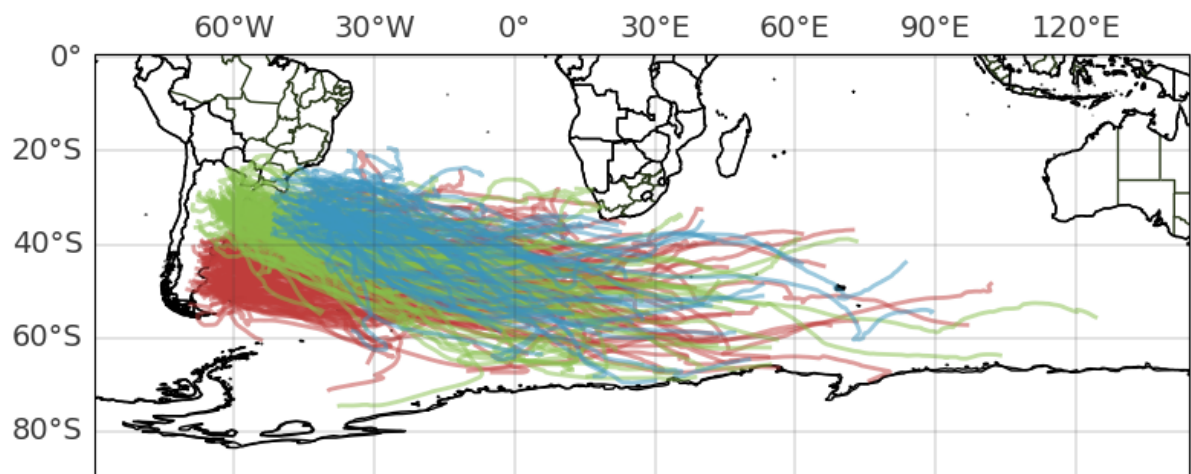


Figure I.1: Cyclone tracks associated with energy pattern (EP) 1.